



2014

# MULTI-COMPONENT MICROPARTICULATE/ NANOPARTICULATE DRY POWDER INHALATION AEROSOLS FOR TARGETED PULMONARY DELIVERY

Xiaojian Li

University of Kentucky, OWENLI6@HOTMAIL.COM

**[Click here to let us know how access to this document benefits you.](#)**

---

## Recommended Citation

Li, Xiaojian, "MULTI-COMPONENT MICROPARTICULATE/NANOPARTICULATE DRY POWDER INHALATION AEROSOLS FOR TARGETED PULMONARY DELIVERY" (2014). *Theses and Dissertations--Pharmacy*. 31.  
[https://uknowledge.uky.edu/pharmacy\\_etds/31](https://uknowledge.uky.edu/pharmacy_etds/31)

This Doctoral Dissertation is brought to you for free and open access by the College of Pharmacy at UKnowledge. It has been accepted for inclusion in Theses and Dissertations--Pharmacy by an authorized administrator of UKnowledge. For more information, please contact [UKnowledge@lsv.uky.edu](mailto:UKnowledge@lsv.uky.edu).

**STUDENT AGREEMENT:**

I represent that my thesis or dissertation and abstract are my original work. Proper attribution has been given to all outside sources. I understand that I am solely responsible for obtaining any needed copyright permissions. I have obtained needed written permission statement(s) from the owner(s) of each third-party copyrighted matter to be included in my work, allowing electronic distribution (if such use is not permitted by the fair use doctrine) which will be submitted to UKnowledge as Additional File.

I hereby grant to The University of Kentucky and its agents the irrevocable, non-exclusive, and royalty-free license to archive and make accessible my work in whole or in part in all forms of media, now or hereafter known. I agree that the document mentioned above may be made available immediately for worldwide access unless an embargo applies.

I retain all other ownership rights to the copyright of my work. I also retain the right to use in future works (such as articles or books) all or part of my work. I understand that I am free to register the copyright to my work.

**REVIEW, APPROVAL AND ACCEPTANCE**

The document mentioned above has been reviewed and accepted by the student's advisor, on behalf of the advisory committee, and by the Director of Graduate Studies (DGS), on behalf of the program; we verify that this is the final, approved version of the student's thesis including all changes required by the advisory committee. The undersigned agree to abide by the statements above.

Xiaojian Li, Student

Dr. Heidi M. Mansour, Major Professor

Dr. Jim Pauly, Director of Graduate Studies

---

MULTI-COMPONENT MICROPARTICULATE/NANOPARTICULATE DRY  
POWDER INHALATION AEROSOLS FOR TARGETED PULMONARY DELIVERY

---

DISSERTATION

---

A dissertation submitted in partial fulfillment of the  
requirements for the degree of Doctor of Philosophy in the  
College of Pharmacy  
at the University of Kentucky

By  
Xiaojian Li

Lexington, Kentucky

Co-Directors: Dr. Heidi M. Mansour, Assistant Professor of Pharmaceutics  
The University of Arizona, Tucson, Arizona  
and Dr. Paul M. Bummer, Associate Professor of Pharmaceutical Sciences  
University of Kentucky, Lexington, Kentucky  
2014

Copyright © Xiaojian Li 2014

## ABSTRACT OF DISSERTATION

### MULTI-COMPONENT MICROPARTICULATE/NANOPARTICULATE DRY POWDER INHALATION AEROSOLS FOR TARGETED PULMONARY DELIVERY

The aim of the work was to design, manufacture, and characterize targeted multi-component dry powder aerosols of (non-destructive) mucolytic agent (mannitol), antimicrobial drug (tobramycin or azithromycin), and lung surfactant mimic phospholipids (DPPC:DPPG=4:1 in molar ratio). The targeted dry powder for inhalation formulation for deep lung delivery with a built-in rationale of specifically interfering several disease factors of chronic infection diseases in deep lungs such as cystic fibrosis, pneumonia, chronic bronchitis, and etc. The dry powder aerosols consisting of selected chemical agents in one single formulation was generated by using spray drying from organic solution.

The physicochemical properties of multi-component dry powder inhaler (DPI) formulation were characterized by a number of techniques. In addition, the *in vitro* aerosol dispersion performance, storage stability test, and *in vitro* drug release of selected spray-dried (SD) multi-component systems were conducted.

The physicochemical study revealed that multi-component aerosol particles possessed essential particle properties suitable for deep lung delivery. In general, the multi-component particles (typically 0.5 to 2  $\mu\text{m}$ ) indicated that the designed SD aerosol particles could potentially penetrate deep lung regions (such as respiratory bronchiolar and alveolar regions) by sedimentation and diffusion, respectively. The essential particle properties including narrow size distribution, spherical particle and smooth surface morphologies, and low water content (or water vapor sorption) could potentially minimize interparticulate interactions. The study of *in vitro* aerosol dispersion performance showed that majority of SD multi-component aerosols exhibited low values (less than 5 $\mu\text{m}$ ) of MMAD, high values (approximately above 30% up to 60.4%) of FPF, and high values (approximately above 90%) of ED, respectively. The storage stability study showed that azithromycin-incorporated multi-component aerosol particles stored at 11 and 40% RH with no partial crystallization were still suitable for deep lung delivery. Compared to SD pure azithromycin particles, the azithromycin-incorporated multi-component particles exhibited an enhanced initial release.

The targeted microparticulate and nanoparticulate multi-component dry powder aerosol formulations with essential particle properties for deep lung pulmonary delivery were successfully produced by using spray drying from organic solution. The promising experimental data suggest the multi-component formulations could be further investigated in *in vivo* studies for the purpose of commercialization.

**KEYWORDS:** aerosol dispersion performance, dry powder inhaler (DPI), spray drying, physicochemical characterization, *in vitro* storage stability and drug release

Xiaojian Li  
\_\_\_\_\_  
Student's Signature

04/11/2014  
\_\_\_\_\_  
Date

MULTI-COMPONENT MICROPARTICULATE/NANOPARTICULATE DRY  
POWDER INHALATION AEROSOLS FOR TARGETED PULMONARY DELIVERY

By

Xiaojian Li

Heidi M. Mansour, Ph.D.  
Co-Director of Dissertation

Paul M. Bummer, Ph.D.  
Co-Director of Dissertation

Jim Pauly, Ph.D.  
Director of Graduate Studies

04/11/2014

Date

## ACKNOWLEDGEMENTS

I would like to express my sincerest thanks to many people for their kind supports and helps during my graduate study at the University of Kentucky. First, I am grateful to my advisor, Dr. Heidi Mansour, who brought me into this field and patiently guided me throughout my graduate study. Her hard-working inspired me a lot. In addition, I would like to thank my co-advisor Dr. Paul Bummer. He trained me how to solve research problems with critical and logical thinking which will benefit my future career and whole life. With his advice, encouragement, and help, I was able to complete the rest part of my research and get a job on time. I would like my committee member, Dr. Tonglei Li, for his insightful comments on my research and for using the instruments in his lab. I would like to thank my committee member, Dr. Barbara Knutson, for her great advices and patience throughout my study. I would also like to thank Dr. William Stoops for serving as the outside examiner of my thesis defense.

Besides, I would like to thank my previous labmates of Dr. Yun-Seok Rhee, Dr. Xiao Wu, Dr. Chun-Woong Park, Dr. Samantha Meenach, Dr. Jinghua Duan, Dr. Weifen Zhang, Minji Sohn, Oreoluwa Adedoyin, Jiayue Ma, and Nathanael Stocke and current group members of Dr. Eric Munson (professor), Dr. Matthew Nethercott, Dr. Sarah Pyszcinski, Dr. Andrei Ponta, Xiaoda Yuan, Nico Setiawan, Nickolas Winkvist, and Kanika Sarpal for their helps, supports and friendship in the past years. I also thank Ms. Catina Rossoll for her kind help throughout my graduate study.

Finally, I would like to thank my father (Ruiyun Li), my mother (Caiwei Ye), and my brother (Xiaoqi Li) for their selfless and endless love, sacrifices, and constant supports during my whole life. I would also thank my wife, Chaoqun Wang, whose love and support are my immeasurable strengths. Finally, I would like to specially thank my son, Carson C. Li, who has been inspiring me to work hard for my career development.

## TABLE OF CONTENTS

ACKNOWLEDGEMENTS.....	iii
TABLE OF CONTENTS.....	iv
LIST OF TABLES.....	ix
LIST OF FIGURES .....	xi
Chapter 1 General Introduction .....	1
1.1 Characteristics of the Lung.....	1
1.1.1 Anatomy of the Airways.....	1
1.1.2 Physiology of the Airways.....	3
1.1.3 Blood Circulation.....	5
1.2 Aerosol Particle Deposition Mechanisms in Human Lungs.....	5
1.3 Pulmonary Aerosol Drug Delivery .....	7
1.3.1 Nebulizers .....	7
1.3.2 Pressurized Metered-Dose Inhaler (pMDIs).....	8
1.3.3 Dry Powder Inhalers (DPIs).....	10
1.3.4 Soft-Mist Inhalers (SMIs) .....	11
1.4 Interparticulate Forces .....	12
1.5 Spray Drying.....	15
1.6 Chronic Infections in the Deep Lungs (Cystic Fibrosis/Pulmonary Infections).....	17
1.6.1 Disease Background.....	17
1.6.2 Disease Treatment.....	18
Chapter 2 Statement of Aims.....	22
2.1 Statement of Problem.....	22
2.2 Goal of Dissertation and Specific Aims.....	22



2.2.1 Goal of Dissertation .....	22
2.2.2 Specific Aims.....	22
2.3 Significance.....	23
Chapter 3 Aerosol Particle Design and Manufacturing .....	24
3.1 Introduction.....	24
3.2 Materials and Methods.....	26
3.2.1 Materials .....	26
3.2.2 Methods.....	27
3.3 Results.....	29
3.3.1 Scanning Electron Microscopy (SEM) .....	29
3.3.2 Particle Sizing and Size Distribution .....	35
3.4 Discussion .....	38
3.4.1 Pump Rate Effect .....	38
3.4.2 Formulation Composition Effect .....	38
3.5 Conclusions.....	39
Chapter 4 Physicochemical Characterization .....	40
4.1 Introduction.....	40
4.2 Materials and Methods.....	42
4.2.1 Materials .....	42
4.2.2 Methods.....	43
4.3 Results.....	45
4.3.1 Crystallinity and Polymorphism .....	45
4.3.2 Solid-State Phase Transition .....	50
4.3.3 Water Content .....	63
4.3.4 Water Vapor Sorption .....	65

4.3.5 Chemical Spectroscopy.....	68
4.4 Discussion .....	77
4.4.1 Crystallinity and Polymorphism .....	77
4.4.2 Solid-State Phase Transition .....	77
4.4.3 Water Content .....	82
4.4.4 Water Vapor Sorption .....	84
4.4.5 Chemical Spectroscopy.....	87
4.5 Conclusions.....	88
Chapter 5 <i>in vitro</i> Aerosol Dispersion .....	89
5.1 Introduction.....	89
5.2 Materials and Methods.....	91
5.2.1 Materials .....	91
5.2.2 Methods.....	91
5.3 Results.....	93
5.3.1 One-component System (Spray-dried Pure Drug).....	93
5.3.2 Two-component System (Spray-dried Drug:Mannitol and Drug:Phospholipids) .....	95
5.3.3 Three-component System (Spray-dried Drug:Phospholipids:Mannitol) .....	99
5.3.4 Validation of Gravimetric Analysis Method.....	101
5.4 Discussion .....	102
5.4.1 Effect of Mannitol on Spray-Dried Drug:Mannitol .....	103
5.4.2 Effect of Phospholipids on Spray-Dried Drug:Phospholipids .....	104
5.4.3 Effect of Mannitol on Spray-Dried Drug:Phospholipids:Mannitol .....	105
5.5 Conclusions.....	105
Chapter 6 Storage Stability .....	107

6.1 Introduction.....	107
6.2 Materials and Methods.....	107
6.2.1 Materials .....	107
6.2.2 Methods.....	108
6.3 Results.....	108
6.3.1 X-Ray Powder Diffraction (XRPD).....	108
6.3.2 Aerosol Dispersion Performance .....	119
6.4 Discussion .....	126
6.5 Conclusions.....	129
Chapter 7 <i>in vitro</i> Drug Release.....	130
7.1 Introduction.....	130
7.2 Materials and Methods.....	131
7.2.1 Materials .....	131
7.2.2 Methods.....	131
7.3 Results.....	131
7.3.1 Validations .....	131
7.3.2 Release Data.....	134
7.4 Discussion .....	138
7.4.1 Validation of Release Assumptions .....	138
7.4.2 Drug Release.....	141
7.5 Conclusions.....	143
Chapter 8 Summary and Conclusions.....	144
8.1 General Conclusions .....	144
8.2 Future Work .....	145
Appendices.....	147

Appendix A Spray-Dried Mannitol Aerosols .....	148
Appendix B Spray-Dried Trehalose Aerosols .....	171
Appendix C Spray-Dried Itraconazole Aerosols .....	189
References .....	197
Vita.....	218

## LIST OF TABLES

Table 3.1. Summary of spray drying conditions of tobramycin relevant formulations....	28
Table 3.2. Summary of spray drying conditions of azithromycin relevant formulations..	28
Table 3.3. Laser diffraction sizing of SD pure tobramycin particles (mean $\pm$ SD, n=3)...	35
Table 3.4. Image sizing of SD pure azithromycin primary particles (mean $\pm$ SD, n $\geq$ 100).....	35
Table 3.5. Laser diffraction sizing of SD tobramycin:mannitol particles (mean $\pm$ SD, n=3).....	36
Table 3.6. Image sizing of SD azithromycin:mannitol primary particles (mean $\pm$ SD, n $\geq$ 100).....	36
Table 3.7. Image sizing of SD drug:phospholipids primary particles (mean $\pm$ SD, n $\geq$ 100).....	37
Table 3.8. Image sizing of SD drug:phospholipids:mannitol primary particles (mean $\pm$ SD, n $\geq$ 100).....	37
Table 4.1. SD particles for physicochemical characterization.....	43
Table 4.2. Glass transition temperatures for SD tobramycin:mannitol and SD azithromycin:mannitol (mean $\pm$ SD, n=3).....	53
Table 4.3. Summary of glass transition temperature ( $T_g$ ), main phase transition temperature of phospholipid bilayer ( $T_m$ ), adjusted enthalpy of main phase transition of phospholipid bilayer ( $\Delta H_m$ ), crystallization temperature ( $T_c$ ), and melting temperature ( $T_{m1}$ ) for SD tobramycin:phospholipids (TOB:PLS) and SD azithromycin:phospholipids (AZI:PLS) formulations in DSC (mean $\pm$ SD, n=3).....	57
Table 4.4. Summary of glass transition temperature ( $T_g$ ), main phase transition temperature of phospholipid bilayer ( $T_m$ ), adjusted enthalpy of main phase transition of phospholipid bilayer ( $\Delta H_m$ ), crystallization temperature ( $T_c$ ), and melting temperature ( $T_{m1}$ and $T_{m2}$ ) for tobramycin:phospholipids:mannitol and azithromycin:phospholipids:mannitol in DSC (mean $\pm$ SD, n=3).....	60
Table 4.5. Water content for tobramycin and azithromycin formulations (mean $\pm$ SD, n=3).....	64
Table 4.6. Calculated water content for tobramycin and azithromycin formulations (mean $\pm$ SD, n=3).....	83
Table 5.1. SD particles for the NGI study.....	91

Table 5.2. Aerosol dispersion performance parameters of SD pure tobramycin and SD pure azithromycin dry powders (mean $\pm$ margin of error for 95% confidence, n=3).....	95
Table 5.3. Aerosol dispersion performance parameters of SD tobramycin:mannitol particles (mean $\pm$ margin of error for 95% confidence, n=3).....	97
Table 5.4. Aerosol dispersion performance parameters of SD azithromycin:mannitol particles (mean $\pm$ margin of error for 95% confidence, n=3).....	97
Table 5.5. Aerosol dispersion performance parameters of SD tobramycin:phospholipids particles (mean $\pm$ margin of error for 95% confidence, n=3).....	99
Table 5.6. Aerosol dispersion performance parameters of SD azithromycin:phospholipids particles (mean $\pm$ margin of error for 95% confidence, n=3).....	99
Table 5.7. Aerosol dispersion performance parameters of SD tobramycin:phospholipids:mannitol particles (mean $\pm$ margin of error for 95% confidence, n=3).....	101
Table 5.8. Aerosol dispersion performance parameters of SD azithromycin:phospholipids:mannitol particles (mean $\pm$ margin of error for 95% confidence, n=3).....	101
Table 5.9. The data for glass filter treatment experiment.....	101
Table 6.1. Aerosol dispersion performance parameters of SD tobramycin powders (fresh vs stored at 11% RH and 40°C) (mean $\pm$ SD, n=3). Definition: ED[%]=emitted dose fraction; FPF[%]=fine particle fraction; RF[%]=respirable fraction; MMAD[ $\mu$ m]=mass median aerodynamic diameter; GSD=geometric standard deviation.....	124
Table 6.2. Aerosol dispersion performance parameters of SD azithromycin powders (fresh vs stored at three different RH % and 40°C) (mean $\pm$ SD, n=3). Definition: ED[%]=emitted dose fraction; FPF[%]=fine particle fraction; RF[%]=respirable fraction; MMAD[ $\mu$ m]=mass median aerodynamic diameter; GSD=geometric standard deviation.....	125
Table 7.1. The mean response factor and coefficient of variance for each standard azithromycin solution.....	132
Table 7.2. The azithromycin adsorbance data for centrifugal filter units.....	134
Table 7.3. The azithromycin absorbance data for release vials.....	134

## LIST OF FIGURES

Figure 1.1. Schematic of the respiratory system.....	1
Figure 1.2. Schematic of Weibel airway model.....	2
Figure 1.3. Comparison of the lung epithelium at different airways.....	3
Figure 1.4. Structure of an alveolus.....	4
Figure 1.5. Schematic of a jet nebulizer.....	7
Figure 1.6. Schematic of an ultrasonic nebulizer.....	8
Figure 1.7. Schematic of a pressurized metered-dose inhaler.....	9
Figure 1.8. Schematic of the Handihaler <sup>®</sup> DPI device.....	11
Figure 1.9. Schematic of the Respimat <sup>®</sup> soft-mist inhaler.....	12
Figure 1.10. Schematic of a spray dryer.....	16
Figure 3.1. Illustration of interparticulate forces in static dry powder.....	24
Figure 3.2. The chemical structures for: (a) tobramycin; (b) azithromycin; (c) dipalmitoylphosphatidylcholine (DPPC); (d) dipalmitoylphosphatidylglycerol sodium salt (DPPG); and (e) D-mannitol.....	27
Figure 3.3. SEM micrographs of as received particles (magnification 100X) and SD pure particles (magnification 10,000X) of tobramycin (TOB) and azithromycin (AZI) for: (a) As received TOB; (b) SD pure TOB (10%P); (c) SD pure TOB (50%P); (d) SD pure TOB (100%P); (e) As received AZI; (f) SD pure AZI (10%P); (g) SD pure AZI (50%P); and (h) SD pure AZI (100%P).....	31
Figure 3.4. SEM micrographs of SD tobramycin:mannitol (TOB:MAN) and SD azithromycin:mannitol (AZI:MAN) particles (magnification 10,000X) for: (a) TOB:MAN=1:0.1; (b) TOB:MAN=1:0.25; (c) TOB:MAN=1:0.5; (d) TOB:MAN=1:0.75; (e) TOB:MAN=1:1; (f) AZI:MAN=1:0.1; (g) AZI:MAN=1:0.25; (h) AZI:MAN=1:0.5; (i) AZI:MAN=1:0.75; and (j) AZI:MAN=1:1.....	32
Figure 3.5. SEM micrographs of SD tobramycin:phospholipids (TOB:PLS) and SD azithromycin:phospholipids (AZI:PLS) particles (magnification 10,000X) for: (a) TOB:PLS=1:2; (b) TOB:PLS=1:1; (c) TOB:PLS=1:0.5; (d) AZI:PLS=1:2; (e) AZI:PLS=1:1; and (f) AZI:PLS=1:0.5.....	33

Figure 3.6. SEM micrographs of SD tobramycin:phospholipids:mannitol (TOB:PLS:MAN) and SD azithromycin:phospholipids:mannitol (AZI:PLS:MAN) particles (magnification 10,000X) for: (a) TOB:PLS:MAN=1:0.5:0.1; (b) TOB:PLS:MAN=1:0.5:0.25; (c) TOB:PLS:MAN=1:0.5:0.5; (d) TOB:PLS:MAN=1:0.5:0.75; (e) TOB:PLS:MAN=1:0.5:1; (f) AZI:PLS:MAN=1:0.5:0.1; (g) AZI:PLS:MAN=1:0.5:0.25; (h) AZI:PLS:MAN=1:0.5:0.5; (i) AZI:PLS:MAN=1:0.5:0.75; and (j) AZI:PLS:MAN=1:0.5:1.....	34
Figure 4.1. X-ray powder diffractograms for: (a) SD pure and as received tobramycin particles (offset by 4000 counts); and (b) SD pure and as received azithromycin particles (offset by 7000 counts).....	46
Figure 4.2. X-ray powder diffraction patterns for: (a) SD tobramycin:mannitol formulations (offset by 500 counts between patterns); and (b) SD azithromycin:mannitol formulations (offset by 500 counts between patterns for the bottom four; offset by 1000 counts between patterns for the top two).....	47
Figure 4.3. X-ray powder diffraction patterns for: (a) SD tobramycin:phospholipids formulations (offset by 500 counts between patterns); and (b) SD azithromycin:phospholipids formulations (offset by 500 counts between patterns).....	49
Figure 4.4. X-ray powder diffraction patterns for: (a) SD tobramycin:phospholipids:mannitol formulations (offset by 500 counts between patterns); and (b) SD azithromycin:phospholipids:mannitol formulations (offset by 500 counts between patterns).....	50
Figure 4.5. Schematic of a typical glass transition of drug and a main phase transition of phospholipid bilayer in the spray-dried powder.....	51
Figure 4.6. DSC thermograms for: (a) as received tobramycin; (b) SD pure tobramycin; (c) as received azithromycin; (d) SD pure azithromycin.....	52
Figure 4.7. DSC thermograms for: (a) tobramycin:mannitol=1:0.1; (b) tobramycin:mannitol=1:0.25; (c) tobramycin:mannitol=1:0.5; (d) tobramycin:mannitol=1:0.75; and (e) tobramycin:mannitol=1:1.....	54
Figure 4.8. DSC thermograms for: (a) azithromycin:mannitol=1:0.1; (b) azithromycin:mannitol=1:0.25; (c) azithromycin:mannitol=1:0.5; (d) azithromycin:mannitol=1:0.75; and (e) azithromycin:mannitol=1:1.....	55
Figure 4.9. DSC thermograms (non-hermetic) for: (a) azithromycin:mannitol=1:0.1; (b) azithromycin:mannitol=1:0.25; (c) azithromycin:mannitol=1:0.5; (d) azithromycin:mannitol=1:0.75; and (e) azithromycin:mannitol=1:1.....	56
Figure 4.10. DSC thermograms of SD drug:phospholipids formulations for: (a) tobramycin:phospholipids=1:2; (b) tobramycin:phospholipids=1:1; (c)	



tobramycin:phospholipids=1:0.5; (d) azithromycin:phospholipids=1:2; (e) azithromycin:phospholipids=1:1; and (f) azithromycin:phospholipids=1:0.5.....	58
Figure 4.11. DSC thermograms of SD tobramycin three-components formulations for: (a) tobramycin:phospholipids:mannitol=1:0.5:0.1; (b) tobramycin:phospholipids:mannitol=1:0.5:0.25; (c) tobramycin:phospholipids:mannitol=1:0.5:0.5; (d) tobramycin:phospholipids:mannitol=1:0.5:0.75; and (e) tobramycin:phospholipids:mannitol=1:0.5:1.....	61
Figure 4.12. DSC thermograms of SD azithromycin three-components formulations for: (a) azithromycin:phospholipids:mannitol=1:0.5:0.1; (b) azithromycin:phospholipids:mannitol=1:0.5:0.25; (c) azithromycin:phospholipids:mannitol=1:0.5:0.5; (d) azithromycin:phospholipids:mannitol=1:0.5:0.75; and (e) azithromycin:phospholipids:mannitol=1:0.5:1.....	62
Figure 4.13. Water vapor sorption isotherms at 25°C for as received vs SD powders (weight change % vs RH; n=1).....	65
Figure 4.14. Water vapor sorption isotherms at 25°C for SD tobramycin:mannitol=1:0.5 and SD azithromycin:mannitol=1:0.5 (weight change % vs RH; n=1).....	66
Figure 4.15. Water vapor sorption isotherms at 25°C for SD tobramycin:phospholipids=1:0.5 and SD azithromycin:phospholipids=1:0.5 (weight change % vs RH; n=1).....	67
Figure 4.16. Water vapor sorption isotherms at 25°C for SD tobramycin:phospholipids:mannitol=1:0.5:0.5 and SD azithromycin:phospholipids:mannitol=1:0.5:0.5 (weight change % vs RH; n=1).....	68
Figure 4.17. (a). Raman spectrum of SD pure tobramycin compared to that of as received tobramycin obtained using CRM; (b). Brightfield micrograph of SD pure tobramycin obtained using a 10x objective; and (c). Fluorescence micrograph of SD pure tobramycin obtained using a 10x objective. The red points show the location at which the SD spectrum in (a) was obtained. Courtesy of Dr. Frederick Vogt at GlaxoSmithKline.....	69
Figure 4.18. (a). Raman spectrum of SD pure azithromycin compared to that of as received azithromycin obtained using CRM; (b). Brightfield micrograph of SD pure azithromycin obtained using a 10x objective; and (c). Fluorescence micrograph of SD pure azithromycin obtained using a 10x objective. The red points show the location at which the SD spectrum in (a) was obtained. Courtesy of Dr. Frederick Vogt at GlaxoSmithKline.....	70
Figure 4.19. (a) Brightfield micrograph of SD tobramycin:mannitol=1:0.5 particles	

obtained using a 10x objective. CRM mapping was performed in the region marked with the red box; increasing blue color corresponds to increasing intensity of Raman signal in the 1425 to 1480 $\text{cm}^{-1}$ region. (b) Fluorescence micrograph of the same region. (c) Raman spectra from three points obtained using CRM, shown in comparison to SD pure tobramycin and alpha mannitol prepared as pure materials. Courtesy of Dr. Frederick Vogt at GlaxoSmithKline.....	72
Figure 4.20. (a) Brightfield micrograph of SD azithromycin:mannitol=1:0.5 particles obtained using a 50x objective. CRM mapping was performed in the region marked with the red box; increasing blue color corresponds to increasing intensity of Raman signal in the 845 to 900 $\text{cm}^{-1}$ region. (b) CRM mapping results with increasing red color corresponding to increasing intensity of Raman signal in the 1670 to 1750 $\text{cm}^{-1}$ region. (c) Raman spectra from three points obtained using CRM, shown in comparison to SD pure azithromycin and alpha mannitol prepared as pure materials. Courtesy of Dr. Frederick Vogt at GlaxoSmithKline.....	73
Figure 4.21. ATR-FTIR spectra of: (a) SD pure and as received tobramycin particles (full scan range); (b) SD pure and as received azithromycin particles (zoomed in spectra from (a)); and (c) SD pure and as received azithromycin particles (full scan range).....	75
Figure 4.22. ATR-FTIR spectra for: (a) SD tobramycin:mannitol formulations; and (b) SD azithromycin:mannitol formulations.....	76
Figure 4.23. Thermogravimetric analysis (TGA) for: (a) as received tobramycin; and (b) SD pure azithromycin.....	78
Figure 4.24. HSM micrographs of as received tobramycin.....	79
Figure 4.25. DSC thermogram (non-hermetic) of SD pure azithromycin.....	80
Figure 4.26. Water vapor sorption isotherms at 25°C for as received vs SD powders (water vapor sorbed/dry compound mole/mole vs RH; n=1).....	85
Figure 4.27. DSC thermograms of SD pure tobramycin after completion of water vapor sorption study.....	86
Figure 4.28. An experimental summary graph of water vapor sorption isotherms at 25°C for as received AZI.....	86
Figure 5.1. Schematic representation of the principle of inertial impaction for aerodynamic sizing of cascade inertial impactors.....	89
Figure 5.2. Closed (operating) condition (a) with pre-separator and internal construction (b) of the next generation impactor.....	90
Figure 5.3. Aerosol dispersion performance using the NGI under an airflow rate (Q) of	

60 L/min with the HandiHaler <sup>®</sup> DPI device for: (a) SD pure tobramycin powder; and (b) SD pure azithromycin powder (mean $\pm$ SD, n=3).....	94
Figure 5.4. Aerosol dispersion performance using the NGI under an airflow rate (Q) of 60 L/min with the HandiHaler <sup>®</sup> DPI device for: (a) tobramycin:mannitol powders; and (b) azithromycin:mannitol powders (mean $\pm$ SD, n=3).....	96
Figure 5.5. Aerosol dispersion performance using the NGI under an airflow rate (Q) of 60 L/min with the HandiHaler <sup>®</sup> DPI device for: (a) tobramycin:phospholipids powders; and (b) azithromycin:phospholipids powders (mean $\pm$ SD, n=3)...	98
Figure 5.6. Aerosol dispersion performance using the NGI under an airflow rate (Q) of 60 L/min with the HandiHaler <sup>®</sup> DPI device for: (a) tobramycin:phospholipids:mannitol powders; and (b) azithromycin:phospholipids:mannitol powders (mean $\pm$ SD, n=3).....	100
Figure 5.7. Aerosol dispersion performance using the NGI under an airflow rate (Q) of 60 L/min with the HandiHaler <sup>®</sup> DPI device for azithromycin:phospholipids=1:0.5. The particle deposition was determined by both weight and chemical analysis (mean $\pm$ SD, n=3).....	102
Figure 6.1. XRPD patterns of SD pure tobramycin (offset by 500 counts between patterns) at 11% RH (a), 40% RH (b), and 75% RH (c) at 40°C during storage.....	109
Figure 6.2. XRPD patterns of SD tobramycin:mannitol=1:0.5 (offset by 500 counts between patterns) at 11% RH (a), 40% RH (b), and 75% RH (c) at 40°C during storage.....	110
Figure 6.3. XRPD patterns of SD tobramycin:phospholipids=1:0.5 (offset by 500 counts between patterns) at 11% RH (a), 40% RH (b), and 75% RH (c) at 40°C during storage.....	111
Figure 6.4. XRPD patterns of SD tobramycin:phospholipids:mannitol=1:0.5:0.5 (offset by 500 counts between patterns) at 11% RH (a), 40% RH (b), and 75% RH (c) at 40°C during storage.....	112
Figure 6.5. Photograph of capsules of SD pure tobramycin stored at three different RH % and 40°C for 2 weeks.....	113
Figure 6.6. DSC thermograms of main phase transition of tobramycin:phospholipids=1:0.5 (a) and azithromycin:phospholipids=1:0.5 (b) after 3 months storage at 11% RH and 40°C; DSC thermogram of SD pure tobramycin (c) after 3 months storage at 75% RH and 40°C.....	114
Figure 6.7. XRPD patterns of SD pure azithromycin (offset by 500 counts between patterns) at 11% RH (a), 40% RH (b), and 75% RH (c) at 40°C during storage.....	115

Figure 6.8. XRPD patterns of SD azithromycin:mannitol=1:0.5 (offset by 500 counts between patterns) at 11% RH (a), 40% RH (b), and 75% RH (c) at 40°C during storage.....	116
Figure 6.9. XRPD patterns of SD azithromycin:phospholipids=1:0.5 (offset by 500 counts between patterns) at 11% RH (a), 40% RH (b), and 75% RH (c) at 40°C during storage.....	117
Figure 6.10. XRPD patterns of SD azithromycin:phospholipids:mannitol=1:0.5:0.5 (offset by 500 counts between patterns) at 11% RH (a), 40% RH (b), and 75% RH (c) at 40°C during storage.....	118
Figure 6.11. Aerosol dispersion performance using the NGI under an airflow rate (Q) of 60 L/min with the HandiHaler® DPI device for: (a) fresh SD tobramycin powders; and (b) stored SD tobramycin powders at 11% RH and 40°C (mean ± SD, n=3).....	120
Figure 6.12. Aerosol dispersion performance using the NGI under an airflow rate (Q) of 60 L/min with the HandiHaler® DPI device for fresh and stored SD pure azithromycin at three different RH % and 40°C (mean ± SD, n=3).....	121
Figure 6.13. Aerosol dispersion performance using the NGI under an airflow rate (Q) of 60 L/min with the HandiHaler® DPI device for fresh and stored SD azithromycin:mannitol=1:0.5 at three different RH % and 40°C (mean ± SD, n=3).....	122
Figure 6.14. Aerosol dispersion performance using the NGI under an airflow rate (Q) of 60 L/min with the HandiHaler® DPI device for fresh and stored SD azithromycin:phospholipids=1:0.5 at three different RH % and 40°C (mean ± SD, n=3).....	122
Figure 6.15. Aerosol dispersion performance using the NGI under an airflow rate (Q) of 60 L/min with the HandiHaler® DPI device for fresh and stored SD azithromycin:phospholipids:mannitol=1:0.5:0.5 at three different RH % and 40°C (mean ± SD, n=3).....	123
Figure 7.1. A representative HPLC chromatogram of a standard azithromycin solution.....	132
Figure 7.2. A representative HPLC chromatogram of an azithromycin solution in stability indicating assay.....	133
Figure 7.3. The apparent <i>in vitro</i> release profile of SD pure azithromycin formulation in PBS at 37°C.....	135
Figure 7.4. The apparent <i>in vitro</i> release (a) full profiles and (b) first 60min profiles of azithromycin:phospholipids vs azithromycin in PBS at 37°C.....	136

Figure 7.5. The apparent <i>in vitro</i> release profiles of (a) azithromycin vs azithromycin:mannitol=1:0.5, (b) azithromycin:phospholipids=1:0.5 vs azithromycin:phospholipids:mannitol=1:0.5:0.5, and (c) azithromycin:phospholipids=1:2 vs azithromycin:phospholipids:mannitol=1:2:2 in PBS at 37°C.....	138
Figure 7.6. The representative HPLC chromatograms of the samples in phospholipids assay.....	140
Figure 7.7. The proposed scenarios of location of azithromycin drug molecules and phospholipid bilayer in SD azithromycin:phospholipids particles.....	142

## Chapter 1 General Introduction

### 1.1 Characteristics of the Lung

#### 1.1.1 Anatomy of the Airways

The lungs are the major respiratory organs in human body. The lungs are divided into two parts, including one on the right and the other on the left as shown in Figure 1.1. Respiratory system is responsible for transporting oxygen to the blood and removing carbon dioxide from the blood. It has two airway tracts, including upper and lower respiratory parts. The upper respiratory tract is defined as the region, starting from nose or mouth passages, through pharynx and larynx, to the trachea. The lower respiratory tract includes bronchi, bronchioles (including terminal bronchioles and respiratory bronchioles), and gas-exchanging regions (including alveolar ducts and alveolar sacs). However, based on functionality, airways can also be categorized into conducting and respiratory parts. The conducting airways do not involve in gas exchange, and consist of regions from the trachea to the terminal bronchioles. The respiratory airways, responsible for gas exchange, are respiratory bronchioles, alveolar ducts, and alveolar sacs.

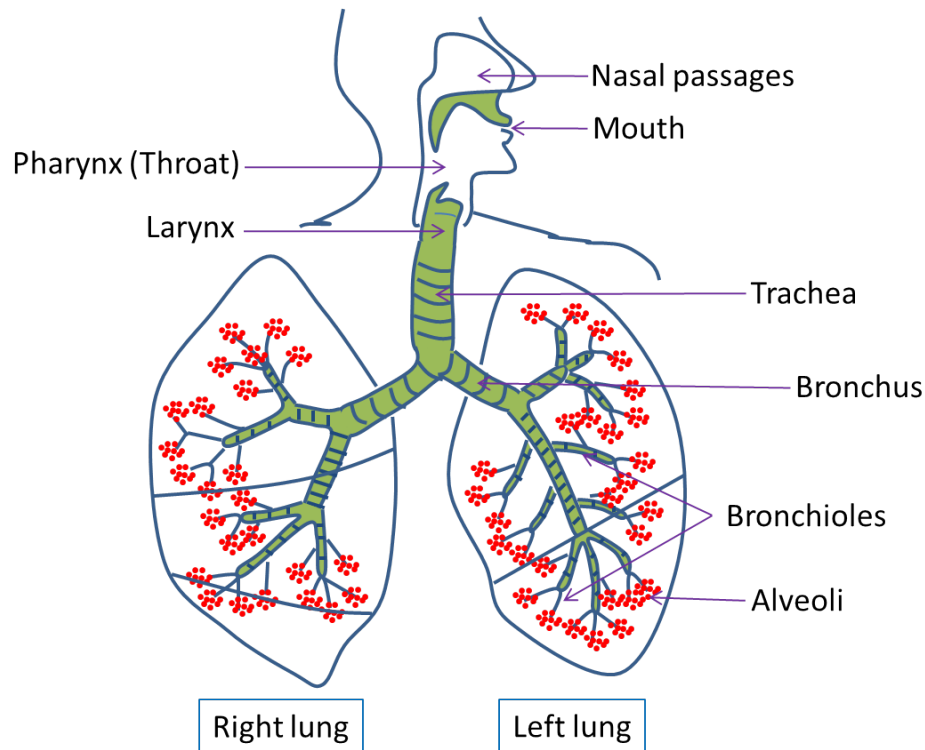


**Figure 1.1.** Schematic of the respiratory system. Adapted from [1].

The lung airways are recognized as a bronchial tree in structure[2]. Analogous to the trunk and branches of a tree, the trachea bifurcates to form bronchi and bronchioles. The sac-like alveoli could be viewed as the leaves of a tree. Weibel airway model[3] (Figure

1.2) is used to characterize airway structure and represents the airway divisions before alveolar sacs are reached. Up to 24 airway generations are proposed in the Weibel model, with trachea and alveolar sacs being generation 0 and 23, respectively. Compared to the previous generation, the number of airways at each generation is doubled. Each airway generation exhibits a characteristic range of sizes in lengths and diameters of the branches[4].

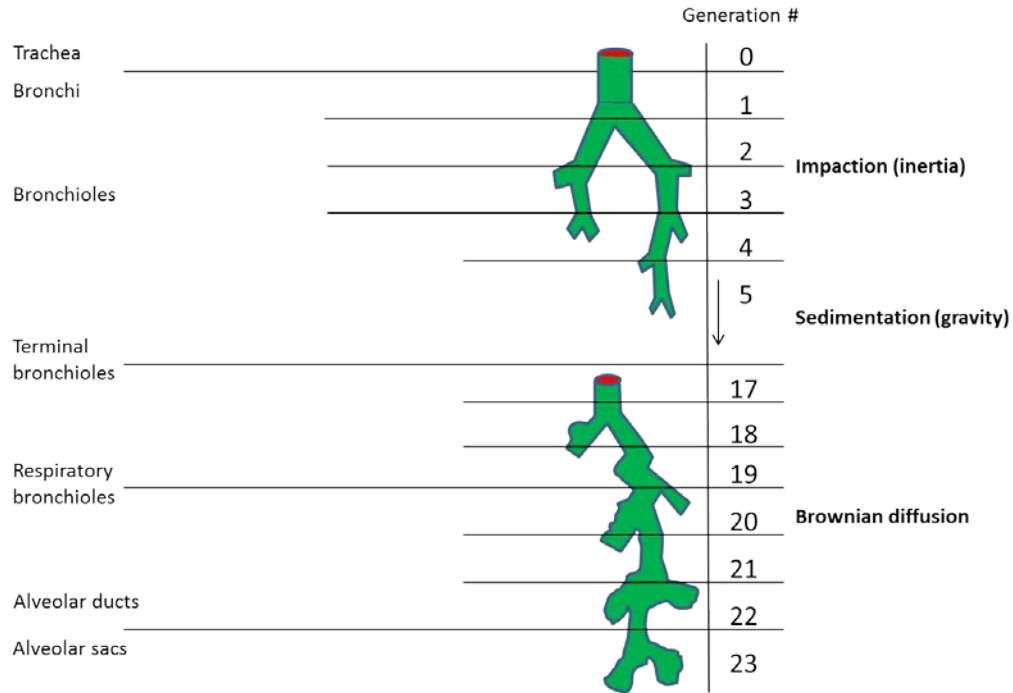


**Figure 1.2.** Schematic of Weibel airway model. Adapted from [2].

Two characteristics of the lungs exhibit important influences in airway function. The first characteristic is that airway diameters decrease with increasing generations (in Weibel model). For instance, with an alveolar diameter being 0.04 cm, a tracheal diameter in the adult is on the order of 1.8 cm[5]. During inspiration, this physical characteristic permits easy air penetration into the lower airway regions. The second characteristic is that surface area in airways increases dramatically with each succeeding generation. With a presence of ~ 600 millions alveoli, the total surface area in the alveolar region is estimated to be ~ 140 m<sup>2</sup> in an adult human[5]. Alveoli are the main region for gas exchange between air and blood. Each alveolus is surrounded and separated from one another by thin blood capillaries. An exchanging gas molecule in an alveolus has to travel a distance of approximately being 500 nm, from the alveolar epithelium, through capillary endothelium, and to basement membrane before arriving into the blood[5].

### 1.1.2 Physiology of the Airways

Lining on the luminal surface is the epithelium of the airways. The epithelial cells are the barrier of absorption into the bloodstream. The cell productions are markedly different depending on locations in the lungs. As shown in Figure 1.3, the epithelial cells are drawn at the corresponding relative sizes. In the bronchial airways, a wide range of cells make up the epithelium[2]: the basal cells are the stem cells for the epithelium, differentiating to form the other cells in the case of injury or apoptosis; the goblet cells secrete the mucus; the ciliated cells provide the mechanism for moving the mucus; the brush cells participate in drug metabolism. The gradually thinning epithelium, with many mucus and ciliated cells, acts as so called “mucociliary escalator”. Absorptive epithelium becomes thinner until alveoli are reached. All the above listed types of cells exist in the smaller airways, but as a thinner layer.

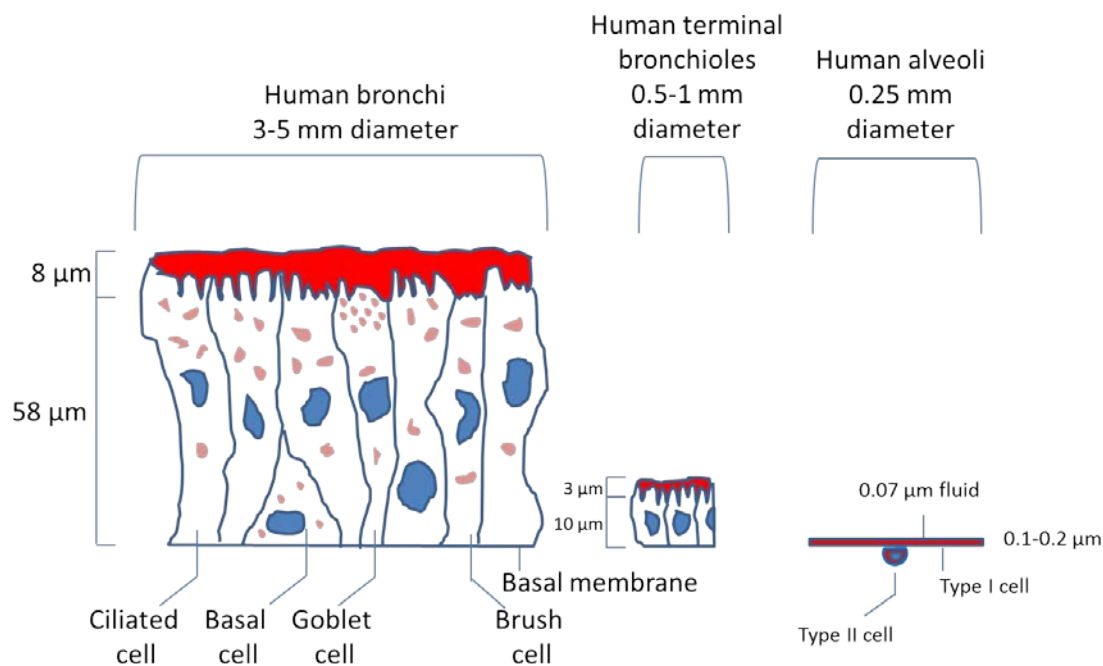


**Figure 1.3.** Comparison of the lung epithelium at different airways. Adapted from [2].

However, as different to bronchial airways, alveolar epithelium is a monolayer of cells. The alveolus mainly consists of Type I and Type II alveolar cells as shown in Figure 1.4. Type I cells are very broad and extremely thin ( $< 0.1 \mu\text{m}$ ) squamous cells that form most (about 95 %) of the surface of the alveoli. The exchange of oxygen and carbon dioxide takes place through the cell membranes and cytoplasm of Type I cells. As numerous as Type I cells, Type II cells are located among the Type I cells and cover only 5% of the alveolar surface. Type II cells possess three main functions[6]: 1) secretion of pulmonary surfactant; 2) control of alveolar fluid levels; 3) act as the stem cells to replace both Type I and II cells after injury. On average, about 12-14 alveolar macrophages range over the air-side of 500 alveoli spaces[2]. A morphometric study of human lung tissue indicated that 90% of alveolar macrophages are observed at or near alveolar septal junctional



zones[7]. Alveolar macrophages engulf and ingest any foreign particles and infectious microorganisms that may exist in the alveoli. The indigestible materials are frequently transported to the lymph nodes of the lungs[6].

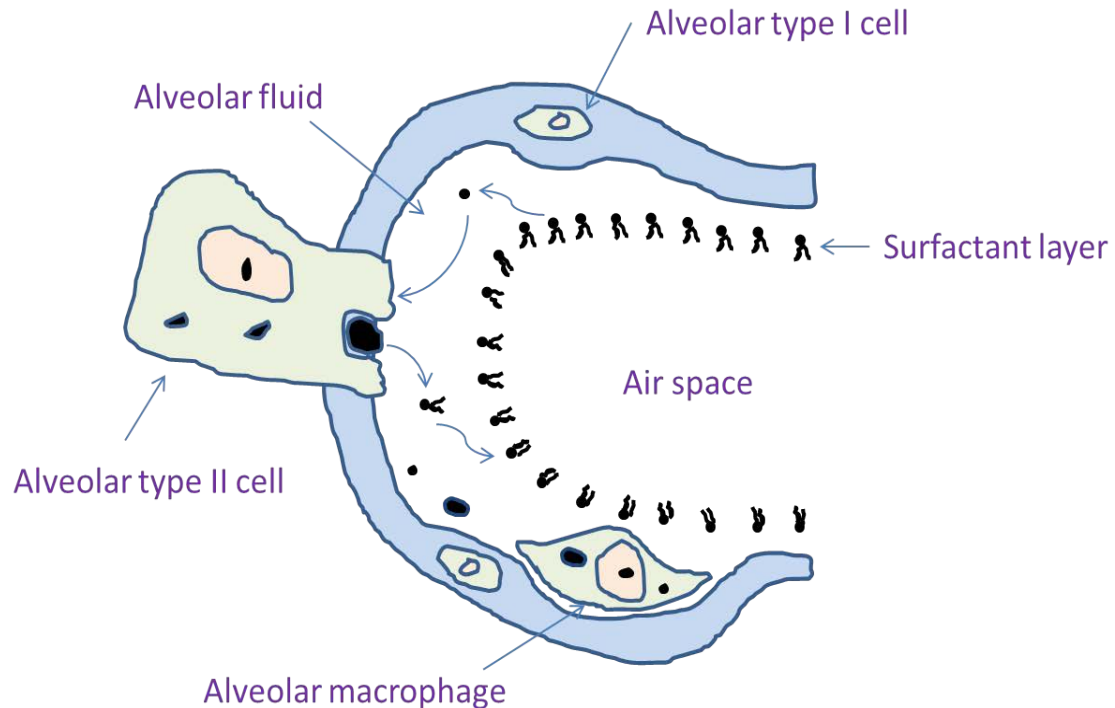


**Figure 1.4.** Structure of an alveolus. Adapted from [8].

Released by Type II alveolar cells, pulmonary surfactant is a mixture of surface-active lipids (90% by weight) and proteins (10% by weight). The lipids and proteins have both a hydrophilic region and a hydrophobic regions. Pulmonary surfactant adsorbs to the air-water interface of alveoli with the hydrophilic head groups in the water and the hydrophobic tails facing towards the air. Therefore, it reduces the surface tension of interface. Dipalmitoylphosphatidylcholine (DPPC), a predominant lipid (40% by weight) with saturated fatty acid chains, contributes substantially to the unique properties of pulmonary surfactant.[9] In addition to DPPC, pulmonary surfactant also contains unsaturated phosphatidylcholine (~35%), phosphatidylglycerol (~10%), phosphatidylinositol (~2%), phosphatidylethanolamine (~3%), sphingomyelin (~2.5%), and cholesterol (~3%).[10] The proteins are comprised of a highly variable amount of serum proteins and four apoproteins (surfactant protein A (SP-A), surfactant protein B (SP-B), surfactant protein C (SP-C), and surfactant protein D (SP-D)). Associated with lipids, the proteins contribute to specific functions of pulmonary surfactant.[9] Pulmonary surfactant stabilizes the alveoli during the respiratory cycle by reducing surface tension of water-air interface. Therefore, it prevents the tendency of alveolar collapse in expiration and makes lung inflation easy in inspiration.[10] The function of host defense in alveoli relies on the nature of SP-A and SP-D.[9] In addition, surfactant also possesses anti-inflammatory functions[11], promotes mucus clearance[12], prevents pulmonary

infection[11], and eliminates extracellularly generated oxyradicals and enhances intracellular antioxidant enzyme content[13].

### 1.1.3 Blood Circulation

Pulmonary and systemic circulation both exist in the lungs. Drug delivered to the lower airways could be absorbed into body through both of the circulations. Pulmonary circulation conducts the blood from the heart to the lungs for oxygen. Oxygen-depleted blood travels through capillaries on alveoli, removing carbon dioxide and absorbing oxygen into the blood. The alveoli provide the tremendous surface for gas exchanging during respiration. Thereafter, the oxygenated blood leaves the lungs through pulmonary vein and returns to the left atrium of heart. Pulmonary circulation operates on a low-pressure and low-resistance vascular bed with a flow rate of 5 L/min[10].

Systemic circulation is the blood movement from the heart through the body to provide oxygen and nutrients. During systemic circulation oxygen in the blood diffuses into the respiratory cells, while waste and carbon dioxide are carried into the blood. In addition, systemic circulation assists in the humidification and warming of inspired air in the trachea and bronchi[10]. Moreover, it also plays a key role in anti-inflammation of lungs by mucosal swelling and delivery of inflammatory cells and mediators to the airways[10].

## 1.2 Aerosol Particle Deposition Mechanisms in Human Lungs

Local delivery of drugs to the lungs attracts tremendous attention for the treatment of a variety of pulmonary diseases. The therapeutic efficacy by dry powder for inhalation is highly influenced the dose delivered to the target regions. Given the characteristics of the lungs and respiratory pattern, aerosol particle properties (e.g. particle size and size distribution, particle morphology, hygroscopicity, and etc.) mainly determine the airways deposition[14]. There are three major particle deposition mechanisms[14] in the lungs, including inertial impaction, sedimentation, and Brownian diffusion. Other mechanisms, including interception, electrostatic precipitation, and hygroscopic particle growth, have also been reported[10]. Various deposition mechanisms may be involved simultaneously for one particular aerosol formulation.

Inertial impaction is the main deposition mechanism for particles more than 5  $\mu\text{m}$  in diameter with high velocity[14]. These particles are unable to follow the air streamlines due to high inertia. It takes place commonly in extrathoracic and large conducting airways, where air flow velocities are high and airway directional changes are fast. The probability of inertial impaction of aerosol particles increases with increasing air flow velocity, rate of breathing, particle size ( $> 5 \mu\text{m}$ ) and particle density[10]. Stokes number (Stk) influences the particle deposition by inertial impaction[15]:

$$\text{Stk} = \frac{\rho_p d_p^2 V}{18\mu D} \quad (\text{Equation 1.1})$$

Where  $\rho_p$  is the particle mass density,  $d_p$  is the particle diameter,  $V$  is the air flow velocity,  $\mu$  is the dynamic viscosity of the surrounding air, and  $D$  is a characteristic dimension of the obstacle obstructing air flow (usually in a daughter airway).

Sedimentation (gravitational settling) is deposition mechanism for particles (typically 1-5  $\mu\text{m}$ ) in the small conducting airways where air flow velocity is slow[14]. The deposition is high for large particles (gravitational drag) with long residence time[14]. However, it decreases with increasing breathing rate[10]. As similar to inertial impaction, sedimentation is dependent on the relaxation time of the particles (the time required for the particle to respond to a change of the air flow velocity;  $\tau$ )[16].

$$\tau = \frac{\rho_p d_p^2}{18\mu} \quad (\text{Equation 1.2})$$

Where  $\rho_p$  is the particle density,  $d_p$  is the particle diameter, and  $\mu$  is the dynamic viscosity of the surrounding air.

Brownian diffusion dominates the deposition of particles with submicron in size (typically 0.5-1  $\mu\text{m}$ )[14]. Brownian diffusion results from random motion of particles impacted by the surrounding air molecules. It occurs in the deep lungs, especially respiratory bronchial and alveolar regions where air flow is minimal. Stokes-Einstein equation (for diffusion of spherical particle through medium with low Reynolds number) defines the diffusion constant ( $D$ ) of Brownian motion:

$$D = \frac{k_B T}{6\pi\eta r} \quad (\text{Equation 1.3})$$

Where  $k_B$  is Boltzmann's constant,  $T$  is the absolute temperature,  $\eta$  is viscosity, and  $r$  is the radius of the spherical particle.

Interception is mainly relevant to particles with high aspect ratio (elongated particles) such as fibers and aggregates. The use of elongated particles for deep lung delivery has been attracting attentions due to the characteristic aerodynamic behaviors (such as an increase in fine particle fraction (FPF))[17-19]. Elongated particles preferably align with the long axis in air streamlines when penetrating into airways. Therefore, the short axis of elongated particle is mainly related to the aerodynamic diameters. Moreover, once deposited, elongated particles are less rapidly cleared by macrophages due to the long length[20]. However, the aerosol dispersion of elongated particles relies on the form of loose agglomeration of the particles. Low aerosol performance arises as the particles are in contact with long axis[21]. In addition, powder flow and content uniformity could be problematic with elongated particles in dry powder formulations[16].

Electrostatic precipitation could occur on charged particles generated by mechanical forces. However, this electrostatic attraction/repulsion between charging in particles and airway surface only is a minor contributor to particle deposition[22].

Particle growth of hygroscopic aerosols at elevated relative humidity and temperature in the respiratory tracts may affect particle deposition[23].

### 1.3 Pulmonary Aerosol Drug Delivery

Efficiency of pulmonary drug delivery is dependent upon both the aerosol formulation and inhalation device. Modern inhalation devices can be divided into four principle categories: nebulizers, pressurized metered-dose inhalers (pMDIs), dry powder inhalers (DPIs), and soft-mist inhalers (SMIs). Each class possesses its unique strengths and weaknesses.

#### 1.3.1 Nebulizers

Two typical nebulizers are commercially available, including air jet and ultrasonic nebulizers. Marketed respiratory solutions are usually drug in isotonic aqueous solutions. In addition, these solutions may contain preservative to inhibit microbial growth.

Jet nebulizers (Figure 1.5), the most commonly used nebulizers, are also named as “atomizers”[24]. Jet nebulizers are connected to a compressor used as a source of gas. The compressed air or oxygen in a compressor flows at high velocity through a liquid. It turns the liquid into aerosol droplets inhaled by patients. Approximately 50 to 60% of the aerosols produced by jet nebulizers are in the respirable range ( $< 10\ \mu\text{m}$ )[10].

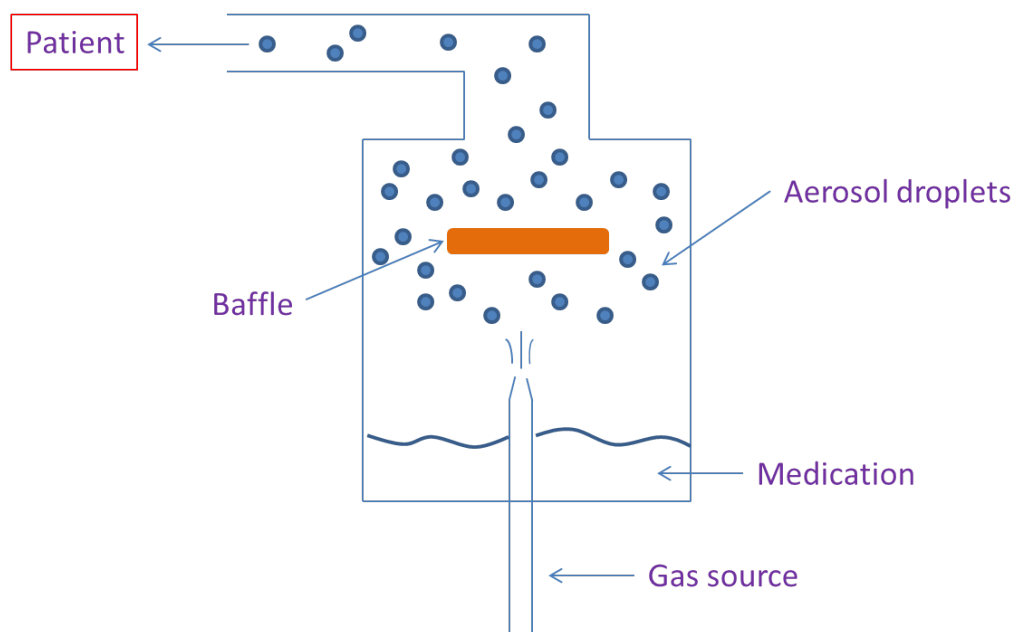


**Figure 1.5.** Schematic of a jet nebulizer. Adapted from [25].

Ultrasonic nebulizers (Figure 1.6) use an electronic oscillator to generate a high frequency ultrasonic wave, causing a mechanical vibration of a piezoelectric transducer. The vibration provides the energy to aerosolize the liquid. The frequency of the vibrating piezoelectric transducer determines the droplet size for a given solution. Generated by ultrasonic nebulizers, approximately 70% of the particles exhibit particle size in range from 1 to 5  $\mu\text{m}$ [10]. However, heat generated from frictional forces by movement of the transducer may be detrimental to thermolabile formulations[10].

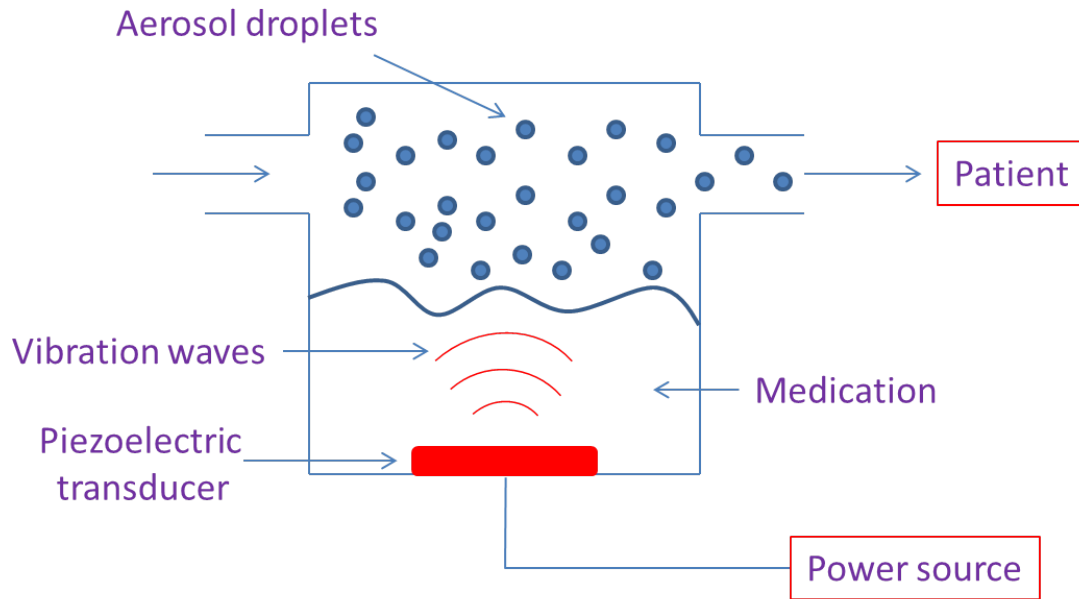


**Figure 1.6.** Schematic of an ultrasonic nebulizer. Adapted from [25].

Commonly used in hospital, the old models of both jet and ultrasonic nebulizers usually generate a lot of noise and are not portable due to a heavy weight. Advances in technology have led to the development of novel nebulizers. These miniaturized novel nebulizers are portable with high-output, generating small droplets capable of penetrating deeply into the lungs ( $< 5 \mu\text{m}$ ). New techniques in liquid spray delivery devices are employed including high pressure micro-spray nozzle systems and electrostatic generation of aerosol clouds[26]. Some of the commonly available drug solutions delivered by nebulizers are Ventolin<sup>®</sup> (salbutamol, beta 2-mimetic bronchodilator), Bricanyl<sup>®</sup> (terbutaline, beta 2-mimetic bronchodilator), Atrovent<sup>®</sup> (ipratropium, anticholinergic bronchodilator), Pulmozyme<sup>®</sup> (dornase alpha, mucolytic), and Tobi<sup>®</sup> (tobramycin, antibiotic)[10].

In general, the advantages of using nebulizers are: 1) constant output of delivering aerosols; 2) large dose delivery; 3) low requirement on coordination between aerosol generation and breathing of patients. However, well-documented disadvantages of using nebulizers are: 1) time-consuming; 2) high cost; 3) inefficiency[27]; 4) poor reproducibility and great variability; 5) risk of bacterial contamination; 6) constant cleaning[28]; 7) inconvenient (bulky)[29]; 8) waste of active ingredient (dead volume of solution)[30].

### 1.3.2 Pressurized Metered-Dose Inhaler (pMDIs)

Pressurized metered-dose inhalers (pMDIs) can deliver a specific amount of drug to the lungs in the form of a short aerosol burst. pMDIs are usually self-administered by the patient. These devices are commonly used in treatment of asthma, chronic obstructive pulmonary disease (COPD), and other respiratory diseases.

pMDIs (Figure 1.7) are composed of three major components[5, 31]: 1) a canister made of aluminum or stainless steel, where the formulation resides; 2) a metering valve allowing a metered quantity of the formulation to be dispensed with each actuation; 3) an actuator (or mouthpiece) allowing the release of aerosols and directing the aerosols into the patient's lungs. The formulation itself consists of the medication (either dissolved or suspended in the propellant), a liquefied gas propellant, and possibly stabilizing excipients. Actuation of the device releases a single metered dose of the formulation liquid through the control valve. With expansion and evaporation of propellant in formulation liquid, it leaves the drug in the form of aerosols at a high velocity. The liquefied propellant are used both as an energy source for expelling the formulation from the valve and a dispersion medium for the drug and other excipients.

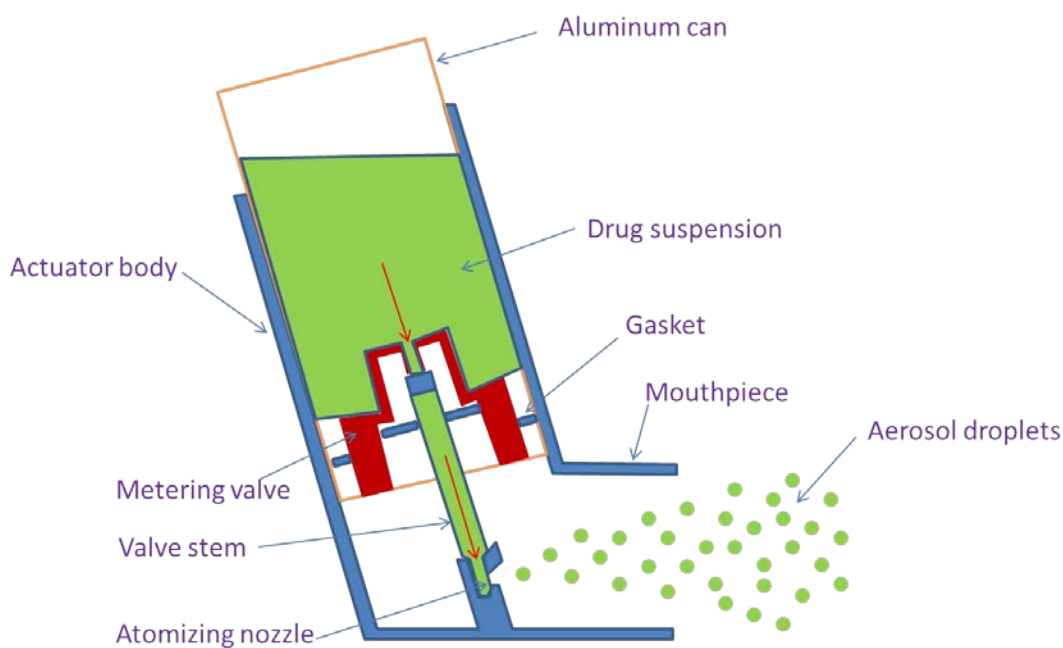


**Figure 1.7.** Schematic of a pressurized metered-dose inhaler. Adapted from [32].

Particle size and size distribution of aerosols from a pMDI are dependent on the physicochemical properties of the formulation. Size of aerosol droplets from suspension formulation in pMDIs could be reduced by using a low drug concentration, or small drug particles, or a system with high vapor pressure[33]. In addition, low concentration of a surfactant helps the dispersion of suspended particles or dissolution of a partially soluble drug, and lubricates the metering system[34]. Antioxidant or chelating agent may be added to enhance chemical stability of the formulation[10]. Unpleasant taste of formulations might be masked by adding flavors or sweeteners[10]. Some of the commercially available pMDIs include Flixotide<sup>®</sup> (fluticasone, corticosteroid), Atrovent<sup>®</sup> (ipratropium bromide, anticholinergic bronchodilator), Ventolin<sup>®</sup> (salbutamol, beta 2-mimetic bronchodilator), and Combivent<sup>®</sup> (ipratropium bromide and salbutamol, anticholinergic and beta 2-mimetic bronchodilator).

There are several disadvantages of drug delivery by pMDIs. Chlorofluorocarbons (CFCs)

as a propellant have been banned by 2000 by “Montreal Protocol” (due to the contribution to ozone depletion and health effects)[35]. The replacement propellant, hydrofluoroalkane (HFA), is an extremely poor solvent. Therefore, formulation surfactants are totally insoluble in HFA, resulting in physical stability issue of drug particles. Numerous approaches are employed to overcome the issues associated with HFA propellants, including addition of a co-solvent, development of a new surfactant, and particle engineering[10].

In general, only a small fraction of drug dose (approximately 10 to 20% of emitted dose) could be delivered by pMDIs to the lungs. A well-known issue, so-called “cold-Freon effect”, can be experienced by using pMDIs. It is attributed to the evaporation of propellant when the aerosols impact on the back of the throat, causing patients to stop inhaling[36]. Poor hand-mouth coordination is another issue associated with the use of pMDIs[37]. However, the introduction of breath-actuated pMDIs (such as Autohaler<sup>®</sup>) provides a convenient means to overcome the poor coordination[10].

### **1.3.3 Dry Powder Inhalers (DPIs)**

Dry powder inhalers (DPIs) are devices that deliver drug to the lungs as a dry powder. The emergence of DPIs was largely driven by the “Montreal Protocol” that addressed elimination of CFCs from traditional pMDIs[38, 39]. DPI products combine powder technology and device design in order to disperse dry aerosol particles in the lungs of patients. Commercially available DPI devices range from single-dose devices (e.g., Aerolizer<sup>®</sup> (Novartis) and Handihaler<sup>®</sup> (Boehringer Ingelheim)) to multi-dose devices in form of a blister pack (e.g., Diskhaler<sup>®</sup> and Diskus<sup>®</sup> (GlaxoSmithKline)) or reservoir-type system (e.g., Turbuhaler<sup>®</sup> (AstraZeneca))[5]. For instance, a schematic of the Handihaler<sup>®</sup> DPI device (open state) from Boehringer Ingelheim (Germany) is shown in Figure 1.8. Drug particles in a capsule (placed in center chamber (#6 in Figure 1.8)) are released via a rumbling motion once the capsule is pierced by two pins (placed inside of the piercing button (#5 in Figure 1.8)). The drug particles are dispersed through the turbulent air flow generated by a stainless grid (placed inside of the mouthpiece (#2 in Figure 1.8)) at the time of inhalation[10].

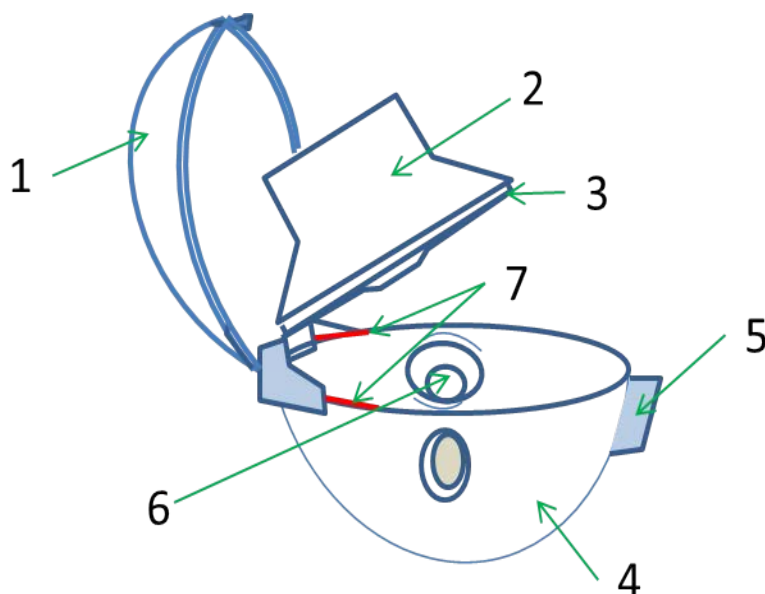


**Figure 1.8.** Schematic of the Handihaler<sup>®</sup> DPI device. Adapted from [40].

DPIs have three basic features including device, formulation, and dose-metering system[16]. The pre-metered (single-dose or multi-dose) devices are further classified into active (device actuated) and passive (breath actuated) DPIs. As to passive DPIs, the inspiration is the only energy source for particle resuspension from static powder state. The device itself is designed to allow efficient particle resuspension through powder fluidization and deaggregation[41]. DPI formulation could either be lactose carrier-free (respirable drug particles alone with aerodynamic diameter about 1-5  $\mu\text{m}$  depending on the target site)[42-44] or lactose carrier-based (blends of respirable drug particles and lactose particles)[45].  $\alpha$ -lactose monohydrate is commonly used as carrier particles. In addition to acting as a bulking agent for uniform capsule filling, the carrier particles (typically > 30  $\mu\text{m}$  in diameter) are used to increase powder flow and facilitate the release of respirable drug aerosols[16]. Dose-metering system includes the pre-metered individual capsules, multiple dose blisters or strips, and dose reservoirs.

Efficiency and reproducibility of aerosols reaching the desired site of action are determined by DPIs device, formulation, and inspiratory maneuver of patients[45]. The new generation of DPIs under developments includes extra mechanisms (such as the employment of impellers, compressed air assistance, vibration, and impact hammers) to enhance aerosolization of drug particles[16]. Recently novel DPIs, standardized entrainment tubes (SETs; a series DPIs with unique features and design, but different turbulent shear forces), have been developed, leading to prediction, modeling, and fundamental understanding of particle resuspension from static powder state[46-48].

#### 1.3.4 Soft-Mist Inhalers (SMIs)

Soft-mist inhaler (SMI; Respimat<sup>®</sup>), as shown in Figure 1.9, is a new generation inhaler



invented by Boehringer Ingelheim in 1997[49]. This device provides a metered dose to the users. As the bottom of the inhaler is rotated clockwise 180 degrees by hand, a tension is built up into a spring around the flexible liquid container. Upon activation, the release of energy from the spring imposes pressure on the flexible liquid container. It produces two fine jets of liquid that converge at a pre-set angle through precisely engineered nozzle (in uniblock), forming a soft inhalable mist. With no propellant and no need for a battery, the device employs only mechanical energy. The relatively long generation time of aerosol cloud (approximately 1.5 s) facilitates coordination of actuation and inhalation which is a major problem with pMDIs. With the slow velocity of the soft mist, it results in larger amounts of the drug deposited in the lungs and less deposited in the oropharynx compared with either pMDIs and DPIs[49]. In general, the soft mist contains a high fine particle fraction of approximately 65 to 80%[49].

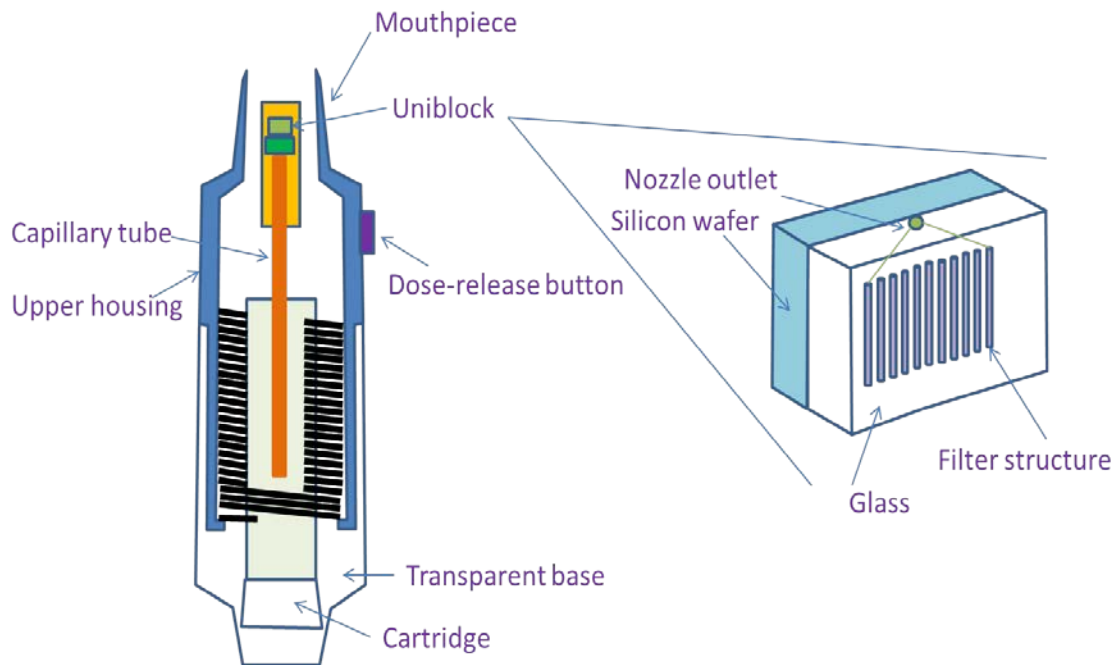


**Figure 1.9.** Schematic of the Respimat<sup>®</sup> soft-mist inhaler. Adapted from [49].

#### 1.4 Interparticulate Forces

Dry powder aerosol particles prepared in respirable sizes exhibit unique properties based on the forces of interaction. The interparticulate forces need to be overcome before the inhalable aerosol particles generated in circumstance of either carrier-free or carrier-based DPI formulations. Interparticulate or surface forces (adhesive and cohesive forces) in the dry powder formulations are a result of complex combination of physical forces including van der Waals forces, electrostatic forces, capillary forces[16, 50]. In addition, other forces, such as mechanical interlocking, frictional forces, and hydrogen bonding, are not frequently mentioned, but still important[41]. Particle aggregation is a

result of interparticulate forces. The contribution of each force to the particle aggregation is dependent on numerous factors such as surface morphology, crystallinity, intrinsic material properties, and environmental conditions[41]. The calculated magnitude of interparticulate forces (van der Waals, electrostatic, and capillary forces between ideal binary system) was previously reported[41, 51]. In general, at normal environmental conditions, the strength of van der Waals forces is about two orders of magnitude higher than electrostatic and capillary forces. However, capillary forces would dominate at condition of high relative humidity[16].

van der Waals forces ( $F_{vdw}$ ) can be defined as below[16]:

$$F_{vdw} = \frac{A}{6h^2} * \frac{R_1 R_2}{R_1 + R_2} = \frac{AR}{12h^2} \quad (R_1 = R_2 = R, \text{ for two identical spheres}) \quad (\text{Equation 1.4})$$

$$F_{vdw} = \frac{AR}{6h^2} \quad (R_1 \ll R_2, \text{ for sphere and surface}) \quad (\text{Equation 1.5})$$

Where A is the Hamaker constant (typically  $\sim 10^{-19}$  J) dependent on the molecular properties of the materials, R is the particle radius (m), and h is the separation distance (m). As compared to van der Waals force, gravitational forces are lowered greater when size of drug particles becomes small[16]. Therefore, the dry particles, with size less than 10  $\mu\text{m}$ , become adhesive/cohesive as van der Waals forces become predominant[16]. Based on the Equation 1.4 and 1.5, van der Waals forces, effective within a separation distance  $< 100 \mu\text{m}$ [16], diminish rapidly with increasing separation distance. Therefore, van der Waals forces are sensitive to the change of particle shape and surface morphology[52]. The magnitude of van der Waals forces is greatly affected by the number of mutual points of contact known as the coordination number[41]. The van der Waals forces of particles could be also influenced by surface roughness (such as kinks and defects) by several orders of magnitude. The surface roughness of particles can be evaluated by mathematical models (e.g. Fourier, fractal, and chaos analysis) in terms of irregular oscillations around a mean value[53].

Electrostatic forces (including contact charging, coulombic interaction, and induced charging) could be either attractive or repulsive[16]. Contact charging involves the contact of a charged object to a neutral object until electron transfer reaches equilibrium. The contact charging force ( $F_c$ ) is defined as[16, 50]:

$$F_c = \frac{2\pi q^2}{A} \quad (\text{Equation 1.6})$$

Where q is charge detachment between two objects, A is the contact area between two objects.

Coulombic interaction occurs in two charged objects. Dependent upon the sign of electrical charge, it could be either attraction or repulsion. Coulombic force ( $F_q$ ) is expressed as[16]:

$$F_q = \frac{q_1 q_2}{4\pi\epsilon h^2} \quad (\text{Equation 1.7})$$

Where  $q_1$  and  $q_2$  are the charge on two objects, respectively,  $\epsilon$  is the permittivity, and h is

the separation distance.

Induced charging appears when a charged object approaches an uncharged object. Induced charging ( $F_e$ ) is calculated as[16]:

$$F_e = q^2 \left( 1 - \frac{h}{(R^2 + h^2)^{0.5}} \right) * \frac{1}{16\pi\epsilon h^2} \quad (\text{Equation 1.8})$$

Where  $q$  is the charging on charged object,  $h$  is the separation distance,  $R$  is the radius of uncharged object, and  $\epsilon$  is the permittivity.

As LaPlace pressure develops, capillary forces cause capillary condensation of water vapor. The formation of liquid bridge formation between solid particles due to water vapor condensation brings particles together. Capillary forces take places because of intermolecular forces between the liquid and surrounding solid surfaces. The capillary forces ( $F_{cp}$ ) between two spherical particles are described as[16, 50]:

$$F_{cp} = 4\pi R^* \gamma_L \cos\theta + 4\pi R^* \gamma_{SL} \quad (\text{Equation 1.9})$$

Where  $R^*$  is the harmonic mean of radii of the particles,  $\gamma_L$  is the surface tension of water,  $\gamma_{SL}$  is the solid-liquid interfacial energy, and  $\theta$  is the contact angle of liquid film to particle surface.

Mechanical interlocking arises with an increase in surface roughness. Mechanical interlocking of the particles is a prominent mechanism preventing particle dispersion for carrier-based DPI formulations. Moreover, surface roughness may also alter van der Waals forces, surface charging density, water vapor condensation in dry powders[54]. It has been reported that increased surface smoothness of carrier particles enhanced the fine particle fraction (FPF) of the DPI formulations[55-57]. In addition, dependent on the physicochemical and viscoelastic properties, aerosol particles may deform, which changes the effective contact area[16].

In reality, the forces of interaction between pharmaceutical particles are difficult to characterize or be controlled due to the heterogeneity in particle composition and physicochemical characteristics. Therefore, it is not practical to consider each of the forces independently. Nonetheless, key features of inhalation powders that critically influence interparticulate forces could be evaluated, including particle size and size distribution, particle shape, surface asperities (roughness), crystallinity, particle density, and presence of impurities[10]. Adhesion/cohesion of dry powder for inhalation could be indirectly estimated by using inverse gas chromatography (IGC)[58-64] and contact angle[65], and directly measured by using atomic force microscopy (AFM)[66, 67]. The efficiency of deaggregation in aerosolization is highly influenced by existing adhesive/cohesive forces in formulations. For instance of carrier-based dry powder formulation for inhalation, strong adhesive (drug-carrier) interaction may prevent the release of respirable drug particles from the surface of carriers, leading into a high deposition in upper airways. Therefore, the adhesive forces between respirable drug particles and large carrier particles strongly influences the delivered dose, since only drug particles separated from carrier surface are able to reach to the deep lungs. Similarly,

excessive cohesive forces could lead to agglomerate formation, affecting powder fluidization and dispersion characteristics of formulations[66]. The balance of these forces is very critical in drug-carrier blending, drug particle deaggregation, and drug particle resuspension.

### **1.5 Spray Drying**

There are several methods available to make respirable particles for dry powder inhalation, including micronization, freeze drying, and spray drying, and etc.[68-70]. Micronization, a simple and easy process by particle-particle and particle-solid collisions, is a classical approach in particle size reduction. However, in addition to produce cohesive particle aggregates, it is difficult to the control of particle size, size distribution, and morphology[45]. Many particles (e.g. protein drug) are produced by freeze drying due to stability issue. However, in addition to formation of undesired particles which are not suitable for inhalation, it is time and energy consuming[71].

Spray drying is a one-step continuous particle process operation. It exhibits a high ability to produce particles in a controlled manner, such as directing particle size and size distribution, particle shape, and particle morphology, which are important particle features for pulmonary drug delivery by inhalation. The process of spray drying converts a liquid feed (such as solutions, suspension, emulsions and etc.) to dried particles. A schematic of spray dryer is shown in Figure 1.10. Some key components of a spray dryer include: 1) electric device that elevates the temperature of drying gas; 2) nozzle that atomizes liquid feed into droplets by compressed air; 3) spray drying glass chamber for primary drying of droplets with drying gas; 4) cyclone that separates dried particles from drying gas; 5) filter that removes fine particles (not collected by cyclone); 6) aspirator that generates air flow in system; 7) liquid collecting system (not show in Figure 1.10) that condenses water vapor, organic vapor, or both into liquid state.

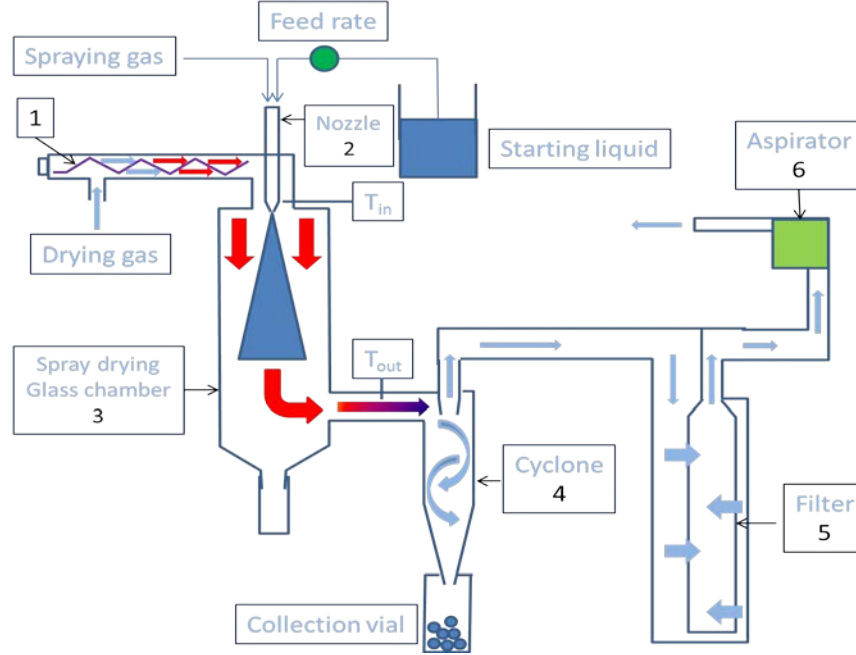


**Figure 1.10.** Schematic of a spray dryer. Adapted from [72].

In general, the process of spray drying involves three stages, including atomization, drying, and separation[30]. Atomization is the process of droplet generation from liquid feed. A spray of millions of droplets is formed when a liquid feed is forced through a nozzle by a pressurized atomizing gas at high velocity. The nozzle dimensions influence the size of produced droplet, and thus the size of resultant dry particle. In addition, pump feeding rate, liquid feed concentration, liquid feed type (i.e. solution, suspension, or an emulsion), solvent type (i.e. aqueous vs organic liquid), liquid viscosity, atomizing gas type, and aspiration rate may impact the particle size of final powder. However, regarding to the role of viscosity, opposite views has been expressed. It is suggested[30] that an increase in viscosity of feed increase the size of droplet and its dried particle. It is also reported[73, 74] that smaller particles are generated by using liquid with higher viscosity and faster feeding rate. These conditions are thought to generate a larger back-pressure in a nozzle, producing a finer spray due to an increase in sheer during atomization.

Drying of droplets takes place when contacting heated gas in the primary drying chamber. The type of drying gas with the associated moisture level may affect particle properties.[30]The rate of drying is mainly influenced by drying temperatures (both independent inlet and dependent outlet temperatures) and the flow rate of drying air[75]. The thermal efficiency of spray drying is generally defined as[75, 76].

$$\eta_{\text{overall}} = 100 * \left( \frac{T_{\text{in}} - T_{\text{out}}}{T_{\text{in}} - T_{\text{room}}} \right) \text{ (Equation 1.10)}$$

Where  $\eta_{\text{overall}}$  is overall thermal efficiency,  $T_{\text{in}}$  is the inlet temperature,  $T_{\text{out}}$  is the outlet temperature, and  $T_{\text{room}}$  is the room temperature. Using a low airflow rate exhibit a high efficient drying for dried particles due to a long resident time. However, a low airflow rate during spray drying associate with a low yield and possible large final particles[75].

Separation of dried particles from air stream is achieved by using a cyclone. With an application of centrifugal force, particles impact on the wall of cyclone. Particles are eventually collected in a bottom vial as removed from the cyclone wall. The effective particle collection is dependent upon geometry of the cyclone. With a given cyclone, the particle collection efficiency is enhanced with increasing airflow rate and powder mass loading[30].

## **1.6 Chronic Infections in the Deep Lungs (Cystic Fibrosis/Pulmonary Infections)**

Chronic infection diseases in lower respiratory regions[77] include cystic fibrosis (CF), pneumonia, chronic bronchitis, and etc. Chronic bronchitis, a type of chronic obstructive pulmonary disease (COPD), is highly caused cigarette smoking[78]. However, environment, occupation, and social class have also been associated to the development of chronic bronchitis[79-81]. Both bacterial (about 90%)[82] and viral (about 10%)[83] infections were observed in sputum of patients with chronic bronchitis. Pneumonia is an infectious lung disease, primarily in alveoli, with an inflammatory condition. Pneumonia is often caused by bacteria or virus such as *pneumococcus*, *klebsiella*, *Haemophilus influenza*, *staphylococcus* or *rhinoviruses*, *influenza virus* and etc.[77, 84].

### **1.6.1 Disease Background**

As a disease example of deep lung chronic infections, only CF is focused in details in this section. CF is an inherited life-shortening autosomal recessive disease, affecting about 30,000 children and adults in the United States (70,000 worldwide). The defective gene, CF transmembrane conductance regulator (CFTR), results in dysfunction of apical membrane CFTR protein. CFTR protein disrupts ion (chloride and sodium) transport in systems, including pulmonary airways, pancreatic ducts, sweat ducts, and intestine[85, 86]. Therefore, it results in the production of an abnormally viscous secretion[87].

The clinical consequences of this multi-system disease are characterized by progressive pulmonary damage leading to respiratory failure, pancreatic dysfunction, liver disease progressing to cirrhosis, gut motility problems, infertility and elevated sweat electrolytes[87, 88]. Nevertheless, the major causes of morbidity and mortality in patients with CF are obstruction of pulmonary airways and bronchiectasis[89].

CF originates from the deep lungs such as respiratory bronchiolar and alveolar regions. The lower airways of CF lungs are coated with thick and tenacious secretions, resulting in diminished function of mucociliary clearance. This creates an ideal environment for chronic lung infections, leading to cardiopulmonary failure. There are several bacterial species, such as *Pseudomonas aeruginosa*, *Staphylococcus aureus*, and *Burkholderia cepacia*, that appear to be especially well-adapted to cause chronic lung infections in CF lungs[90]. In young children of CF, *Staphylococcus aureus* and *Haemophilus influenza* are the two predominant pathogens. As increasing age, most patients will eventually progress to infection with *Pseudomonas aeruginosa* or a variety of other gram-negative organisms, including *Alcaligenes xylosoxidans*, *Stenotrophomonas maltophilia*, and ect.

Even in adult CF patients, the bacterial pathogens may change gradually with time. However there is one constant: endobronchial bacterial infection, once established, can't be completely eradicated. The therapeutic advances over the last several decades largely responsible for the dramatic increase in life expectancy in CF have been aimed primarily at decreasing the density of endobronchial *Pseudomonas aeruginosa* infection, thereby reducing the local inflammatory reaction that accounts for the progressive airway destruction characteristic of CF[91].

A proportion of CF patients are also affected by allergic bronchopulmonary aspergillosis (ABPA). This is a disease characterized by lung hypersensitivity due to endobronchial colonization with *Aspergillus fumigatus*[92]. The strains of *Aspergillus* have been isolated from the sputum of more than 20% and up to 52% of CF patients[93, 94]. ABPA is associated with an accelerated decline in lung function of CF patients[95]. The reported prevalence of ABPA in CF patient is around 10%, which is much higher than the non-CF population[94-96]. Many of the findings of ABPA overlap with common manifestation of the lung disease of CF. *Scedosporium apiospermum* is the second-most-frequent genus of fungi isolated from the sputa of CF patients. It exhibits a pathogenicity similar to that of *Aspergillus* species[97].

Patients suffering from CF are probably at particular risk of losing the ability of the surfactant to maintain airway potency. The disease is associated with inflammation, which cause a leakage of plasma proteins into the airway lumen. This is a likely cause of a disturbed function of the pulmonary surfactant[98, 99]. However, it is probably a more important reason that surfactant dysfunction is caused by a *Pseudomonas aeruginosa* infection in CF patients, in which *Pseudomonas aeruginosa* bacteria can synthesize and release phospholipase C (PLC) to the lung lumen[100-104]. This enzyme can catalyze a hydrolysis of phosphatidylcholine (PC), the main and most active surfactant component.

## **1.6.2 Disease Treatment**

Cystic fibrosis (CF) is a multisystem disorder disease. However, pulmonary disease is the predominant cause of morbidity and mortality. The treatment of CF is directed toward alleviation of symptoms and correction of organ dysfunction due to disease complications. Advances in research and medical treatments have enhanced and extended life for children and adults with CF. Many patients with CF are expected to live into their 30s, 40s, or beyond. In 2009, the median predicted age of survival was in the mid-30s[105]. There are some standard therapies and advanced treatments for CF patients, including restoration of airway surface liquid, mucus alteration, antimicrobial therapy, lung transplantation, and etc.

### **1.6.2.1 Restoration of Airway Surface Liquid**

Hydration of airway secretion offers an approach to improve mucociliary transport by using osmotic agents. A study[106] has suggested that twice-daily inhalation of a

hypertonic saline solution (osmotic agent) over 48 weeks has positive effects on two important aspects (improvement of lung function and reduction in the frequency of pulmonary exacerbations) of CF lung disease, compared to the control group of inhaled normal saline. Moreover, the study provided the evidence of long-term efficacy in patients with CF. In addition, mannitol, another osmotic agent, is being evaluated. Mannitol can be administered as a dry powder by metered-dose inhaler, which offering a less time-consuming alternative to hypertonic saline[107]. In addition, hypertonic saline and dry-powder mannitol are also considered as non-destructive mucolytic agents[108]. These two osmotic agents hydrate the mucus matrix, breaking upon ionic and hydrogen bonds, rather than covalent bonds, in mucous gel. Without reducing polymer chain length in mucus matrix, these osmotic agents alter the crosslink density of mucus, decreasing the physical entanglement. It results into a reduction in both elasticity and viscosity of mucus, a preferential improvement in mucociliary clearance. The detailed mechanism of action[108] is discussed in the literature. Hypertonic saline (known as MucoClear<sup>TM</sup>)[109] has been marketed. Mannitol dry powder for inhalation (known as Bronchitol<sup>TM</sup>) is in phase III clinical trial in the US[105].

#### **1.6.2.2 Mucolytics (Destructive)**

To alter the physical properties of the viscous and rigid mucus, the direct strategy is mucolysis (destructive). Normally, it is desirable to reduce the crosslinking and viscoelasticity in the mucus in order to improve mucus clearance. Mucins, generally, are secreted as heavily glycosylated peptide oligomers, holding together by –S-S- bridges derived from unpaired cysteine units near the non-glycosylated C-terminus end of the mucin peptide[110, 111]. Classical mucolytic, N-acetylcysteine (NAC; a thiol reducing agent), degrades the three-dimensional network that forms the mucous gel by breaking macromolecular backbone. Although not in the USA or Canada, NAC has been widely used as a mucolytic agent in many countries[108]. It is suggested that there is a risk of bronchospasm in hyper-reactive patients by using NAC.

Mucus also contains products of inflammation including cellular debris, neutrophil derived DNA, and filamentous actin (F-actin). DNA and F-actin co-localize in mucus to form a rigid network entangled with the mucins[112]. Dornase alfa (a recombinant human enzyme DNase I) and gelsolin (F-actin depolymerizing agent) reduces mucus viscosity and tenacity, leading to a reduction in frequency of pulmonary exacerbation and an improvement in measured quality of life for CF patients[108]. At present, dornase alfa (Pulmozyme<sup>®</sup>) is an only FDA-approved mucolytic medication in the US.

#### **1.6.2.3 Antimicrobial Therapies**

Chronic bacterial infection induces inflammation of the airways, obstructive airways disease, and bronchiectasis. Antibiotic therapies for patients with CF have remained as a cornerstone of treatment. Indeed, the advance in development of potent broad-spectrum



antibiotics, particularly antipseudomonal antibiotics, impact on the increasing survival rate of CF patient[113]. *Pseudomonas aeruginosa* is not able to be eradicated. However, the burden of infection usually can be reduced by antibiotic therapy, with improvement in symptoms and lung function[114]. Antibiotics can be administered via oral, parenteral, and pulmonary deliveries. The aminoglycoside (e.g., tobramycin)[115], macrolide (e.g., azithromycin)[116], and quinolone (e.g., ciprofloxacin)[117] antibiotic drugs are often administered to CF patient with improvement of pulmonary functions. Administration of antibiotics by inhalation offers an attractive way to deliver high dose to the site of infection. It minimizes the systemic effects which are often observed when antibiotics are administered in other delivery routes. For instance, the therapeutic plasma concentration of tobramycin may cause severe ototoxicity and nephrotoxicity in a long-term therapy[115]. Studies have shown that inhalation of antibiotics increased the therapeutic index of the drugs[118]. The inhaled tobramycin (solution), TIP<sup>®</sup> (tobramycin inhaled powder), azithromycin (tablet), and Cayston<sup>®</sup> (inhaled aztreonam solution) are available on the market[105].

Allergic bronchopulmonary aspergillosis (ABPA), due to lung hypersensitivity to *Aspergillus*, has been reported to occur in some CF patients. Steroids remain the mainstay of treatment for ABPA[119]. An oral antifungal agent, itraconazole, has been reported to be of benefit in patients when used in addition to prednisone treatment[120].

#### **1.6.2.4 Lung Transplantation**

In terms of facing of incipient death due to respiratory failure, attention has been directly at ensuring comfort and minimizing distress of CF patients. The development of successful lung transplantation brings a new hope for CF patient with severe respiratory disease. Lung transplantation offers an opportunity to prolong the duration and to significantly improve the quality of patients' lives[121, 122]. However, Infectious, pharmacologic, and nutritional issues inherent to CF add some complexity to the care of a given lung transplant patients. The 5-year survival rate of lung transplantation is 48%[123, 124].

#### **1.6.2.5 Advanced Therapies**

##### **1.6.2.5.1 Gene Therapies**

Currently, an intense research effort is underway to develop more specific therapies for CF patients. These specific therapies target the underlying pathophysiology of the disease. The new approaches could address the underlying pathophysiological defects resulting from the mutated CFTR at several levels[119]. Rather than only treating the symptoms, gene therapies treat the disease by tackling the root cause of CF. The basic concept behind gene therapies is to identify the defective gene and replace the defect with a normal one. There are two forms of gene therapies, including germ line gene therapy (inheritable to future generations) and somatic gene therapy (not inheritable to future

generations)[125]. Several promising clinical trials of using virus and non-viral vectors have been carried out, supporting gene transfer to the airway epithelium is feasible[126]. However, gene therapy studies have revealed safety and efficiency issues in gene transfer in the lungs[127]. Additionally, it has been shown that the immune system of CF patient posed a significant barrier, hampering the efforts of vector administration[127].

#### **1.6.2.5.2 CFTR modulation**

Unlike gene therapy which replacing defective gene, the CFTR modulation approaches either repair the defective gene or play a role in fixing CFTR proteins. This approach is directed at the ion transport defects in CF, including the use of amiloride and uridine-5'-triphosphate (UTP). The approach of CFTR modulation normalizes ion transport by inhibiting excessive sodium absorption and enhancing defective chloride secretion[128]. Amiloride blocks the excessive sodium transport into CF airway epithelia. UPT stimulates chloride secretion via the alternative (not the CFTR) chloride channel. The studies have shown that inhaled amiloride[129, 130] and UTP[131, 132] improved mucociliary clearance in healthy subjects and CF patients. Several CFTR modulation therapies are currently in clinical trials, such as Ataluren, VX-809 + ivacaftor, VX-661 + ivacaftor, and N6022[105]. Kalydeco<sup>TM</sup> is currently in market in the US[105].

## Chapter 2 Statement of Aims

### 2.1 Statement of Problem

Chronic infection diseases in the deep lungs (such as cystic fibrosis (CF), pneumonia, and etc.) are characterized by accumulation of thick and sticky mucus, chronic lung infections, and compromised lung surfactant composition. These multi-factored diseases, originating in the deep lungs (respiratory bronchiolar and alveolar regions), mainly contributes to the death of patients in the early ages. However, the unmet medical needs in the chronic deep lungs infections are not fulfilled. This is mainly due to a lack of a multiple-component formulation specifically targeting the deep lung regions with co-deposition of medicines and effectively interfering several disease factors simultaneously. As a consequence, patients with chronic infections in the deep lungs massively are under threats of progressive pulmonary damage and respiratory failure.

This dissertation is designed to test whether the proposed multi-component dry powder formulation for inhalation could be produced with essential particle properties suitable for deep lung delivery. Specifically, microparticulate and nanoparticulate aerosol particles (typically 0.5 to 2  $\mu\text{m}$ ) are required to have efficient particle deposition in respiratory bronchiolar and alveolar regions by sedimentation and diffusion, respectively. In addition, in the proposed multi-component particles, mannitol, azithromycin or tobramycin, dipalmitoylphosphatidylcholine (DPPC):dipalmitoylphosphatidylglycerol (DPPG)=4:1 (molar ratio) are used as (non-destructive) mucolytic agent, antimicrobial drug, lung surfactant mimic phospholipids, respectively.

### 2.2 Goal of Dissertation and Specific Aims

#### 2.2.1 Goal of Dissertation

The overall goal of this dissertation is to manufacture and characterize multi-component inhalable microparticulate and nanoparticulate aerosol particles with essential particle properties suitable for deep lung delivery by spray drying from organic solution.

#### 2.2.2 Specific Aims

In order to achieve the goal of this dissertation in Section 2.2.1, there are five specific aims for this dissertation:

- 1) Produce multi-component microparticulate and nanoparticulate aerosols in solid-state with particle properties of narrow size distribution, and spherical and smooth surface morphologies (Chapter 3)
- 2) Characterize physicochemical properties of aerosol particles (Chapter 4)
- 3) Conduct *in vitro* aerosol dispersion performance of aerosol particles (Chapter 5)
- 4) Evaluate storage stability of aerosol particles (Chapter 6)
- 5) Assess *in vitro* drug release of aerosol particles (Chapter 7)

### **2.3 Significance**

It is envisioned that successful completion of this work can provide a novel and targeted multi-component dry powder aerosol formulation for the treatment of chronic infection in the deep lungs. The multi-component therapies in a single inhalation aerosol formulation (co-deposition) of targeting deep lung regions could potentially enhance the therapeutic outcome in CF treatment. Administration by multi-component formulations would likely reduce the total dosing frequencies with a single therapy, lowering the burden of diseased lungs and improving the quality-of-life for patients. Moreover, understanding of physicochemical properties and pharmaceutical performance of the formulations may aid formulation scientist in more rationally selecting the components to achieve desired performance of multi-component dry powder formulations in future.

## Chapter 3 Aerosol Particle Design and Manufacturing

### 3.1 Introduction

In order to deliver aerosol particles to the lower respiratory tract and small peripheral airways[133], nano and microparticles ( $\sim 0.5\text{-}2\mu\text{m}$ )[134-136] are required. Moreover, with a relatively narrow (unimodal) size distribution ( $\sim 0.5\text{-}2\mu\text{m}$ ) of aerosol particles, reproducibility of deposition in a specific deep lung region may be ensured.

Interparticulate forces in dry powders[64] are illustrated in Figure 3.1. Interparticulate forces including cohesive/adhesive van der Waals, electrostatic, capillary forces, and mechanical interlocking, impact particle interactions during aerosol dispersion[41, 63, 64]. van der Waals forces dominate interparticulate forces at low relative humidity (RH)  $< 65\%$ , while capillary forces may exhibit a major influence at RH  $> 65\%$ [41]. The extent of the forces is dependent on the particle properties (size, shape, geometry, and etc.) and ambient conditions (humidity, electrostatics, and etc.)[41, 63, 64]. The magnitude of interparticulate forces could be lowered by producing spherical particles with smooth surface and low water content[63, 64]. For example, spherical particles enable one-point contact, lowering van der Waals forces. Moreover, the curvature of particles decreases surface charge density, leading to a drop in electrostatic forces[63, 64]. In addition, relatively smooth surface morphology of particles could minimize the potential of mechanical interlocking, as well as further decrease van der Waals and electrostatic forces. Reproducibility of dosing in specific regions in lungs is a primary advantage of spherical particles with narrow size distribution. Capillary forces, forming high tensile liquid bridges between particles, are lowered by decreasing the condensation of water vapor. For the purpose of flow of dissertation, water content determination will be covered in Chapter 4.

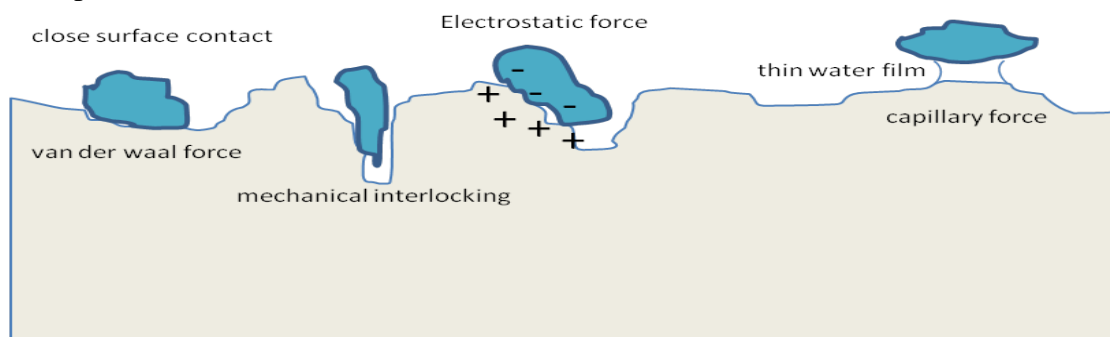


**Figure 3.1.** Illustration of interparticulate forces in static dry powder. Adapted from [64].

There are several methods available to make respirable particles, including micronization, precipitation, supercritical fluids, and spray drying[68-70]. Spray drying (SD) is a one-step high through-put process with the ability to produce particles in a controlled manner, such as directing particle size and size distribution, particle shape, and particle morphology, which are important particle features for pulmonary drug delivery by inhalation. Co-spray drying a solution containing two APIs is a potential alternative to

produce particles with uniform drug composition[137]. Several studies of co-spray drying of two drugs have been reported, including inhaled corticosteroid (ICS)/short-acting  $\beta_2$ -agonist[138, 139], antibiotics[140, 141], terbutaline sulfate and beclomethasone propionate[139]. Alcohols, such as methanol (which is regarded as a “green chemical”), have lower surface tension in the range of 22 to 25 mN/m with comparison to water (72 mN/m). Due to the lower surface tension, spray drying from an alcohol solution efficiently reduces the size of droplets during atomization and results in small particle size of powders. Furthermore, the moisture % in the SD powders could be minimized by employing organic solvents.

Particle morphology and surface morphology of spray-dried (SD) particles are examined by microscopy. Scanning electron microscopy (SEM) employs electrons, instead of light, for particle viewing by scanning a focused beam of electrons on a sample. Electrons interact with the sample, producing secondary electrons. The secondary electrons are collected, converted to voltage, and amplified. Depending upon the topography of the sample, a SEM image consists of countless spots with various signal intensities. In order to have electrically conductive, most organic substances require a thin coating of conductive material (e.g., gold, platinum, and etc.). With a resolution better than 1 nanometer, SEM is an excellent technique to evaluate particle structure and characteristic surface appearance of SD particles.

Laser diffraction is commonly used for the determination of particle size and distribution of a sample. The measurement is based on the scattering light with an intensity pattern at various angles after particles are passing through a beam of a monochromatic light laser. An algorithm, based on Fraunhofer or Mie theory, is used to calculate particle size and distribution from the diffraction pattern. Laser diffraction analysis yields volume-average size and distribution in volume, based upon the theory of “equivalent spherical diameter”. Besides the media of particle size, a series of distribution parameters from laser diffraction could be calculated:  $D_{V10}$  = 10% of particles are below this size;  $D_{V50}$  = 50% of particles are smaller (volumetric median diameter);  $D_{V90}$  = 90% of particles are below this size. Thereafter, size distribution of samples could be expressed by span value as below:

$$\text{span value} = (D_{V90} - D_{V10})/D_{V50} \quad (\text{Equation 2.1})$$

The laser diffraction is conducted through a wet sampling system in this study, requiring spray-dried particles to be dispersed in an appropriate dispersant. Occasionally, due to the lack of an appropriate dispersant, image size analysis is used as an alternative method. SigmaScan<sup>TM</sup> is used to determine primary particle size (projected geometric diameter) and distribution for some particular formulations to which laser diffraction approach is not applicable. To determine the projected geometric particle size, a line is drawn, across the center, on a primary particle on SEM micrograph. The mean particle size (projected mean geometric diameter) and size range are determined by measuring over 100 primary particles to get statistically meaningful data.

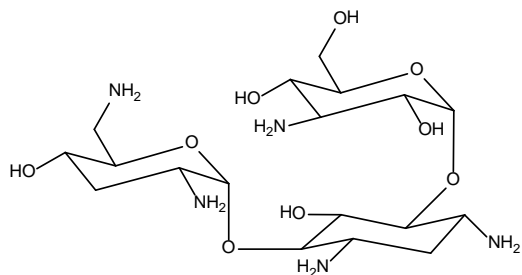
In this chapter, the effects of spray-drying conditions (such as pump rate) of one-component and multi-component systems on particles size, particle morphology and

surface morphology of SD particles will be examined.

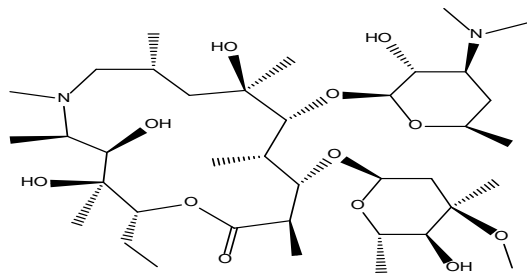
### 3.2 Materials and Methods

#### 3.2.1 Materials

Tobramycin (TOB) (U.S.P. grade) ( $C_{18}H_{37}N_5O_9$ ; MW.: 467.515 g/mol) was obtained from Spectrum (New Brunswick, New Jersey). Azithromycin (AZI) (U.S.P. grade) ( $C_{38}H_{72}N_2O_{12}$ ; MW.: 748.984 g/mol) was purchased from APAC pharmaceutical LLC (Hangzhou, China) with purity of 98%. Dipalmitoylphosphatidylcholine (DPPC) ( $C_{40}H_{80}NO_8P$ ; MW.: 734.05g/mol) and dipalmitoylphosphatidylglycerol sodium (DPPG) ( $C_{38}H_{74}NO_{10}PNa$ ; MW.: 744.96g/mol) were purchased from Avanti Polar Lipids, Inc. (Alabaster, Alabama). D-Mannitol (MAN) (SigmaUltra) ( $C_6H_{14}O_6$ ; MW.: 182.17 g/mol) was from Sigma-Aldrich (France). The chemical structures of the compounds are shown in Figure 3.2. Methanol (HPLC grade, ACS-certified grade, purity 99.9%) was obtained from Fisher Scientific (Fair Lawn, New Jersey). All nitrogen gas used for experiments was an ultra-high purity (UHP) nitrogen gas manufactured by Scotts Gross (Lexington, Kentucky). TOB and AZI were stored in the sealed glass desiccators over Indicating Drierite/Drierite<sup>TM</sup> desiccant at 4°C under ambient pressure. DPPC and DPPG were stored in the sealed glass desiccators over Indicating Drierite/Drierite<sup>TM</sup> desiccant at -20°C under ambient pressure. MAN was stored under room conditions. All materials were used as received.



(a)



(b)

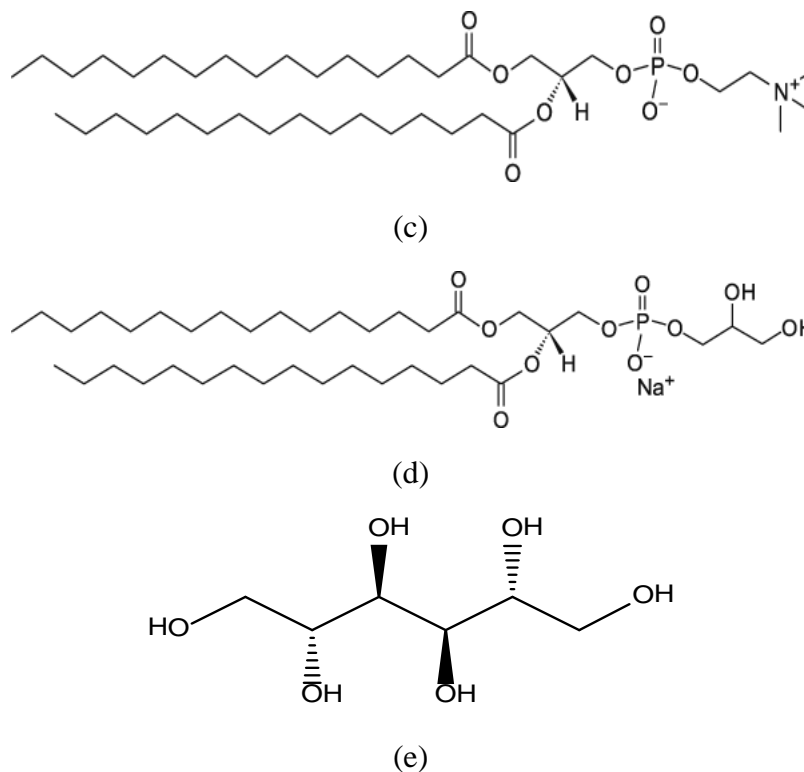


**Figure 3.2.** The chemical structures for: (a) tobramycin; (b) azithromycin; (c) dipalmitoylphosphatidylcholine (DPPC); (d) dipalmitoylphosphatidylglycerol sodium salt (DPPG); and (e) D-mannitol.

### 3.2.2 Methods

#### 3.2.2.1 Preparation of Spray-dried (SD) Particles by Organic Solution Spray Drying

Neat organic solution spray-drying process was performed using a Büchi B-290 Mini Spray Dryer (Büchi, Switzerland) in closed-mode. With connection to a B-295 Inert Loop (Büchi, Switzerland), the spray dryer employed a high performance cyclone to increase powder yield. Dry nitrogen gas (UHP) was used as the atomizing drying gas. Feeding stock solution was made by dissolving as received material(s) to make a concentration of 0.1% w/v in methanol. Inlet temperature was set at 150°C. A stainless steel nozzle with diameter of 0.7mm was used. Atomization rate of 600L/h and aspirate rate of 35m<sup>3</sup>/h were used. Spray-drying pump rates varied with formulation systems: A) one-component system: 3 ml/min (10%; low pump rate), 15 ml/min (50%; medium pump rate), and 30 ml/min (100%; high pump rate); B) multi-component system (with change of formulation composition): 15 ml/min (50%; medium pump rate). The corresponding outlet temperatures for each SD formulations of tobramycin and azithromycin are summarized in Table 3.1 and Table 3.2, respectively. SD particles were separated from the nitrogen drying air in a cyclone and collected in a sample collection vial. All SD powders were carefully stored in sealed glass vials that were stored in sealed glass desiccators over Indicating Drierite/Drierite<sup>TM</sup> desiccant at -20°C under ambient pressure.



**Table 3.1.** Summary of spray drying conditions of tobramycin relevant formulations.

Formulation System	Pump Rate (%)	Outlet Temperature (°C)
Pure TOB	10	88
	50	69
	100	35
TOB:MAN=1:0.1	50	63
TOB:MAN=1:0.25	50	61
TOB:MAN=1:0.5	50	59
TOB:MAN=1:0.75	50	58
TOB:MAN=1:1	50	55
TOB:PLS=1:2	50	57
TOB:PLS=1:1	50	54
TOB:PLS=1:0.5	50	65
TOB:PLS:MAN=1:0.5:0.1	50	58
TOB:PLS:MAN=1:0.5:0.25	50	65
TOB:PLS:MAN=1:0.5:0.5	50	54
TOB:PLS:MAN=1:0.5:0.75	50	66
TOB:PLS:MAN=1:0.5:1	50	61

**Table 3.2.** Summary of spray drying conditions of azithromycin relevant formulations.

Formulation System	Pump Rate (%)	Outlet Temperature (°C)
Pure AZI	10	89
	50	75
	100	50
AZI:MAN=1:0.1	50	67
AZI:MAN=1:0.25	50	66
AZI:MAN=1:0.5	50	64
AZI:MAN=1:0.75	50	65
AZI:MAN=1:1	50	59
AZI:PLS=1:2	50	66
AZI:PLS=1:1	50	60
AZI:PLS=1:0.5	50	59
AZI:PLS:MAN=1:0.5:0.1	50	60
AZI:PLS:MAN=1:0.5:0.25	50	68
AZI:PLS:MAN=1:0.5:0.5	50	67
AZI:PLS:MAN=1:0.5:0.75	50	66
AZI:PLS:MAN=1:0.5:1	50	58

### **3.2.2.2 Scanning Electron Microscopy (SEM)**

Visualization of particle morphology (or structure) and surface morphology of samples was achieved by using a Hitachi S-800 microscope (Tokyo, Japan). Samples were placed on double-sided adhesive carbon tabs (TedPella, inc.) which were adhered to aluminum stubs (TedPella, inc.) and coated with gold/palladium alloy thin film using a Hummer VI sputtering system (Technics). The coating process operated at 10 AC milliAmperes with 8 kV of voltage for 3min. The electron beam with an accelerating voltage of 20 kV was used at a working distance of 30mm. SEM images were captured by Evex NanoAnalysis. Several magnification levels were used.

### **3.2.2.3 Particle Sizing and Size Distribution**

#### **3.2.2.3.1 Laser Light Diffraction**

Particle size and size distributions of SD particles (SD pure tobramycin and SD tobramycin:mannitol) were determined by laser diffraction using SALD-7101 (Shimadzu Scientific Instruments, Japan). Samples were dispersed in chloroform and ultrasonicated for 10 s in a water bath ultrasonicator Branson 5210 (Danbury, Connecticut) before measuring particle size. Particle dispersions of samples were immediately transferred to a measuring cell and kept stirring during measurement in the nano particle size analyzer. Due to the use of chloroform, a refractive index 1.60-0.10 was selected for the experiments. Volume-based dimension of particle amount distribution was obtained for samples.  $D_{V10}$ ,  $D_{V50}$ , and  $D_{V90}$  from Shimadzu software were used as particle size characterization parameters. The span value was calculated using Equation 2.1. All experiments were done in triplicate (n=3) for each formulation.

#### **3.2.2.3.2 Image Size Analysis**

As an alternative way to determine primary particle size and size distribution, SigmaScan<sup>TM</sup> Pro 5 (Jandel Scientific, CA) was used due to the difficulty of samples being dispersed in various dispersants for laser diffraction. Image size analysis was based on SEM micrographs. Calibration of distance measurement was done on the scaling bar on micrographs. The diameter was measured for at least 100 particles and statistical data was calculated (mean  $\pm$  S.D. & size range).

## **3.3 Results**

### **3.3.1 Scanning Electron Microscopy (SEM)**

#### **3.3.1.1 One-component System (Spray-dried Pure Drug)**

SEM micrographs of spray-dried (SD) pure tobramycin (TOB) and pure azithromycin (AZI) particles[43], produced from low (10%), medium (50%), and high (100%) pump

rates, respectively, are shown in Figure 3.3. As received particles of TOB and AZI possessed sharp edges and particle sizes far beyond the respiratory range for dry powder inhalation (DPI), a value less than  $10\mu\text{m}$ [142]. In general, relatively spherical particle morphology and smooth surface morphology of SD particles were produced for each component from various pump rates. However, as shown in Figure 3.3d and 3.3h, more corrugated surface of SD particles generated from high pump rate was also observed.

### **3.3.1.2 Two-component System**

#### **3.3.1.2.1 Spray-dried Drug:Mannitol**

SEM micrographs of SD tobramycin:mannitol (TOB:MAN) and azithromycin:mannitol (AZI:MAN) particles[143] are shown in Figure 3.4. Under the same spray-drying conditions, relatively spherical particle morphology and smooth surface morphology of SD particles were produced for each system with various composition ratios. In addition, it was noticed that some AZI:MAN (e.g., Figure 3.4i and 3.4j) appeared to have relatively more corrugations on surface than TOB:MAN.

#### **3.3.1.2.2 Spray-dried Drug:Phospholipids**

SEM micrographs of SD tobramycin:phospholipids (TOB:PLS) and azithromycin:phospholipids (AZI:PLS) particles are shown in Figure 3.5. Relatively spherical particle morphology and smooth surface morphology of TOB:PLS were produced with various PLS content in the system. However, it is noticed that incomplete particle formation was observed for AZI:PLS=1:1 (Figure 3.5e) and AZI:PLS=1:2 (Figure 3.5d). Contrastingly, relatively spherical particle morphology and smooth surface morphology of AZI:PLS were produced at molar ratio of 1:0.5 in Figure 3.5f.

### **3.3.1.3 Three-component System (Spray-dried Drug:Phospholipids:Mannitol)**

SEM micrographs of SD tobramycin:phospholipids:mannitol (TOB:PLS:MAN) and azithromycin:phospholipids:mannitol (AZI:PLS:MAN) particles are shown in Figure 3.6. For the three-component systems, the ratio of antibiotics:phospholipids was fixed at 1:0.5 in order to get a high antibiotic drug loading. The MAN content in three-component formulations varied from 0.1 to 1. All TOB:PLS:MAN particles possessed relatively spherical particle shape and smooth surface except for TOB:PLS:MAN=1:0.5:0.75 (Figure 3.6d) with incomplete particle formation. In general, regardless of AZI:PLS:MAN=1:0.5:0.25 (Figure 3.6g) with some aggregation, AZI:PLS:MAN particles were produced with desired particle properties of relatively spherical particle morphology and smooth surface morphology.

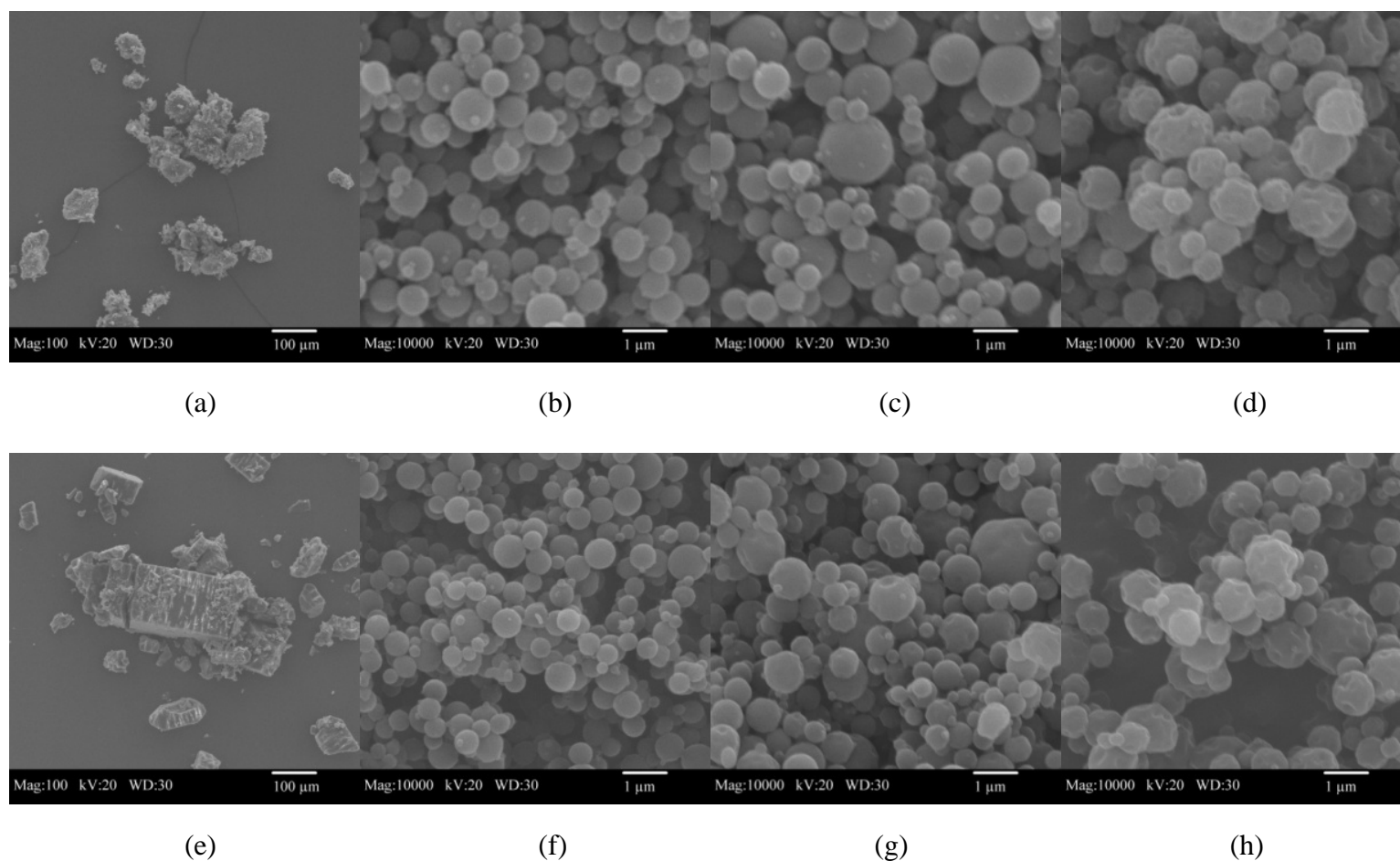


**Figure 3.3.** SEM micrographs of as received particles (magnification 100X) and SD pure particles (magnification 10,000X) of tobramycin (TOB) and azithromycin (AZI)[43] for: (a) As received TOB; (b) SD pure TOB (10%P); (c) SD pure TOB (50%P); (d) SD pure TOB (100%P); (e) As received AZI; (f) SD pure AZI (10%P); (g) SD pure AZI (50%P); and (h) SD pure AZI (100%P).

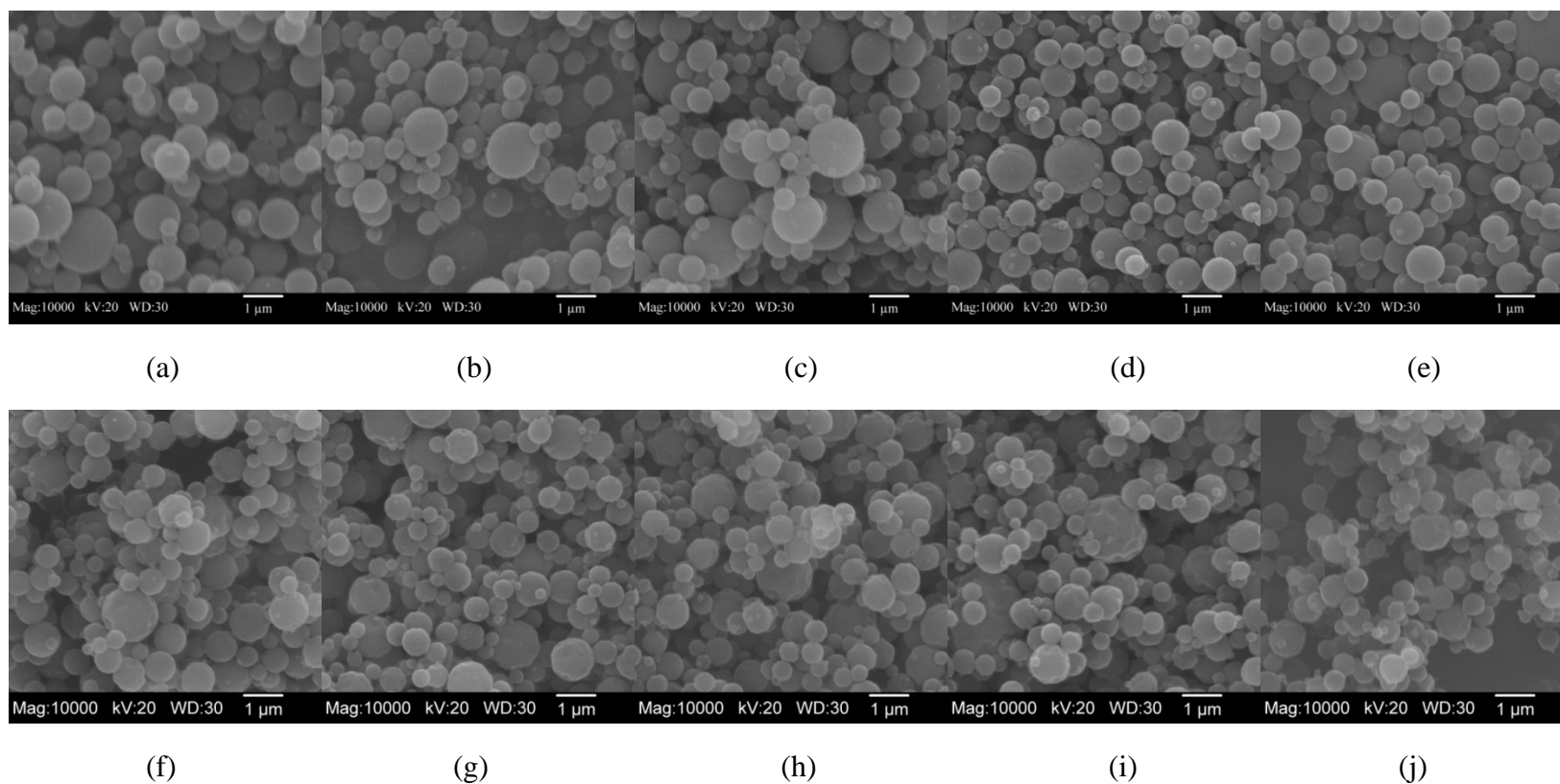


**Figure 3.4.** SEM micrographs of SD tobramycin:mannitol (TOB:MAN) and SD azithromycin:mannitol (AZI:MAN) particles[143] (magnification 10,000X) for: (a) TOB:MAN=1:0.1; (b) TOB:MAN=1:0.25; (c) TOB:MAN=1:0.5; (d) TOB:MAN=1:0.75; (e) TOB:MAN=1:1; (f) AZI:MAN=1:0.1; (g) AZI:MAN=1:0.25; (h) AZI:MAN=1:0.5; (i) AZI:MAN=1:0.75; and (j) AZI:MAN=1:1.

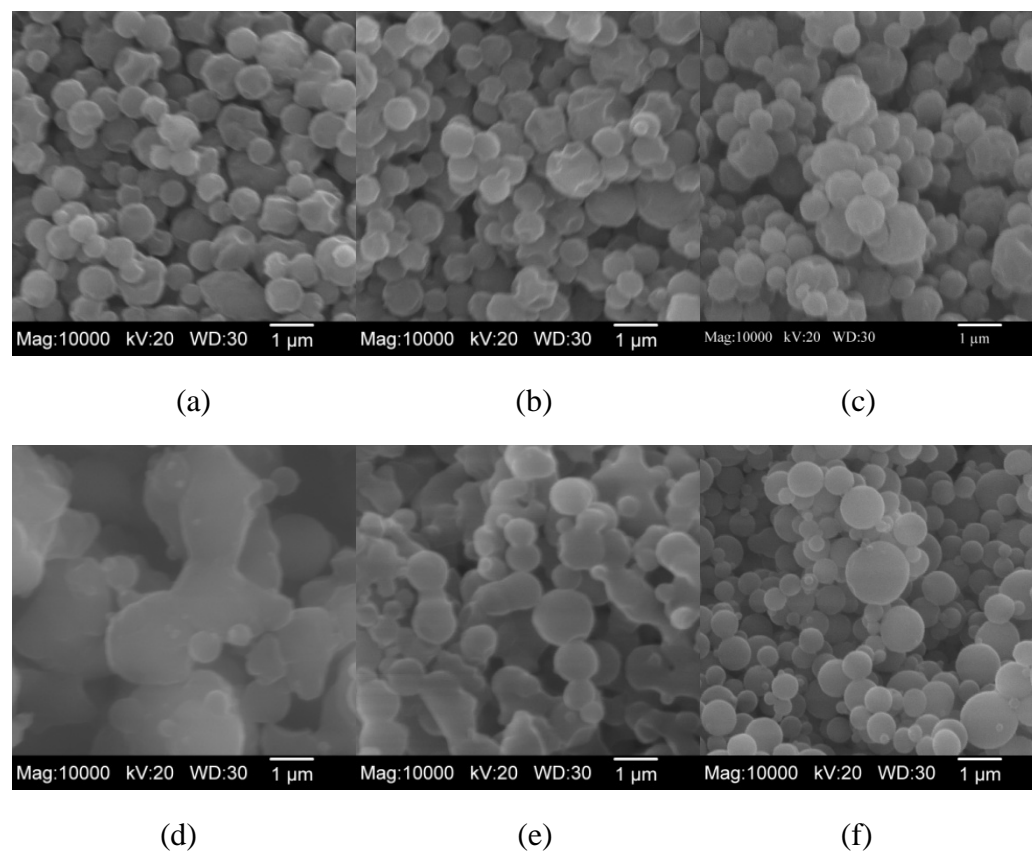


**Figure 3.5.** SEM micrographs of SD tobramycin:phospholipids (TOB:PLS) and SD azithromycin:phospholipids (AZI:PLS) particles (magnification 10,000X) for: (a) TOB:PLS=1:2; (b) TOB:PLS=1:1; (c) TOB:PLS=1:0.5; (d) AZI:PLS=1:2; (e) AZI:PLS=1:1; and (f) AZI:PLS=1:0.5.

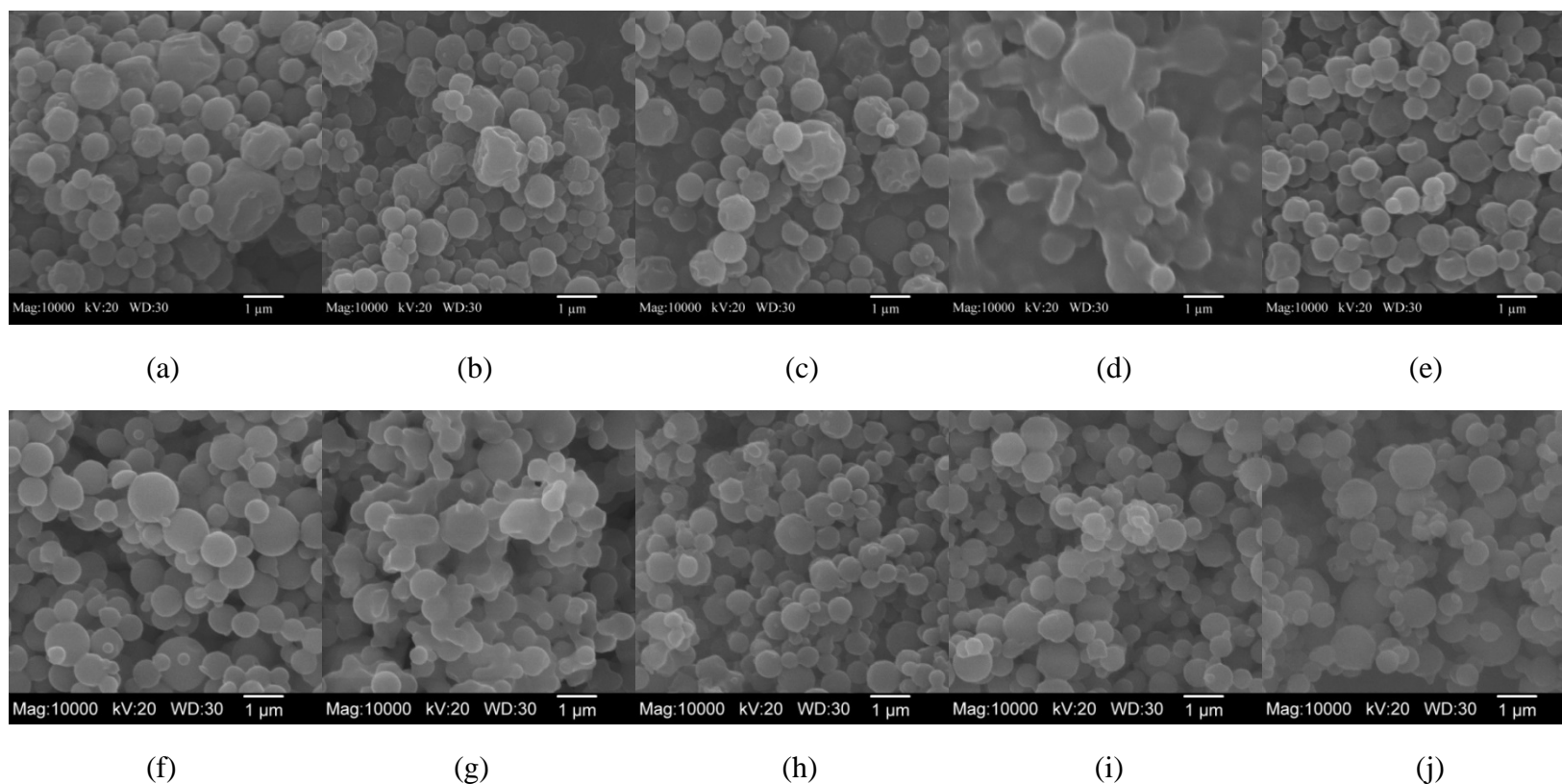


**Figure 3.6.** SEM micrographs of SD tobramycin:phospholipids:mannitol (TOB:PLS:MAN) and SD azithromycin:phospholipids:mannitol (AZI:PLS:MAN) particles (magnification 10,000X) for: (a) TOB:PLS:MAN=1:0.5:0.1; (b) TOB:PLS:MAN=1:0.5:0.25; (c) TOB:PLS:MAN=1:0.5:0.5; (d) TOB:PLS:MAN=1:0.5:0.75; (e) TOB:PLS:MAN=1:0.5:1; (f) AZI:PLS:MAN=1:0.5:0.1; (g) AZI:PLS:MAN=1:0.5:0.25; (h) AZI:PLS:MAN=1:0.5:0.5; (i) AZI:PLS:MAN=1:0.5:0.75; and (j) AZI:PLS:MAN=1:0.5:1.

### 3.3.2 Particle Sizing and Size Distribution

#### 3.3.2.1 One-component System (Spray-dried Pure Drug)

By laser diffraction, SD pure TOB particles all exhibited a unimodal size distribution. The detailed sizing data of SD pure TOB are summarized in Table 3.3[43]. The median volumetric diameter ( $D_{V50}$ ) slightly increased from 0.6 $\mu\text{m}$  to 0.8 $\mu\text{m}$  for SD pure TOB as spray-drying pump rates increased from 10% (low) to 100% (high). The  $D_{V90}$  of particles was in the range from 1.1 to 1.6 $\mu\text{m}$  for SD pure TOB, consistent with the presence of microsized particles. However, majority of SD pure TOB particles were under micro-size range. Span value of SD TOB was in the range between 1.3 and 1.4, suggesting a relatively narrow size distribution.

Image sizing analysis results of SD AZI primary particles are summarized in Table 3.4[43]. SD AZI increased projected mean geometric diameter from 0.5 $\mu\text{m}$  to 0.7 $\mu\text{m}$  as pump rates employed in spray drying increased from low to high. With upper limit value being equal or over 1 $\mu\text{m}$  (but less than 2 $\mu\text{m}$ ), size range data suggests that SD AZI particles possessed microsized particles. In addition, size range data also indicated a relatively narrow size distribution for SD AZI particles.

**Table 3.3.** Laser diffraction sizing of SD pure tobramycin particles[43] (mean  $\pm$  SD, n=3).

SD Drug	Pump Rate (%)	$D_{V10}(\mu\text{m})$	$D_{V50}(\mu\text{m})$	$D_{V90}(\mu\text{m})$	Span Value
Tobramycin	10	0.4 $\pm$ 0.0	0.6 $\pm$ 0.0	1.1 $\pm$ 0.0	1.3 $\pm$ 0.0
	50	0.4 $\pm$ 0.0	0.6 $\pm$ 0.0	1.4 $\pm$ 0.0	1.4 $\pm$ 0.1
	100	0.5 $\pm$ 0.0	0.8 $\pm$ 0.0	1.6 $\pm$ 0.0	1.4 $\pm$ 0.0

**Table 3.4.** Image sizing of SD pure azithromycin primary particles[43] (mean  $\pm$  SD, n $\geq$ 100).

SD Drug	Pump Rate (%)	Particle Size ( $\mu\text{m}$ )	Size Range ( $\mu\text{m}$ )
Azithromycin	10	0.5 $\pm$ 0.1	0.2-1.0
	50	0.6 $\pm$ 0.3	0.3-1.9
	100	0.7 $\pm$ 0.3	0.2-1.8

#### 3.3.2.2 Two-component System

##### 3.3.2.2.1 Spray-dried Drug:Mannitol

By laser diffraction, SD TOB:MAN particles all exhibited a unimodal distribution. Detailed data of TOB:MAN are summarized in Table 3.5[143]. Relatively consistent size was achieved with changing of composition in TOB:MAN. The  $D_{V50}$  (volumetric median diameter) was in the range from 0.6 $\mu\text{m}$  to 0.7 $\mu\text{m}$  for TOB:MAN particles.  $D_{V90}$  of



TOB:MAN indicating microparticulate particles were also present in formulations. Span value of TOB:MAN was in the range between 1.5 and 1.7, indicating a relatively narrow size distribution.

Image sizing analysis of SD AZI:MAN primary particles are summarized in Table 3.6[143]. With the change of composition in formulations, projected mean geometric diameter of AZI:MAN were constant at 0.6 $\mu$ m. Size range data indicates the presence of microparticulate particles and a relatively narrow size distribution for AZI:MAN.

**Table 3.5.** Laser diffraction sizing of SD tobramycin:mannitol particles[143] (mean  $\pm$  SD, n=3).

Particles	D <sub>V10</sub> ( $\mu$ m)	D <sub>V50</sub> ( $\mu$ m)	D <sub>V90</sub> ( $\mu$ m)	Span Value
TOB:MAN=1:0.1	0.4 $\pm$ 0.0	0.6 $\pm$ 0.0	1.4 $\pm$ 0.0	1.6 $\pm$ 0.1
TOB:MAN=1:0.25	0.4 $\pm$ 0.0	0.7 $\pm$ 0.0	1.4 $\pm$ 0.1	1.5 $\pm$ 0.1
TOB:MAN=1:0.5	0.4 $\pm$ 0.0	0.7 $\pm$ 0.0	1.4 $\pm$ 0.1	1.5 $\pm$ 0.0
TOB:MAN=1:0.75	0.4 $\pm$ 0.0	0.6 $\pm$ 0.0	1.4 $\pm$ 0.0	1.7 $\pm$ 0.1
TOB:MAN=1:1	0.4 $\pm$ 0.0	0.7 $\pm$ 0.0	1.5 $\pm$ 0.1	1.6 $\pm$ 0.0

**Table 3.6.** Image sizing of SD azithromycin:mannitol primary particles[143] (mean  $\pm$  SD, n $\geq$ 100).

Formulation	Particle Size ( $\mu$ m)	Size Range ( $\mu$ m)
AZI:MAN=1:0.1	0.6 $\pm$ 0.2	0.2-1.4
AZI:MAN=1:0.25	0.6 $\pm$ 0.2	0.2-1.3
AZI:MAN=1:0.5	0.6 $\pm$ 0.2	0.2-1.4
AZI:MAN=1:0.75	0.6 $\pm$ 0.2	0.2-1.8
AZI:MAN=1:1	0.6 $\pm$ 0.2	0.3-1.1

### 3.3.2.2.2 Spray-dried Drug:Phospholipids

Image size analysis of SD TOB:PLS and SD AZI:PLS primary particles are summarized in Table 3.7. All particles possessed mean particle size in the range from 0.6 to 0.8 $\mu$ m. In addition to the presence of microparticulate particles, size range data indicated a relatively narrow size distribution for both TOB:PLS and AZI:PLS. Due to incomplete particle formation, size analysis of AZI:PLS=1:2 was not conducted.

**Table 3.7.** Image sizing of SD drug:phospholipids primary particles (mean  $\pm$  SD,  $n \geq 100$ ).

Formulations (molar ratio)	Particle Size ( $\mu\text{m}$ )	Size Range ( $\mu\text{m}$ )
TOB:PLS=1:2	$0.7 \pm 0.2$	0.4-1.2
TOB:PLS=1:1	$0.7 \pm 0.2$	0.3-1.4
TOB:PLS=1:0.5	$0.7 \pm 0.3$	0.3-1.6
AZI:PLS=1:2	-	-
AZI:PLS=1:1	$0.8 \pm 0.2$	0.4-1.4
AZI:PLS=1:0.5	$0.6 \pm 0.2$	0.3-1.5

### 3.3.2.3 Three-component System (Spray-dried Drug:Phospholipids:Mannitol)

Image sizing analysis of SD TOB:PLS:MAN and SD AZI:PLS:MAN primary particles are summarized in Table 3.8. Similar projected mean particle size in the range from 0.6 to  $0.7\mu\text{m}$  was observed for both TOB:PLS:MAN and AZI:PLS:MAN. Moreover, the consistent particle size range from 0.2 to  $2.1\mu\text{m}$  showed the presence of microparticulate particles and indicated a relatively narrow size distribution for both TOB:PLS:MAN and AZI:PLS:MAN. Due to (partially) incomplete particle formation, particle size of TOB:PLS:MAN=1:0.5:0.75 and AZI:PLS:MAN=1:0.5:0.25 were not conducted.

**Table 3.8.** Image sizing of SD drug:phospholipids:mannitol primary particles (mean  $\pm$  SD,  $n \geq 100$ ).

Formulations (molar ratio)	Particle Size ( $\mu\text{m}$ )	Size Range ( $\mu\text{m}$ )
TOB:PLS:MAN=1:0.5:0.1	$0.7 \pm 0.3$	0.3-2.1
TOB:PLS:MAN=1:0.5:0.25	$0.6 \pm 0.3$	0.2-1.7
TOB:PLS:MAN=1:0.5:0.5	$0.7 \pm 0.3$	0.2-1.6
TOB:PLS:MAN=1:0.5:0.75	-	-
TOB:PLS:MAN=1:0.5:1	$0.7 \pm 0.2$	0.3-1.2
AZI:PLS:MAN=1:0.5:0.1	$0.7 \pm 0.2$	0.2-1.4
AZI:PLS:MAN=1:0.5:0.25	-	-
AZI:PLS:MAN=1:0.5:0.5	$0.6 \pm 0.2$	0.3-1.1
AZI:PLS:MAN=1:0.5:0.75	$0.6 \pm 0.2$	0.3-1.1
AZI:PLS:MAN=1:0.5:1	$0.6 \pm 0.2$	0.3-1.4

### 3.4 Discussion

Spray drying is a continuous high through-put particle processing operation. It transforms a liquid feed into dried particles via four stages[144]: (a) atomization of the feed solution into droplets; (b) droplets-air contact; (c) drying of the droplets; and (d) separation of the dried product from air stream. It has been suggested that spray-drying conditions (such as nozzle size, aspirator rate, airflow rate, inlet temperature, concentration of feeding solution, solvent type and etc.) would have potential influence on particle size. Our research group has previously optimized the spray-drying conditions[145] for producing nanoparticulate and microparticulate dry powder aerosol particles as pulmonary drug delivery for the deep lung delivery. Effects of pump rate and formulation composition on particle size, particle morphology, and surface morphology of spray-dried particles were examined in this chapter.

#### 3.4.1 Pump Rate Effect

The pump rate effect was studied on one-component formulations including SD pure tobramycin (TOB) and pure azithromycin (AZI). It appears that the pump rates resulted in slightly increased (medium volumetric or projected geometric mean) particle size, but generated relatively constant size distribution of nanoparticulate and microparticulate particles. In addition, relative spherical particle morphology was generated for SD TOB and SD AZI with various pump rates. However, as pump rate changed from low to high, the particle surface morphology was altered to be relatively more corrugated as shown in Figure 3.3d and 3.3h. It is suggested that larger droplets could be produced from high pump rate during atomization[75]. Consequently, given that the use of dilution concentration of feeding solution and high evaporation rate of organic solvent, the solid shells of larger particles were potentially subject to collapse on surface during drying process. Alternatively, it is reported[146, 147] that an increase in particle surface roughness could be achieved by reducing the viscosity of the feed. However, it is also observed[73, 74] that smaller particles are generated by using liquid with higher viscosity and faster feeding rate. It is speculated that this was caused by the generation of a larger back-pressure in a nozzle, producing a finer spray due to an increase in shear during atomization.

#### 3.4.2 Formulation Composition Effect

In general, at studied formulation compositions, the two-component and three-component systems were successfully produced with desired particle properties (such as nano and micro-sized particles with relatively narrow size distribution; relative spherical particle morphology and smooth surface morphology). It is reasonable to expect that the spray-dried particles exhibited similar particle size and size distribution, since a same total powder concentration in solvent was used in this study. The particles with undesired particle properties were also observed for some formulations such as AZI:PLS=1:2 (Figure 3.5d), AZI:PLS=1:1 (Figure 3.5e), TOB:PLS:MAN=1:0.5:0.75 (Figure 3.6d), and AZI:PLS:MAN=1:0.5:0.25 (Figure 3.6g). As to be discussed in detail in aerosol dispersion chapter, the partial particle aggregation of AZI:PLS=1:2 and 1:1 formulations

may correlate with outlet temperature of spray drying ( $T_o$ ) and main phase transition temperature of phospholipid bilayer ( $T_m$ ). As a consequence, AZI:PLS=1:2 and 1:1 exhibited an worse aerosol dispersion performance in terms of mass median aerodynamic diameter (MMAD) compared to AZI:PLS=1:0.5 with desired particle properties (as shown in Table 5.6 in Chapter 5). In sum, it is believed that particle surface component(s) that undergoes phase transition during both in spray drying and storage plays a critical role in facilitating particle aggregation. Liao YH et al reported[148] that the surface morphology of spray-dried stabilized lysozyme particles was independent in excipient composition. However, the volume median diameter of the powders exhibited a dependence upon the amount of excipients. The proposed possible mechanism(s) for formation of spray-dried particles leading to resultant aerosol dispersion performance will be elaborated in Chapter 5.

### 3.5 Conclusions

Nanoparticulate and microparticulate aerosol particles with desired particle properties necessary for deep lung penetration by pulmonary delivery were successfully designed and produced from dilute organic solution by spray drying. Under optimized spray-drying conditions, pump rate may possibly be used to effectively tailor (volume median or projected geometric mean) particle size of formulations. With change of formulation composition, relatively constant particle properties of spray-dried particles were obtained after spray drying. However, the detailed explanation on some (partially) incomplete particle formations by change formulation composition still remained unexplored.

Portions of Chapter 3 were reproduced with kind permission from: Li, X, Vogt, F.G., Hayes, D. Jr., and Mansour, H.M. Physicochemical Characterization and Aerosol Dispersion Performance of Organic Solution Advanced Spray Dried Microparticulate/Nanoparticulate Antibiotic Dry Powders of Tobramycin and Azithromycin for Pulmonary Inhalation Aerosol Delivery. *European Journal of Pharmaceutical Sciences*, 2014, 15:191-205. Copyright © 2014 Elsevier.

## Chapter 4 Physicochemical Characterization

### 4.1 Introduction

Spray-dried powders are examined in terms of particle size and size distribution, particle morphology, and particle surface morphology. There are, however, a number of important physicochemical properties[41] of aerosol particles that have an impact on the dispersibility in aerosolization and stability of aerosol particles intended for pulmonary delivery. They include crystallinity and polymorphism, solid-state phase transition, water content and vapor sorption, and chemical spectroscopy of component in particles.

In general, pharmaceutical solid compounds are divided into crystalline and amorphous materials. Crystalline materials present structure units that are repeated in a regular manner and form a well-defined lattice[63]. Therefore, it possesses long-range molecular order. The crystalline materials could form a variety of polymorphs[149, 150] and pseudo-polymorphs[151]. Polymorphism describes the ability of a crystalline substance to exhibit different lattice structures and/or molecular conformations. Polymorphs, exhibiting various particle shape, solubility, and water content and hygroscopicity, may have an impact on particle aggregation, through mechanical interlocking, electrostatic charge, and capillary force[41, 63]. Pseudo-polymorphs refer to crystalline hydrate and solvates, having bound water and organic solvent molecules, respectively[63]. Unlike crystalline state, amorphous phase of a material lacks long-range molecular packing, present in metastable state. Therefore, it possesses a relatively higher solubility and molecular mobility, but a less stability over pharmaceutically relevant time scales[63]. Crystallinity is the degree of crystalline phase in a solid. Crystallinity of particles has an impact on the nature of powder mixing and aggregation through energetic forces (e.g., cohesion and adhesion)[41]. In addition, it has an influence on stability of solid-state formulations. Crystallinity of dry powder for inhalation, a main indicative of physical stability affecting aerosol dispersion performance, needs to be studied. Crystallinity and polymorphism of powder are commonly examined by x-ray powder diffraction (XRPD). Atoms or molecules in a crystalline material scatter x-ray beams into many specific directions. In some of the directions, the scattered beams are completely in phase and reinforce into diffracted beams. As defined by Bragg's law[152] (Equation 4.1), diffraction of a x-ray beam is incident on crystalline planes, satisfying the Bragg's law equation:

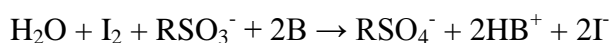
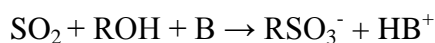
$$n\lambda = 2d \sin \theta \quad (\text{Equation 4.1})$$

Where  $n$  is any integer,  $\lambda$  is the wavelength of the beam,  $d$  is the spacing between diffracting planes, and  $\theta$  is the incident angle. In general, XRPD pattern of a crystalline sample shows a series of intensive peaks measured at different incident angles. No peak is observed for an amorphous sample in its XRPD pattern as an amorphous sample lacks long-range molecular range.

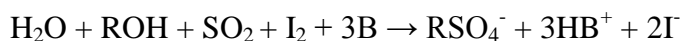
A solid particle may undergo several phase transitions when heated[63]. In general, a crystalline solid could melt upon heating from a solid to a liquid. This is a first-order

thermodynamic phase transition. Upon heating, an amorphous (non-crystalline) solid would possibly exhibit a characteristic reversible transition from the glassy state to the rubbery state with a step change in heat capacity. The temperature at which glassy state converts to rubbery state for an amorphous solid is defined as the glass transition temperature ( $T_g$ ). This is a second-order phase transition. Rubbery state of a solid may further exhibit an exothermic crystallization or/and a melting the crystallized form with heating. A glassy state (low molecular mobility) of an amorphous solid is usually preferred than rubbery state (high molecular mobility) since physical/chemical reactivity and stability are minimized[153]. To understand thermal-induced phase transition(s) of aerosol dry powder is important, especially for a non-crystalline formulation. Understanding the thermal-induced phase transitions of particles, especially for surface component leading to solid bridge, is necessary for dry powder for inhalation. Differential scanning calorimetry (DSC) is a frequently used technique to monitor phase transition of a solid associated with heat transfer. In principle, it measures the heat flow difference between a sample pan and an empty pan in order to keep them at the sample temperature.

Capillary forces take place as water moisture interacts with solid surface. Capillary forces cause formation of liquid bridge between particles by vapor condensation due to lowering of the LaPlace pressure which occurs between particles. Aerosol dispersion performance can be lowered as the result of the presence of liquid bridge between particles. In addition, water molecules act as a plasticizer in amorphous solids by lowering  $T_g$ . Low  $T_g$  of dry powder could trigger the potential physical and chemical instabilities. The equilibrium moisture content at ambient temperature and relative humidity is suggested to be a good indicator of the suitability of aerosol product[41]. Therefore, water content of powder needs to be assessed for dry powder formulations. Coulometric titration is commonly employed to determine water content of powder. Determination of water content based on a quantitative reaction of water ( $H_2O$ ) with iodine ( $I_2$ ), sulfur dioxide ( $SO_2$ ), alcohol (ROH; e.g. methanol), and an organic base (B; e.g. imidazole) as shown in Equation 4.2[154]:



(Equation 4.2)



Water content of sample is determined by measuring the quantity of electric current required for production of  $I_2$  by electrolysis of iodine ions in reagent.

Hygroscopicity is an intrinsic nature of a material with tendency to take up moisture from surrounding environment. Hygroscopic material suffers a great risk of physical and chemical instability. Hygroscopic aerosols are susceptible to hygroscopic growth resulting in larger particles in aerosolization[41]. In addition, moisture uptaking and

losing over a narrow range of relative humidity (RH) could result in local dissolution and recrystallization. This leads to an irreversible aggregation through formation of solid bridge, which adversely affects aerosol dispersion and lung deposition.[41, 155-157] Thus, it is essential to examine water vapor sorption of aerosol particles. Gravimetric water vapor sorption (GVS) is used to study equilibrium water content of aerosol particles at a series of RH %. The weight change of particle due to moisture uptake and loss is monitored by an integrated microbalance in GVS as exposed to increment of RH %. Regarding to metastable materials (e.g. amorphous), the lyotropic-induced phase transition would possibly be detected[43, 145, 158]. As similar to thermal-induced phase transition, the lyotropic-induced phase transition would also have an adverse effect on aerosol performance.

Component homogeneity in powder necessarily needs to be characterized for multi-component aerosol particles. An indication of heterogeneity of powder has an impact on physical stability of molecularly mixed particles. Confocal Raman microscopy (CRM) has demonstrated an utility in the non-invasive and non-destructive microspectroscopic analysis of aerosol formulations as described in detail in the studies[159, 160]. Confocal Raman microscopy (CRM) and spectroscopy provides chemical imaging and mapping of particles[160]. These functions can reveal component homogeneity for molecularly mixed particles. Raman spectroscopy is a spectroscopic technique used to observe vibrational, rotational, and other low-frequency modes in a system. A laser light (in visible, near infrared, or near ultraviolet range) interacts with molecular vibrations, photons, or other excitations in system. It results in the energy of the laser photons shifts up or down. The shift in energy usually reveals information on the vibrational modes in a system. Infrared spectroscopy yields similar, but complementary, information to Raman spectroscopy. Both Raman and infrared spectroscopies are capable of probing molecular conformation, degree of molecular order, and polymorphic system.

In the following sections, the physicochemical properties of crystallinity and polymorphism, solid-state phase transition (thermal analysis), water content and vapor sorption, and chemical spectroscopy of component of spray-dried aerosol particles are described.

## **4.2 Materials and Methods**

### **4.2.1 Materials**

The spray-dried (SD) particles selected for physicochemical characterization are listed in Table 4.1. TOB, AZI, MAN, and PLS stand for tobramycin, azithromycin, mannitol, and phospholipids, respectively. All the studied particles were generated employing a 50% pump rate in spray drying. All SD powders were carefully stored in sealed glass vials that were stored in sealed glass desiccators over Indicating Drierite/Drierite<sup>TM</sup> desiccant at -20°C under ambient pressure for up to one week. The outlet temperatures of SD particles are referred to Table 3.1 and Table 3.2 in Chapter 3.

**Table 4.1.** SD particles for physicochemical characterization.

Formulation System	SD TOB formulations (molar ratio)	SD AZI formulations (molar ratio)
One-component	Pure TOB	Pure AZI
Two-component	TOB:MAN=1:0.1	AZI:MAN=1:0.1
	TOB:MAN=1:0.25	AZI:MAN=1:0.25
	TOB:MAN=1:0.5	AZI:MAN=1:0.5
	TOB:MAN=1:1	AZI:MAN=1:1
	TOB:PLS=1:0.5	AZI:PLS=1:0.5
	TOB:PLS=1:1	AZI:PLS=1:1
	TOB:PLS=1:2	AZI:PLS=1:2
Three-component	TOB:PLS:MAN=1:0.5:0.1	AZI:PLS:MAN=1:0.5:0.1
	TOB:PLS:MAN=1:0.5:0.5	AZI:PLS:MAN=1:0.5:0.5
	TOB:PLS:MAN=1:0.5:1	AZI:PLS:MAN=1:0.5:1

## 4.2.2 Methods

### 4.2.2.1 Crystallinity and Polymorphism

X-ray powder diffraction (XRPD) patterns of samples were collected with a Rigaku x-ray diffractometer (Japan) with Cu K $\alpha$  radiation (40kV, 44mA, and  $\lambda = 1.5406\text{\AA}$ ) between  $5.0 - 60.0^\circ$  ( $2\theta$ ) using a scan rate of  $2.00^\circ/\text{min}$  at ambient temperature as reported[161-164]. Samples were placed on a quartz plate in an aluminum sample holder without further grinding. Only one experiment was done for each formulation in this study.

### 4.2.2.2 Solid-State Phase Transition

Thermal properties of samples were measured using a TA Q200 differential scanning calorimetry (DSC; TA Instruments, New Castle, DE, USA) equipped with T-Zero<sup>®</sup> technology and an automated computer-controlled RSC-90 cooling accessory as reported[161-164]. Approximate 3mg of samples was packed into hermetic anodized aluminum T-Zero<sup>®</sup> DSC pan. It was then hermetically sealed with the Tzero hermetic sealer (TA Instruments, New Castle, DE, USA) unless otherwise specified. An empty hermetically sealed aluminum pan was used as a reference pan. Experiments were conducted under both hermetic and non-hermetic conditions. In hermetic conditions, hermetically sealed sample pan and reference pan were used. Whereas in non-hermetic conditions, both pin-holed sample pan and reference pan were used. The non-hermetic DSC conditions will be specially mentioned in this chapter if necessary. The use of non-hermetic conditions allowed the release of moisture from samples, minimizing moisture effect on thermal events. Ultra-high purity (UHP) nitrogen was used as a purging gas at a rate of 50 ml/min. Sample was heated from  $10-200^\circ\text{C}$  at a scanning rate of  $5.00^\circ\text{C}/\text{min}$ . The onset temperature of main phase transition ( $T_m$ ) was reported for



phospholipid-containing powders. Detailed report methods are referred to Section 4.3.2. All experiments were done in triplicate (n=3).

#### **4.2.2.3 Water Content**

Water content of powders was assessed by Karl Fischer (KF) coulometric titration. The measurements were performed with a 737 KF Coulometer coupled with 703 Ti Stand (Metrohm Ltd., Antwerp, Belgium) as reported[161-164]. Approximately 6 to 7mg of sample was dissolved in AQUA STAR methanol using a 5mL volumetric. The solution was injected into reaction cell filled with HYDRANAL KF reagent. After obtaining the reading from KF coulometer, the water content of sample was obtained from simple calculation. The experiments were done in triplicate (n=3).

#### **4.2.2.4 Water Vapor Sorption**

Water vapor sorption isotherms of powders were measured gravimetrically using an automated microelectronic balance coupled to a computerized VTI SGA-CX symmetric vapor sorption analyzer (Hialeah, Florida) as previously reported[161, 162, 164, 165]. All measurements were taken at 25°C using a sample size of  $\sim 1.0$  to 1.5mg. Samples were subjected to pre-drying treatment at 25°C under 0% relative humidity (RH) (nitrogen gas purging) for up to a maximum of 7h with equilibrium criterion of weight change less than or equal to 0.0001% in 10min interval. At the end of the pre-drying cycle, the samples were exposed to a sequence of increasing RH with increment of 5% RH on each step, which started at 5% RH until 95% RH. The criterion used to establish equilibrium during sorption was a weight change of less than or equal to 0.03% in 10min interval for up to 3h. The data point was acquired at every 2min or 0.01% weight change. Standby temperature was set at 25°C.

#### **4.2.2.5 Chemical Spectroscopy**

##### **4.2.2.5.1 Confocal Raman Microscopy and Spectroscopy for Chemical Imaging and Mapping**

Using conditions previously reported[160, 166], dispersive Raman spectra and mapping images of samples were obtained using an Aramis confocal Raman spectrometer and fluorescence microscope system (Horiba Jobin Yvon, Edison, NJ, USA). The system was equipped with an Olympus BX41 confocal optical microscope, an Olympus U-LH 100W Hg lamp, and a U-RFL-T power source used for fluorescence excitation and brightfield illumination (Olympus America, Inc., Chester Valley, PA). Filters were used to achieve fluorescence excitation in the range of 330-385nm, with emission observed using a 425nm cutoff filter. Neutral density filters were used to adjust fluorescence intensity. Raman spectra were obtained using both a 785nm diode laser and a 633nm HeNe laser. Raman spectral maps were obtained using either a 10x or 50x objective with the stage moved in increments of 5 to 10 $\mu$ m. Each map point was acquired using 32 to 128 accumulations each with 2s of detector exposure time. A confocal hole of 500 $\mu$ m with a

grating of 600-900 grooves/mm and a slit width of 100 $\mu$ m were used. Spectra were subjected to baseline correction and smoothing prior to further analysis.

#### 4.2.2.5.2 Attenuated Total Reflectance-Fourier Transform Infrared Spectroscopy

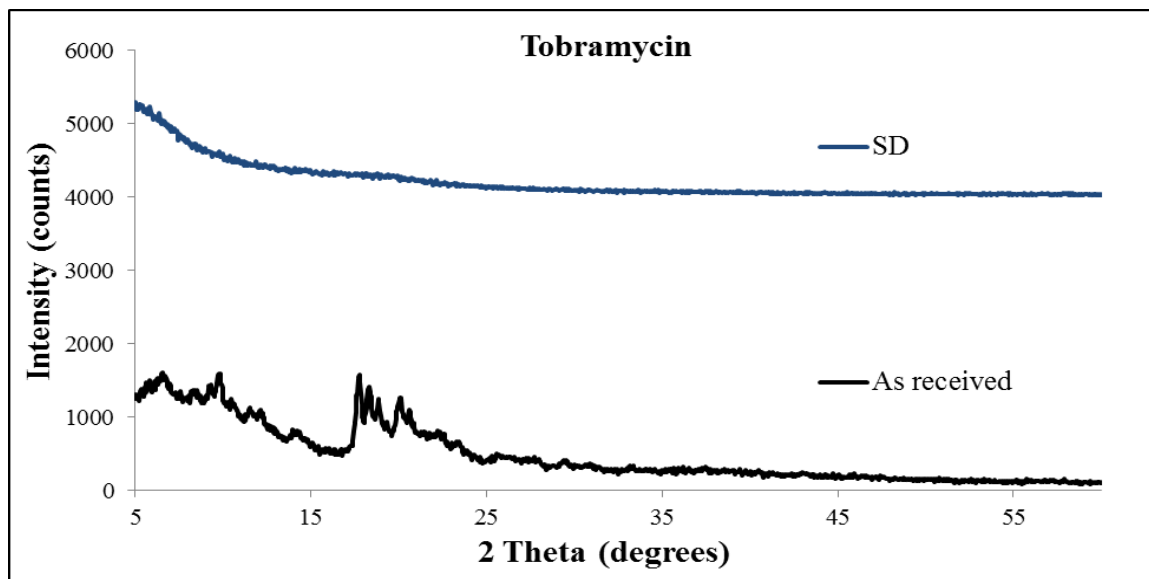
A Varian FTS-7000e attenuated total reflectance-Fourier transform infrared spectrometer (ATR-FTIR; Varian Inc., CA) equipped with a DTGS detector and a PIKE MIRacle ATR ZnSe accessory was used. Each spectrum was collected for 32 scans at a spectral resolution of 8 $\text{cm}^{-1}$  over the wavelength number range of 4,000-700 $\text{cm}^{-1}$ . A background spectrum was done under the same experimental conditions. Spectral data were acquired with Varian Resolutions Pro software.

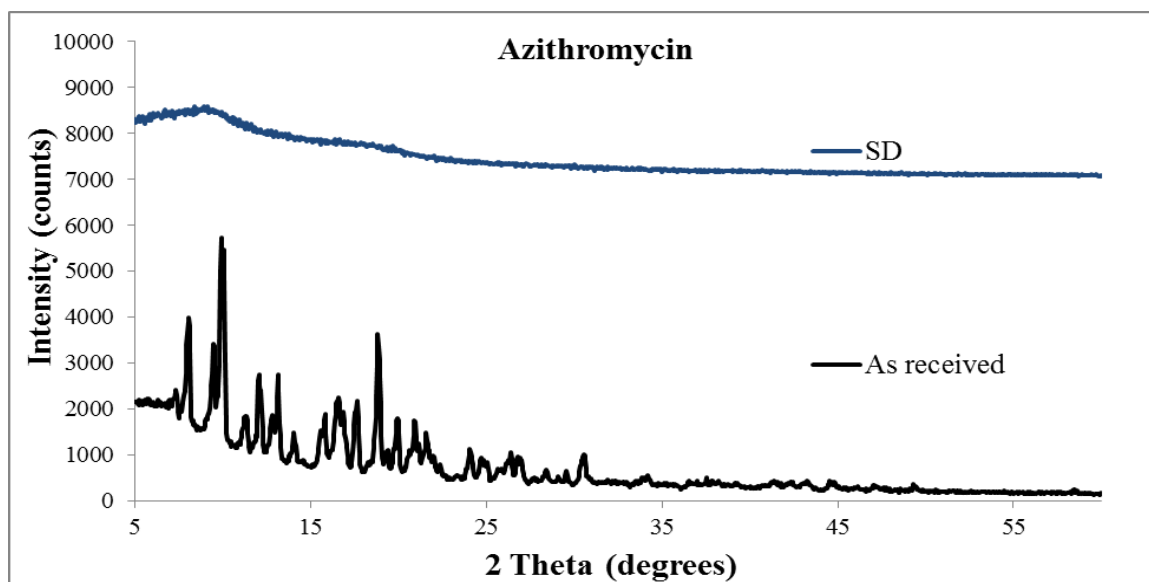
### 4.3 Results

#### 4.3.1 Crystallinity and Polymorphism

##### 4.3.1.1 One-component System (Spray-dried Pure Drug)

X-ray powder diffraction (XRPD) pattern in Figure 4.1a indicates as received tobramycin (TOB) was partially crystalline as the peaks were broad and not well-defined.[43] As shown in Figure 4.1b, as received azithromycin (AZI) appeared to be in crystalline phase with intensive peaks[43]. Both SD pure TOB (Figure 4.1a) and SD pure AZI (Figure 4.1b) particles lacked their characteristic crystalline peaks[43]. The data indicated SD pure TOB and SD pure AZI lost long-range molecular order compared to the corresponding as received material.





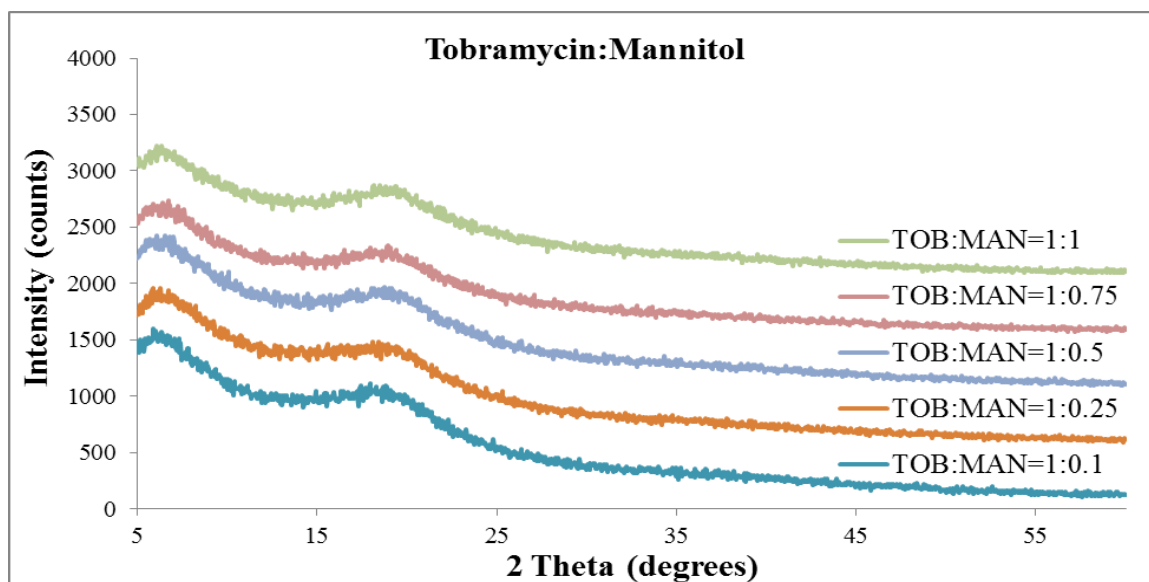
(b)

**Figure 4.1.** X-ray powder diffractograms for: (a) SD pure and as received tobramycin particles (offset by 4000 counts); and (b) SD pure and as received azithromycin particles (offset by 7000 counts)[43].

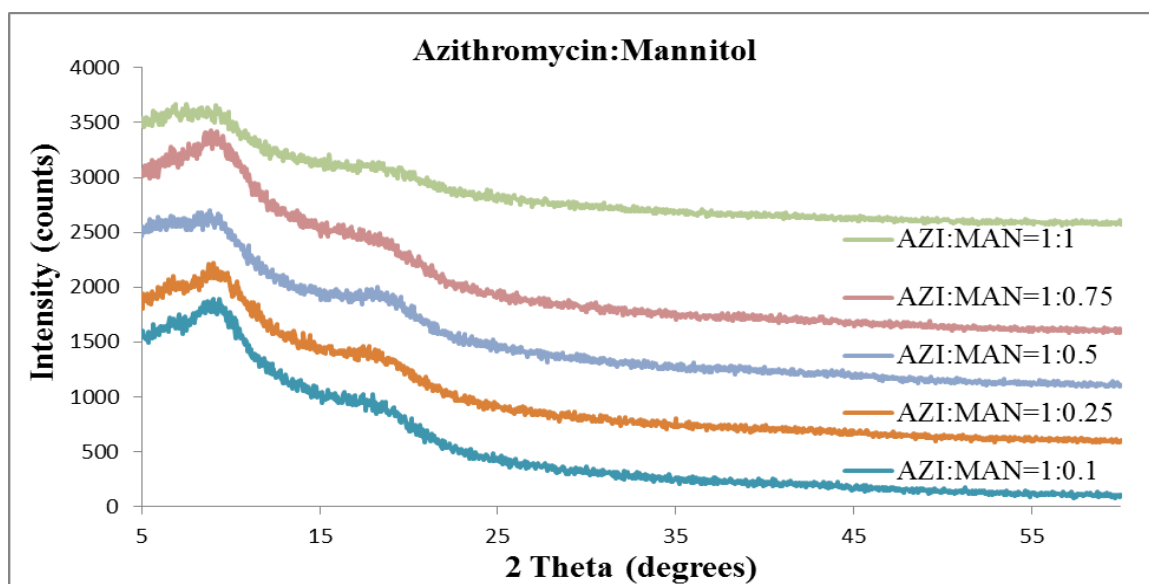
#### 4.3.1.2 Two-component System

##### 4.3.1.2.1 Spray-dried Drug:Mannitol

The XRPD patterns suggest that SD tobramycin:mannitol (TOB:MAN) (Figure 4.2a) and azithromycin:mannitol (AZI:MAN) (Figure 4.2b) were lacking of long-range molecular order as the characteristic peaks of crystalline phase were not observed[143]. Apparently, at the studied molar ratios, MAN component exhibited no effect on XRPD patterns for both TOB:MAN and AZI:MAN.



(a)



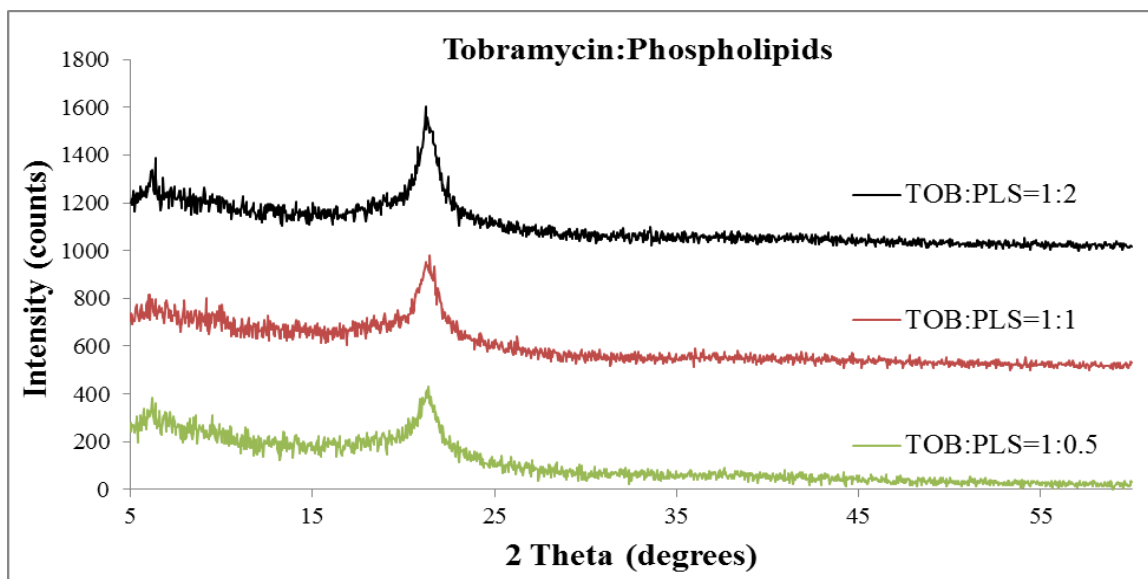
(b)

**Figure 4.2.** X-ray powder diffraction patterns for: (a) SD tobramycin:mannitol formulations (offset by 500 counts between patterns); and (b) SD azithromycin:mannitol formulations (offset by 500 counts between patterns for the bottom four; offset by 1000 counts between patterns for the top two)[143].

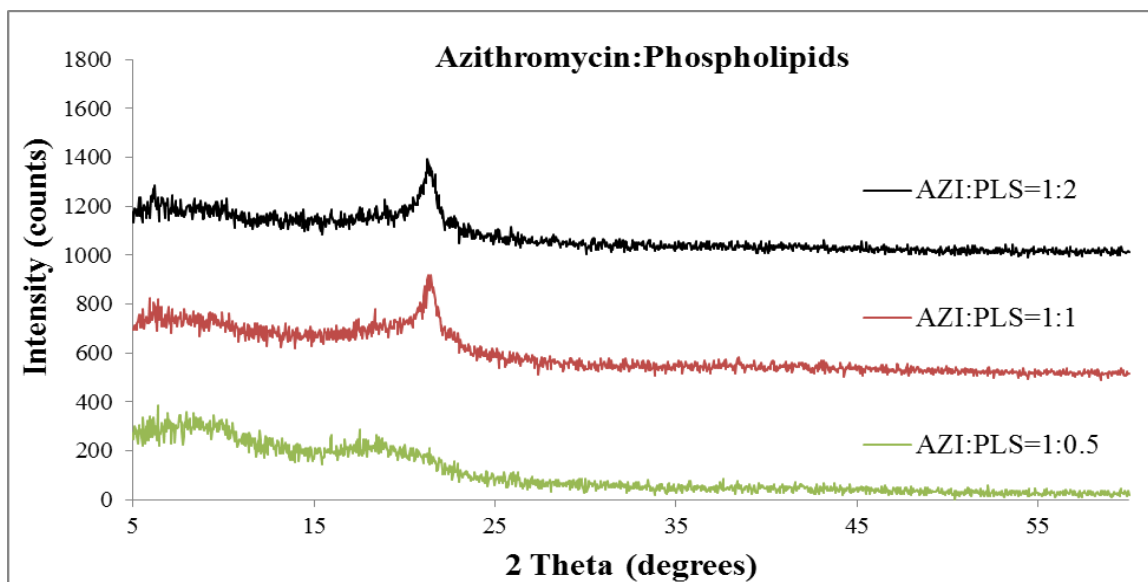
#### 4.3.1.2.2 Spray-dried Drug:Phospholipids

As shown on XRPD patterns of SD tobramycin:phospholipids (TOB:PLS) in Figure 4.3a, intensive characteristic peak of phospholipid bilayer structure at  $\sim 20\text{--}23^\circ$  of 2 theta was observed with various molar ratios of PLS. In addition, the characteristic peak of

phospholipid bilayer structure of SD azithromycin:phospholipids (AZI:PLS) on XRPD patterns was observed in Figure 4.3b. In comparison, the peak intensity of phospholipid bilayer structure from AZI:PLS was lower than TOB:PLS at same molar ratio of PLS. The crystalline peaks of TOB and AZI were not observed in any TOB:PLS and AZI:PLS samples.



(a)

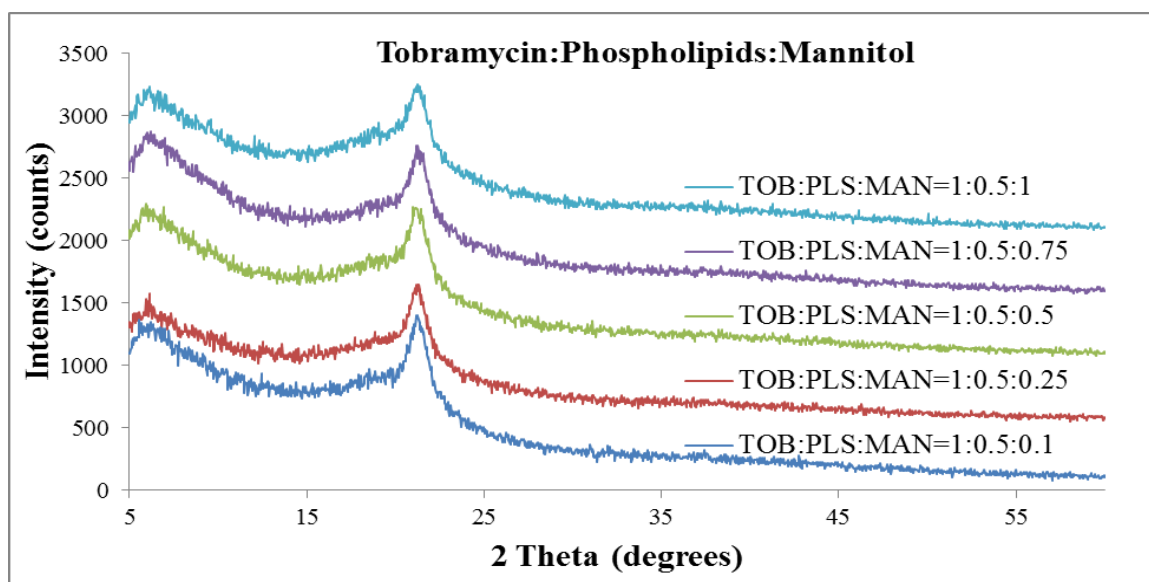


(b)

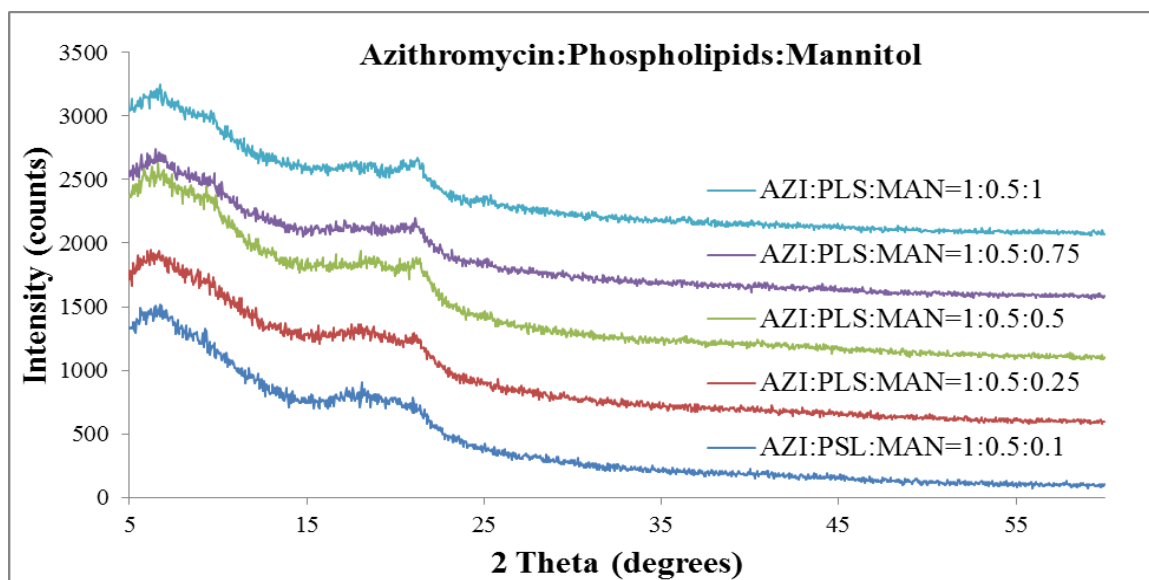
**Figure 4.3.** X-ray powder diffraction patterns for: (a) SD tobramycin:phospholipids formulations (offset by 500 counts between patterns); and (b) SD azithromycin:phospholipids formulations (offset by 500 counts between patterns).

#### 4.3.1.3 Three-component System (Spray-dried Drug:Phospholipids:Mannitol)

With the incorporation of MAN, SD tobramycin:phospholipids:mannitol (TOB:PLS:MAN) in Figure 4.4a and SD azithromycin:phospholipids:mannitol (AZI:PLS:MAN) in Figure 4.4b exhibited a similar characteristic of XRPD patterns to the corresponding TOB:PLS=1:0.5 and AZI:PLS=1:0.5. Phospholipid bilayer structure was retained for both TOB:PLS:MAN and AZI:PLS:MAN. The characteristic crystalline peaks from other components (e.g., TOB/AZI and MAN (Appendix A)) were not observed.



(a)



(b)

**Figure 4.4.** X-ray powder diffraction patterns for: (a) SD tobramycin:phospholipids:mannitol formulations (offset by 500 counts between patterns); and (b) SD azithromycin:phospholipids:mannitol formulations (offset by 500 counts between patterns).

#### 4.3.2 Solid-State Phase Transition

In order to present clear differential scanning calorimetry (DSC) data, a scheme for a typical glass transition of a drug and a main phase transition of phospholipid bilayer in spray-dried (SD) particles is shown in Figure 4.5. The two phase transitions result in an increased molecular mobility of the corresponding component. Glass transition is a second-order phase transition with a step change in heat capacity that an amorphous phase of drug component undergoes from the glassy state to rubbery state. The glass transition temperature ( $T_g$ ) is the mid-point temperature at which glass transition takes place. The main phase transition of phospholipid bilayer is the first-order thermodynamic process that phospholipid bilayer changes from the gel phase (low degree of molecular mobility) to liquid crystalline phase (high degree of molecular mobility). The  $\Delta H_m$  and  $T_m$  are defined as the adjusted enthalpy change and the onset temperature of main phase transition of phospholipid bilayer. The  $\Delta H_m$  data in this dissertation is adjusted to the weight of phospholipids in a particular phospholipid containing formulation. Due to some baseline shift on thermograms and for purpose of consistent reporting, the peak temperatures are used to define the temperatures for other phase transitions.

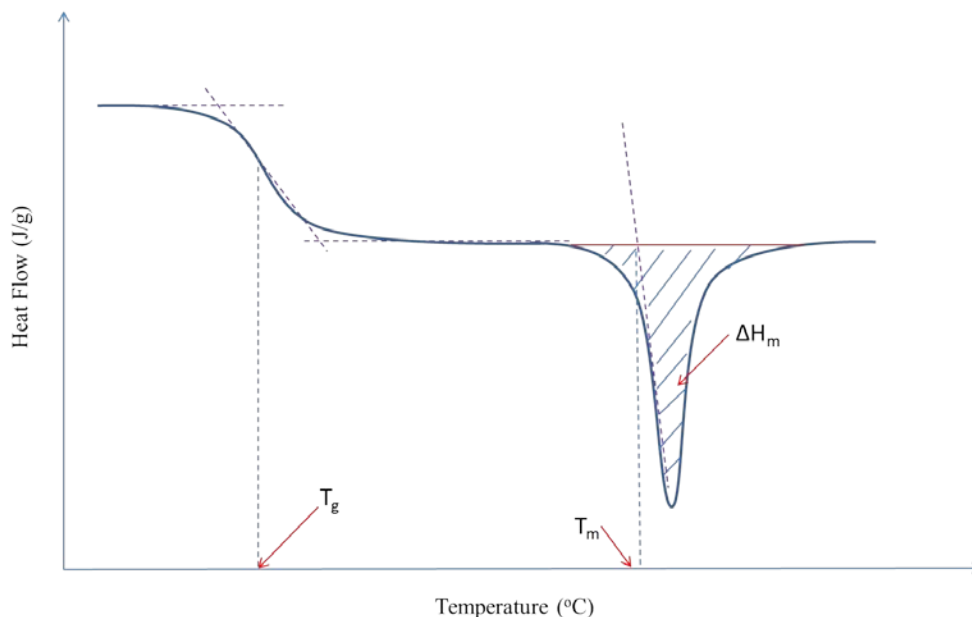


**Figure 4.5.** Schematic of a typical glass transition of drug and a main phase transition of phospholipid bilayer in the spray-dried powder.

#### 4.3.2.1 One-component System (Spray-dried Pure Drug)

Differential scanning calorimetry (DSC) thermograms of TOB and AZI one-component powders[43] are shown in Figure 4.6. As received TOB (Figure 4.6a) exhibited three major endotherms at temperatures of  $\sim 146^{\circ}\text{C}$ ,  $156^{\circ}\text{C}$  and  $200^{\circ}\text{C}$ , respectively. As expected, there was no glass transition observed for as received TOB. As shown Figure 4.6b, SD pure TOB showed a glass transition at  $\sim 50^{\circ}\text{C}$  and a major endotherm peak at  $\sim 158^{\circ}\text{C}$ .

Only a single endothermic peak was observed at  $\sim 137^{\circ}\text{C}$  for as received AZI (Figure 4.6c). Thermogram of SD pure AZI is shown in Figure 4.6d. An evident glass transition was present at  $\sim 94^{\circ}\text{C}$  for SD pure AZI. The glass transition was followed by an endotherm at temperature range between  $160^{\circ}\text{C}$  and  $170^{\circ}\text{C}$  for SD pure AZI.



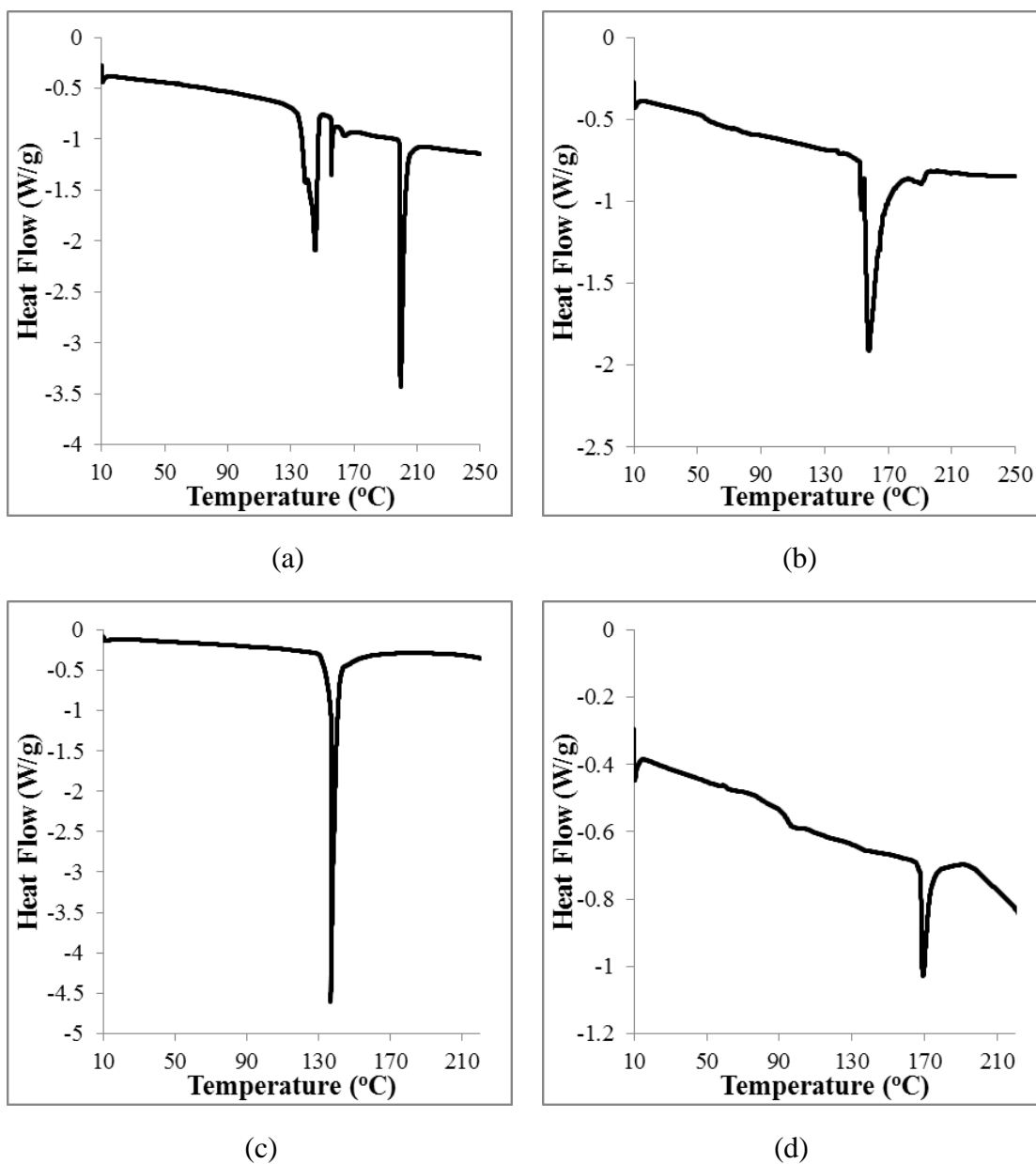


**Figure 4.6.** DSC thermograms for: (a) as received tobramycin; (b) SD pure tobramycin; (c) as received azithromycin; (d) SD pure azithromycin.[43]

#### 4.3.2.2 Two-component System

##### 4.3.2.2.1 Spray-dried Drug:Mannitol

SD TOB:MAN (Figure 4.7) exhibited three phase transitions[143]. A glass transition was observed at temperature range between  $\sim 42^{\circ}\text{C}$  and  $69^{\circ}\text{C}$ . It was followed by a small

endotherm at temperature around from 95°C to 96°C. The last phase transition with base line shift took place at ~ 169°C to 180°C. The detailed glass transition temperatures ( $T_g$ ) of SD TOB:MAN were presented in Table 4.2[143].

SD AZI:MAN (Figure 4.8) showed two different thermograms as molar ratio of MAN increased from 1:0.1 to 1:1[143]. SD AZI:MAN with molar ratios of 1:0.1, 1:0.25, and 1:0.75 presented similar characteristic thermograms. SD AZI:MAN=1:0.5 and 1:1 exhibited similar thermal events with more complication than the formulations with other molar ratios. Glass transitions were observed for all SD AZI:MAN. DSC thermograms from non-hermetic conditions (Figure 4.9) revealed a similarity for AZI:MAN=1:0.1 and 1:0.75, and AZI:MAN=1:0.5 and 1:1, respectively. Interestingly, AZI:MAN=1:0.25 (Figure 4.9b) exhibited a characteristic thermogram under non-hermetic conditions. The detailed glass transition temperatures ( $T_g$ ) of SD AZI:MAN from hermetic DSC studies were presented in Table 4.2[143].

**Table 4.2.** Glass transition temperatures for SD tobramycin:mannitol and SD azithromycin:mannitol[143] (mean  $\pm$  SD, n=3).

Molar Ratio	Glass Transition Temperature (°C)	
	TOB:MAN	AZI:MAN
1:0.1	69.2 $\pm$ 0.2	92.9 $\pm$ 0.5
1:0.25	66.5 $\pm$ 0.2	93.7 $\pm$ 0.5
1:0.5	59.4 $\pm$ 0.9	94.9 $\pm$ 0.0
1:0.75	55.2 $\pm$ 0.9	94.0 $\pm$ 0.2
1:1	41.7 $\pm$ 0.4	93.8 $\pm$ 0.6

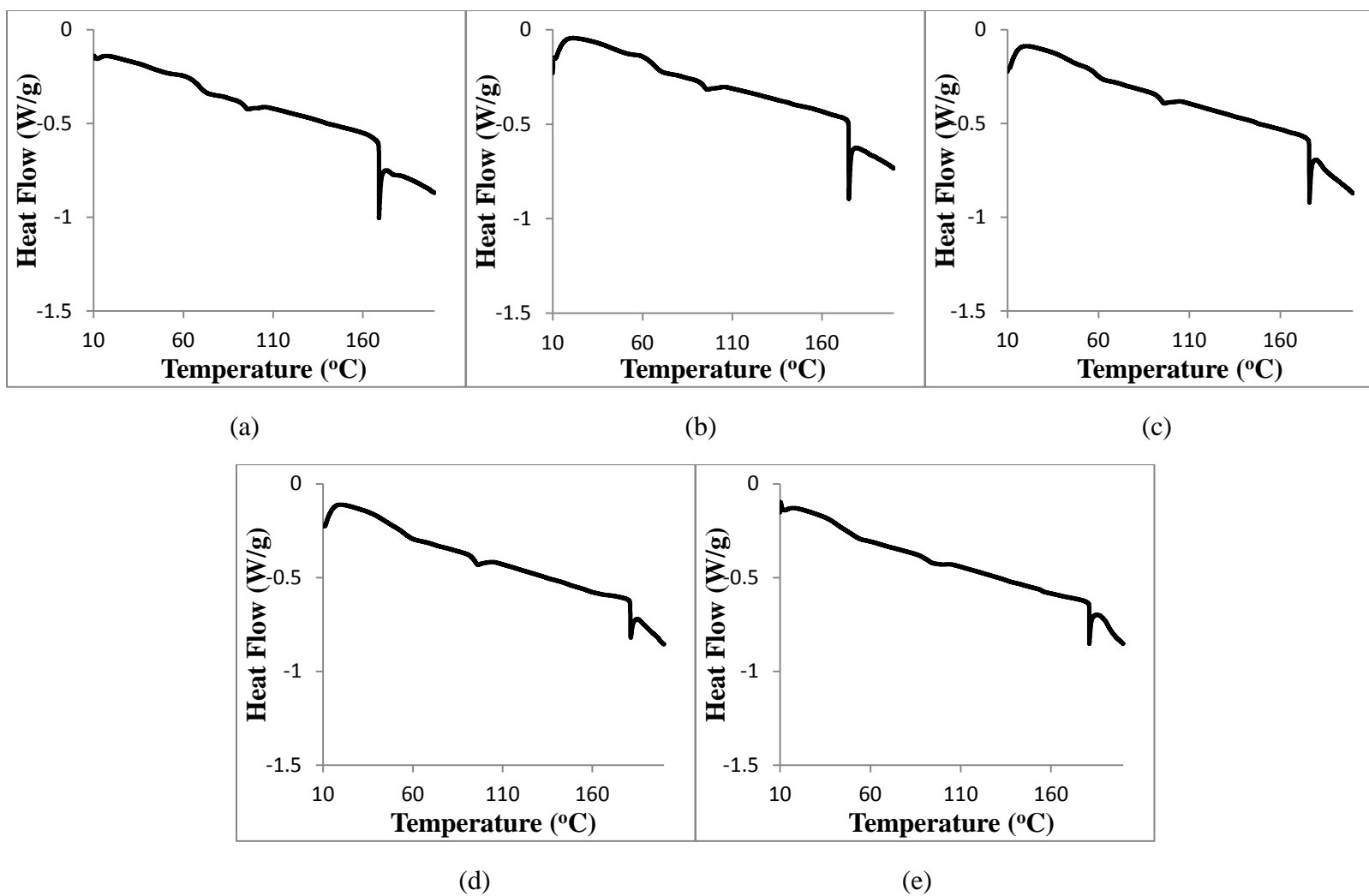


**Figure 4.7.** DSC thermograms for: (a) tobramycin:mannitol=1:0.1; (b) tobramycin:mannitol=1:0.25; (c) tobramycin:mannitol=1:0.5; (d) tobramycin:mannitol=1:0.75; and (e) tobramycin:mannitol=1:1[143].

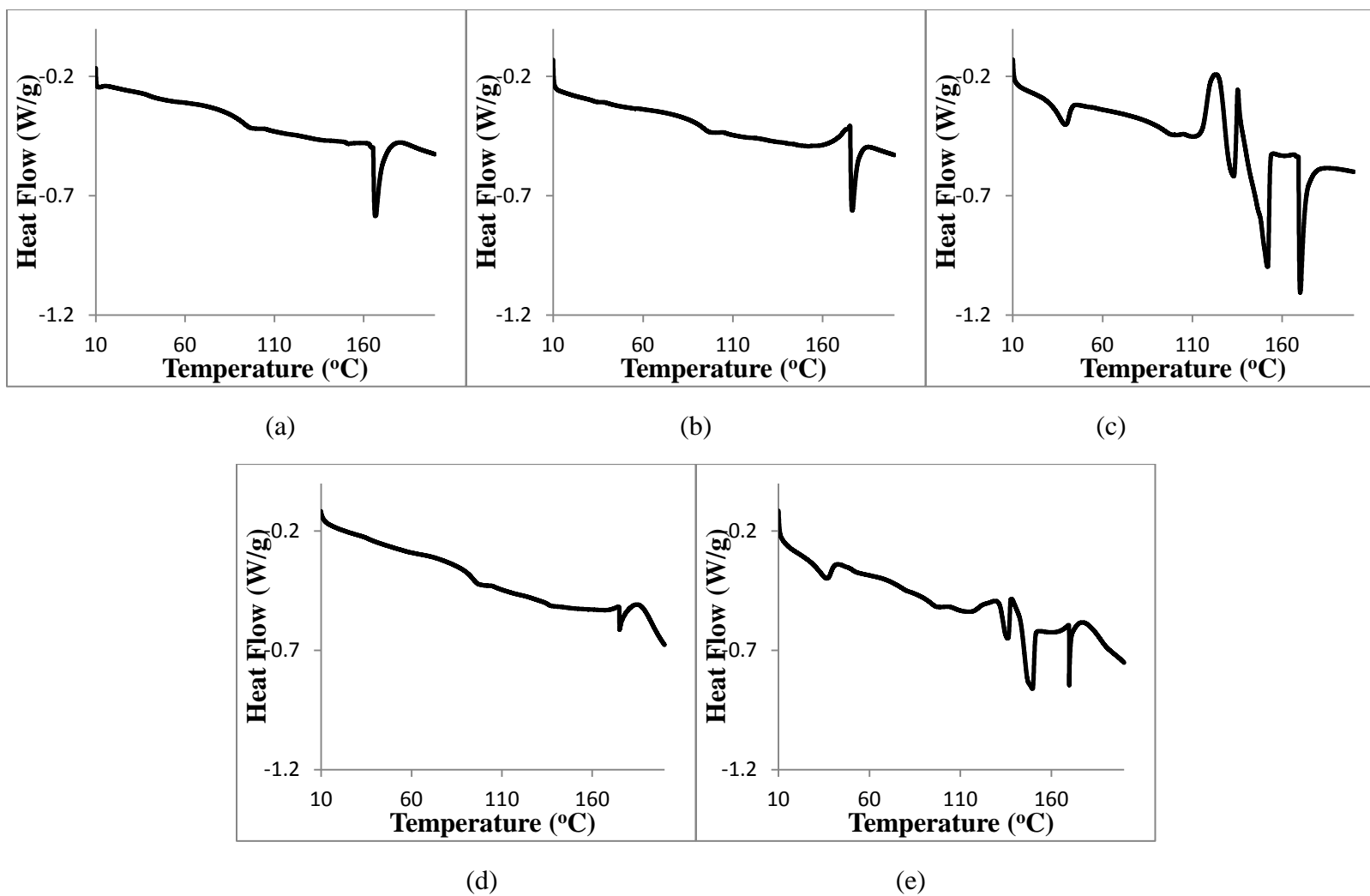


**Figure 4.8.** DSC thermograms for: (a) azithromycin:mannitol=1:0.1; (b) azithromycin:mannitol=1:0.25; (c) azithromycin:mannitol=1:0.5; (d) azithromycin:mannitol=1:0.75; and (e) azithromycin:mannitol=1:1[143].

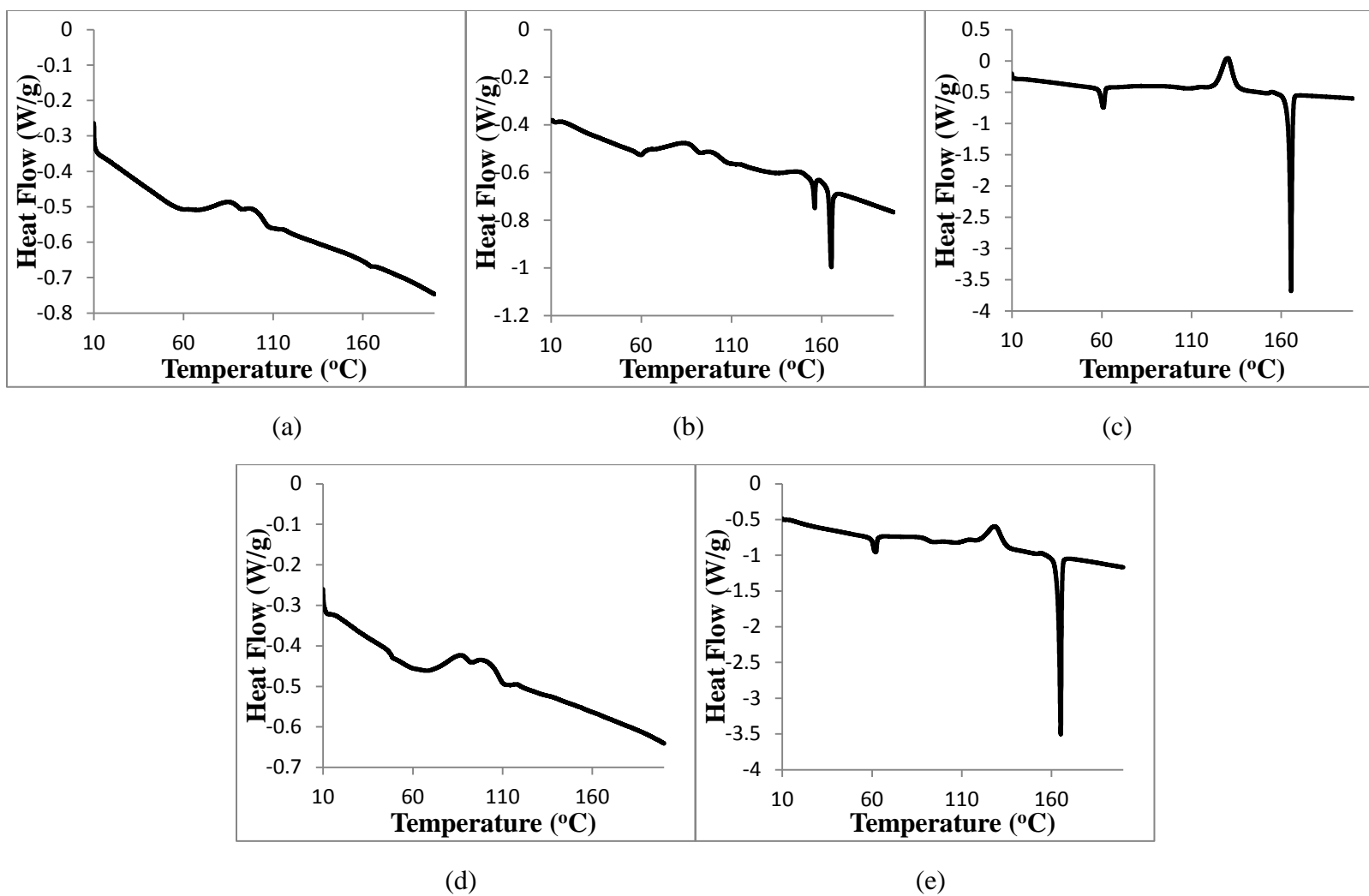


**Figure 4.9.** DSC thermograms (non-hermetic) for: (a) azithromycin:mannitol=1:0.1; (b) azithromycin:mannitol=1:0.25; (c) azithromycin:mannitol=1:0.5; (d) azithromycin:mannitol=1:0.75; and (e) azithromycin:mannitol=1:1[143].

#### 4.3.2.2.2 Spray-dried Drug:Phospholipids

DSC thermograms of TOB:PLS (Figure 4.10a-c) exhibited four phase transitions, including a glass transition of TOB[43], a main phase transition of phospholipid bilayer[167], a exothermic crystallization transition, and an endothermic melting. As shown in DSC thermograms (Figure 4.10d-e), AZI:PLS mainly showed three phase transitions. It included a main phase transition of phospholipid bilayer, a glass transition of AZI[43], and one endothermic melting peak. The detailed DSC data of the formulations are summarized in Table 4.3.

**Table 4.3.** Summary of glass transition temperature ( $T_g$ ), main phase transition temperature of phospholipid bilayer ( $T_m$ ), adjusted enthalpy of main phase transition of phospholipid bilayer ( $\Delta H_m$ ), crystallization temperature ( $T_c$ ), and melting temperature ( $T_{m1}$ ) for SD tobramycin:phospholipids (TOB:PLS) and SD azithromycin:phospholipids (AZI:PLS) formulations in DSC (mean  $\pm$  SD, n=3).

Formulations (molar ratio)		$T_g$ (°C)	$T_m$ (°C)	$\Delta H_m$ (J/g)	$T_c$ (°C)	$T_{m1}$ (°C)
TOB:PLS	1:2	32.6 $\pm$ 0.9	61.9 $\pm$ 0.4	36.6 $\pm$ 2.8	143.1 $\pm$ 0.8	149.4 $\pm$ 2.2
	1:1	37.7 $\pm$ 1.1	62.6 $\pm$ 1.0	34.7 $\pm$ 1.8	141.0 $\pm$ 1.0	147.4 $\pm$ 1.5
	1:0.5	41.9 $\pm$ 2.4	66.4 $\pm$ 0.1	27.9 $\pm$ 0.9	152.2 $\pm$ 1.1	156.2 $\pm$ 1.9
AZI:PLS	1:2	77.9 $\pm$ 0.9	61.2 $\pm$ 0.2	29.1 $\pm$ 0.2	-	159.2 $\pm$ 5.3
	1:1	79.9 $\pm$ 0.2	61.5 $\pm$ 0.1	22.9 $\pm$ 0.3	-	158.8 $\pm$ 7.8
	1:0.5	76.6 $\pm$ 0.6	60.4 $\pm$ 0.1	7.6 $\pm$ 0.1	-	163.3 $\pm$ 2.8

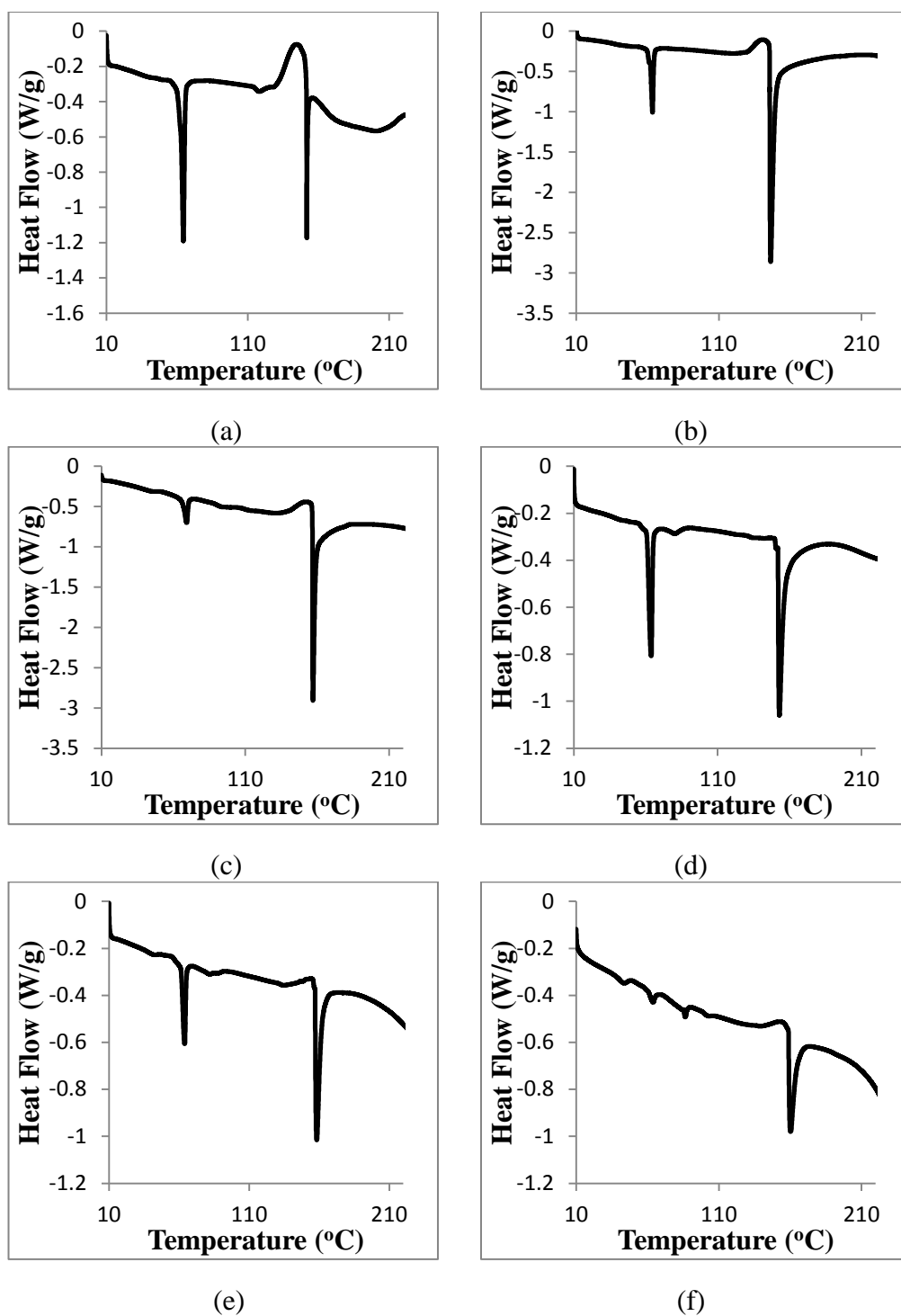


**Figure 4.10.** DSC thermograms of SD drug:phospholipids formulations for: (a) tobramycin:phospholipids=1:2; (b) tobramycin:phospholipids=1:1; (c) tobramycin:phospholipids=1:0.5; (d) azithromycin:phospholipids=1:2; (e) azithromycin:phospholipids=1:1; and (f) azithromycin:phospholipids=1:0.5.

#### 4.3.2.3 Three-component System (Spray-dried Drug:Phospholipids:Mannitol)

DSC thermograms of TOB:PLS:MAN and AZI:PLS:MAN are shown in Figure 4.11 and Figure 4.12, respectively. In Figure 4.11a-c, a glass transition of TOB, a main phase transition of phospholipid bilayer, and one endothermic melting peak were observed for TOB:PLS:MAN=1:0.5:0.1, 1:0.5:0.25, and 1:0.5:0.5. Additionally, a possible phase transition from lamellar to hexagonal of PLS (after main phase transition of phospholipid bilayer)[167] and an exothermic crystallization peak (before endothermic melting peak) were observed for TOB:PLS:MAN=1:0.5:0.75 (Figure 4.11d) and 1:0.5:1 (Figure 4.11e).

Similarly, AZI:PLS:MAN exhibited a main phase transition of phospholipid bilayer, a glass transition of AZI and one or two endothermic melting peak(s) depending on amount of MAN in the formulations. As shown in Figure 4.12a-c, one endothermic peak was observed for AZI:PLS:MAN with molar ratios from 1:0.5:0.1 to 1:0.5:0.5. However, additional endothermic peak was present for AZI:PLS:MAN=1:0.5:0.75 (Figure 4.12d) and 1:0.5:1 (Figure 4.12e). Table 4.4 summarizes the detailed DSC data for TOB:PLS:MAN and AZI:PLS:MAN.



**Table 4.4.** Summary of glass transition temperature ( $T_g$ ), main phase transition temperature of phospholipid bilayer ( $T_m$ ), adjusted enthalpy of main phase transition of phospholipid bilayer ( $\Delta H_m$ ), crystallization temperature ( $T_c$ ), and melting temperature ( $T_{m1}$  and  $T_{m2}$ ) for tobramycin:phospholipids:mannitol and azithromycin:phospholipids:mannitol in DSC (mean  $\pm$  SD, n=3).

Formulations		$T_g$ ( $^{\circ}\text{C}$ )	$T_m$ ( $^{\circ}\text{C}$ )	$\Delta H_m$ (J/g)	$T_c$ ( $^{\circ}\text{C}$ )	$T_{m1}$ ( $^{\circ}\text{C}$ )
TOB:PLS:MAN	1:0.5:0.1	$37.2 \pm 1.2$	$63.8 \pm 0.1$	$30.6 \pm 0.2$	-	$156.9 \pm 3.9$
	1:0.5:0.25	$43.1 \pm 0.1$	$61.2 \pm 0.2$	$28.7 \pm 0.9$	-	$163.7 \pm 3.3$
	1:0.5:0.5	$37.0 \pm 1.5$	$59.9 \pm 0.0$	$39.8 \pm 0.8$	-	$160.4 \pm 3.5$
	1:0.5:0.75	$44.1 \pm 0.2$	$57.6 \pm 0.1$	$38.9 \pm 1.8$	$156.1 \pm 0.6$	$160.8 \pm 1.3$
	1:0.5:1	$43.6 \pm 0.1$	$55.8 \pm 0.1$	$42.1 \pm 1.0$	$158.7 \pm 0.3$	$169.4 \pm 1.2$
Formulations		$T_g$ ( $^{\circ}\text{C}$ )	$T_m$ ( $^{\circ}\text{C}$ )	$H_m$ (J/g)	$T_{m1}$ ( $^{\circ}\text{C}$ )	$T_{m2}$ ( $^{\circ}\text{C}$ )
AZI:PLS:MAN	1:0.5:0.1	$80.4 \pm 0.4$	$55.7 \pm 0.1$	$7.7 \pm 0.4$	-	$161.7 \pm 2.3$
	1:0.5:0.25	$84.2 \pm 0.6$	$50.5 \pm 0.1$	$4.8 \pm 0.1$	-	$158.7 \pm 2.7$
	1:0.5:0.5	$84.6 \pm 0.8$	$44.2 \pm 0.1$	$7.1 \pm 0.6$	-	$162.3 \pm 5.4$
	1:0.5:0.75	$83.5 \pm 1.3$	$44.0 \pm 0.2$	$11.7 \pm 1.7$	$142.4 \pm 1.0$	$157.3 \pm 3.0$
	1:0.5:1	$76.7 \pm 0.1$	$42.2 \pm 0.2$	$12.2 \pm 0.3$	$147.1 \pm 0.4$	$161.3 \pm 4.9$

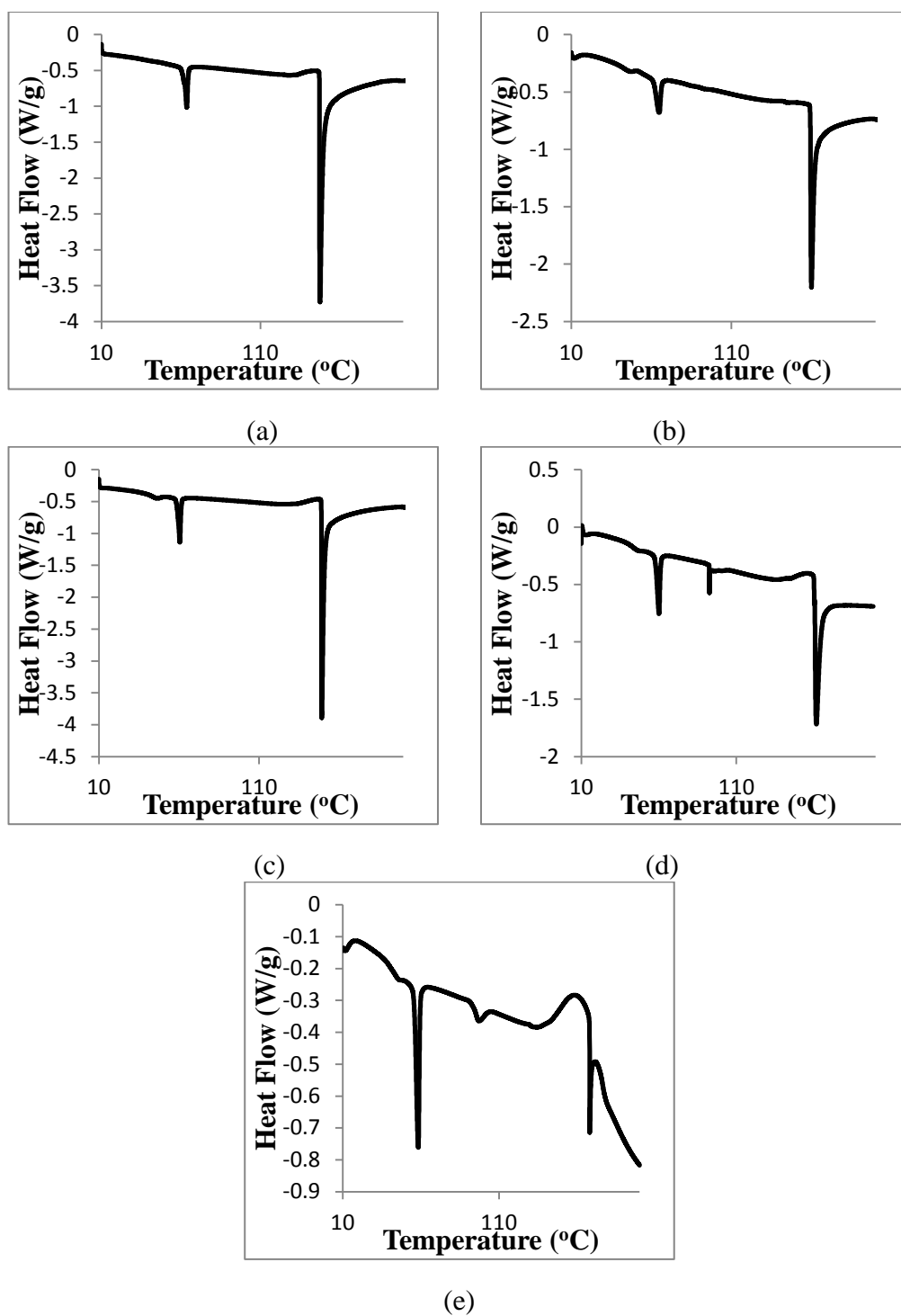


**Figure 4.11.** DSC thermograms of SD tobramycin three-components formulations for:

(a) tobramycin:phospholipids:mannitol=1:0.5:0.1;

(b) tobramycin:phospholipids:mannitol=1:0.5:0.25;

(c) tobramycin:phospholipids:mannitol=1:0.5:0.5;

(d) tobramycin:phospholipids:mannitol=1:0.5:0.75;

(e) tobramycin:phospholipids:mannitol=1:0.5:1.

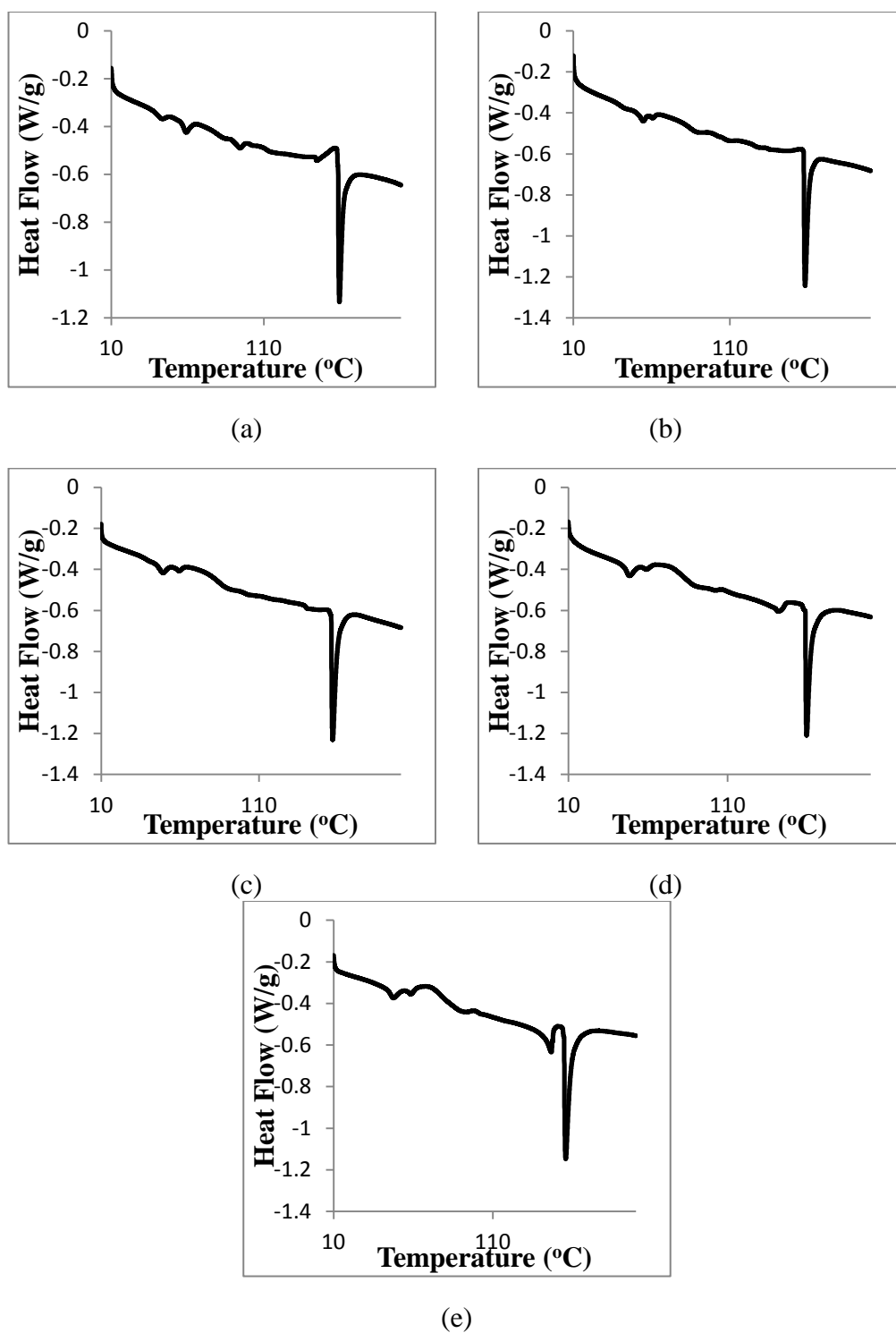


**Figure 4.12.** DSC thermograms of SD azithromycin three-components formulations for: (a) azithromycin:phospholipids:mannitol=1:0.5:0.1; (b) azithromycin:phospholipids:mannitol=1:0.5:0.25; (c) azithromycin:phospholipids:mannitol=1:0.5:0.5; (d) azithromycin:phospholipids:mannitol=1:0.5:0.75; and (e) azithromycin:phospholipids:mannitol=1:0.5:1.

### **4.3.3 Water Content**

The water content of all formulations (as received drugs and spray-dried powders) is listed in Table 4.5. SD powders exhibited water content less than 7% except for TOB:PLS:MAN=1:0.5:0.25 with 11%.

#### **4.3.3.1 One-component System (Spray-dried Pure Drug)**

Theoretically, the monohydrate, dihydrate, and trihydrate crystalline forms of TOB[168] contain 3.7, 7.1, and 10.3% (w/w) water, respectively. KF data shows as received TOB contained  $7.47 \pm 0.18\%$  (w/w)[43]. It suggests as received TOB was possibly present as a dihydrate with some moisture sorbed[43]. Monohydrate and dihydrate of AZI[169] possess 2.29% and 4.58% (w/w) water, respectively. As-received AZI was possibly present in dihydrate rich as supported by water content of  $4.35 \pm 0.14\%$  (w/w)[43]. Compared to the corresponding crystalline material, residual water content of SD pure TOB and SD pure AZI powders was lower after spray drying.

#### **4.3.3.2 Two-component System**

##### **4.3.3.2.1 Spray-dried Drug:Mannitol**

As expected, the incorporation of non-hygroscopic MAN[170] lowered water content of TOB:MAN from 3.54% (w/w) to 0.41% (w/w) as increasing MAN from 1:0.1 to 1:1[143]. A similar descending trend was observed for AZI:MAN with an increase in amount of MAN from 1:0.1 to 1:0.25[143]. However, water content of AZI:MAN increased as MAN further increased from 1:0.25 to 1:1[143].

##### **4.3.3.2.2 Spray-dried Drug:Phospholipids**

PLS showed an molar ratio effect on water content of TOB:PLS and AZI:PLS. With molar ratios of 1:2 and 1:1, the water content of TOB:PLS and AZI:PLS was approximately from 5% to 7%. However, it was significantly reduced down to < 2% in the formulations of 1:0.5.

#### **4.3.3.3 Three-component System (Spray-dried Drug:Phospholipids:Mannitol)**

A notable water content of 11% was observed for the TOB:PLS:MAN=1:0.5:0.25 formulation. It is unclear as to why such high water content was observed.

**Table 4.5.** Water content for tobramycin and azithromycin formulations[43, 143] (mean  $\pm$  SD, n=3).

Tobramycin Formulations	Water Content (% w/w)	Azithromycin Formulations	Water Content (% w/w)
As received TOB	7.47 $\pm$ 0.18	As received AZI	4.35 $\pm$ 0.14
SD pure TOB	5.24 $\pm$ 0.12	SD pure AZI	1.30 $\pm$ 0.21
TOB:MAN=1:0.1	3.54 $\pm$ 0.23	AZI:MAN=1:0.1	2.67 $\pm$ 0.66
TOB:MAN=1:0.25	2.79 $\pm$ 0.87	AZI:MAN=1:0.25	0.24 $\pm$ 0.05
TOB:MAN=1:0.5	2.21 $\pm$ 0.45	AZI:MAN=1:0.5	0.50 $\pm$ 0.14
TOB:MAN=1:0.75	0.89 $\pm$ 0.18	AZI:MAN=1:0.75	1.50 $\pm$ 0.52
TOB:MAN=1:1	0.41 $\pm$ 0.17	AZI:MAN=1:1	2.25 $\pm$ 0.54
TOB:PLS=1:2	6.35 $\pm$ 1.53	AZI:PLS=1:2	4.92 $\pm$ 1.11
TOB:PLS=1:1	6.84 $\pm$ 0.90	AZI:PLS=1:1	6.21 $\pm$ 1.05
TOB:PLS=1:0.5	1.53 $\pm$ 0.26	AZI:PLS=1:0.5	1.42 $\pm$ 0.72
TOB:PLS:MAN=1:0.5:0.1	3.15 $\pm$ 0.41	AZI:PLS:MAN=1:0.5:0.1	2.47 $\pm$ 0.45
TOB:PLS:MAN=1:0.5:0.25	11.00 $\pm$ 0.86	AZI:PLS:MAN=1:0.5:0.25	5.20 $\pm$ 0.74
TOB:PLS:MAN=1:0.5:0.5	3.38 $\pm$ 0.39	AZI:PLS:MAN=1:0.5:0.5	4.57 $\pm$ 0.63
TOB:PLS:MAN=1:0.5:0.75	4.10 $\pm$ 0.43	AZI:PLS:MAN=1:0.5:0.75	3.28 $\pm$ 0.38
TOB:PLS:MAN=1:0.5:1	4.55 $\pm$ 0.25	AZI:PLS:MAN=1:0.5:1	4.43 $\pm$ 0.84

### 4.3.4 Water Vapor Sorption

#### 4.3.4.1 One-component System (Spray-dried Pure Drug)

Equilibrated water vapor sorption isotherms at 25°C of as received TOB and AZI[43] with corresponding SD samples are plotted in Figure 4.13. Overall, TOB powders exhibited a higher water vapor sorption than AZI.

As-received TOB slowly increased weight with RH %, exhibiting ~ 22% weight change at 95% RH. Water vapor isotherm was more complex for SD TOB. SD TOB took up relatively higher water vapor (than as received TOB) until 60% RH, reaching a ~ 20% weight increase. Thereafter, weight change of SD TOB started to drop to ~ 12% at 65% RH and reached a plateau until 75% RH. The decrease in weight (at 65% RH) may be due to lyotropic-induced crystallization transition with expulsion of free water[145, 158, 171]. At the end of the study, a 65% weight increase was observed for SD pure TOB. As-received AZI gained approximately 4% weight. SD pure AZI gained 5% weight by 95% RH[43].

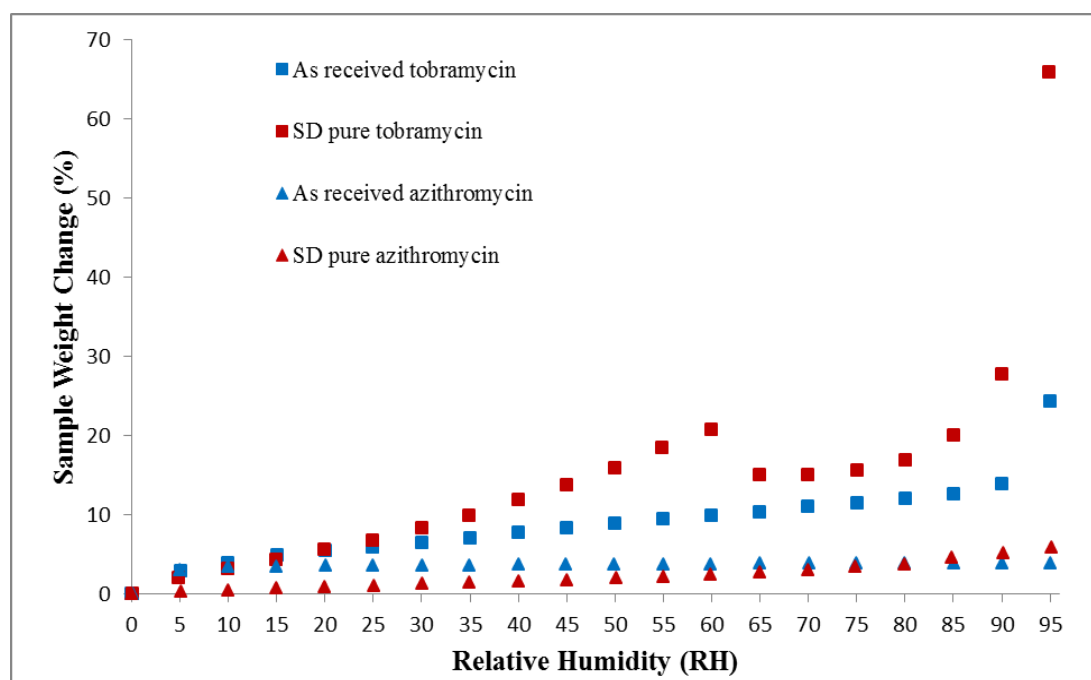


**Figure 4.13.** Water vapor sorption isotherms at 25°C for as received vs SD powders[43] (weight change % vs RH; n=1).

#### 4.3.4.2 Two-component System

##### 4.3.4.2.1 Spray-dried Drug:Mannitol

Equilibrated water vapor sorption isotherms of SD TOB:MAN=1:0.5 and AZI:MAN=1:0.5[143] are plotted in Figure 4.14. Overall, TOB:MAN=1:0.5 took up more water vapor than AZI:MAN=1:0.5. TOB:MAN=1:0.5 gradually sorbed water

vapor until 65% RH, followed by a drop in weight (possibly lyotropic-induced crystallization transition) at 70% RH. A plateau region from 70% to 80% RH was observed, followed by a sharp increase of weight after 85% RH. Weight change of TOB:MAN=1:0.5 increased up to ~117% at 95% RH. As similar to the water vapor sorption isotherm of SD AZI, AZI:MAN=1:0.5 exhibited a slight increase in weight up to ~32% at 95% RH without any evident phase transition, remaining in an amorphous state[143].

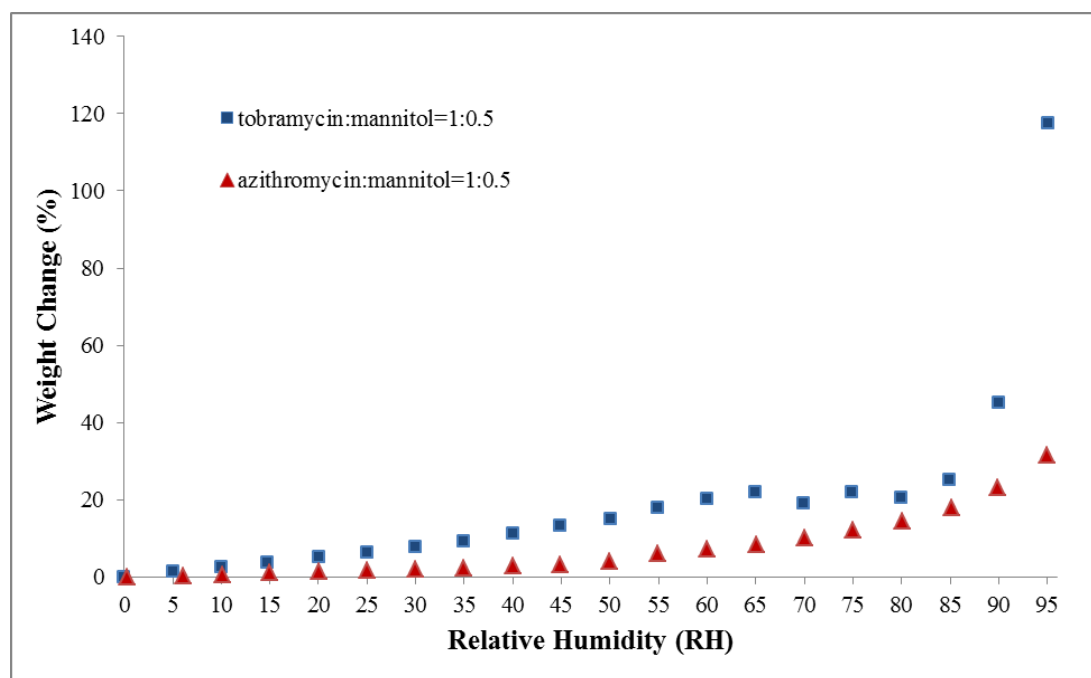


**Figure 4.14.** Water vapor sorption isotherms at 25°C for SD tobramycin:mannitol=1:0.5 and SD azithromycin:mannitol=1:0.5[143] (weight change % vs RH; n=1).

#### 4.3.4.2.2 Spray-dried Drug:Phospholipids

Equilibrated water vapor sorption isotherms of SD TOB:PLS=1:0.5 and AZI:PLS=1:0.5 are plotted in Figure 4.15. The profiles were similar to the corresponding TOB:MAN=1:0.5 and AZI:MAN=1:0.5, respectively. TOB:PLS=1:0.5 gradually took up water vapor until 65% RH. It was followed by a drop in weight (possibly lyotropic-induced crystallization transition) at 70% RH. A sharp increase in weight change was observed after 75% RH. The weight change of TOB:PLS=1:0.5 was ~ 57% at 95% RH. As expected, AZI:PLS=1:0.5 slightly increased weight up to ~13% at 95% RH.

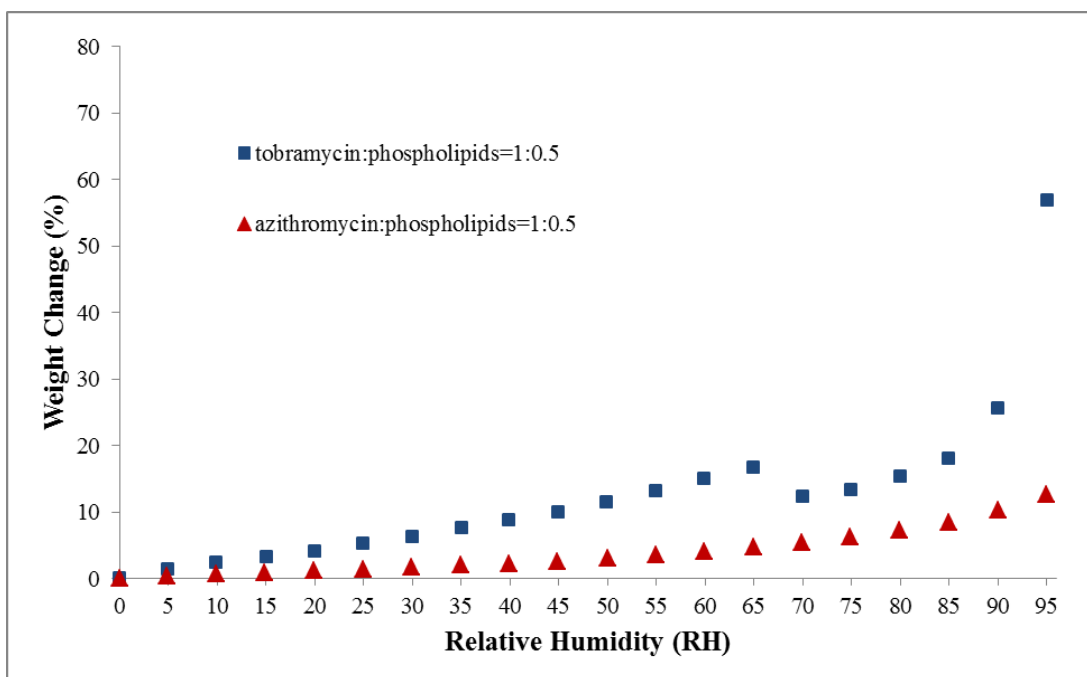


**Figure 4.15.** Water vapor sorption isotherms at 25°C for SD tobramycin:phospholipids=1:0.5 and SD azithromycin:phospholipids=1:0.5 (weight change % vs RH; n=1).

#### 4.3.4.3 Three-component System (Spray-dried Drug:Phospholipids:Mannitol)

Equilibrated water vapor sorption isotherms of SD TOB:PLS:MAN=1:0.5:0.5 and AZI:PLS:MAN=1:0.5:0.5 are plotted in Figure 4.16. The profiles were similar to the corresponding drug:mannitol or drug:phospholipids formulation, respectively. TOB:PLS:MAN=1:0.5:0.5 gradually took up water vapor until 65% RH. It was followed by a possibly lyotropic-induced crystallization transition with a drop in weight change at 70% RH. A sharp increase of weight was observed after 75% RH. Weight change of TOB:PLS:MAN=1:0.5:0.5 was up to ~71% at 95% RH. As expected, weight change of AZI:PLS:MAN=1:0.5:0.5 slightly increased ~15% at 95% RH.



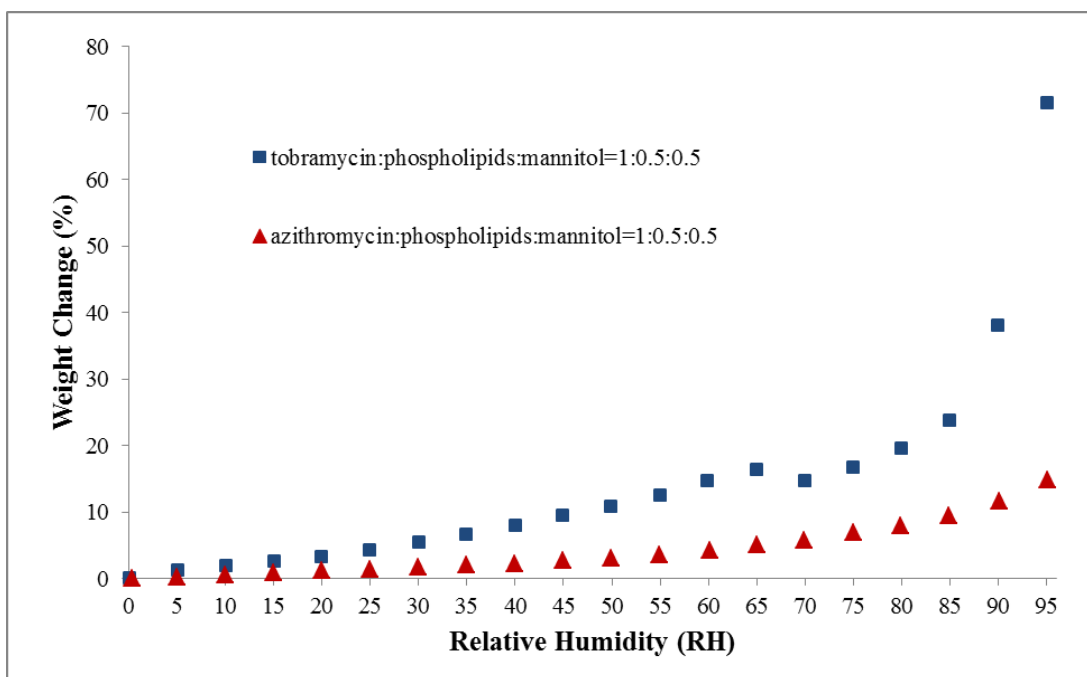


**Figure 4.16.** Water vapor sorption isotherms at 25°C for SD tobramycin:phospholipids:mannitol=1:0.5:0.5 and SD azithromycin:phospholipids:mannitol=1:0.5:0.5 (weight change % vs RH; n=1).

### 4.3.5 Chemical Spectroscopy

#### 4.3.5.1 Confocal Raman Microscopy and Spectroscopy for Chemical Imaging and Mapping

##### 4.3.5.1.1 One-component System (Spray-dried Pure Drug)

Confocal Raman microscopy and spectroscopy (CRM) analysis of SD pure TOB particles[43] is shown in Figure 4.17. In Figure 4.17a, a typical spectrum taken via CRM at the point indicated on the images in Figure 4.17b and Figure 4.17c is shown in comparison to as received TOB used as input. The Raman spectra in Figure 4.17a were obtained using a 785 nm laser to minimize the effects of fluorescence. However, to the author's knowledge, it is not clear yet why TOB emitted fluorescence, since no double or triple bond(s) is present in the chemical structure. The broad vibrational bands in the SD TOB were characteristic of an amorphous substance. Raman spectra taken from several SD particles by CRM were indistinguishable, indicating no heterogeneity in powder, from the spectrum in Figure 4.17a[43].

A similar result was obtained from the CRM analysis of SD AZI[43] as shown in Figure 4.18. Although AZI showed weaker fluorescence than TOB in the amorphous state, a spectrum was again taken via CRM using the 785 nm laser to avoid fluorescence. Spectra taken by CRM across many particles of SD AZI were indistinguishable, suggesting that the particles were uniformly amorphous[43].

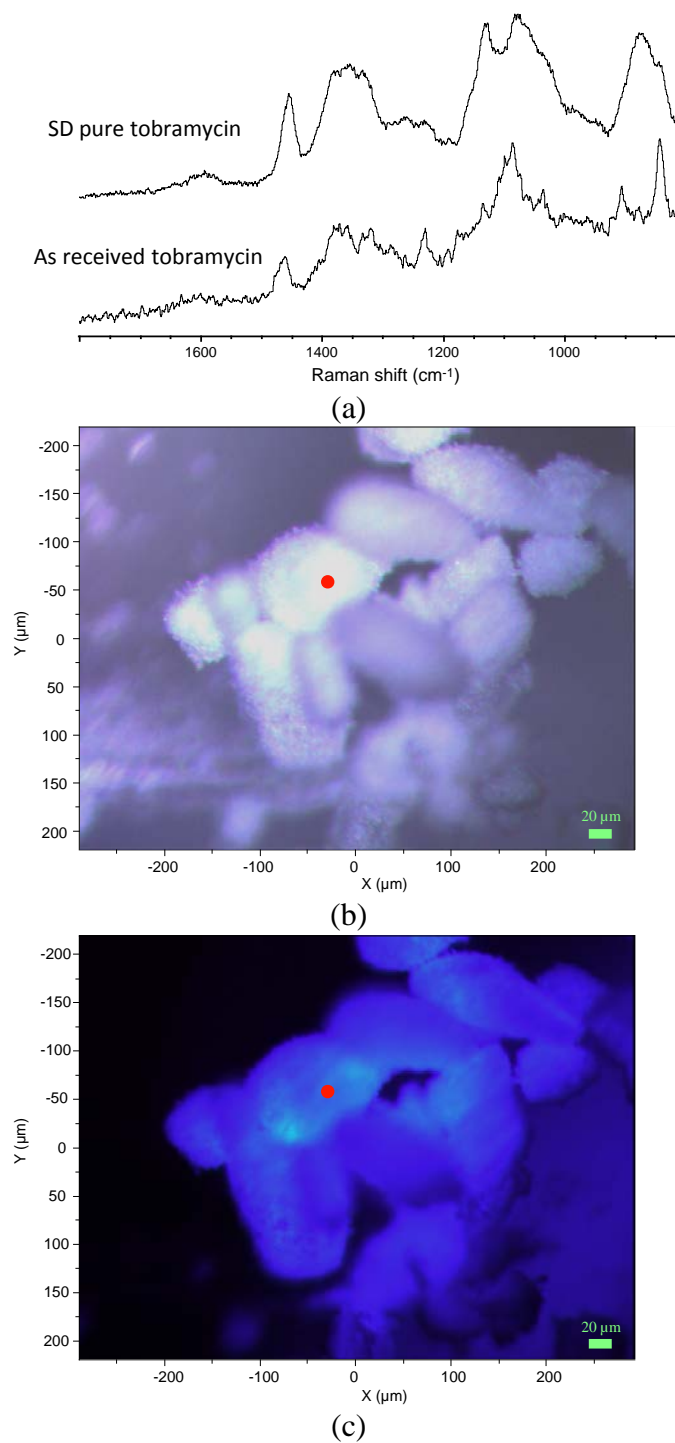


**Figure 4.17.** (a). Raman spectrum of SD pure tobramycin compared to that of as received tobramycin obtained using CRM; (b). Brightfield micrograph of SD pure tobramycin obtained using a 10x objective; and (c). Fluorescence micrograph of SD pure tobramycin obtained using a 10x objective. The red points show the location at which the SD spectrum in (a) was obtained[43]. Courtesy of Dr. Frederick Vogt at GlaxoSmithKline.

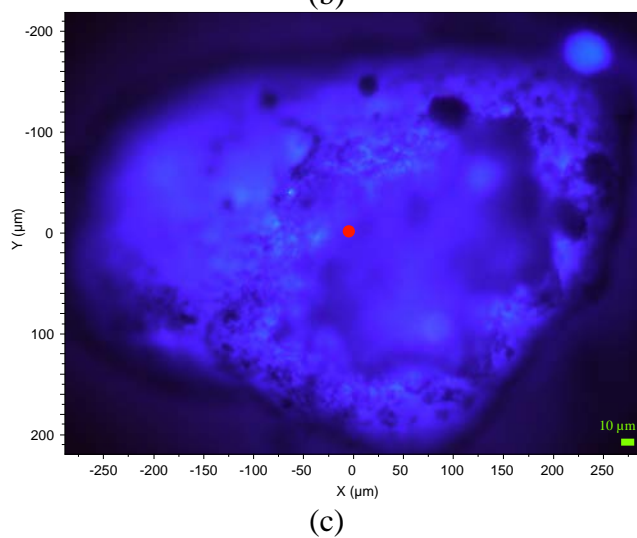
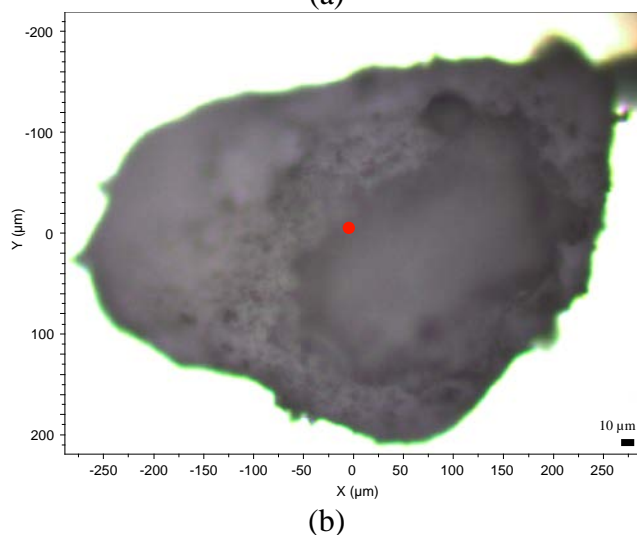
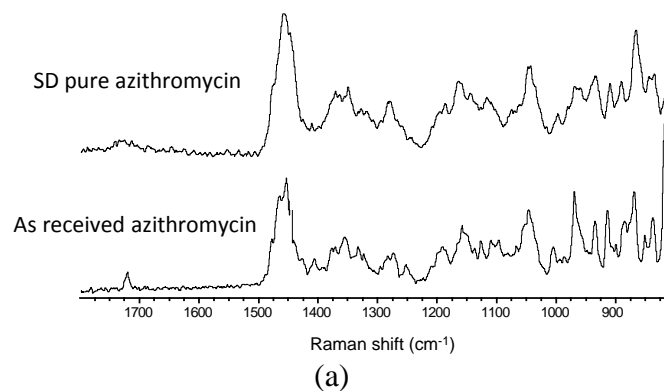


**Figure 4.18.** (a). Raman spectrum of SD pure azithromycin compared to that of as received azithromycin obtained using CRM; (b). Brightfield micrograph of SD pure azithromycin obtained using a 10x objective; and (c). Fluorescence micrograph of SD pure azithromycin obtained using a 10x objective. The red points show the location at which the SD spectrum in (a) was obtained[43]. Courtesy of Dr. Frederick Vogt at GlaxoSmithKline.

#### 4.3.5.1.2 Two-component System

#### 4.3.5.1.3 Spray-dried Drug:Mannitol

CRM analysis was performed for TOB:MAN=1:0.5 particles to investigate the physical form and homogeneity of TOB and MAN in SD particles[143]. Amorphous SD pure TOB was previously observed to show significant fluorescence, necessitating the use of a near-infrared laser wavelength (785 nm) for Raman spectroscopy of these materials. In Figure 4.19a, a brightfield micrograph obtained with a 10x objective is shown for a region of SD TOB:MAN=1:0.5 particles. Superimposed on this image is a  $25 \times 25$  CRM map, with greater blue intensity indicating stronger Raman signal from 1425 to 1480  $\text{cm}^{-1}$ , a characteristic region for TOB. The CRM map indicates that the TOB was homogeneously distributed, with the only area of reduced signal corresponding to a depression in the particle surface seen primarily on the upper left portion of the mapped region. A fluorescence microscopy image of the particles, shown in Figure 4.19b, also showed no indication of heterogeneity. In Figure 4.19c, a comparison is shown between three representative Raman spectra obtained from the map in Figure 4.19a and reference spectra of SD pure TOB and alpha polymorphic form of MAN. The three representative spectra taken from TOB:MAN=1:0.5 particles were similar, showing no evidence of heterogeneity. There was no evidence of crystalline alpha MAN present in the spectra of SD particles. In addition, the broad vibrational bands observed were in good agreement with amorphous TOB[143].

SD pure AZI was previously observed to show less fluorescence than SD pure TOB. When spray dried with MAN, it was found that a higher-sensitivity Raman laser utilizing a shorter wavelength (633 nm) could be used for analysis of AZI:MAN=1:0.5 particles. In Figure 4.20, the CRM results are shown for AZI:MAN=1:0.5 particles using a 50x objective. In Figure 4.20a, a  $25 \times 25$  CRM map is shown using a set of bands in the 845 to 900  $\text{cm}^{-1}$  region (characteristic of alpha MAN). The distribution was seen to be relatively homogenous. This map can be compared with a map shown in Figure 4.20b where increasing red color corresponding to increasing intensity of Raman bands in the 1470 to 1550  $\text{cm}^{-1}$  (characteristic of SD pure AZI). The two maps generally agreed, suggesting that components of MAN and AZI were closely associated, and did not show any indication of heterogeneity between the two components at the high magnification used here. Spectra (Figure 4.20c) taken from three regions supported this conclusion. In addition, it also suggests that the MAN in the SD particles may possibly be amorphous[143].

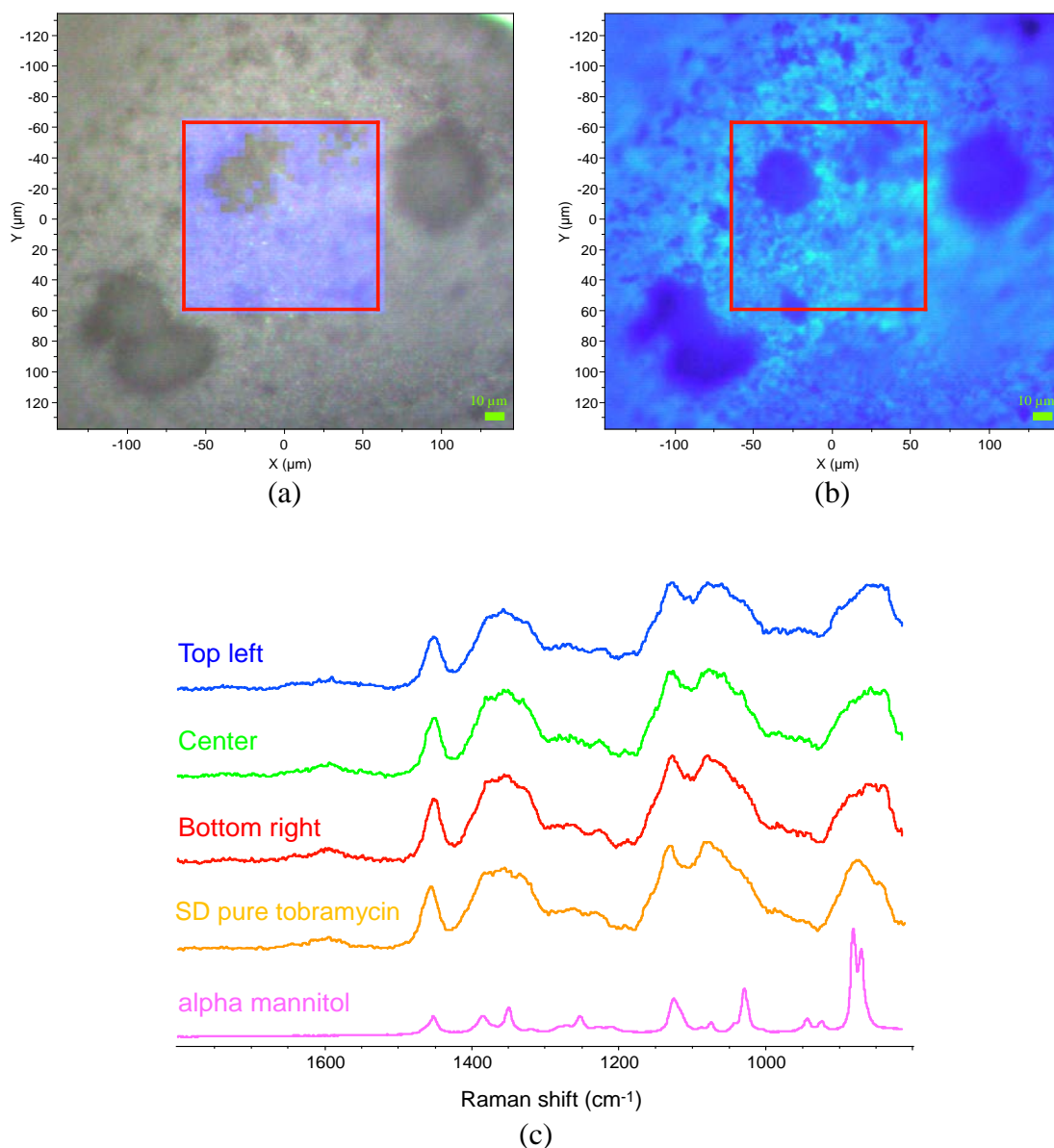


**Figure 4.19.** (a) Brightfield micrograph of SD tobramycin:mannitol=1:0.5 particles obtained using a 10x objective. CRM mapping was performed in the region marked with the red box; increasing blue color corresponds to increasing intensity of Raman signal in the 1425 to 1480 cm<sup>-1</sup> region. (b) Fluorescence micrograph of the same region. (c) Raman spectra from three points obtained using CRM, shown in comparison to SD pure tobramycin and alpha mannitol prepared as pure materials[143]. Courtesy of Dr. Frederick Vogt at GlaxoSmithKline.

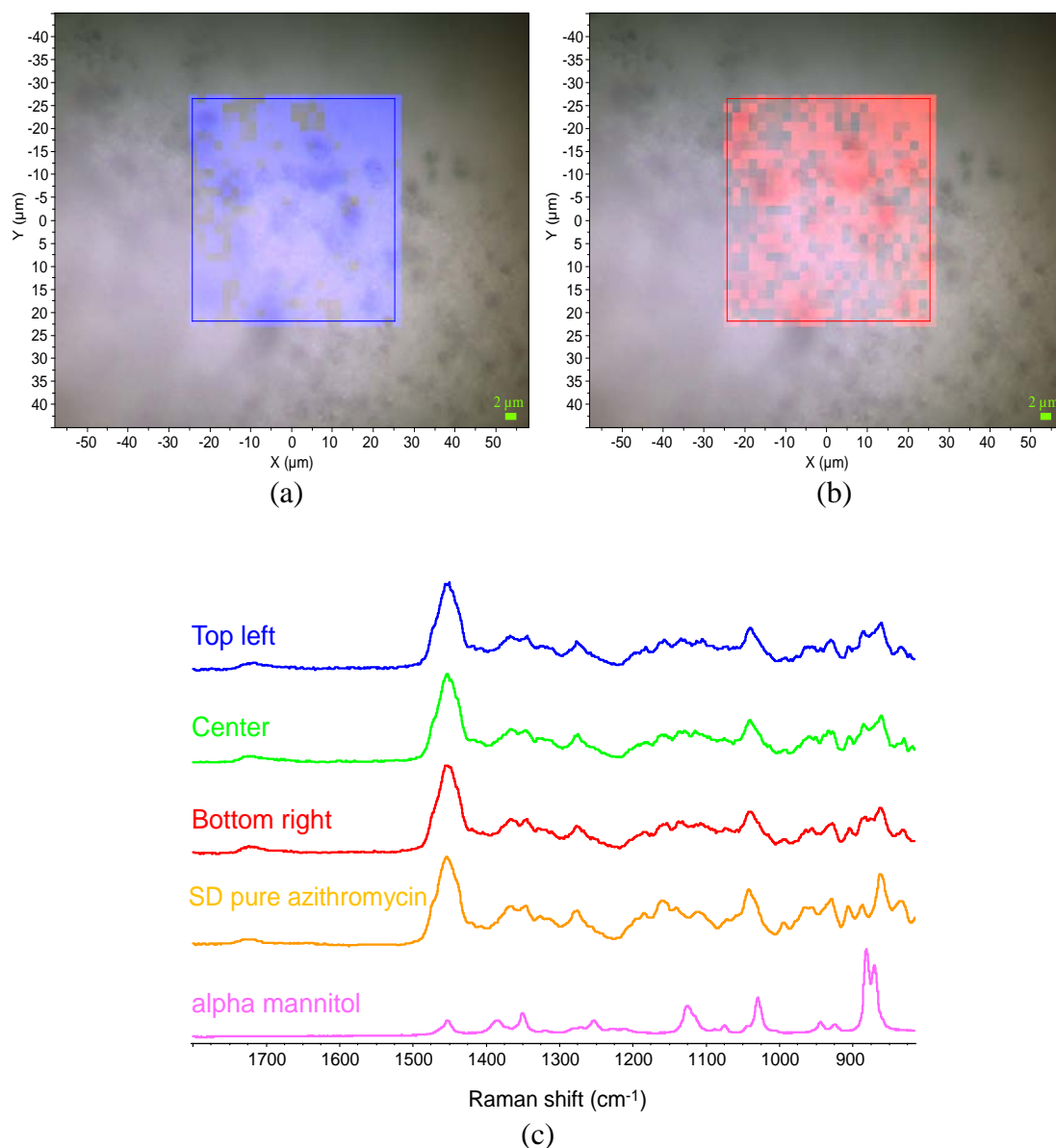
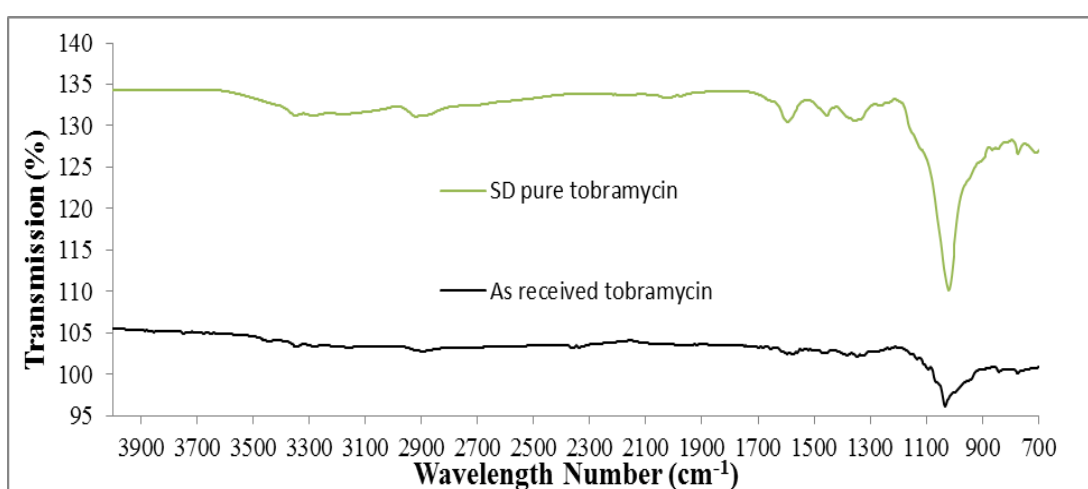


**Figure 4.20.** (a) Brightfield micrograph of SD azithromycin:mannitol=1:0.5 particles obtained using a 50x objective. CRM mapping was performed in the region marked with the red box; increasing blue color corresponds to increasing intensity of Raman signal in the 845 to 900 cm<sup>-1</sup> region. (b) CRM mapping results with increasing red color corresponding to increasing intensity of Raman signal in the 1670 to 1750 cm<sup>-1</sup> region. (c) Raman spectra from three points obtained using CRM, shown in comparison to SD pure azithromycin and alpha mannitol prepared as pure materials[143]. Courtesy of Dr. Frederick Vogt at GlaxoSmithKline.

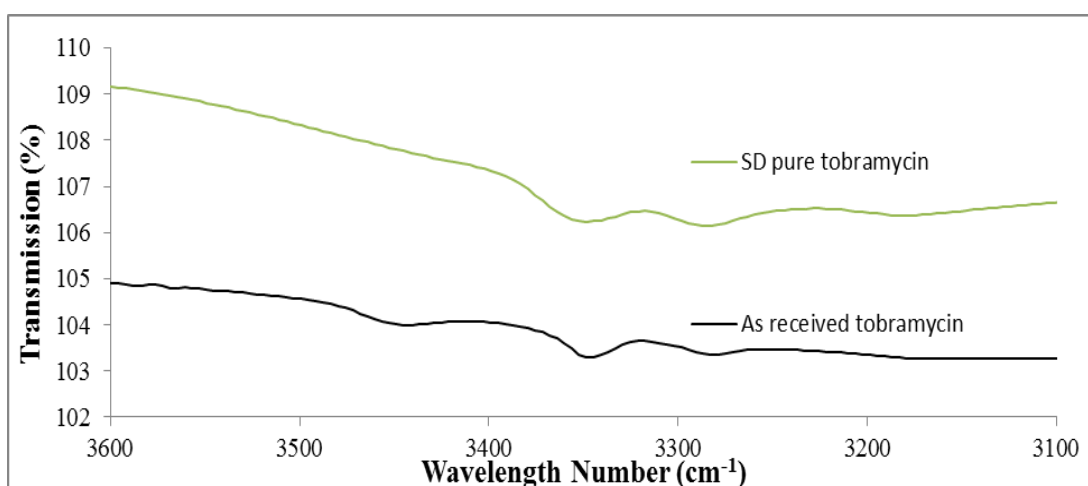
### 4.3.5.2 Attenuated Total Reflectance-Fourier Transform Infrared Spectroscopy

#### 4.3.5.2.1 One-component System (Spray-dried Pure Drug)

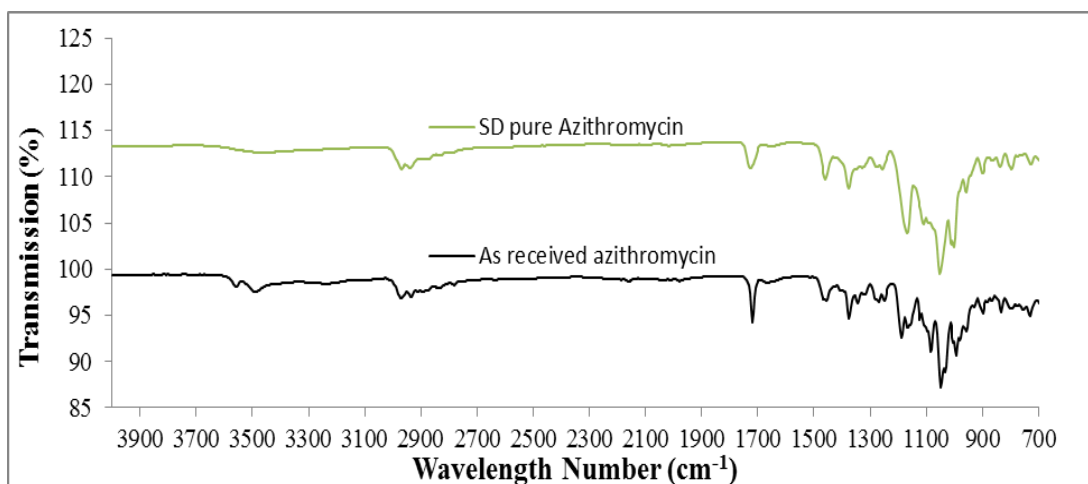
Attenuated total reflectance-Fourier transform infrared spectroscopy (ATR-FTIR) spectra of TOB[43] (Figure 4.21a and Figure 4.21b (zoomed in data)) and AZI[43] (Figure 4.21c) indicated a loss of the peak at  $\sim 3500\text{ cm}^{-1}$  after spray drying, although the as received TOB did not show an strong spectrum possibly due to poor contact with ATR crystal. This peak may be tentatively assigned to O-H stretching vibration mode in the particles. Instead, the SD pure TOB and AZI particles exhibited a broad band at region of  $\sim 3600\text{-}3000\text{ cm}^{-1}$ . In comparison to as received sample, the SD pure AZI showed additional spectral differences at band region of  $\sim 1400\text{ to }1100\text{ cm}^{-1}$ . This band region may be tentatively assigned to C-O stretching[43].



(a)



(b)



(c)

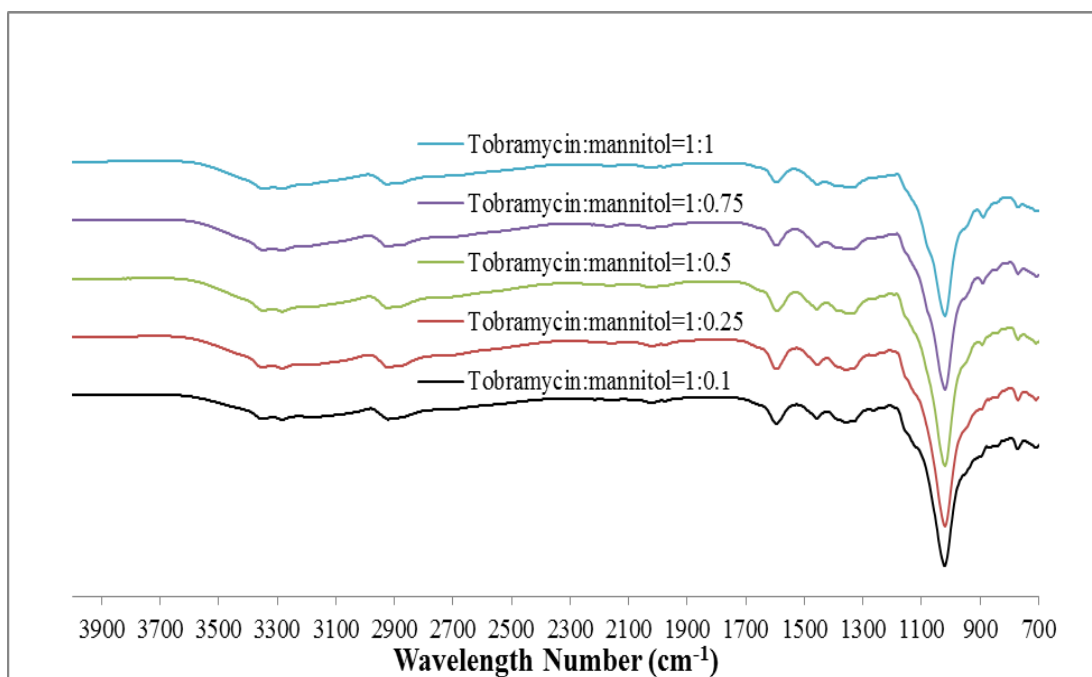
**Figure 4.21.** ATR-FTIR spectra of: (a) SD pure and as received tobramycin particles (full scan range); (b) SD pure and as received azithromycin particles (zoomed in spectra from (a)); and (c) SD pure and as received azithromycin particles (full scan range)[43].

#### 4.3.5.2.2 Two-component System

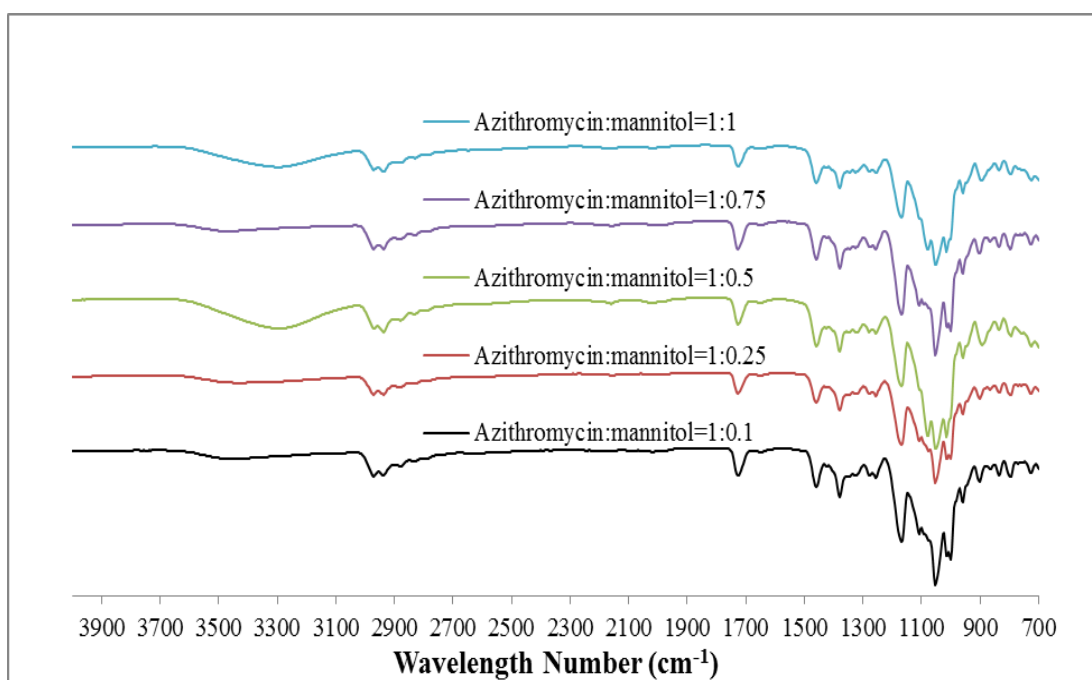
##### 4.3.5.2.3 Spray-dried Drug:Mannitol

ATR-FTIR spectra of TOB:MAN[143] (Figure 4.22a) and AZI:MAN[143] (Figure 4.22b) showed similar spectra to the corresponding SD pure TOB and AZI. No significant peak shift was observed in the binary systems. Similar to spectrum of SD pure AZI, AZI:MAN=1:0.5 and AZI:MAN=1:1 showed a slight spectral difference at band of  $\sim 1100\text{ cm}^{-1}$  to the other compositions. In addition, a broad peak at band region of  $\sim 3600\text{--}3100\text{ cm}^{-1}$ , possibly reflecting water molecules in samples, was observed in AZI:MAN=1:0.5 and AZI:MAN=1:1. This data may possibly suggest that water molecules could be present with AZI component. Therefore, it would possibly facilitate the conversion of AZI component (in AZI:MAN=1:0.5 and AZI:MAN=1:1) to a hydrate form. However, as water content data (Table 4.5) being considered, it is unclear why the two formulations exhibited differently to other formulations[143].





(a)



(b)

**Figure 4.22.** ATR-FTIR spectra for: (a) SD tobramycin:mannitol formulations; and (b) SD azithromycin:mannitol formulations[143].

## 4.4 Discussion

### 4.4.1 Crystallinity and Polymorphism

As shown, XRPD diffractograms indicates that both SD pure drug (Figure 4.1) and SD drug:mannitol (Figure 4.2) were lacking of long-range molecular order after spray drying. XRPD diffractograms of SD drug:phospholipids (Figure 4.3) and SD drug:phospholipids:mannitol (Figure 4.4) particles showed that phospholipid bilayer structure was retained after spray drying. However, the other component(s) in drug:phospholipids and drug:phospholipids:mannitol was/were lacking long-range molecular order.

The presence of amorphous character in SD dry powder particles may lead to the physical and chemical instabilities. Therefore, stability tests are of importance to study the effect of storage conditions on SD dry powder formulations. Besides the chemical stability issue, the physical change that can occur in powders upon storage is expected to adversely alter the aerosol dispersion performance.

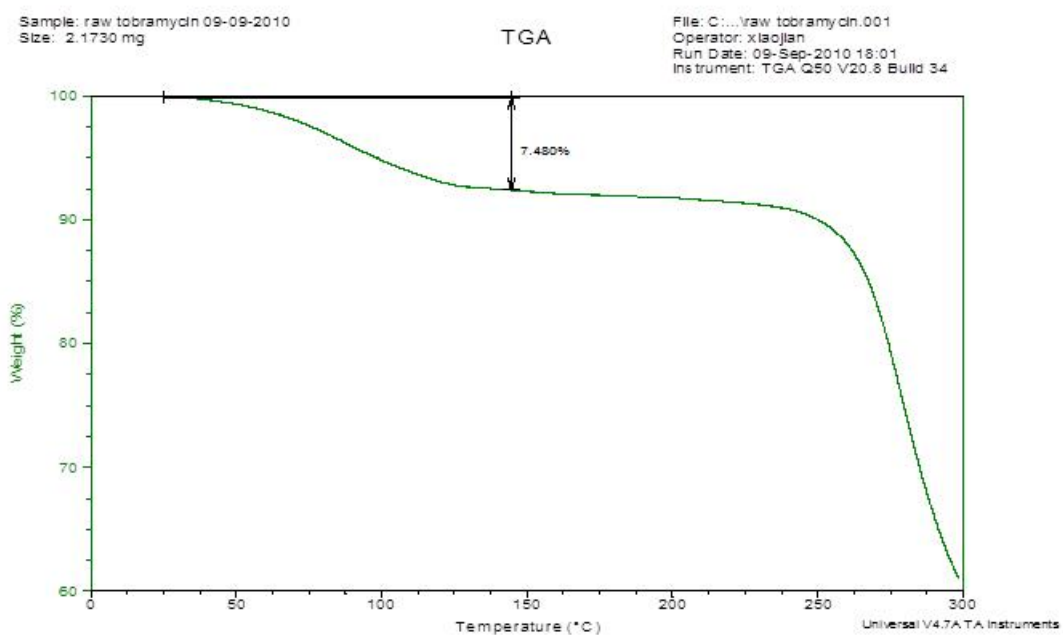
### 4.4.2 Solid-State Phase Transition

Understanding the thermal-induced phase transition(s) is important for a non-crystalline formulation intended for dry powder inhalation. Phase transitions that result in particle aggregation or solid-state bridging between particles may lead to the failure of powder delivery to the deep lungs. Therefore, solid-state phase transition of formulations, especially dry powders for inhalation is of importance.

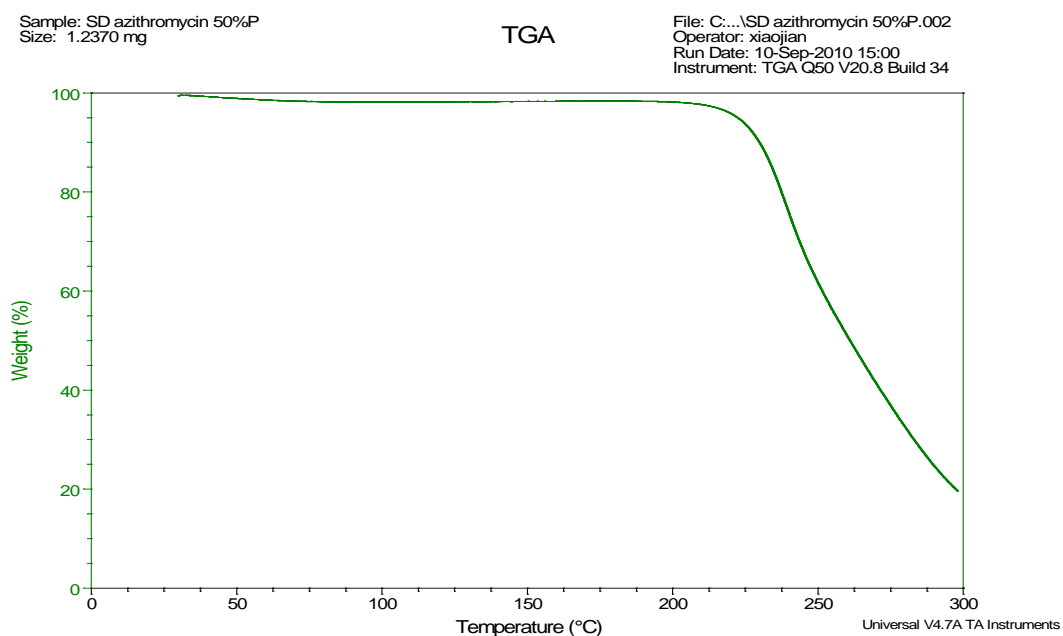
#### 4.4.2.1 One-component System (Spray-dried Pure Drug)

Before our work[43], the thermogram of as received TOB in hermetically sealed DSC pan has not been reported in the scientific literature. However, it has been done under non-hermetic conditions[168]. As mentioned earlier, commercially available crystalline TOB consists of stoichiometric hydrate forms of monohydrate, dihydrate, and trihydrate[168]. Compared to thermograms of TOB published previously, it indicates the first endothermic peak at  $\sim 146^{\circ}\text{C}$  (in Figure 4.6a) may correspond to the dehydration of as received TOB dihydrate. As-received TOB presented as a dihydrate form was possibly supported by KF titration (Table 4.5) and thermogravimetric analysis (TGA) data (Figure 4.23a) with  $\sim 7.5\%$  weight (water) loss when heated to  $150^{\circ}\text{C}$ . The TGA was conducted in a pin-holed pan with a scan rate as  $5^{\circ}\text{C}/\text{min}$ . The dehydration was likely followed by the melting of a metastable anhydrous form at  $\sim 156^{\circ}\text{C}$ , and the possible melting of stable anhydrous TOB occurred at  $\sim 200^{\circ}\text{C}$ . In thermal analysis from hermetically sealed DSC pan (Figure 4.6a), the formation of stable anhydrous from the melt by an exothermic crystallization (at the temperature range between  $\sim 156^{\circ}\text{C}$  and  $200^{\circ}\text{C}$ ) was not detected. However, the crystallization process was confirmed by hot stage microscopy (HSM) under cross-polarizer (Figure 4.24) at  $\sim 217^{\circ}\text{C}$ [43]. HSM study was conducted at  $5^{\circ}\text{C}/\text{min}$ . The temperature difference between DSC and HSM was due to open-air conditions in HSM study. The endothermic events at  $158^{\circ}\text{C}$  in the thermograms of SD pure TOB are suggested to be the melting of metastable anhydrous form. However, XRPD diffractogram (Figure 4.1a) exhibited no crystalline peaks from SD pure TOB with some possible extent of

anhydrous form (or even short-rang molecular order) due to the limitation of detection. Therefore, it may suggest that SD pure TOB from spray drying was amorphous-phase rich.



(a)



(b)

**Figure 4.23.** Thermogravimetric analysis for: (a) as received tobramycin; and (b) SD pure azithromycin.

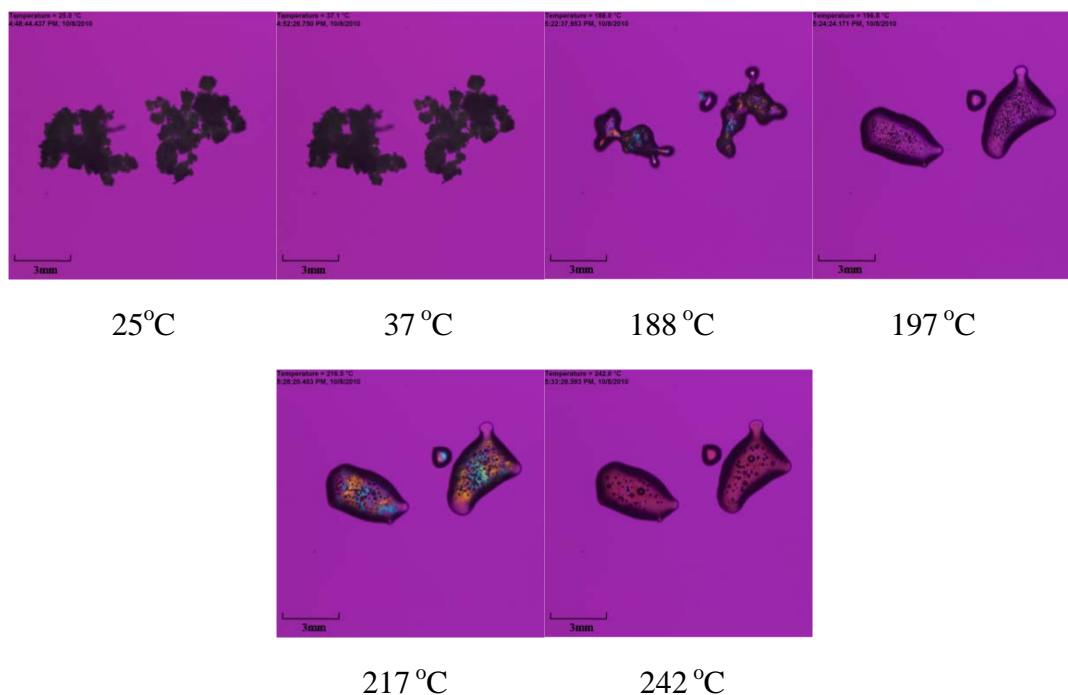


**Figure 4.24.** HSM micrographs of as received tobramycin[43].

As suggested by KF data (Table 4.5), as received AZI was possibly in the dihydrate form. The endothermic peak (Figure 4.6c) at 137°C is suggested to correspond to the concurrent events of dehydration and melting of as received AZI[169]. The endotherm at temperature from 160 to 170°C from SD pure AZI (Figure 4.6d) was possibly the melting of low amount of metastable AZI anhydrate (or short-range molecular order of AZI). This conclusion was supported by TGA data (Figure 4.23b) since there was no weight change at the temperature range of 160 to 170°C.

#### 4.4.2.2 Two-component System

##### 4.4.2.2.1 Spray-dried Drug:Mannitol

The order-to-disorder phase transition (endothermic event) of TOB:MAN (Figure 4.7) was observed and slightly influenced with temperature shift by the molar ratio of incorporated MAN. However, the existence of long-range molecular order of TOB and MAN in TOB:MAN system after spray drying was not suggested by XRPD in Figure 4.2a.

Both hermetic and non-hermetic DSC conditions were studied for AZI:MAN. In hermetic DSC conditions, equilibrium in thermal event is established in a fast manner. However, non-hermetic conditions allow the release of moisture from samples, minimizing moisture effect on thermal events. In Figure 4.8, DSC thermograms under hermetic conditions of AZI:MAN=1:0.1, 1:0.25 and 1:0.75, and AZI:MAN=1:0.5 and 1:1 exhibited similar thermal events, respectively. Under non-hermetic conditions, only the AZI:MAN=1:0.25 exhibited unique behavior (Figure 4.9b). In non-hermetic DSC studies, thermograms of AZI:MAN=1:0.1 (Figure 4.9a) and 1:0.75 (Figure 4.9d)

were similar to SD pure AZI (Figure 4.25). This data may suggest that the MAN component was probably present in amorphous phase. Similar to the discussion of SD pure AZI (in Section 4.4.2.1), a possible low amount of metastable AZI anhydrate (or short-range molecular order of AZI) may be present in AZI:MAN=1:0.1 and 1:0.75. In non-hermetic DSC studies, the two endothermic transition peaks in AZI:MAN=1:0.25 (Figure 4.9b) appeared consistent with the melting of delta and beta forms of MAN, respectively. Hulse, et al observed similar thermograms for the formulation of MAN with protein by co-spray drying[172]. As shown in Figure 4.9b, the beta form of MAN may result from the small exothermic event (crystallization) after the melting of the delta form. The possible melting of beta MAN was observed at 165°C. The thermograms of both formulations AZI:MAN=1:0.5 (Figure 4.9c) and AZI:MAN=1:1 (Figure 4.9e) exhibited a small endothermic peak at around 60°C. This endothermic peak could possibly be the melting/dehydration of a MAN hydrate form[173], although this hypothesis was not supported by XRPD data possibly due to the detection limit.

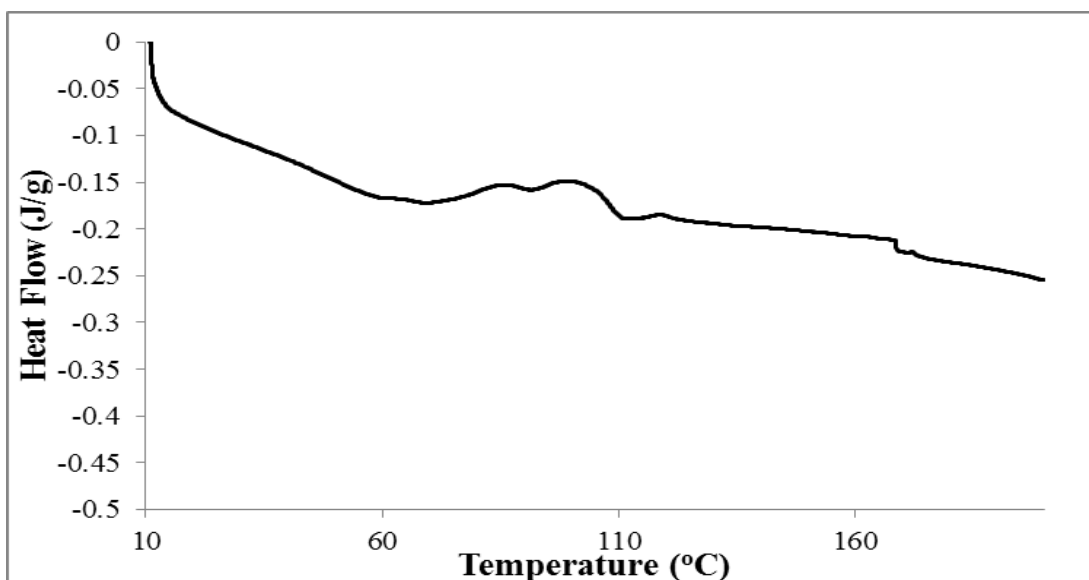


**Figure 4.25.** DSC thermogram (non-hermetic) of SD pure azithromycin.

#### 4.4.2.2.2 Spray-dried Drug:Phospholipids

Glass transition temperatures ( $T_g$ s) of the drugs in phospholipid incorporated two-component formulations (in Table 4.3) were lowered as compared to the SD pure drugs ( $\sim 50^\circ\text{C}$  for SD pure TOB and  $\sim 94^\circ\text{C}$  for SD pure AZI, respectively). The short-range molecular order of TOB component in TOB:PLS may possibly crystallize at  $\sim 141\text{--}152^\circ\text{C}$  as indicated by an exothermic peak. The crystallized TOB melted at  $\sim 147\text{--}156^\circ\text{C}$ . As to AZI:PLS, a possible endothermic peak of AZI was observed without showing an evident exothermic crystallization. It is believed that either a crystallization of AZI was possibly not detected under such DSC conditions or an endothermic peak could be a melting of the AZI component.

Based on the weight fraction of the components, the adjusted values of main phase transition of phospholipid bilayer ( $\Delta H_m$ ) were presented in Table 4.3. The values of  $\Delta H_m$  in phospholipid containing formulations may represent the tight packing of phospholipid bilayer structure in particles. The values of  $\Delta H_m$  from TOB:PLS were relatively constant (between 27.94J/g and 36.63J/g). Overall, AZI:PLS exhibited a lower value of  $\Delta H_m$  than TOB:PLS at same molar ratio. Noticeably,  $\Delta H_m$  values were relatively higher for AZI:PLS=1:2 (29.11J/g) and AZI:PLS=1:1 (22.86J/g), compared to AZI:PLS=1:0.5 (7.58J/g). This result may indicate that the phospholipid bilayer structures, in AZI:PLS=1:2 and 1:1, were well organized. AZI molecules have been reported to bind to phospholipids molecules and interfere with interfacial and hydrophobic parts of fully hydrated phospholipid bilayer[174]. Therefore, with water molecules associated in spray-dried particles (Table 4.5), it is expected that AZI molecules could interact with phospholipid molecules, possibly altering the organization of bilayer structure. Therefore, compared to TOB formulations, a higher reduction in integrity of phospholipid bilayer may be expected for AZI:PLS as a function of ratio composition, resulting in a lower value of  $\Delta H_m$ .

#### 4.4.2.3 Three-component System (Spray-dried Drug:Phospholipids:Mannitol)

Glass transition temperatures ( $T_g$ s) of the drugs in three-component formulations were lowered compared to the SD pure drugs ( $\sim 50^\circ\text{C}$  for SD pure TOB and  $\sim 94^\circ\text{C}$  for SD pure AZI, respectively). In addition to the main phase transition of phospholipid bilayer, an endothermic melting peak was observed for TOB:PLS:MAN=1:0.5:0.1, 1:0.5:0.25, and 1:0.5:0.5 in Figure 4.11a-c. It could possibly be the melting of either TOB or MAN, or simply the co-melting of TOB and MAN since the two components exhibit very close melting points[43, 44]. In TOB:PLS:MAN=1:0.5:0.75 and 1:0.5:1 (Figure 4.11d and 4.11e), TOB and MAN components may possibly crystallize, resulting in one melting peak. There was one (MAN content from 0.1 to 0.5 in the composition ratio) or two (MAN content from 0.75 to 1 in the composition ratio) melting peaks present in formulations in AZI:PLS:MAN (Figure 4.12). The additional endothermic peak at  $\sim 142\text{-}147^\circ\text{C}$  (at relatively lower temperature) was possibly the melting of a thermodynamically metastable polymorph of MAN such as the delta form[175]. Similar to TOB:PLS:MAN, the endothermic melting peak at  $\sim 157\text{-}161^\circ\text{C}$  in AZI:PLS:MAN could possibly be the melting of either AZI or MAN, or simply the co-melting of MAN and AZI components.

As expected, adjusted enthalpy ( $\Delta H_m$ ) values of main phase transition of phospholipid bilayer for TOB:PLS:MAN were higher than AZI:PLS:MAN at various molar ratios. Interestingly, it appeared that the molar ratio of 1:0.5:0.25 and 1:0.5:1 for both formulation systems resulted in lowest and highest  $\Delta H_m$ , respectively. These two specific molar ratios in each drug formulation may possibly indicate the lowest and highest integrity of phospholipid bilayer structure under studied molar ratios, respectively.

#### 4.4.3 Water Content

Water content of a solid formulation is not only related to chemical degradation, but also has an impact on aerosol dispersion performance by formation of liquid bridge. For dry powder inhalation formulations, low water content is essential in order to minimize capillary forces between particles.

In general, water content of final spray-dried powders was dependent on material properties and composition of components in particles. As shown in Table 4.5, water content of spray-dried pure drug was lowered by removing water molecules in as received material after spray drying from organic solution. The incorporation of non-hygroscopic MAN into drug:MAN and PLS with high water affinity into drug:PLS resulted into water content of < 4% and < 7%, respectively. Water content in three component drug:PLS:MAN generally was < 6% except for TOB:PLS:MAN=1:0.5:0.25 (~ 11% water content). This exception was possibly, in part, due to the hygroscopic nature of TOB[176].

In order to compare the water content from the worst case scenario where water is not removed by spray drying with the value obtained by KF, the calculation for theoretical values were conducted. It is assumed that water moisture is only from methanol solvent and as-received materials. Another assumption is that all the moisture is evenly distributed to the powder regardless of particle size. The water content of methanol is 0.01%. As-received TOB, AZI, MAN, DPPC and DPPG possessed water content of 7.47%, 4.35%, 0.53%, 3.76%, and 3.21%, respectively. The concentration of powder in methanol is 0.1%. The calculated values for KF are listed in Table 4.6. It is concluded that all calculated values are higher than the measured, possibly supporting that the spray drying process from organic solution does remove water under these studied spray-drying conditions.

**Table 4.6.** Calculated water content for tobramycin and azithromycin formulations (mean  $\pm$  SD, n=3).

Tobramycin Formulations	Water Content (% w/w)	Tobramycin Formulations	Water Content (% w/w)
SD pure TOB	14.26	SD pure AZI	11.37
TOB:MAN=1:0.1	14.02	AZI:MAN=1:0.1	11.28
TOB:MAN=1:0.25	13.69	AZI:MAN=1:0.25	11.17
TOB:MAN=1:0.5	13.21	AZI:MAN=1:0.5	10.98
TOB:MAN=1:0.75	12.80	AZI:MAN=1:0.75	10.82
TOB:MAN=1:1	12.46	AZI:MAN=1:1	10.68
TOB:PLS=1:2	11.57	AZI:PLS=1:2	10.94
TOB:PLS=1:1	12.09	AZI:PLS=1:1	11.05
TOB:PLS=1:0.5	12.95	AZI:PLS=1:0.5	11.15
TOB:PLS:MAN=1:0.5:0.1	12.59	AZI:PLS:MAN=1:0.5:0.1	11.10
TOB:PLS:MAN=1:0.5:0.25	12.45	AZI:PLS:MAN=1:0.5:0.25	11.02
TOB:PLS:MAN=1:0.5:0.5	12.22	AZI:PLS:MAN=1:0.5:0.5	10.90
TOB:PLS:MAN=1:0.5:0.75	12.02	AZI:PLS:MAN=1:0.5:0.75	10.79
TOB:PLS:MAN=1:0.5:1	11.83	AZI:PLS:MAN=1:0.5:1	10.69



#### 4.4.4 Water Vapor Sorption

Water vapor sorption isotherms indicate the amount of water vapor uptake at individual RH %, providing potential practical storage guidance on dry powders for inhalation. Water vapor sorption data could also reveal any possible lyotropic-induced phase transition, impeding aerosol dispersion performance. As compared to SD pure TOB, the relatively smaller weight drop during possible lyotropic-induced crystallization in SD TOB two-component and three-component powders was due to either a lower TOB component loading or an incompleteness of the phase transition in the powders. The large amount of water vapor uptaken by the particles at high RH % (i.e. above 80% RH) suggests a possible dissolution process[177]. Overall, due to the hygroscopic nature, TOB formulations exhibited water vapor sorption to a higher extent compared to AZI formulations, especially at high RH %.

##### 4.4.4.1 One-component System (Spray-dried Pure Drug)

The stoichiometric plots of mole water vapor sorbed per mole dry compound vs relative humidity[43] (Figure 4.26), translated from water vapor sorption data (Figure 4.13), could provide insightful molecular information. No evidence suggested that the “pre-dried” as-received TOB (possibly in dihydrate; thermodynamic stable) lost H-bonding water molecules. As-received TOB showed no evident lyotropic-induced phase transition. However, the SD pure TOB (possibly amorphous rich) underwent a lyotropic-induced phase transition to a more organized physical form. Without showing a glass transition, DSC data (Figure 4.27) suggest that SD pure TOB after water vapor sorption was possibly present as a hydrate or a mixture of hydrates. It showed two sharp endothermic peaks similar to the dehydration events from as-received TOB (Figure 4.6a). Possibly due to the high amount of sorbed free water vapor, approximately 4 water molecules were associated with SD TOB at 65% RH, as shown in Figure 4.26. In addition, SD TOB took up higher amount of water vapor at 95% RH than as received TOB possibly due to a larger surface area.

As-received AZI decreased weight by approximately 3.5% (shown as blue curve in Figure 4.28), indicating a loss of H-bonding water molecules during the pre-drying process at 0% RH. Upon exposure to water vapor, “pre-dried” as-received AZI gained approximately 1.5 water molecules per molecule and maintained this molecular ratio constant across the whole RH %. This may indirectly indicate as-received AZI was possibly dihydrate rich, which was in agreement with KF data (Table 4.5). However, SD pure AZI took up water vapor slowly and eventually reached ~2 molecules of water per molecule of AZI at 95% RH.

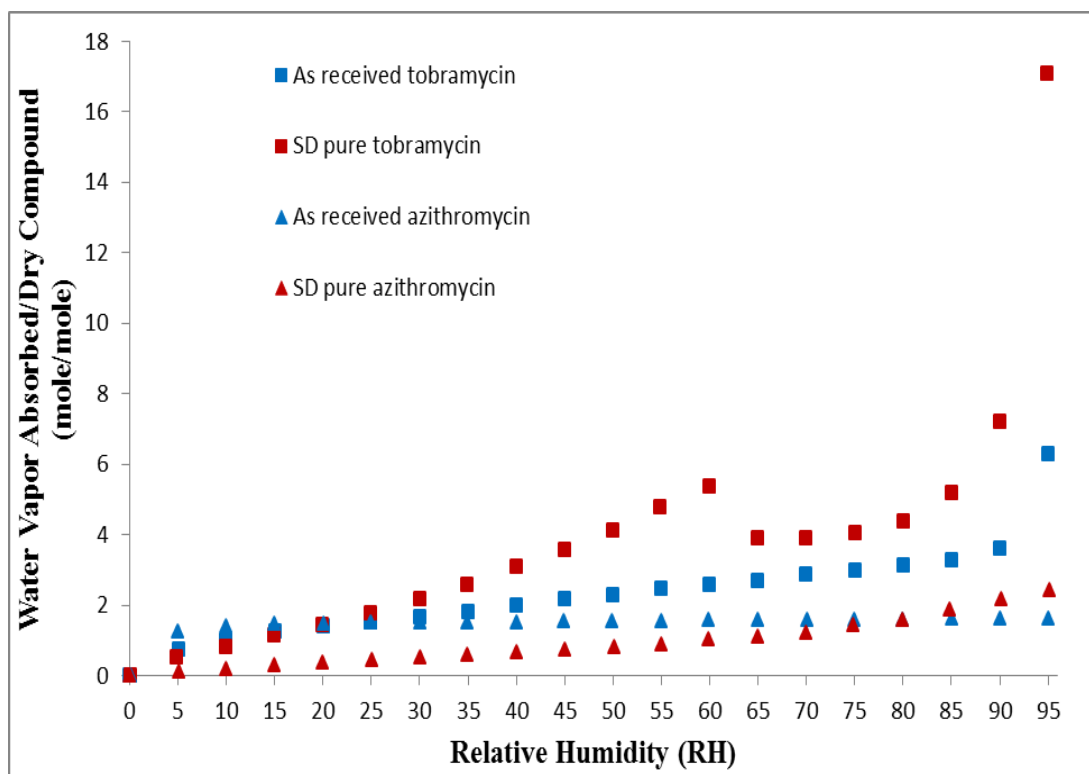


**Figure 4.26.** Water vapor sorption isotherms at 25°C for as received vs SD powders (water vapor sorbed/dry compound mole/mole vs RH; n=1)[43].

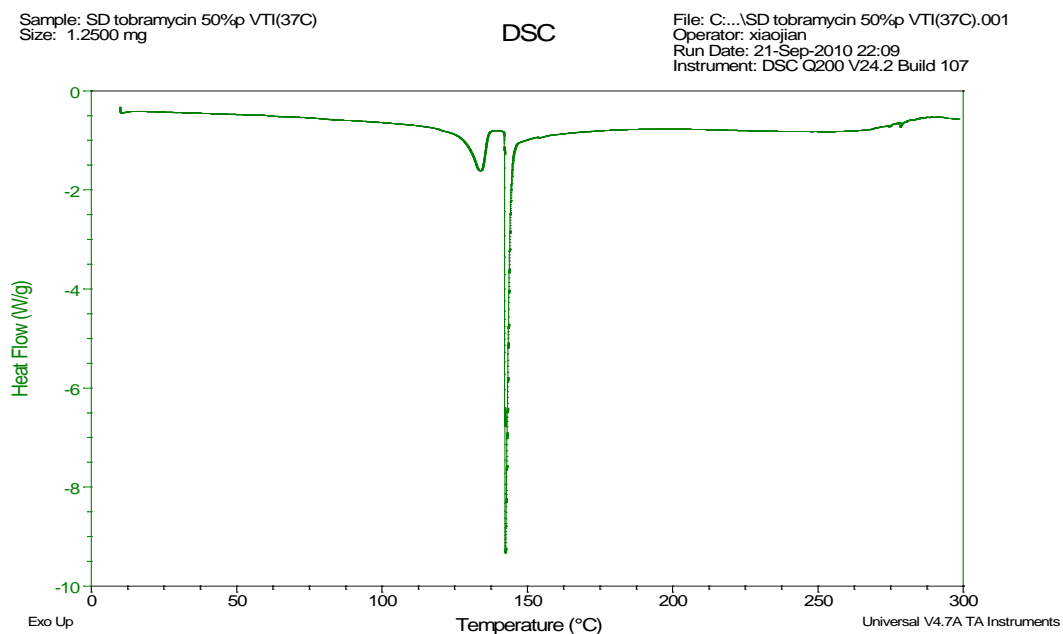


**Figure 4.27.** DSC thermograms of SD pure tobramycin after completion of water vapor sorption study.

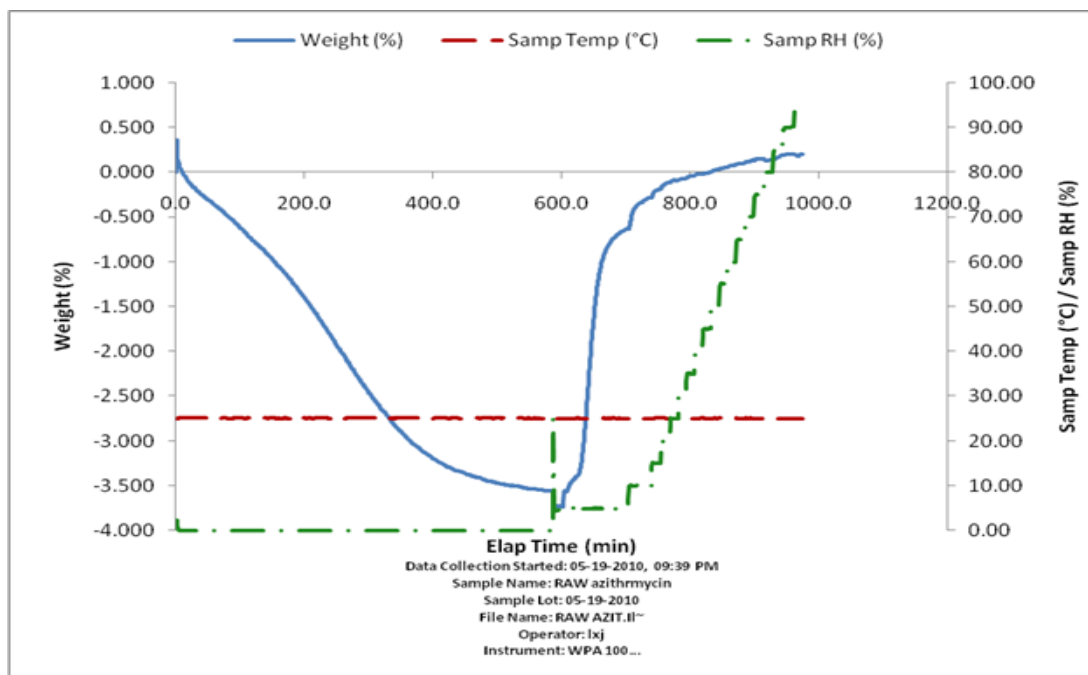


**Figure 4.28.** An experimental summary graph of water vapor sorption isotherms at 25°C for as received AZI.

#### **4.4.4.2 Two-component System**

##### **4.4.4.2.1 Spray-dried Drug:Mannitol**

As similar to SD pure TOB, a possible lyotropic-induced crystallization was observed for TOB in TOB:MAN=1:0.5. However, the phase transition shifted from 65% RH (SD pure TOB) to 70% RH (TOB:MAN=1:0.5). There was no evident phase transition observed for AZI:MAN=1:0.5.

##### **4.4.4.2.2 Spray-dried Drug:Phospholipids**

As similar to SD pure TOB, a possible lyotropic-induced crystallization was observed for TOB in TOB:PLS at 70% RH. No evident lyotropic-induced phase transition was observed for AZI:PLS.

##### **4.4.4.3 Three-component System (Spray-dried Drug:Phospholipids:Mannitol)**

With incorporation of MAN to drug:PLS, drug:PLS:MAN exhibited similar water vapor sorption profiles to the corresponding drug:PLS.

#### **4.4.5 Chemical Spectroscopy**

Uniformity in physical form for and homogeneity of multi-component systems are essential for physical stability or even drug content uniformity of SD dry powder formulations. Therefore, Confocal Raman microscopy (CRM) with non-invasive and non-destructive analysis is employed to examine the SD powders. Infrared spectroscopy yields similar, but complementary, information to Raman spectroscopy. It probes the degree of molecular order and polymorphic system.

##### **4.4.5.1 Confocal Raman Microscopy and Spectroscopy for Chemical Imaging and Mapping**

CRM analysis of SD pure TOB (Figure 4.17) and SD pure AZI (Figure 4.18) particles showed no sign of heterogeneity in physical form. The data suggest there was no presence of any crystalline phase in SD powder. Therefore, it may be consistent with the hypothesis put forth in the DSC studies that SD pure drug was amorphous rich. As to TOB:MAN=1:0.5 (Figure 4.19) and AZI:MAN=1:0.5 (Figure 4.20) particles, CRM analysis suggested no evidence of heterogeneity between the two components in SD binary mixture.

##### **4.4.5.2 Attenuated Total Reflectance-Fourier Transform Infrared Spectroscopy**

FTIR data may suggest that the crystal structure was absent in SD pure TOB (Figure 4.21a and 4.21b) and SD pure AZI (Figure 4.21c) as the vibration of several chemical bonds (TOB: O-H stretching; AZI: O-H and C-O stretching) changed after spray drying. This is in agreement with XRPD and DSC data.

Shown in FTIR data (Figure 4.22), no significant interaction between antibiotic drug and MAN is suggested as peak shifts were not observed. In addition, although CRM

analysis suggested no evidence of heterogeneity, FTIR data indicated that AZI:MAN=1:0.5 and 1:1 may possibly possess relatively more characteristic of crystalline AZI than other molar ratios. The unique characteristic was also supported by DSC data.

#### 4.5 Conclusions

Physicochemical properties of spray-dried powders were characterized by a variety of techniques. In general, the spray-dried powders without incorporation of phospholipids were lacking of long-range molecular order or exhibited as an amorphous solid. With incorporation of phospholipids, the spray-dried powders retained phospholipid bilayer structure. However, the extent of phospholipid bilayer structure was mainly dependent on the antibiotic drug in formulations. The other component(s) in phospholipids-incorporated formulations were lacking in long-range molecular order or exhibited as amorphous solid. The majority of spray-dried powders showed low water content. In contrast to spray-dried azithromycin formulations, the lyotropic-induced phase transition in spray-dried tobramycin formulation may indicate a physical stability or even potential chemical stability issue and aerosol dispersion at high relative humidity conditions. Overall, no evident sign of heterogeneity and presence of significant amount of crystalline phase in spray-dried pure drug and drug:mannitol were observed by chemical spectroscopy.

Portions of Chapter 4 were reproduced with kind permission from: Li, X, Vogt, F.G., Hayes, D. Jr., and Mansour, H.M. Physicochemical Characterization and Aerosol Dispersion Performance of Organic Solution Advanced Spray Dried Microparticulate/Nanoparticulate Antibiotic Dry Powders of Tobramycin and Azithromycin for Pulmonary Inhalation Aerosol Delivery. *European Journal of Pharmaceutical Sciences*, 2014, 15:191-205. Copyright © 2014 Elsevier.

## Chapter 5 *in vitro* Aerosol Dispersion

### 5.1 Introduction

Inertial impactors have been employed to characterize pharmaceutical aerosol formulations for several decades. The results of inertial impactors often correlate with particle deposition within the human lungs. Several apparatuses are documented in the European and United States Pharmacopoeias (USP), such as twin-stage liquid impinger (TSLI), Anderson cascade impactor (ACI), and the next generation impactor (NGI). The principle of inertial impaction for aerodynamic sizing is based on the aerodynamic behavior of aerosol particles, as shown by a cascade inertial impactor in Figure 5.1. When the direction of an air flow changes, the entrained particles in air continue to move in the original direction of flow until they lose inertia as a result of friction with air[5]. A plate is placed to collect particles in the path of the original direction of air flow. The larger particles impact the plate, while the smaller particles relax into a new direction of flow without being collected. With well-defined design and geometry of each impactor or impinge, the collection efficiency on each collection stage is dependent on air flow rate and dry powder inhaler (DPI) device employed.

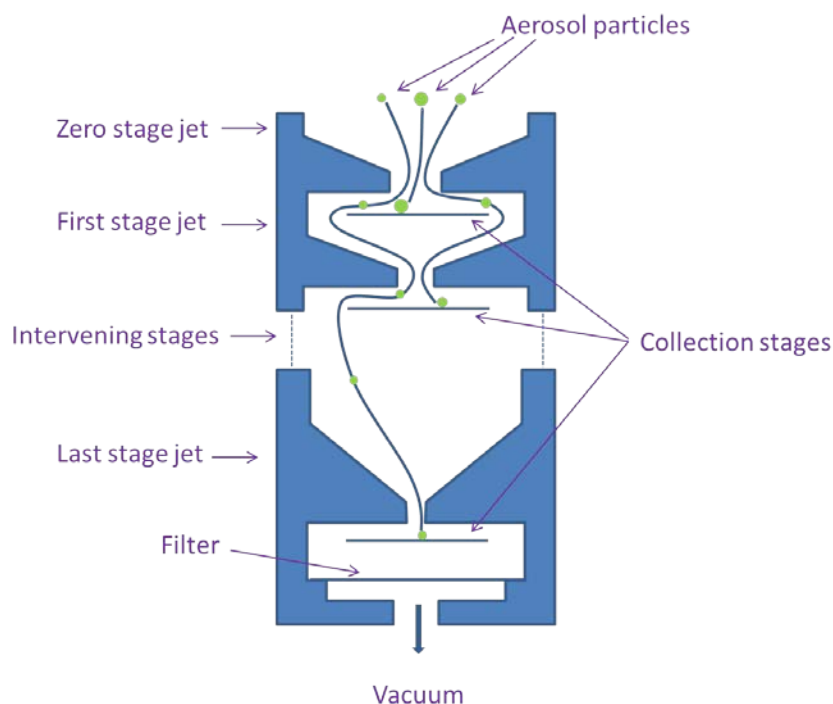


**Figure 5.1.** Schematic representation of the principle of inertial impaction for cascade inertial impactors. Adapted from [178].

In the present study, the NGI is employed for *in vitro* aerosol dispersion performance of spray-dried (SD) particles. As reported, it has been extensively utilized for pulmonary aerosol formulations[179, 180]. The design and assembly of the NGI is shown in Figure 5.2. The induction port (Figure 5.2a) is used to connect the impactor

to a DPI inhaler. The pre-separator (Figure 5.2a) connects between the induction port and the impactor. When necessary, with dry powder inhalers (DPIs), a pre-separator can be added to avoid overloading the first stage and is used with lactose carrier DPI systems. In addition, a suitable mouthpiece adapter is used to provide an airtight seal between the DPI inhaler and the induction port.[178] The NGI is designed with seven stages and a micro-orifice collector (MOC) as shown in Figure 5.2b. It is stated that “over the design flow rate range of 30 to 100 L/minute, the 50% efficiency aerodynamic cutoff diameters of the stages ( $D_{50}$  values) range between  $0.24\mu\text{m}$  to  $11.7\mu\text{m}$ , evenly spaced on a logarithmic scale”[178]. Several removable impaction cups (Figure 5.2b) are placed in one plane on the NGI.[178] The NGI has more collection stages than the TLSI[181] and is easier to use than the ACI[182]. In addition, “the collection efficiency curves for each stage are sharp and minimize overlap between stages”[178] is well known for the NGI. Therefore, the NGI allows a high resolution of particle deposition with an easy operation.

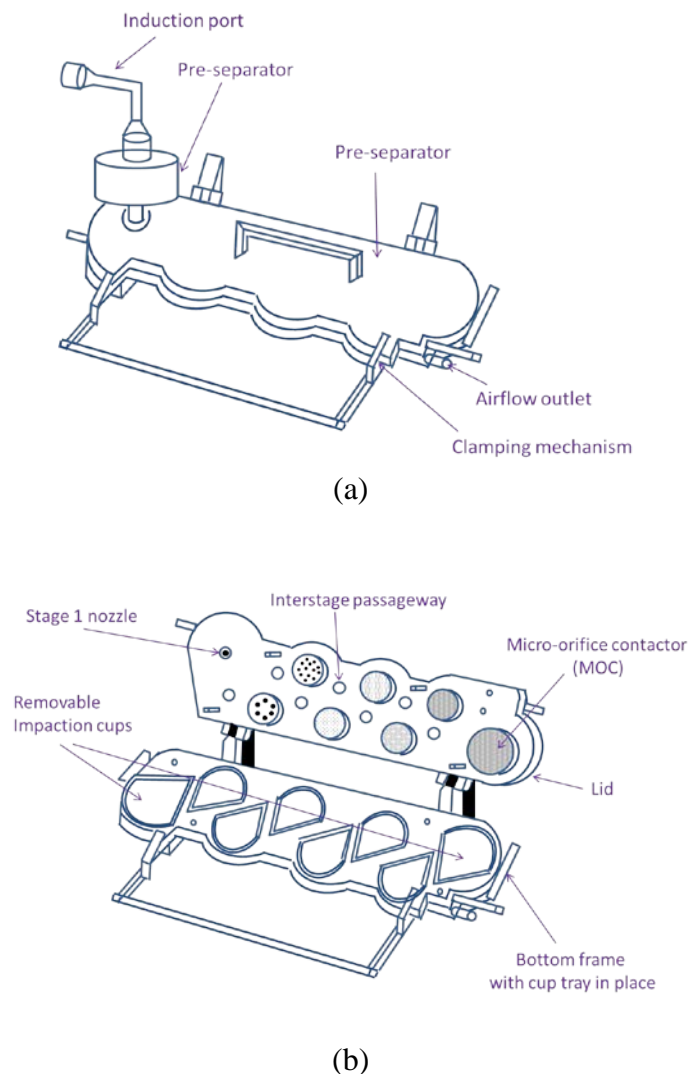


**Figure 5.2.** Closed (operating) condition (a) with pre-separator and internal construction (b) of the next generation impactor. Adapted from [178].

The deposition patterns of spray-dried (SD) particles are assessed by employing the NGI. The NGI data could allow the correlation of particle deposition on stages with various locations in human lungs based on aerodynamic size. In addition, the various aerosol dispersion performance parameters would be able to assess the ability and efficiency of aerosol penetration of SD particles to the deep lung regions.

## 5.2 Materials and Methods

### 5.2.1 Materials

The fresh spray-dried (SD) particles prepared as outlined in Chapter 4 for *in vitro* aerosol dispersion performance study are listed in Table 5.1. TOB, AZI, MAN, and PLS stand for tobramycin, azithromycin, mannitol, and phospholipids, respectively. All the studied particles were generated employing a 50% pump rate during spray drying. The outlet temperatures of SD particles are referred to Table 3.1 and Table 3.2 in Chapter 3. HP clear, size 3 capsule (Quali-V®) was received from Qualicaps (Spain).

**Table 5.1.** SD particles for the NGI study.

Formulation System	SD TOB formulations (molar ratio)	SD AZI formulations (molar ratio)
One-component	Pure TOB	Pure AZI
Two-component	TOB:MAN=1:0.1	AZI:MAN=1:0.1
	TOB:MAN=1:0.5	AZI:MAN=1:0.5
	TOB:MAN=1:1	AZI:MAN=1:1
	TOB:PLS=1:0.5	AZI:PLS=1:0.5
	TOB:PLS=1:1	AZI:PLS=1:1
	TOB:PLS=1:2	AZI:PLS=1:2
Three-component	TOB:PLS:MAN=1:0.5:0.1	AZI:PLS:MAN=1:0.5:0.1
	TOB:PLS:MAN=1:0.5:0.5	AZI:PLS:MAN=1:0.5:0.5
	TOB:PLS:MAN=1:0.5:1	AZI:PLS:MAN=1:0.5:1

### 5.2.2 Methods

#### 5.2.2.1 Mass Analysis

In accordance with USP Chapter <601> specifications[178], the aerosol dispersion performance of the dry powder formulations were determined using the NGI (Model 170, MSP Corporation, Shoreview, Minnesota) equipped with a stainless steel induction port (i.e. USP throat; MSP Corporation, Shoreview, Minnesota), stainless steel NGI gravimetric insert cups (MSP Corporation, Shoreview, Minnesota) and the HandiHaler® (a DPI device with high shear stress; Boehringer Ingelheim Pharmaceuticals, Germany). The NGI was coupled to a Copley HCP5 vacuum pump (Copley Scientific, United Kingdom), and a Copley TPK 2000 critical flow controller (Copley Scientific, United Kingdom). Airflow rate was adjusted before each



experiment by a Copley DFM 2000 flow meter (Copley Scientific, United Kingdom). The NGI experiment was run at a controlled airflow rate at Q=60 L/min (adult air flow rate) with a delay time of 10 seconds. Each HP clear, size 3 capsule contained 10mg SD powders. To start the experiment, the capsule was pierced by pins in the HandiHaler®. Powder in capsule was pulled out by the flow of air and deposited on stages in the NGI. The mass of powder deposited on each stage was quantified by a gravimetric method employing type A/E glass fiber filters with diameter 55mm (PALL Corporation, NY). *In vitro* aerosolization was evaluated in triplicate under normal lab conditions. Three capsules were used in each experiment. The aerosolization experiment was randomized by Design Expert™ 8.0.7.1 software (Stat-Ease Corp., MN).

For the NGI with Q=60 L/min, the effective aerodynamic cutoff diameter for each impactor stage was calibrated by the manufacturer and stated as: stage 1, 8.06µm; stage 2, 4.46µm; stage 3, 2.82µm; stage 4, 1.66µm; stage 5, 0.94µm; stage 6, 0.55µm; stage 7, 0.34µm. Emitted dose fraction (ED[%]; Equation 5.1) is determined as the percentage powder mass emitted from capsules relative to the total dose in capsules (TD). Emitted dose (ED) includes the sum of the powder mass left on inhaler device, USP throat, and deposited on the NGI stages. Fine particle fraction (FPF[%]; Equation 5.2) is expressed as a percentage of fine particle dose (FPD) to ED. FPD is defined as the dose deposited on stage 2 and later stages (3-7). Respirable fraction (RF[%]; Equation 5.3) is defined as the percentage of FPD to deposited dose (DD). Deposited dose (DD) is defined as the dose deposited on all stages.

$$\text{Emitted dose fraction (ED[\%])} = \frac{\text{ED}}{\text{TD}} \times 100\% \quad (\text{Equation 5.1})$$

$$\text{Fine particle fraction (FPF[\%])} = \frac{\text{FPD}}{\text{ED}} \times 100\% \quad (\text{Equation 5.2})$$

$$\text{Respirable fraction (RF[\%])} = \frac{\text{FPD}}{\text{DD}} \times 100\% \quad (\text{Equation 5.3})$$

In addition, mass median aerodynamic diameter (MMAD) of aerosol particles and geometric standard deviation (GSD) of the distribution are determined based on a log-probability distribution (particle size vs particle deposition percentage) obtained from the NGI data. The MMAD and GSD values were computed by using Mathematica (Wolfram Research Inc., Champaign, IL), a calculation program written by Dr. Warren Finlay[183].

#### 5.2.2.2 Method validation of Chemical Analysis

As indicated above, the particle deposition pattern on the various stages of the NGI are evaluated gravimetrically. In one set of experiments, the amount of AZI deposited on each stage was examined by chemical analysis using high performance liquid chromatogram (HPLC). To that end, a standard AZI solution with concentration of ~1000 ug/mL (in methanol) was used to assess possible drug adsorbance on the glass filter to be placed on the NGI stages. Two treatment groups (a and b) with glass filter were compared with the control group:

a) In the first treatment experiment, the glass filter was soaked in 5mL of standard AZI solution for ~1h;

b) In the second treatment experiment, the first step is that the glass filter was soaked in 5mL of standard AZI solution for ~1h in vial A. The solution (3mL) in the vial A with soaked glass filter was collected into a new vial B. The second step is that 10mL solvent (methanol) was added to wash off the possible adsorbed AZI on soaked glass filter in vial A. Eventually, a total 13mL solution was collected in vial B.

The two solutions from two treatment experiments (a and b) were passed through polytetrafluoroethylene (PTFE) syringe filter (organic solvent resistant, 0.22 $\mu$ m pore size; Tisch Scientific, USA) to remove any residual fiber before injecting into HPLC for AZI concentration determination. The details of validated HPLC analysis is reported in Section 6.3.1.1 in Chapter 6.

## **5.3 Results**

### **5.3.1 One-component System (Spray-dried Pure Drug)**

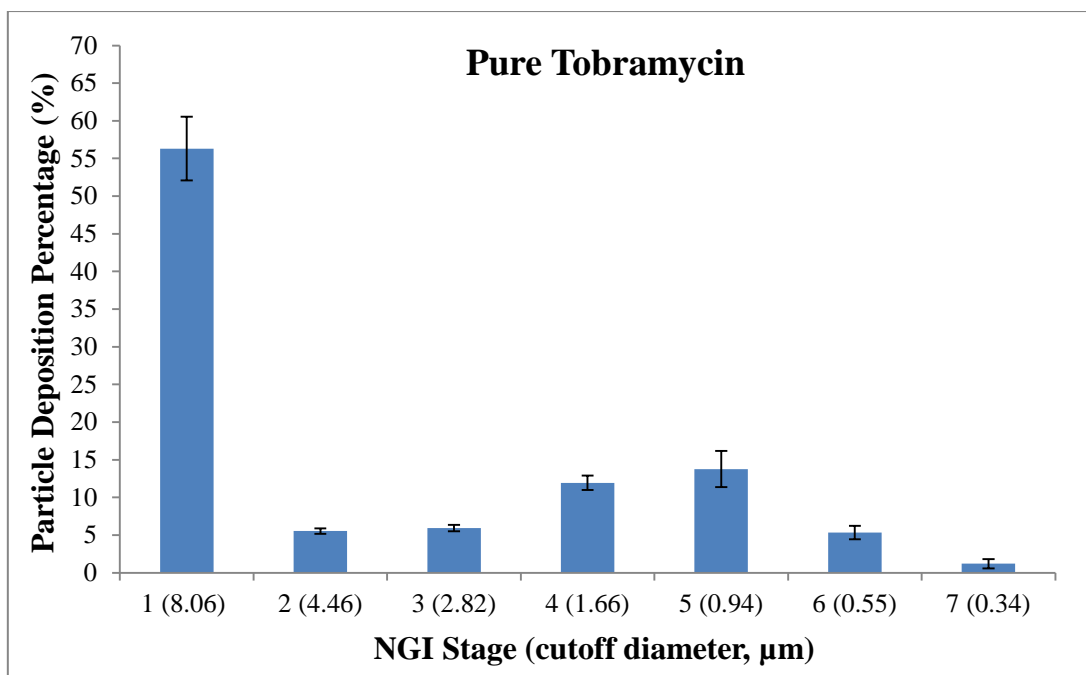
Aerosol dispersion performance results of spray-dried (SD) pure TOB[43] and AZI[43] aerosols on each stage of the NGI from the HandiHaler<sup>®</sup> under Q of 60 L/min is shown in Figure 5.3a and 5.3b, respectively. As indicated in Figure 5.3, the particle deposition profiles of SD pure TOB and SD pure AZI powders differed markedly.

#### **5.3.1.1 SD Pure TOB**

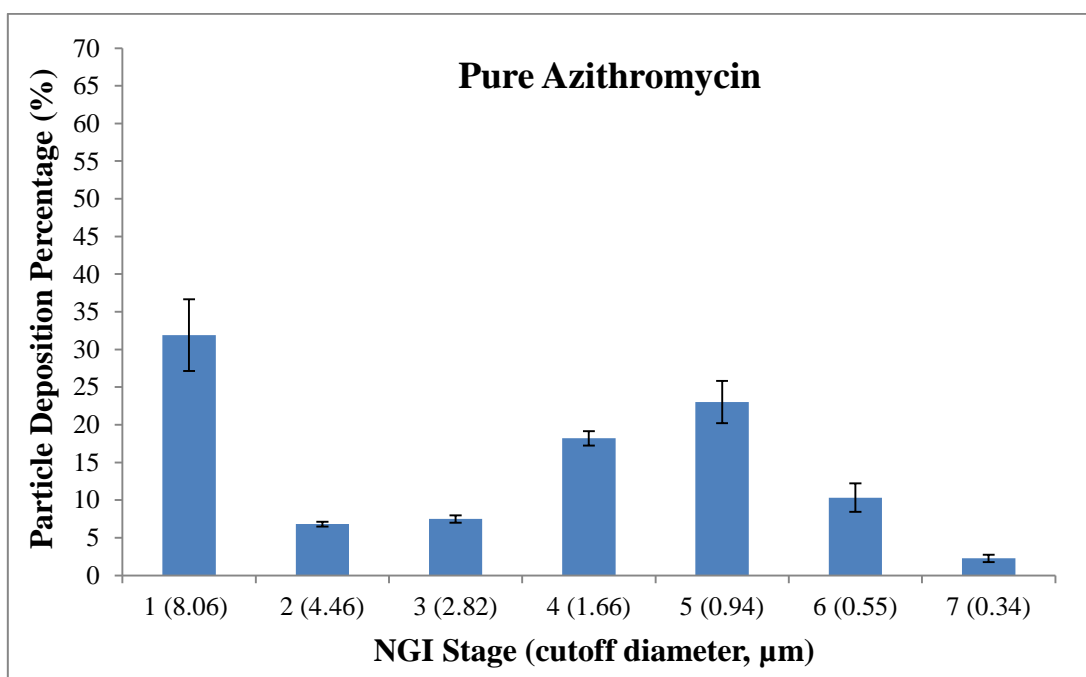
SD pure TOB aerosols exhibited predominant particle deposition on stage 1 (aerodynamic cutoff diameter of 8.06 $\mu$ m) and low particle deposition on later stages (2-7; aerodynamic cutoff diameter < 5 $\mu$ m)[43]. A majority of fine particle mass was observed on stage 4 (aerodynamic cutoff diameter of 1.66 $\mu$ m) and stage 5 (aerodynamic cutoff diameter of 0.94 $\mu$ m). The deposition mode of fine particle dose (FPD) was on stage 5. As indicated in Table 5.2[43], the SD pure TOB aerosols showed 96.2%, 28.5%, and 43.7% for ED, FPF, and RF, respectively. The values of MMAD and GSD were 5.0 $\mu$ m and 3.3, respectively. Therefore, it may be concluded that SD pure TOB aerosols possessed an ability to penetrate into deep lung regions (MMAD  $\leq$  5 $\mu$ m)[64].

#### **5.3.1.2 SD Pure AZI**

In contrast to SD pure TOB aerosols, SD pure AZI aerosols showed a relatively lower deposition on stage 1, and higher depositions on later stages (2-7)[43]. Similarly, SD pure AZI aerosolized particles exhibited a majority of fine particle mass on stage 4 and stage 5. The deposition mode of fine particle dose (FPD) was on stage 5. The detailed aerosol dispersion performance parameters are listed in Table 5.2[43]. The SD pure AZI aerosols exhibited 90.3%, 47.0%, and 68.1% for ED, FPF, and RF, respectively. With MMAD and GSD being 2.3 $\mu$ m and 2.3, respectively, it suggests that SD pure AZI particles were suitable for deep lung delivery (MMAD  $\leq$  5 $\mu$ m)[64].



(a)



(b)

**Figure 5.3.** Aerosol dispersion performance using the NGI under an airflow rate (Q) of 60 L/min with the HandiHaler® DPI device for: (a) SD pure tobramycin powder; and (b) SD pure azithromycin powder (mean  $\pm$  SD, n=3)[43].

**Table 5.2.** Aerosol dispersion performance parameters of SD pure tobramycin and SD pure azithromycin dry powders[43] (mean  $\pm$  margin of error for 95% confidence, n=3).

SD Pure Drug	Aerosol Dispersion Performance Parameters				
	ED[%]	FPF[%]	RF[%]	MMAD[ $\mu$ m]	GSD
TOB	96.2 $\pm$ 0.6	28.5 $\pm$ 3.8	43.7 $\pm$ 4.8	5.0 $\pm$ 1.2	3.3 $\pm$ 0.6
AZI	90.3 $\pm$ 6.7	47.0 $\pm$ 3.7	68.1 $\pm$ 5.4	2.3 $\pm$ 0.4	2.3 $\pm$ 0.2

### 5.3.2 Two-component System (Spray-dried Drug:Mannitol and Drug:Phospholipids)

#### 5.3.2.1 Spray-dried Drug:Mannitol

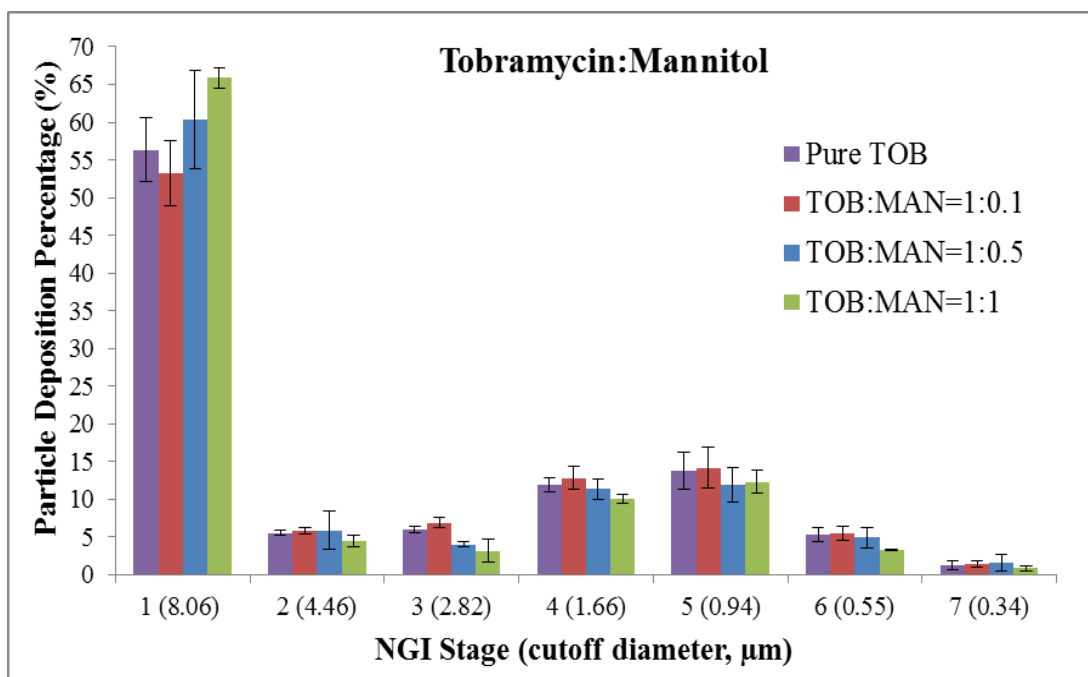
Particle deposition profiles for SD TOB:MAN[143] and AZI:MAN[143] are shown in Figure 5.4a and 5.4b, respectively. The particle deposition of corresponding SD pure drug is plotted in each figure. SD TOB:MAN and SD AZI:MAN exhibited similar deposition patterns to the corresponding SD pure drug.

##### 5.3.2.1.1 SD TOB:MAN

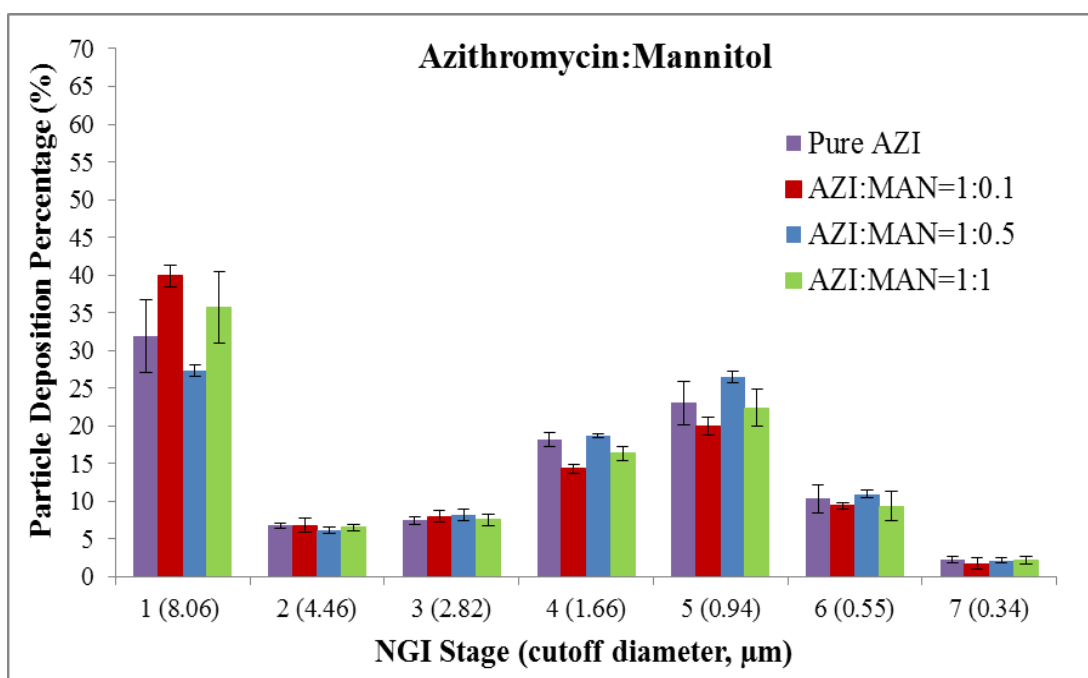
SD TOB:MAN aerosols showed a relatively higher particle deposition percentage on stage 1 with an average of approximately 60%, compared to particle depositions on later stages (2-7)[143]. The deposition modes of FPD for SD TOB:MAN aerosol powders were on stage 5. As indicated in Table 5.3[143], SD TOB:MAN aerosol powders exhibited 90.7% or higher, 15.4% or higher, and 34.2% or higher for ED, FPF, and RF, respectively. The MMAD and GSD values ranged from 4.6 to 7.0 $\mu$ m, and 3.2 to 3.8, respectively. Therefore, the data indicate that only TOB:MAN=1:0.1, with a MMAD value less than 5 $\mu$ m, could be able to penetrate into deep lung regions[64].

##### 5.3.2.1.2 SD AZI:MAN

Aerosol dispersion performance of SD AZI:MAN exhibited a relatively lower particle deposition on stage 1 with approximately 37%, compared to SD TOB:MAN aerosols[143]. The majority of mass of FPD were on stage 4 and 5. The deposition modes of FPD for SD AZI:MAN aerosol powders were on stage 5. Shown in Table 5.4[143], ED, FPF, and RF of SD AZI:MAN were 88.1% or higher, 38.3% or higher, and 60.1% or higher, respectively. In addition, the aerosols showed MMAD and GSD values ranging from 2.0 to 2.7 $\mu$ m, and 2.1 to 2.5, respectively. These data suggest that AZI:MAN aerosol powders were suitable for deep lung penetration[64].



(a)



(b)

**Figure 5.4.** Aerosol dispersion performance using the NGI under an airflow rate ( $Q$ ) of 60 L/min with the HandiHaler<sup>®</sup> DPI device for: (a) tobramycin:mannitol powders; and (b) azithromycin:mannitol powders (mean  $\pm$  SD,  $n=3$ )[143].

**Table 5.3.** Aerosol dispersion performance parameters of SD tobramycin:mannitol particles[143] (mean  $\pm$  margin of error for 95% confidence, n=3).

System	Molar Ratio	Aerosol Dispersion Performance Parameters				
		ED[%]	FPF[%]	RF[%]	MMAD[ $\mu$ m]	GSD
TOB:MAN	1:0.1	96.9 $\pm$ 0.4	28.7 $\pm$ 1.8	46.8 $\pm$ 4.9	4.6 $\pm$ 1.0	3.2 $\pm$ 0.5
	1:0.5	90.7 $\pm$ 7.5	25.0 $\pm$ 3.6	39.6 $\pm$ 7.4	6.1 $\pm$ 1.8	3.8 $\pm$ 0.2
	1:1	98.7 $\pm$ 0.7	15.4 $\pm$ 2.9	34.2 $\pm$ 1.5	7.0 $\pm$ 0.5	3.7 $\pm$ 0.2

**Table 5.4.** Aerosol dispersion performance parameters of SD azithromycin:mannitol particles[143] (mean  $\pm$  margin of error for 95% confidence, n=3).

System	Molar Ratio	Aerosol Dispersion Performance Parameters				
		ED[%]	FPF[%]	RF[%]	MMAD[ $\mu$ m]	GSD
AZI:MAN	1:0.1	92.0 $\pm$ 3.2	38.3 $\pm$ 0.8	60.1 $\pm$ 1.6	2.7 $\pm$ 0.2	2.5 $\pm$ 0.1
	1:0.5	88.1 $\pm$ 1.5	46.4 $\pm$ 1.1	72.7 $\pm$ 0.8	2.0 $\pm$ 0.1	2.1 $\pm$ 0.1
	1:1	91.9 $\pm$ 1.5	43.3 $\pm$ 2.3	64.3 $\pm$ 5.3	2.5 $\pm$ 0.5	2.4 $\pm$ 0.3

### 5.3.2.2 Spray-dried Drug:Phospholipids

Particle deposition profiles for SD TOB:PLS and AZI:PLS aerosols are shown in Figure 5.5a and 5.5b, respectively. In addition, the particle deposition of corresponding SD pure drug is plotted in each figure.

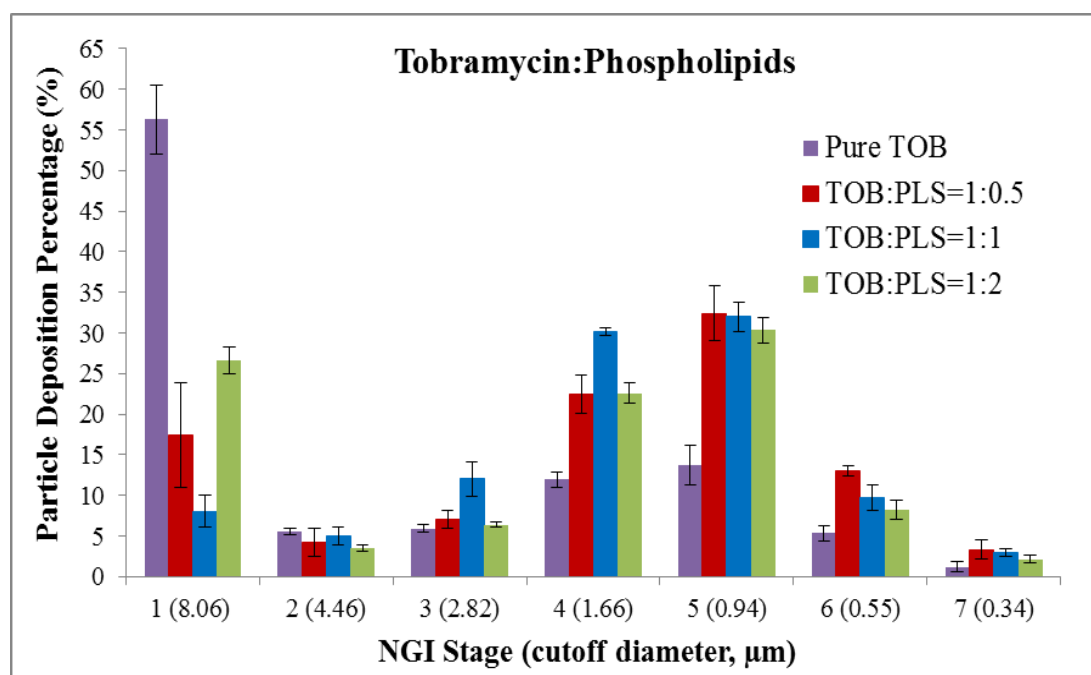
#### 5.3.2.2.1 SD TOB:PLS

As shown in Figure 5.5a, the aerosol particle deposition profiles of TOB:PLS were greatly improved as compared to SD pure TOB. Upon incorporation of phospholipids, the powders exhibited a sharply lowered deposition on stage 1 (from approximately 55% to 17%), and, therefore, enhanced depositions on later stages (2-7). The deposition modes of FPD were on stage 5 for TOB:PLS aerosols. Shown in Table 5.5, TOB:PLS aerosols showed 87.4% or higher, 41.7% or higher, and 73.3% or higher for ED, FPF, and RF, respectively. The MMAD for TOB:PLS aerosols ranged from 1.7 to 2.0 $\mu$ m. The GSD remained constant at 1.9. Therefore, TOB:PLS particles were possibly suitable to be delivered to deep lung regions[64].

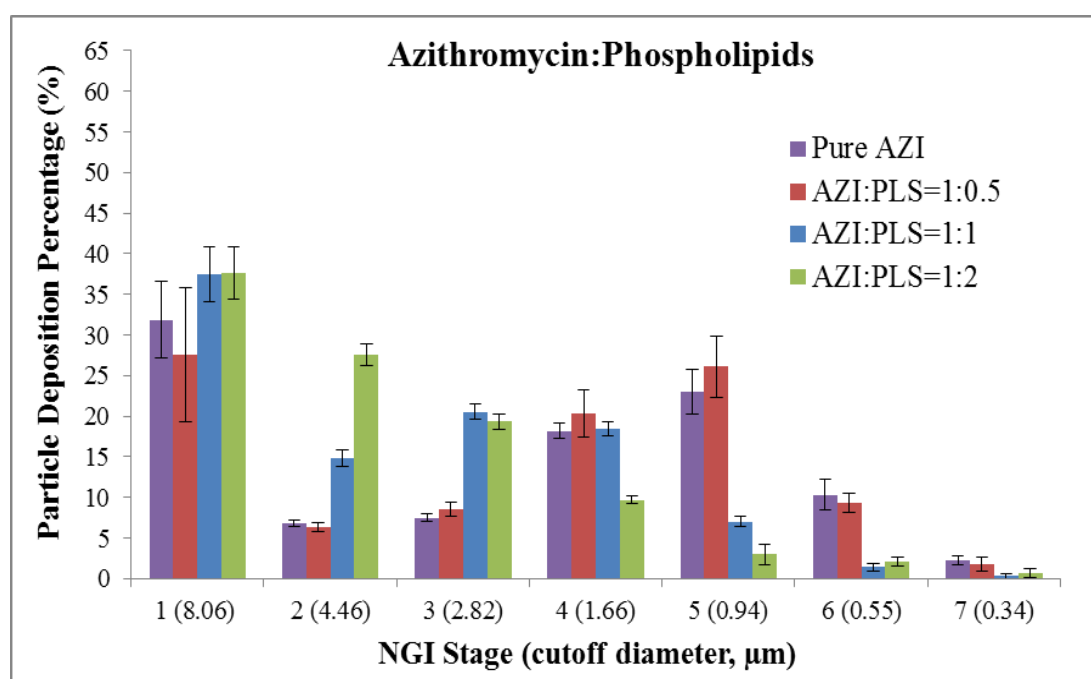
#### 5.3.2.2.2 SD AZI:PLS

AZI:PLS aerosols appeared to have relatively similar deposition on stage 1 compared to SD pure AZI. Deposition modes of FPD of AZI:PLS were dependent on the composition of formulations. As phospholipids molar ratio increased from 1:0.5, to 1:1, and to 1:2, the deposition mode of FPD shifted from stage 5, to stage 3, and to stage 2. As to AZI:PLS aerosols in Table 5.6, the values of ED, FPF, and RF were 95.1% or higher, 27.1% or higher, and 62.4% or higher, respectively. As suggested by particle deposition patterns, the MMAD varied with the composition of AZI:PLS. The MMAD values of the aerosols shifted from 2.2 $\mu$ m, to 4.7 $\mu$ m, and to 6.7 $\mu$ m as the molar ratio changed from 1:0.5, to 1:1, and to 1:2, respectively. The GSD values were

from 2.1 to 2.5. The data suggest that AZI:PLS=1:0.5 and 1:1 aerosol powders would be expected to reach the deep lung regions[64].



(a)



(b)

**Figure 5.5.** Aerosol dispersion performance using the NGI under an airflow rate ( $Q$ ) of 60 L/min with the HandiHaler<sup>®</sup> DPI device for: (a) tobramycin:phospholipids powders; and (b) azithromycin:phospholipids powders (mean  $\pm$  SD,  $n=3$ ).

**Table 5.5.** Aerosol dispersion performance parameters of SD tobramycin:phospholipids particles (mean  $\pm$  margin of error for 95% confidence, n=3).

System	Molar Ratio	Aerosol Dispersion Performance Parameters				
		ED[%]	FPF[%]	RF[%]	MMAD[ $\mu$ m]	GSD
TOB:PLS	1:0.5	86.9 $\pm$ 1.1	47.4 $\pm$ 3.8	82.5 $\pm$ 7.3	1.7 $\pm$ 0.1	1.9 $\pm$ 0.1
	1:1	87.4 $\pm$ 2.0	61.9 $\pm$ 6.3	91.9 $\pm$ 2.3	1.9 $\pm$ 0.1	1.9 $\pm$ 0.1
	1:2	95.9 $\pm$ 0.8	41.7 $\pm$ 2.8	73.3 $\pm$ 1.9	2.0 $\pm$ 0.1	1.9 $\pm$ 0.1

**Table 5.6.** Aerosol dispersion performance parameters of SD azithromycin:phospholipids particles (mean  $\pm$  margin of error for 95% confidence, n=3).

System	Molar Ratio	Aerosol Dispersion Performance Parameters				
		ED[%]	FPF[%]	RF[%]	MMAD[ $\mu$ m]	GSD
AZI:PLS	1:0.5	95.1 $\pm$ 1.2	37.4 $\pm$ 4.0	72.4 $\pm$ 9.3	2.2 $\pm$ 0.3	2.1 $\pm$ 0.3
	1:1	97.8 $\pm$ 0.8	36.4 $\pm$ 1.8	62.6 $\pm$ 3.8	4.7 $\pm$ 0.3	2.2 $\pm$ 0.1
	1:2	95.1 $\pm$ 1.5	27.1 $\pm$ 1.8	62.4 $\pm$ 3.6	6.7 $\pm$ 0.5	2.5 $\pm$ 0.2

### 5.3.3 Three-component System (Spray-dried Drug:Phospholipids:Mannitol)

Particle deposition profiles for SD TOB:PLS:MAN and SD AZI:PLS:MAN aerosols are shown in Figure 5.6a and 5.6b, respectively. The particle deposition of corresponding SD formulation of drug with phospholipids is plotted in each figure.

#### 5.3.3.1 SD TOB:PLS:MAN

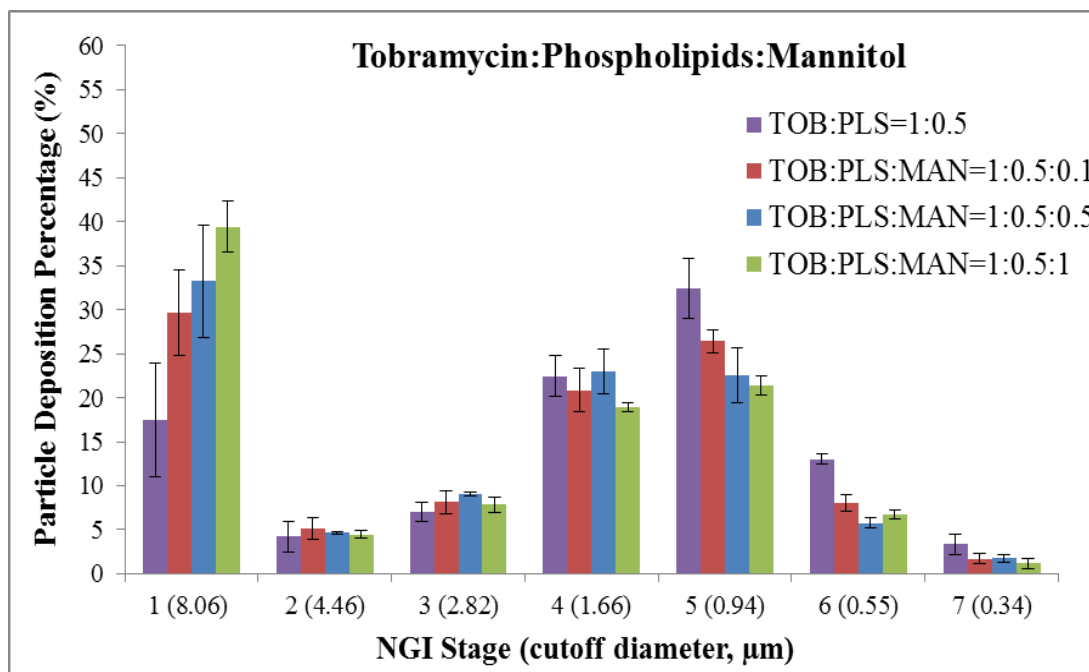
The addition of mannitol to TOB:PLS increased particle deposition on stage 1 from ~17% to 34%. The deposition modes of FPD of TOB:PLS:MAN aerosols were on either stage 4 or 5. Shown in Table 5.7, ED, FPF, and RF values for TOB:PLS:MAN were 91.7% or higher, 38.1% or higher, and 60.6% or higher, respectively. The MMAD and GSD of the aerosols ranged from 2.2 to 2.7 $\mu$ m, and 2.0 to 2.2, respectively. All TOB:PLS:MAN aerosol powders were suitable for penetration into the deep lungs[64].

#### 5.3.3.2 SD AZI:PLS:MAN

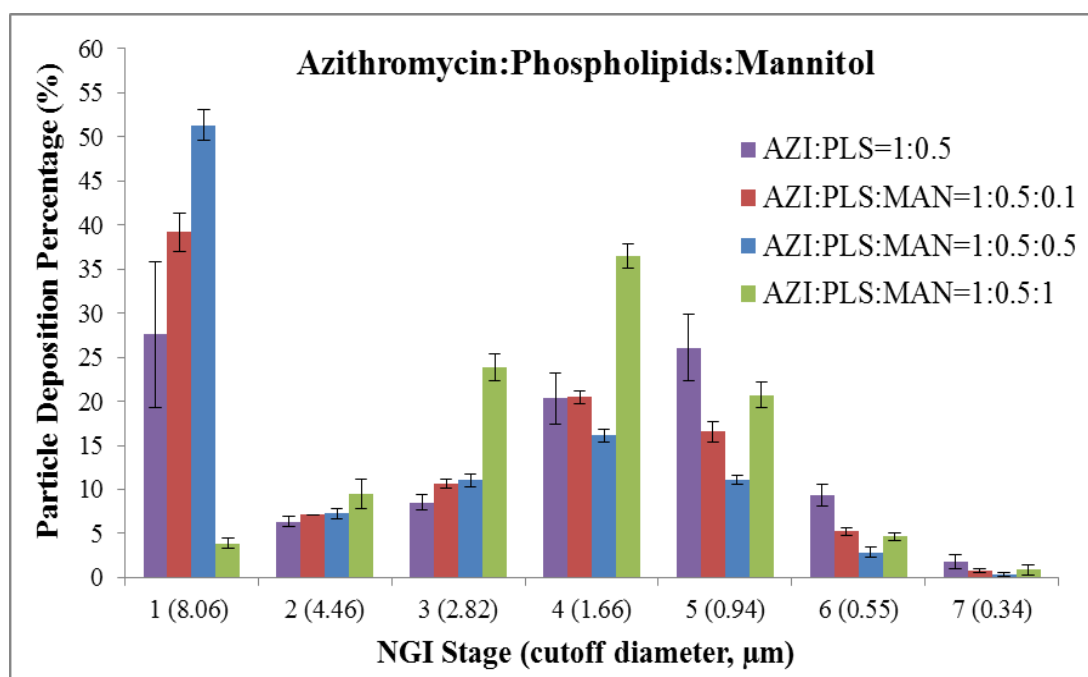
The effect of mannitol incorporation to AZI:PLS was more complicated. The powders of AZI:PLS:MAN=1:0.5:0.1 and 1:0.5:0.5 exhibited an increased deposition on stage 1 with an average ~45%, as compared to ~28% from two-component formulation of AZI:PLS=1:0.5. Interestingly, further increase of mannitol content to 1:0.5:1 in molar ratio of AZI:PLS:MAN highly lowered particle deposition to ~4% on stage 1. The deposition modes of FPD were on stage 4. The values of ED, FPF, and RF for AZI:PLS:MAN were 94.3% or higher, 32.6% or higher, and 48.6% or higher, respectively, as shown in Table 5.8. The MMAD and GSD values of AZI:PLS:MAN aerosols were from 2.4 to 4.9 $\mu$ m, and 1.8 to 2.7, respectively. It is noticeable that AZI:PLS:MAN=1:0.5:1 showed superior aerosol performance, in terms of FPF, RF, MMAD, and GSD, compared to the other two aerosol powder systems



(AZI:PLS:MAN=1:0.5:0.1 and AZI:PLS:MAN=1:0.5:0.5). The data suggest that AZI:PLS:MAN aerosolized powders are suitable to be delivered into deep lung regions[64].



(a)



(b)

**Figure 5.6.** Aerosol dispersion performance using the NGI under an airflow rate (Q) of 60 L/min with the HandiHaler<sup>®</sup> DPI device for: (a) tobramycin:phospholipids:mannitol powders; and (b) azithromycin:phospholipids:mannitol powders (mean  $\pm$  SD, n=3).

**Table 5.7.** Aerosol dispersion performance parameters of SD tobramycin:phospholipids:mannitol particles (mean  $\pm$  margin of error for 95% confidence, n=3).

System	Molar Ratio	Aerosol Dispersion Performance Parameters				
		ED [%]	FPF [%]	RF [%]	MMAD [ $\mu$ m]	GSD
TOB:PLS:MAN	1:0.5:0.1	91.7 $\pm$ 1.0	44.1 $\pm$ 5.2	70.3 $\pm$ 5.5	2.2 $\pm$ 0.2	2.0 $\pm$ 0.2
	1:0.5:0.5	93.0 $\pm$ 1.0	42.7 $\pm$ 4.3	66.8 $\pm$ 7.3	2.6 $\pm$ 0.4	2.1 $\pm$ 0.2
	1:0.5:1	93.1 $\pm$ 3.5	38.1 $\pm$ 1.0	60.6 $\pm$ 3.3	2.7 $\pm$ 0.2	2.2 $\pm$ 0.1

**Table 5.8.** Aerosol dispersion performance parameters of SD azithromycin:phospholipids:mannitol particles (mean  $\pm$  margin of error for 95% confidence, n=3).

System	Molar Ratio	Aerosol Dispersion Performance Parameters				
		ED [%]	FPF [%]	RF [%]	MMAD [ $\mu$ m]	GSD
AZI:PLS:MAN	1:0.5:0.1	96.4 $\pm$ 0.7	36.8 $\pm$ 2.4	60.8 $\pm$ 2.5	3.2 $\pm$ 0.3	2.3 $\pm$ 0.1
	1:0.5:0.5	96.7 $\pm$ 0.2	32.6 $\pm$ 0.7	48.6 $\pm$ 2.0	4.9 $\pm$ 0.3	2.7 $\pm$ 0.1
	1:0.5:1	94.3 $\pm$ 1.0	60.4 $\pm$ 2.3	96.1 $\pm$ 0.6	2.4 $\pm$ 0.1	1.8 $\pm$ 0.0

### 5.3.4 Validation of Gravimetric Analysis Method

An assumption made in the aerosol dispersion performance is that the mass distribution of deposited particles on the NGI stages is equal to chemical distribution. To validate this assumption for AZI, AZI:PLS=1:0.5 was selected as a representative sample. As a first step, a chemical analysis method must be validated. Two different treatments (a and b), detailed in Section 5.2.2.2, were conducted to determine the number of washing necessary to collect all AZI from the glass filter. As shown in Table 5.9, the total drug recoveries from the two glass filter washing treatments (a and b) were not statistically different from the control sample with values of 100.3% and 102.6%, respectively. This method validation indicated that there was no significant adsorbance of AZI on glass filter after one washing. Therefore, the first treatment method (a) was used to determine AZI mass deposited on each stage of the NGI in chemical analysis.

**Table 5.9.** The data for glass filter treatment experiment.

	Standard Solution	First Treatment (a)	Second Treatment (b)
Concentration ( $\mu$ g/mL)	1017.9	1021.0	401.5
Total Drug Recovery (%)	100.0	100.3	102.6

The AZI:PLS=1:0.5 powder was selected to conduct aerosol dispersion performance. By employing the glass filters, the mass of powder on each stage was determined by gravimetric method. Thereafter, the glass filter with captured particles on each stage was soaked in methanol with 10mL for stage 1 and 5mL for each of later stages (2-7). Sonication was applied to make sure all the particles were completely dissolved. After passing through PTFE syringe filter, the solution was injected into HPLC for concentration determination. The aerosolization experiment was conducted in triplicate. The data comparison between mass analysis and chemical analysis are presented in Figure 5.7. The results indicate that there was no significant difference in particle deposition on each NGI stage determined by the two analytical methods. Therefore, it was concluded that the gravimetric method was sufficient to assess the AZI component distribution on NGI stages for all studies. TOB formulations were not tested by this approach due to the lack of appropriate HPLC assay method.

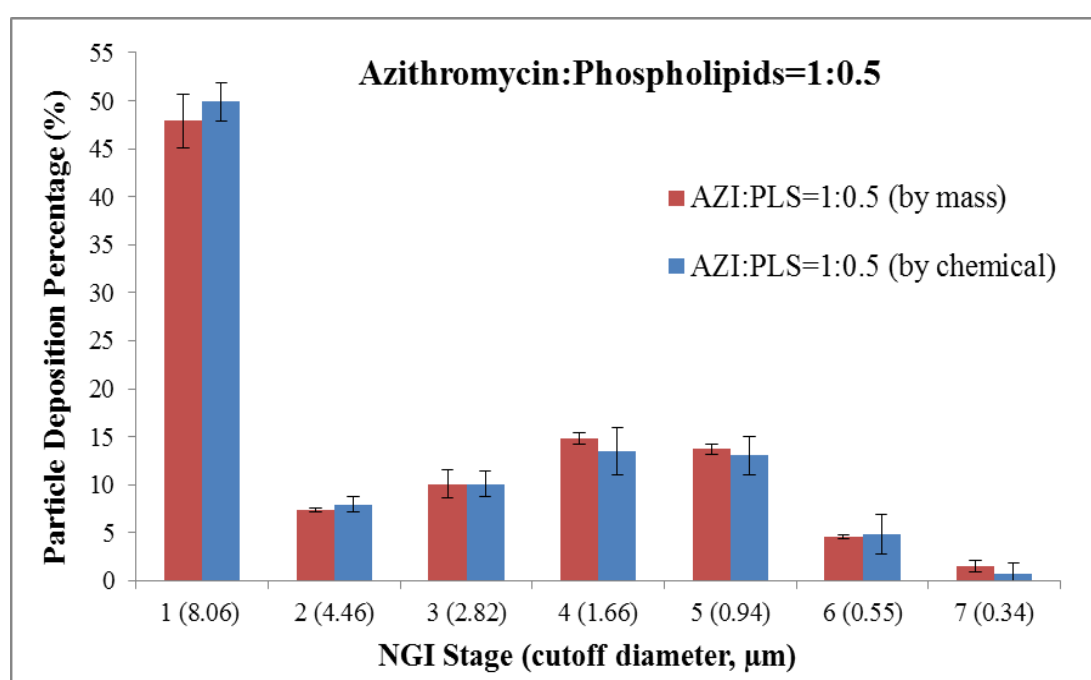


**Figure 5.7.** Aerosol dispersion performance using the NGI under an airflow rate (Q) of 60 L/min with the HandiHaler<sup>®</sup> DPI device for azithromycin:phospholipids=1:0.5. The particle deposition was determined by both weight and chemical analysis (mean  $\pm$  SD, n=3).

## 5.4 Discussion

It is well known that aerodynamic diameters below  $5\mu\text{m}$  are considered as the cutoff for particles capable of penetrating into deep lung regions[184]. The respiratory aerosol formulation with ability of deep lung (including respirable bronchiolar and alveolar regions) penetration is crucial for the treatment of lung diseases such as pneumonia[185], chronic lung infection with cystic fibrosis (CF)[134-136] or non-CF bronchiectasis[186, 187]. Therefore, we defined the sum of particles deposited on stage 2 and later of the NGI (cutoff aerodynamic diameter of  $< 4.51\mu\text{m}$ ) as the fine

particle dose.

Formulation composition may have critical impact on the efficiency of aerosol dispersion performance of the powder. Adler et al[188] reported that the surface composition for spray-dried multi-component powders (e.g. bovine serum albumin, trehalose, and surfactant (polysorbate 80)) was not identical to the overall formulation composition. Therefore, it can be argued that the interparticulate forces may be a function of surface composition[63]. More importantly, it is believed that particle aggregation is prevalent when components that exhibit high crystallization tendency or phase transitions are present on the surface. Obviously such a situation would potentially influence particle aerosol performance. Thus, the effect of composition on aerosol dispersion performance of the powder is discussed below.

#### **5.4.1 Effect of Mannitol on Spray-Dried Drug:Mannitol**

Compared to SD pure TOB, the aerosol dispersion performance of TOB:MAN were independent of mannitol at molar ratios of 1:0.1 and 1:0.5. For TOB:MAN=1:1, the FPF and RF decreased from 28.5% to 15.4%, and from 43.7% to 34.2%, respectively. On the other hand, ED and MMAD of TOB:MAN=1:1 increased, compared to SD pure TOB.

With other aerosol dispersion parameters statistically unchanged, only FPF and RF of AZI:MAN=1:0.1 were lowered from 47.0% to 38.3%, and 68.1% to 60.1%, respectively, compared to SD pure AZI. In comparison to SD pure AZI, aerosol dispersion performance parameters of AZI:MAN=1:0.5 and 1:1 were statistically unchanged.

In summary, based on the obtained aerosol dispersion performance parameters, spray drying drug with various amount of mannitol in drug:mannitol did not appear to improve the aerosol dispersion performance. Lactose is reported to exhibit surface enrichment supported by the formation of a hollow particle at relatively high inlet temperature[189-191]. It is reported[192] that due to the mannitol crystallization in spray-dried recombinant humanized anti-IgE monoclonal antibody (rhuMAbE25):mannitol upon storage, the particles exhibited a significant decrease in FPF. As shown in our previous study[44], mannitol has a high tendency to crystallize after spray drying under these conditions for SD pure mannitol powders. XRPD (Figure 4.2 in Chapter 4) and DSC (Figure 4.7-4.9 in Chapter 4) data did not reveal any evidence of crystalline mannitol in the SD drug:mannitol powders. However, it is possible that the small amount of mannitol, not detected by the techniques employed, on particle surface could be present in the crystalline phase for SD drug:mannitol powders. Even if the mannitol component was initially in the amorphous phase, the low glass transition temperature of mannitol (e.g., 7.4 °C determined from quench-cooled mannitol without additives in DSC at 5°C/min)[193] suggests a high risk of crystallization of mannitol during aerosol dispersion experiments. Therefore, it seems likely that the crystallization of mannitol on SD particles upon certain storage after production would possibly impede the deaggregation of particles due to the formation of bridging in the solid-state. It has been reported[73] that incorporation of mannitol lowered the aerosol dispersion (e.g., FPF) of spray-dried three-component spray-dried powder consisting of albumin, dipalmitoylphosphatidylcholine (DPPC), and a protein stabilizer (lactose, trehalose or mannitol) compared to other sugars (such

as lactose and trehalose).

#### **5.4.2 Effect of Phospholipids on Spray-Dried Drug:Phospholipids**

Incorporation of phospholipids in TOB:PLS improved markedly the aerosol dispersion performance of the powders compared to SD pure TOB. The FPF and RF of TOB:PLS formulations increased from 28.5% to 41.7% or higher, and from 43.7% to 73.3% or higher, respectively. In addition, MMAD and GSD decreased significantly from 5.0 $\mu$ m to 2.0 $\mu$ m or lower, and from 3.3 to 1.9, respectively. However, with TOB:PLS=1:2 unchanged, the ED of TOB:PLS=1:0.5 and 1:1 decreased.

In contrast to TOB formulations, incorporation of phospholipids did not significantly change the ED, RF, and GSD of AZI:PLS aerosols, while FPF decreased from 47.0% to 37.4% or lower. With the exception of AZI:PLS=1:0.5, MMAD increased significantly from 2.3 $\mu$ m to 4.7 $\mu$ m or higher for the other compositions.

In summary, incorporation of phospholipids into formulations exhibited remarkably different effects on the aerosol dispersion performance of TOB:PLS and AZI:PLS. At present, it is not clear why TOB:PLS and AZI:PLS particles performed differently. The interfacial properties of antimicrobial compounds have been extensively explored[194-200]. Therefore, tobramycin may possibly compete with surface-active phospholipids for the air/methanol interface on droplets during spray drying. Moreover, tobramycin has a smaller molecular weight compared to phospholipids (e.g., tobramycin: 467g/mol vs DPPC: 734g/mol and DPPG: 745g/mol). This may suggest that tobramycin possibly had a faster molecular diffusion. Therefore, it could be reasonably suggested that significant amount of tobramycin is present on the surface of particles.

Azithromycin may also possess interfacial activity. The molecular weight of azithromycin is approximately equal to that of the phospholipids (e.g. azithromycin: 749g/mol vs DPPC: 734g/mol and DPPG: 745g/mol). Moreover, the hydrophobic nature of azithromycin would possibly indicate azithromycin may interact through favorable hydrophobic interactions with the hydrophobic chains on the phospholipids molecule. The interaction of azithromycin and phospholipids have been reported in the literature[174] suggesting that these two different molecules could co-localize on particle surface. However, during spray drying, phospholipids would possibly undergo main phase transition from gel phase to liquid crystalline phase as the temperature (such as outlet temperature of spray drying ( $T_o$ )) (Table 3.2 in Chapter 3) was higher than main phase transition temperature of phospholipid bilayer ( $T_m$ ) (Table 4.3 in Chapter 4). After phase transition, sticky phospholipids (due to increased molecular mobility) on particle surface would possibly facilitate the irreversible formation of particle aggregation. This lowered the aerosol dispersion performance of AZI:PLS compared to SD pure AZI, while the FPF values of AZI:PLS were still regarded as high.

### 5.4.3 Effect of Mannitol on Spray-Dried Drug:Phospholipids:Mannitol

When compared with TOB:PLS formulations, aerosol dispersion performance of TOB:PLS:MAN decreased with increasing amount of mannitol. For TOB:PLS:MAN=1:0.5:0.1, MMAD increased significantly from 1.7 $\mu$ m to 2.2 $\mu$ m. For TOB:PLS:MAN=1:0.5:0.5, RF decreased significantly from 82.5% to 66.8% and MMAD increased significantly from 1.7 $\mu$ m to 2.6 $\mu$ m. As for TOB:PLS:MAN=1:0.5:1, the FPF and RF were significantly lowered from 47.4% to 38.1%, and from 82.5% to 60.6%, respectively. Moreover, MMAD and GSD increased significantly from 1.7 $\mu$ m to 2.7 $\mu$ m, and from 1.9 to 2.2, respectively. With incorporation of mannitol in TOB:PLS:MAN, ED overall increased from 86.9% to 91.7% or higher.

The mannitol effect on aerosol dispersion performance for AZI:PLS:MAN differed with compositions. Based on aerosol dispersion performance parameters, AZI:PLS:MAN=1:0.5:0.1 and 1:0.5:0.5 did not improve aerosol dispersion performance compared to AZI:PLS=1:0.5. As for AZI:PLS:MAN=1:0.5:0.1, only MMAD was affected, increasing significantly from 2.2 $\mu$ m to 3.2 $\mu$ m. In addition, FPF and RF of AZI:PLS:MAN=1:0.5:0.5 decreased significantly from 37.4% to 32.6%, and from 72.4% to 48.6%, respectively. Moreover, the GSD increased significantly from 2.1 to 2.7. However, in AZI:PLS:MAN=1:0.5:1, sharply elevated FPF and RF from 27.1% to 60.4%, and 62.4% to 96.1%, respectively, were observed. With AZI:PLS:MAN=1:0.5:0.1 and 1:0.5:1 unchanged, the ED of AZI:PLS:MAN=1:0.5:0.5 increased.

In summary, addition of mannitol did not appear to improve the aerosol dispersion performance of TOB:PLS:MAN. However, the effect of incorporation of mannitol on the aerosol dispersion performance of AZI:PLS:MAN is composition dependent. As discussed in Section 5.4.2.1, mannitol may possibly play a same role in three-component systems such as all TOB:PLS:MAN formulations, AZI:PLS:MAN=1:0.5:0.1, and AZI:PLS:MAN=1:0.5:0.5. Other mechanism(s) (such as particle density change[201], surface energetics change[202], and etc.) may have contributed to the sharp increase in aerosol dispersion performance of AZI:PLS:MAN=1:0.5:1.

## 5.5 Conclusions

The aerosol dispersion performance of spray-dried particle was studied employing the next generation impactor (NGI) with the HandiHaler<sup>®</sup> at adult air flow rate (60 L/min). It was demonstrated that the validated gravimetric method was sufficient to assess the azithromycin component distribution on the NGI stages. In almost all cases, spray-dried inhalable multi-component particles exhibited mass median aerodynamic diameter (MMAD) less than 5 $\mu$ m suitable for deep lung deposition. In general, based on the obtained aerosol dispersion performance parameters, addition of mannitol did not improve aerosol dispersion performance of spray-dried particles except for AZI:PLS:MAN=1:0.5:1. The effect of addition of phospholipids was mainly dependent upon the drug properties.

Portions of Chapter 5 were reproduced with kind permission from: Li, X, Vogt, F.G., Hayes, D. Jr., and Mansour, H.M. Physicochemical Characterization and Aerosol Dispersion Performance of Organic Solution Advanced Spray Dried Microparticulate/Nanoparticulate Antibiotic Dry Powders of Tobramycin and Azithromycin for Pulmonary Inhalation Aerosol Delivery. *European Journal of Pharmaceutical Sciences*, 2014, 15:191-205. Copyright © 2014 Elsevier.

Copyright © Xiaojian Li 2014

## Chapter 6 Storage Stability

### 6.1 Introduction

Stability in pharmaceuticals is defined as the ability of a drug substance or a pharmaceutical product to resist specific physical, chemical, and biopharmaceutical alterations during the product shelf-life. Therefore it is essentially important to consider formulation stability during early drug formulation development. The chemical and physical stability of the dry powder formulation could be affected by moisture content and hygroscopicity of the formulation[64, 155, 156], chemistry of the excipient and carrier particles[64, 203-205], interparticulate forces within the formulation[64, 206], particle size (including size distribution) and surface morphology[64, 207, 208]. Moreover, the storage conditions, such as relative humidity (RH) and temperature, could often affect the physical and chemical stability of a dry powder formulation, leading an unsuccessful delivery to the lungs of patients. There are three recommended storage test conditions[209] from Food and Drug Administration (FDA):  $25 \pm 2^{\circ}\text{C}$  and  $60 \pm 5\%$  RH (long-term conditions);  $30 \pm 2^{\circ}\text{C}$  and  $60 \pm 5\%$  RH (intermediate conditions);  $40 \pm 2^{\circ}\text{C}$  and  $70 \pm 5\%$  RH (accelerated conditions). In this storage stability study, we examine the effect of relative humidity on spray-dried (SD) particles at  $40^{\circ}\text{C}$ . Three different RH % represents low (11%), medium (40%), and high (75%) in practical storage conditions. By x-ray powder diffraction (XRPD) and thermal analysis such as differential scanning calorimetry (DSC), the storage stability of SD powders is studied during the storage. It would be expected that the component, lacking of long-range molecular order, in SD powders may possibly be subjected to phase transition(s) during storage. With the occurring of phase transition(s), the aerosol dispersion performance of SD powders could be highly impeded due to possible solid-state bridging. Therefore, after storage, the aerosol dispersion performance of SD powders is examined by using the next generation impact (NGI).

### 6.2 Materials and Methods

#### 6.2.1 Materials

The fresh spray-dried (SD) tobramycin (TOB) formulations (including pure TOB, tobramycin:mannitol (TOB:MAN)=1:0.5, tobramycin:phospholipids (TOB:PLS)=1:0.5, and tobramycin:phospholipids:mannitol (TOB:PLS:MAN)=1:0.5:0.5) and azithromycin (AZI) formulations (including pure AZI, azithromycin:mannitol (AZI:MAN)=1:0.5, azithromycin:phospholipids (AZI:PLS)=1:0.5, and azithromycin:phospholipids:mannitol (AZI:PLS:MAN)=1:0.5:0.5) were selected for storage stability test. All the studied particles were generated employing a 50% pump rate during spray drying. Lithium chloride (ACS, 99% min) and potassium carbonate (ACS, 99% min) were purchased from Alfa Aesar (Massachusetts, USA). Sodium chloride ( $\geq 99.5\%$ ) was received from Fisher Scientific (USA). Incubator (Napco, Model 320) (USA) was used as temperature controller in sample storage. HP clear, size 3 capsule (Quali-V®) was



received from Qualicaps (Spain). Aluminum foil (624 heavy duty; food-service) was obtained from Reynolds® (made in China; packed in USA).

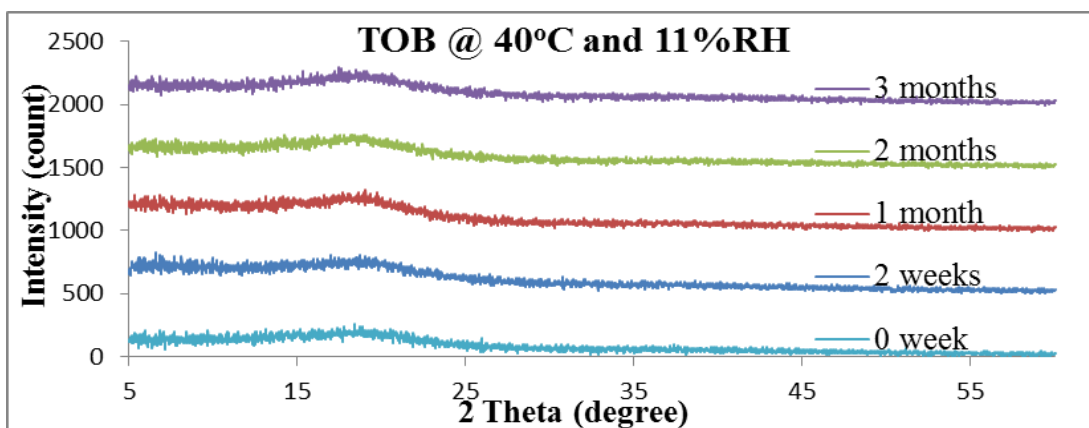
### 6.2.2 Methods

Each capsule was filled with ~10mg pre-weighed powder. A piece of uniformly cut aluminum foil (3 x 3cm) was used to wrap each capsule containing powder. Several filled capsules from the same formulation were stored in a pin-holed sandwich bag. Three sandwich bags containing the same formulation were placed in three glass desiccators with pre-equilibrated relative humidity (RH) by making saturated lithium chloride, potassium carbonate, or sodium chloride solutions in DI water. The three glass desiccators were stored in an incubator at  $40 \pm 1^\circ\text{C}$ . At equilibrium, the RH of saturated solution lithium chloride, potassium carbonate, and sodium chloride were 11%, 40%, and 75%, respectively, at  $40^\circ\text{C}$ . [210] In addition to differential scanning calorimetry (DSC) and thermal gravity analysis (TGA), the physicochemical properties of SD powders were examined by x-ray powder diffraction (XRPD) at pre-determined time points of 2 weeks, 1 month, 2 months, and 3 months of storage. The *in vitro* aerosol dispersion performance was conducted by using the next generation impactor (NGI) only after 3 months storage. The experimental conditions of XRPD, DSC and TGA are reported previously in Chapter 4. The experimental conditions of *in vitro* aerosol dispersion performance are described previously in Chapter 3.

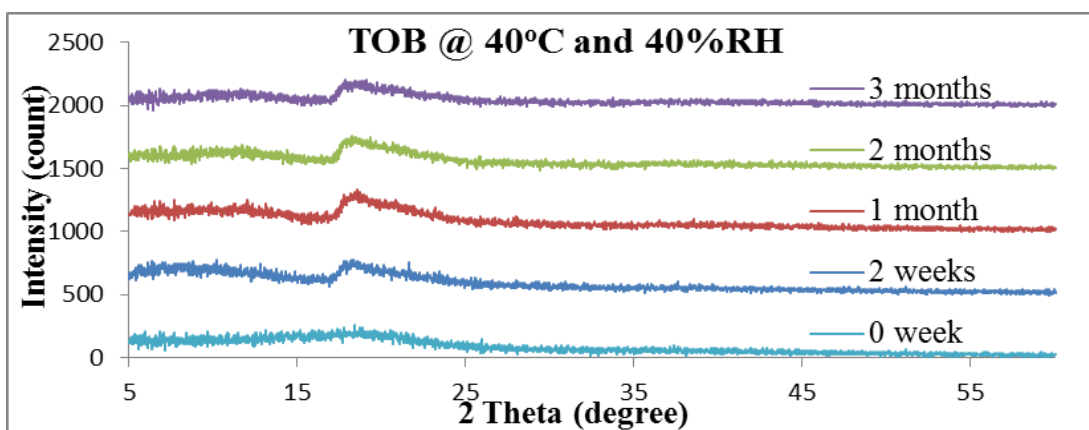
## 6.3 Results

### 6.3.1 X-Ray Powder Diffraction (XRPD)

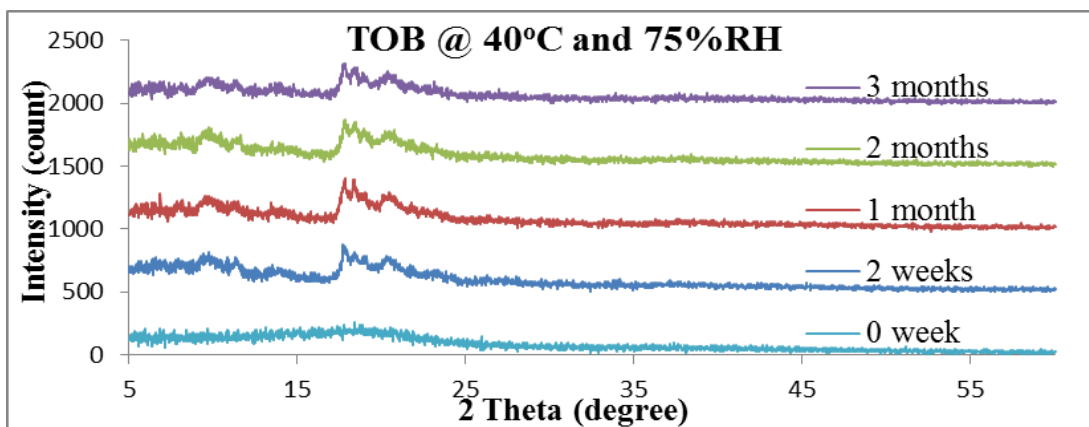
Figure 6.1 to 6.4 shows the XRPD data of stored SD pure TOB, TOB:MAN=1:0.5, TOB:PLS=1:0.5, and TOB:PLS:MAN=1:0.5:0.5, respectively. The SD tobramycin particles stored at 11% RH and  $40^\circ\text{C}$  exhibited non-crystalline XRPD patterns (Figure 6.1a to 6.4a, respectively) similar to that of the corresponding fresh samples. These results suggested there was no significant change in physical form of the component(s) in formulations upon storage. The appearance of crystalline peaks of TOB component from the SD tobramycin particles were observed when the particles were stored under conditions of either RH of 40% or 75% at  $40^\circ\text{C}$ . In addition, these particles also exhibited a color change, indicating a potential chemical stability issue. A representative picture of SD pure TOB (Figure 6.5) shows that the powder changed from colorless to yellow stored at conditions of 40% and 75% RH. It was also noticed that a small crystalline peak from beta form of mannitol emerged at  $\sim 23^\circ$  of 2 Theta (Appendix I) from TOB:MAN=1:0.5 (Figure 6.2b-c) stored at RH of 40% and 75%. Supported by differential scanning calorimetry (DSC) data (endothermic peak at  $69^\circ\text{C}$  indicative of main phase transition of phospholipid bilayer in Figure 6.6a), the phospholipid bilayer structure showed a characteristic crystalline peak at range from  $20^\circ$  to  $23^\circ$  of 2 Theta in XRPD in phospholipid containing TOB formulations (Figure 6.3-6.4) under all studied storage conditions.



(a)

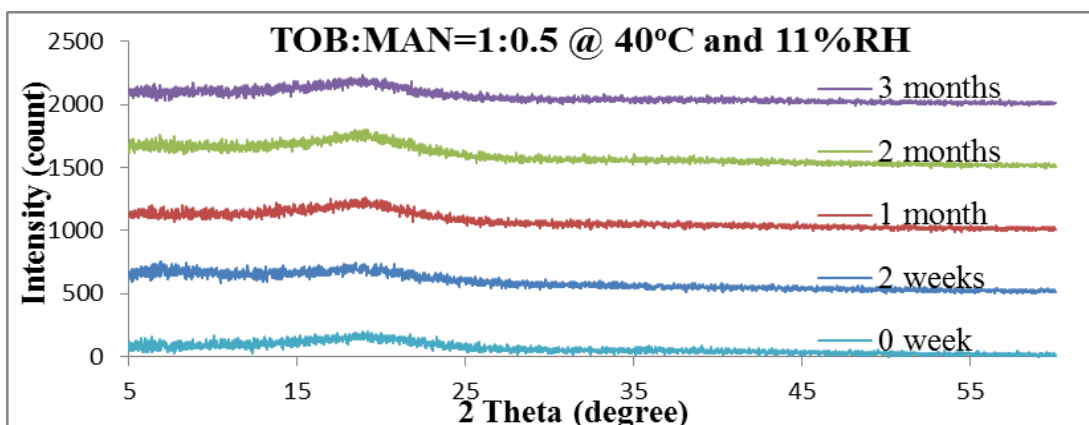


(b)

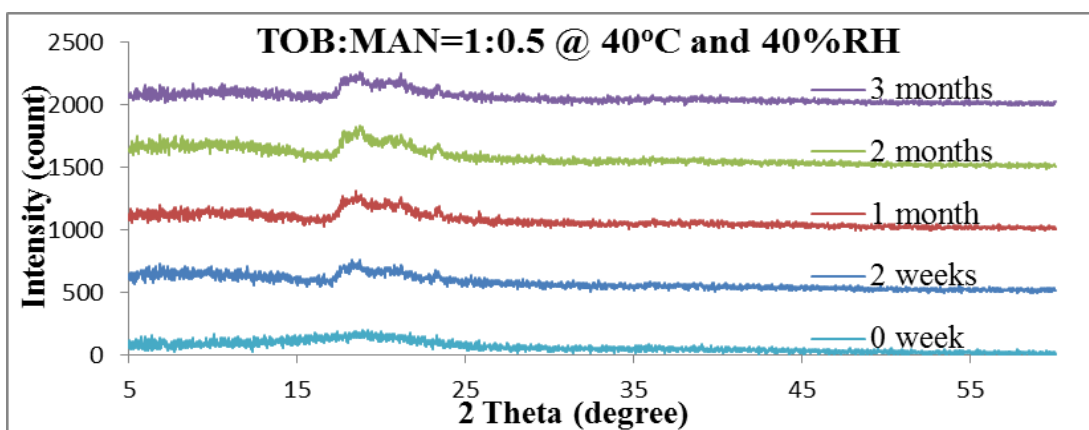


(c)

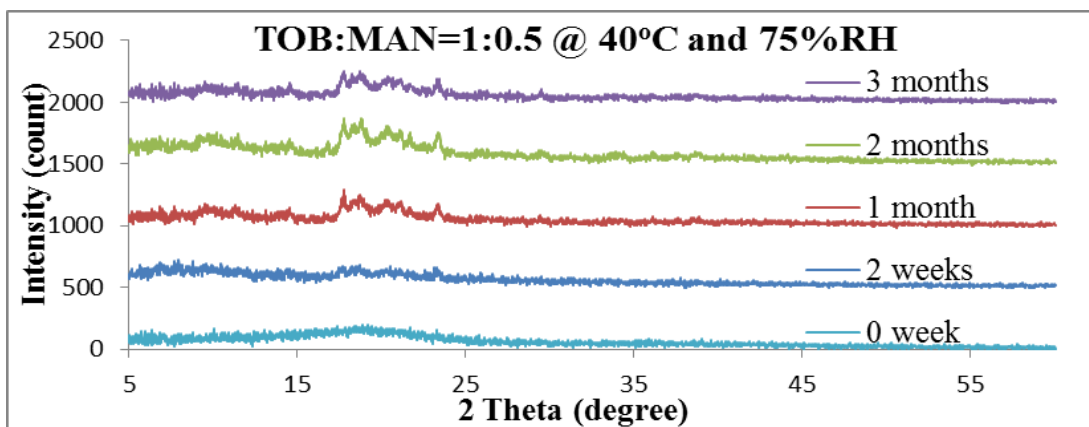
**Figure 6.1.** XRPD patterns of SD pure tobramycin (offset by 500 counts between patterns) at 11% RH (a), 40% RH (b), and 75% RH (c) at 40°C during storage.



(a)

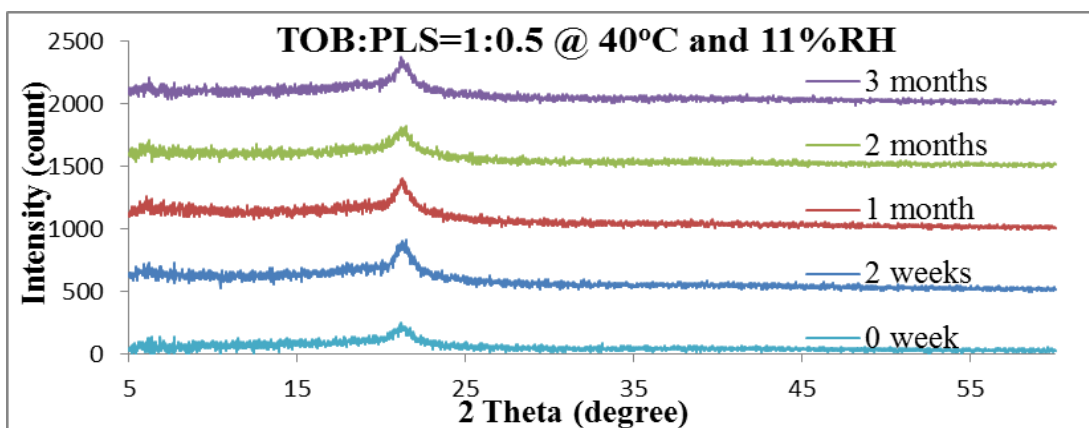


(b)

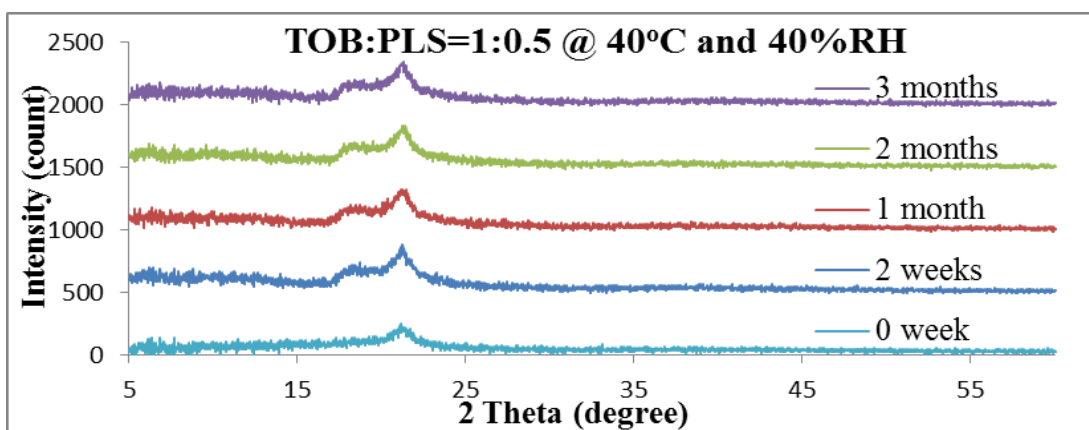


(c)

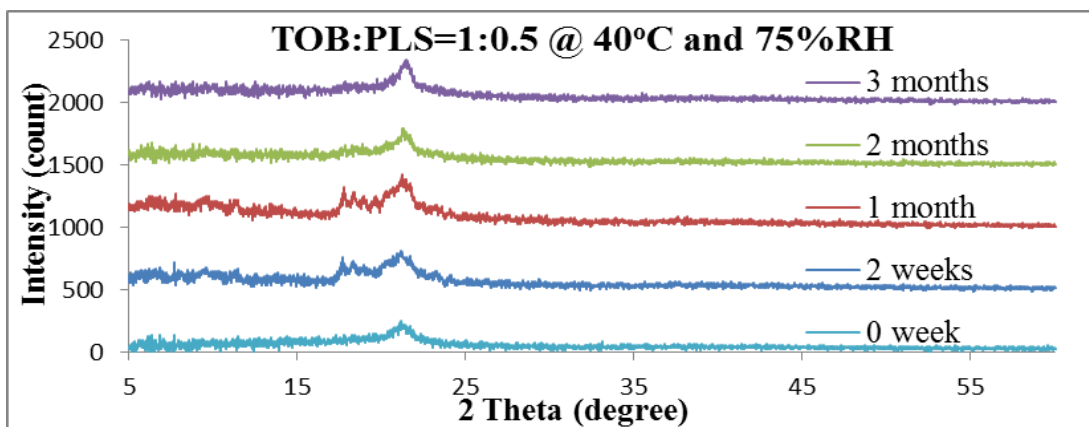
**Figure 6.2.** XRPD patterns of SD tobramycin:mannitol=1:0.5 (offset by 500 counts between patterns) at 11% RH (a), 40% RH (b), and 75% RH (c) at 40°C during storage.



(a)

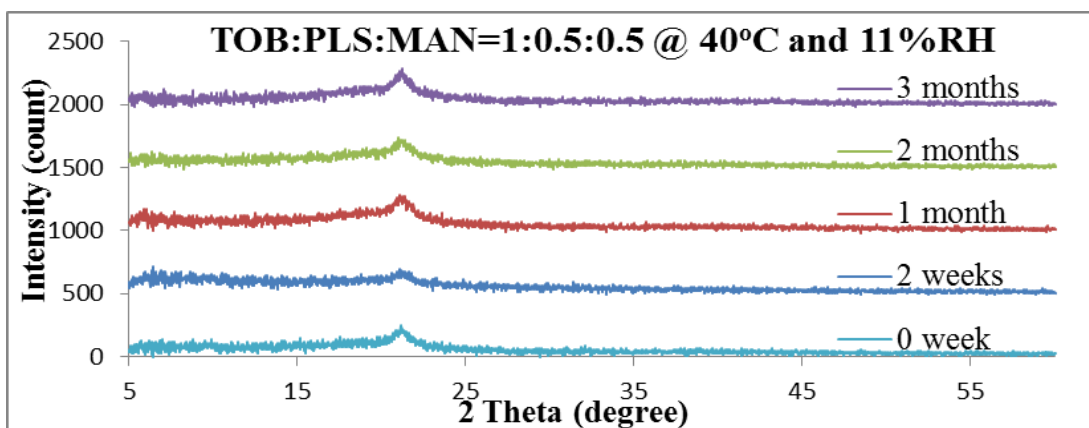


(b)

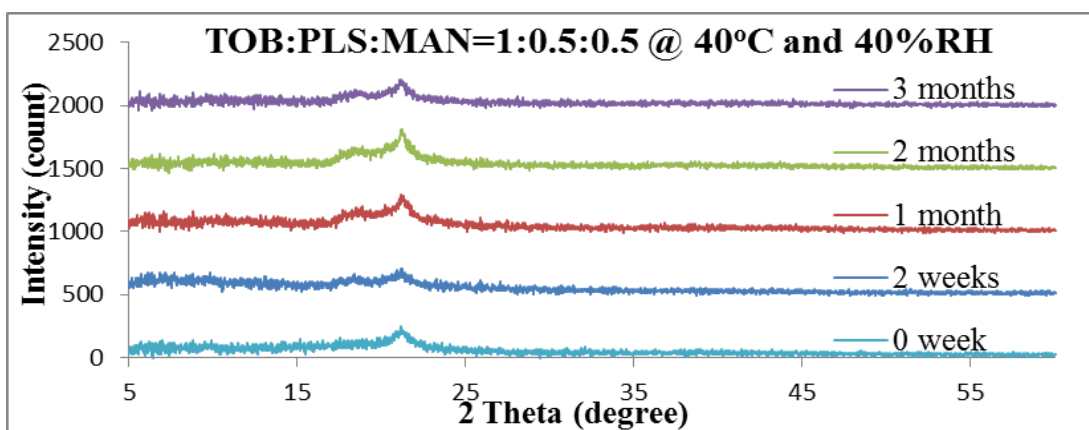


(c)

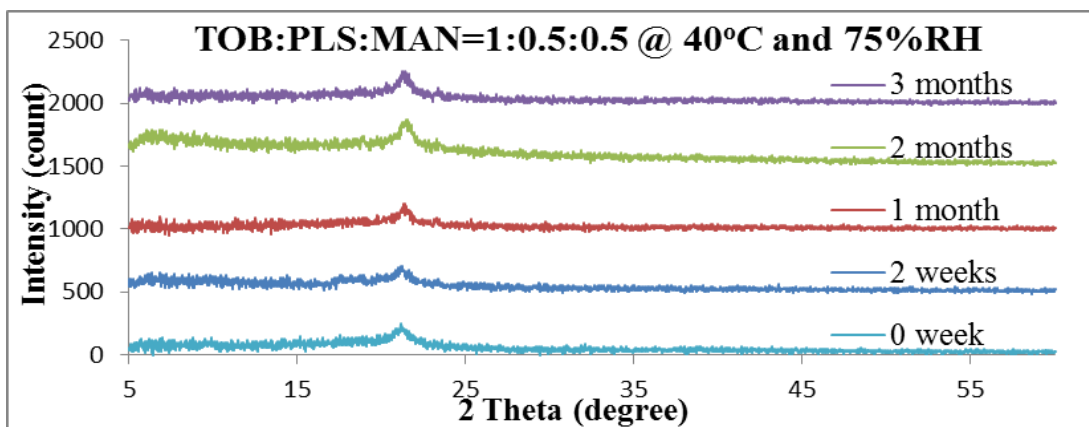
**Figure 6.3.** XRPD patterns of SD tobramycin:phospholipids=1:0.5 (offset by 500 counts between patterns) at 11% RH (a), 40% RH (b), and 75% RH (c) at 40°C during storage.



(a)



(b)

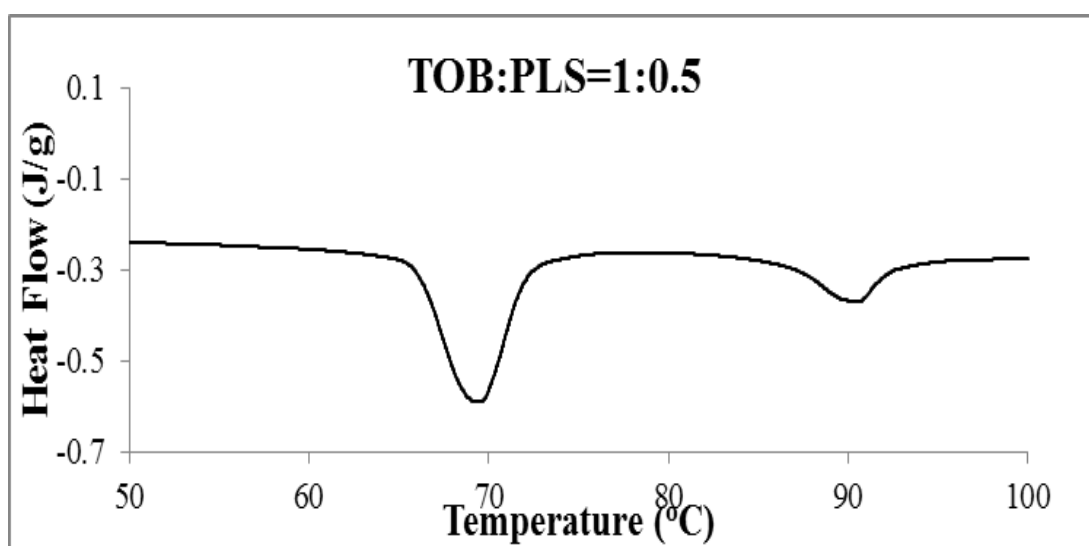


(c)

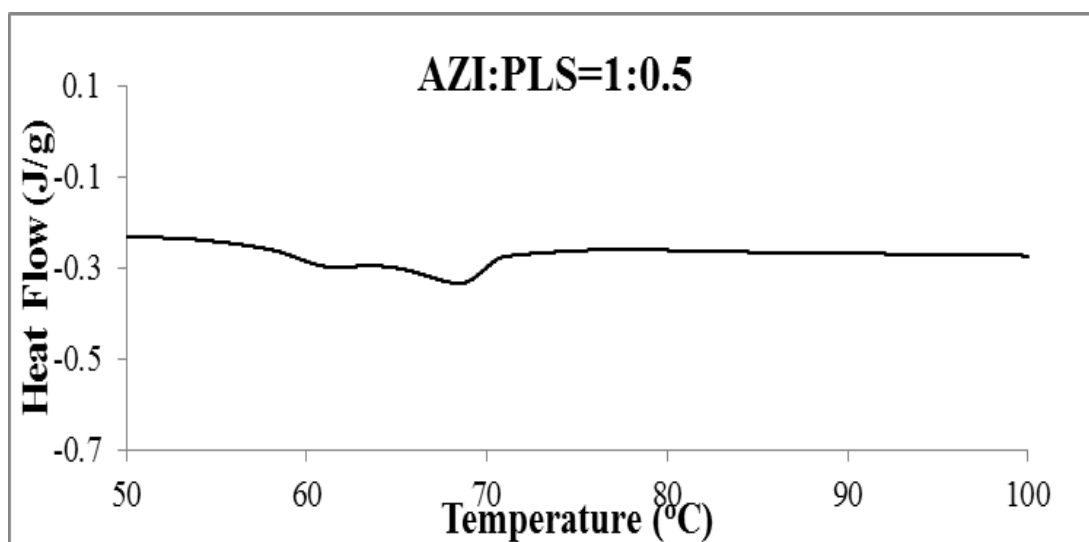
**Figure 6.4.** XRPD patterns of SD tobramycin:phospholipids:mannitol=1:0.5:0.5 (offset by 500 counts between patterns) at 11% RH (a), 40% RH (b), and 75% RH (c) at 40°C during storage.



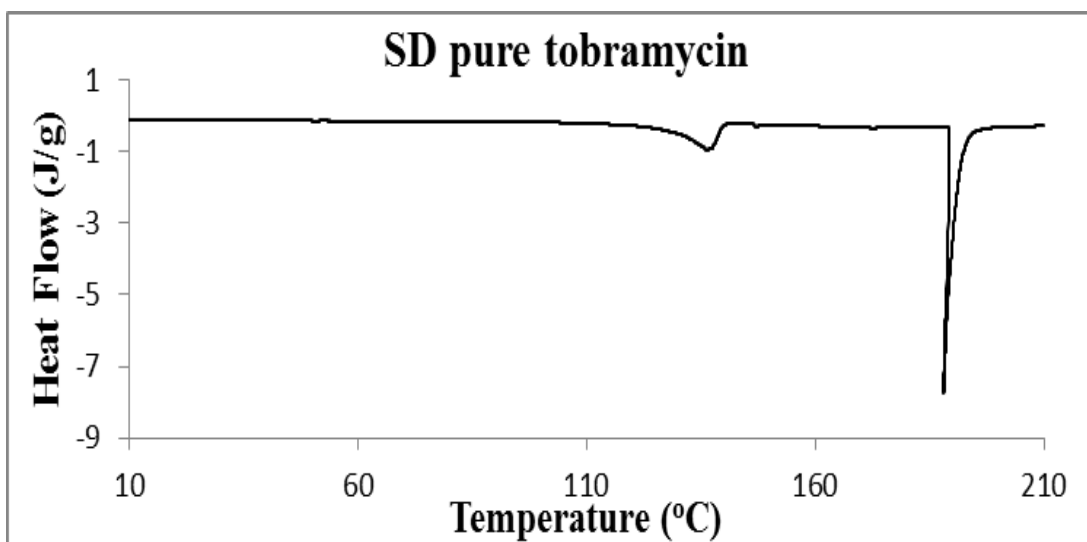
**Figure 6.5.** Photograph of capsules of SD pure tobramycin stored at three different RH % and 40°C for 2 weeks.



(a)



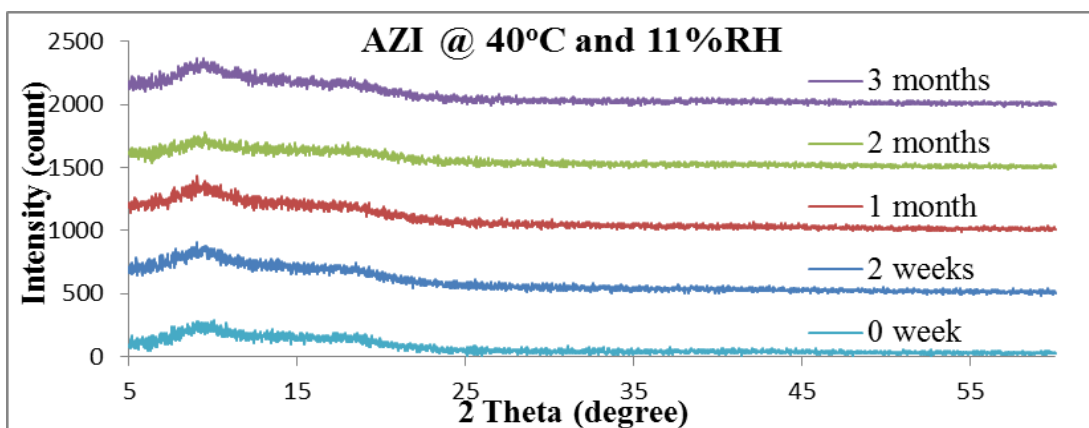
(b)



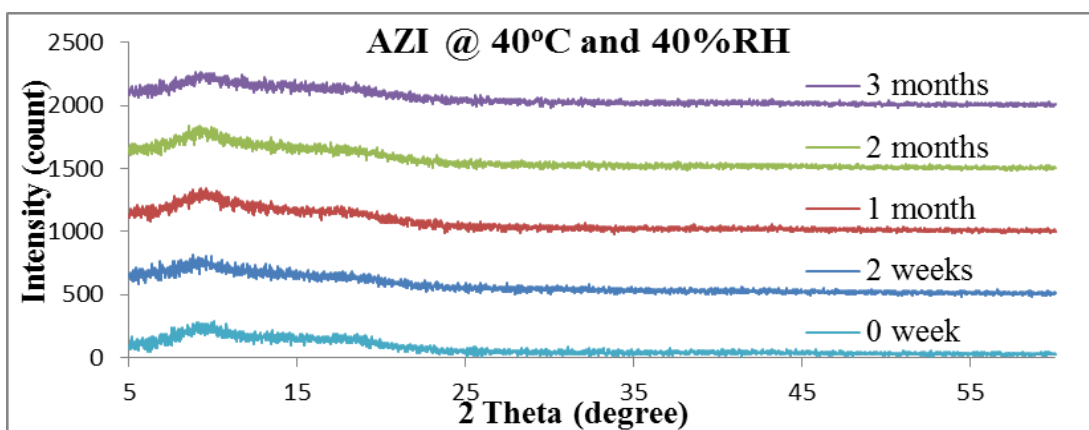
(c)

**Figure 6.6.** DSC thermograms of main phase transition of tobramycin:phospholipids=1:0.5 (a) and azithromycin:phospholipids=1:0.5 (b) after 3 months storage at 11% RH and 40°C; DSC thermogram of SD pure tobramycin (c) after 3 months storage at 75% RH and 40°C.

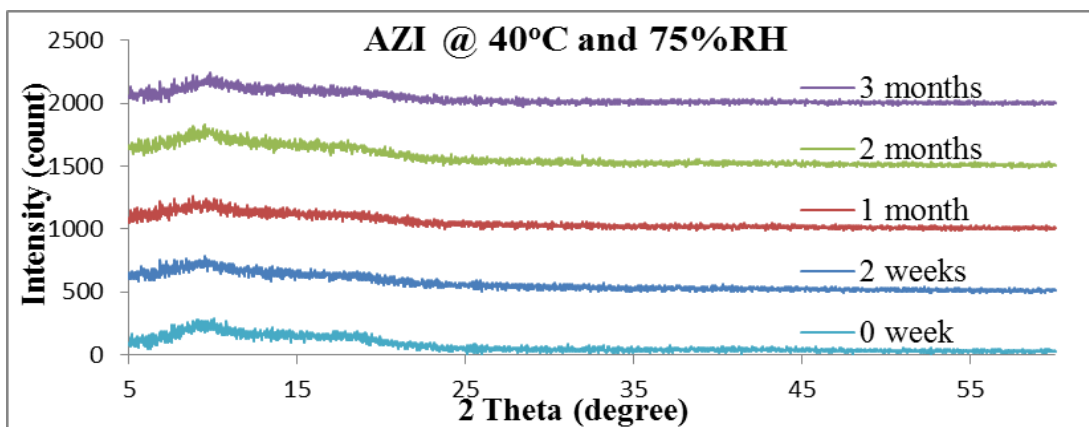
As no new XRPD peaks, compared to freshly-prepared material, were observed, SD pure AZI and AZI:MAN=1:0.5 were physically stable in solid phase under the storage conditions as shown in Figure 6.7 and 6.8, respectively. Supported by DSC data (two possibly separated peaks, at 60°C and 68°C, of main phase transition of phospholipid bilayer in Figure 6.6b), AZI:PLS=1:0.5 (Figure 6.9) and AZI:PLS:MAN=1:0.5:0.5 (Figure 6.10) maintained the phospholipid bilayer structure with the presence of a characteristic crystalline peak at range from 20° to 23° of 2 Theta in XRPD under all the studied conditions. However, the AZI component in these two formulations started to crystallize into its dihydrate crystalline form (with the appearance of characteristic peaks at 7.4°, 9.4° and 9.5° of 2 Theta; Figure 4.1b in Chapter 4) after 1 month storage at conditions of 75% RH and 40°C in temperature (Figure 6.9c and Figure 6.10c, respectively). The crystalline peaks from mannitol were not observed in all SD AZI formulations. In addition, there was no observed color change in SD AZI particles.



(a)



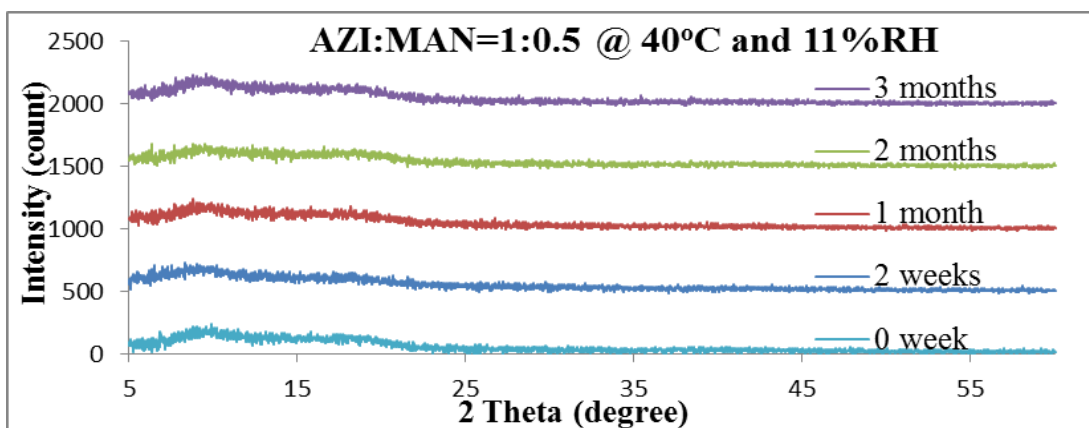
(b)



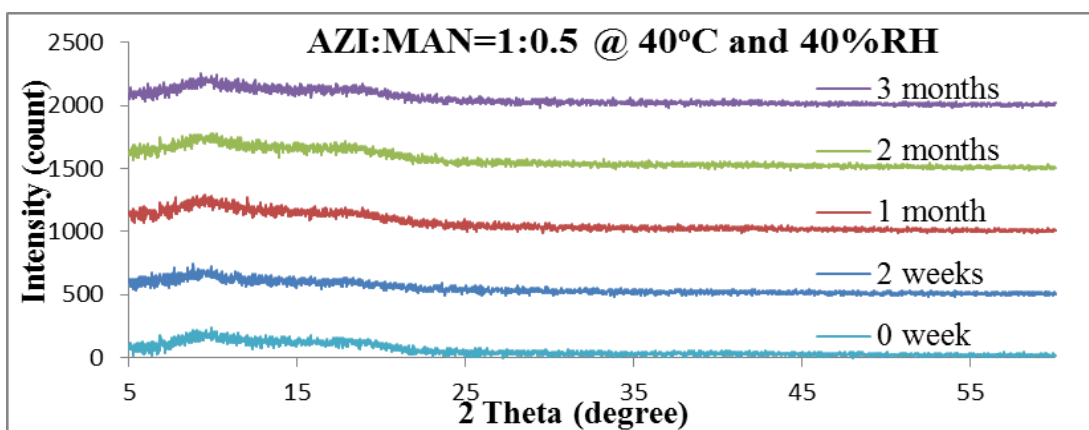
(c)

**Figure 6.7.** XRPD patterns of SD pure azithromycin (offset by 500 counts between patterns) at 11% RH (a), 40% RH (b), and 75% RH (c) at 40°C during storage.

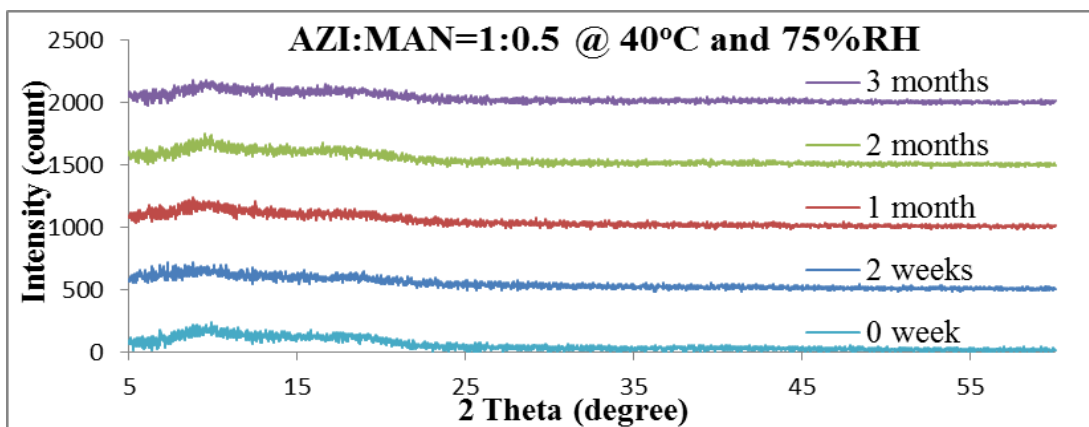




(a)

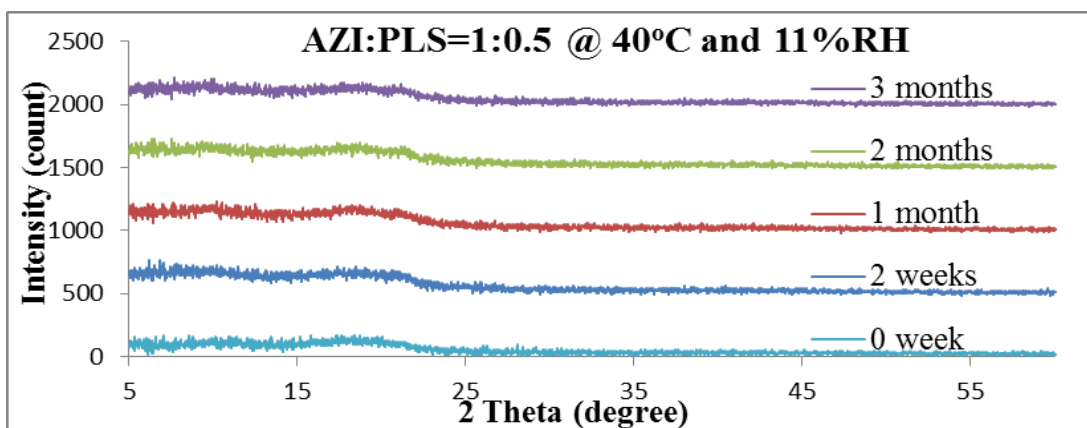


(b)

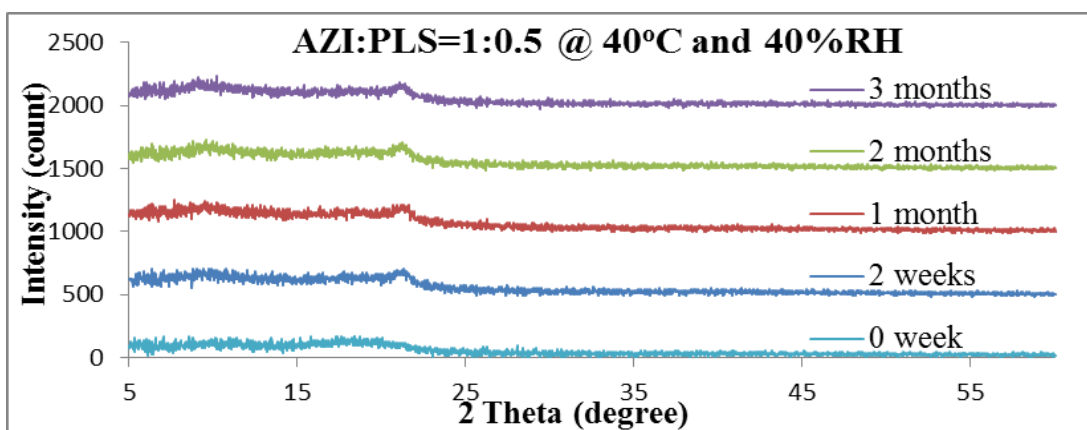


(c)

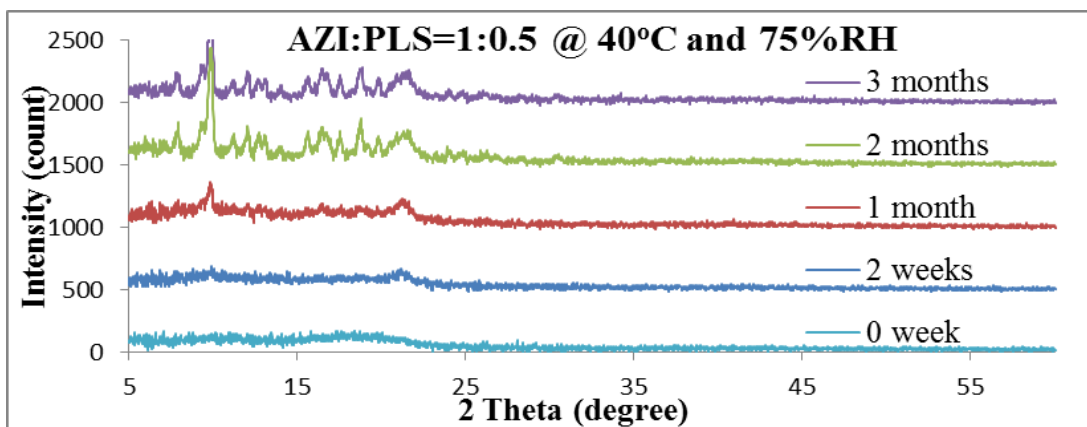
**Figure 6.8.** XRPD patterns of SD azithromycin:mannitol=1:0.5 (offset by 500 counts between patterns) at 11% RH (a), 40% RH (b), and 75% RH (c) at 40°C during storage.



(a)

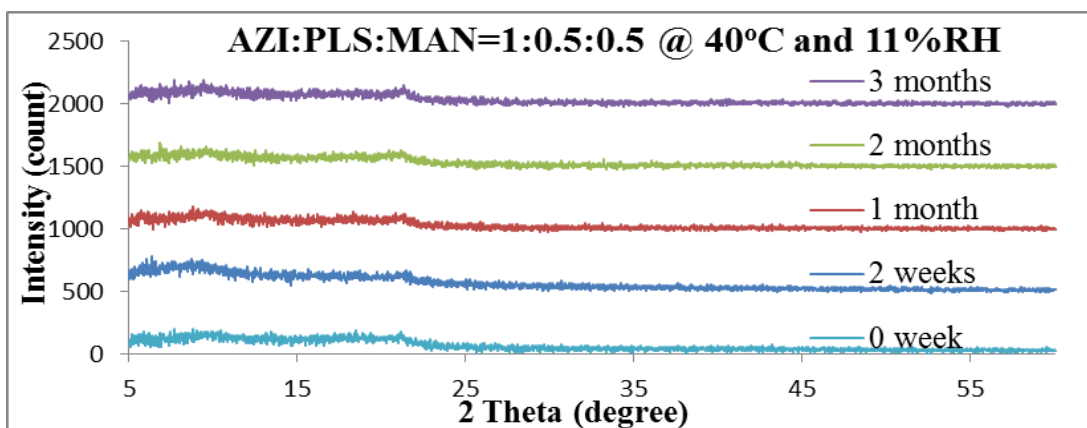


(b)

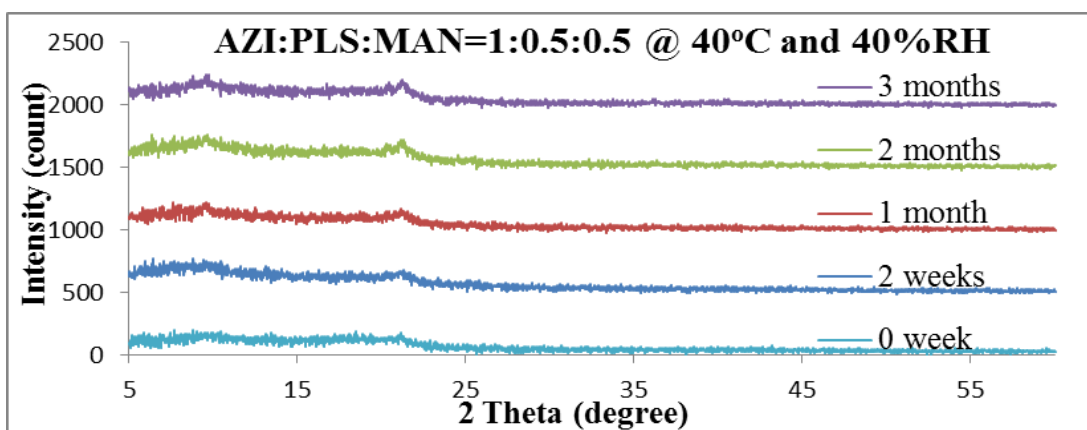


(c)

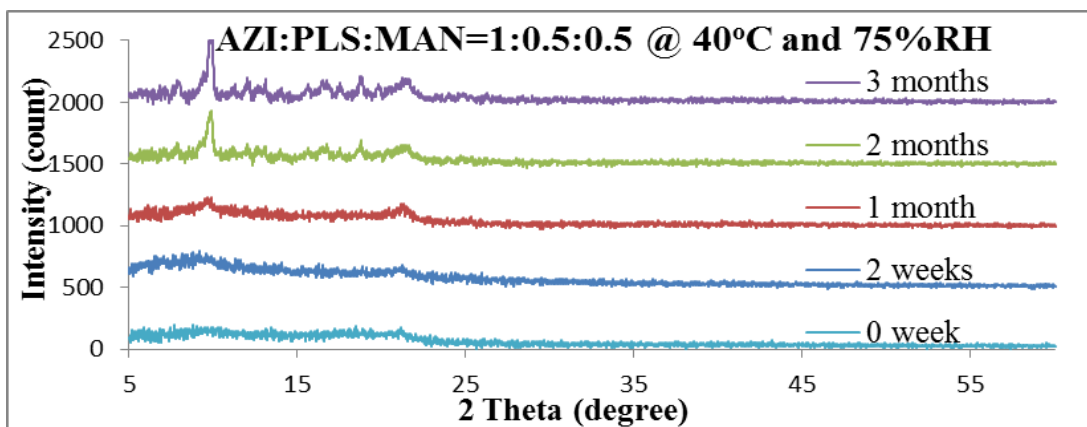
**Figure 6.9.** XRPD patterns of SD azithromycin:phospholipids=1:0.5 (offset by 500 counts between patterns) at 11% RH (a), 40% RH (b), and 75% RH (c) at 40°C during storage.



(a)



(b)



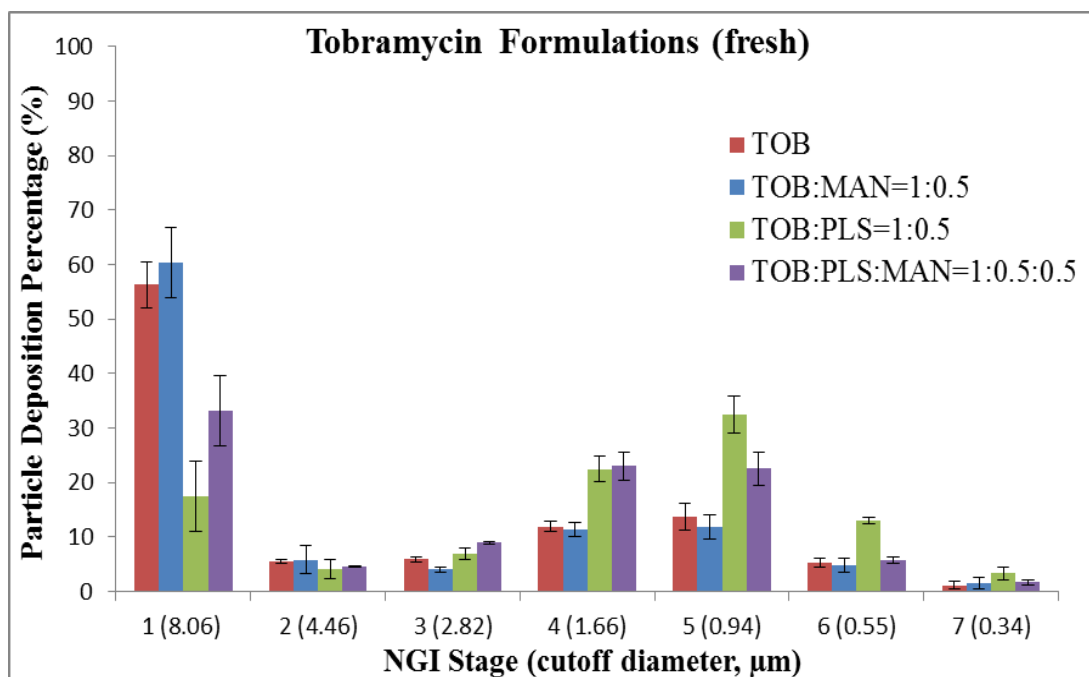
(c)

**Figure 6.10.** XRPD patterns of SD azithromycin:phospholipids:mannitol=1:0.5:0.5 (offset by 500 counts between patterns) at 11% RH (a), 40% RH (b), and 75% RH (c) at 40°C during storage.

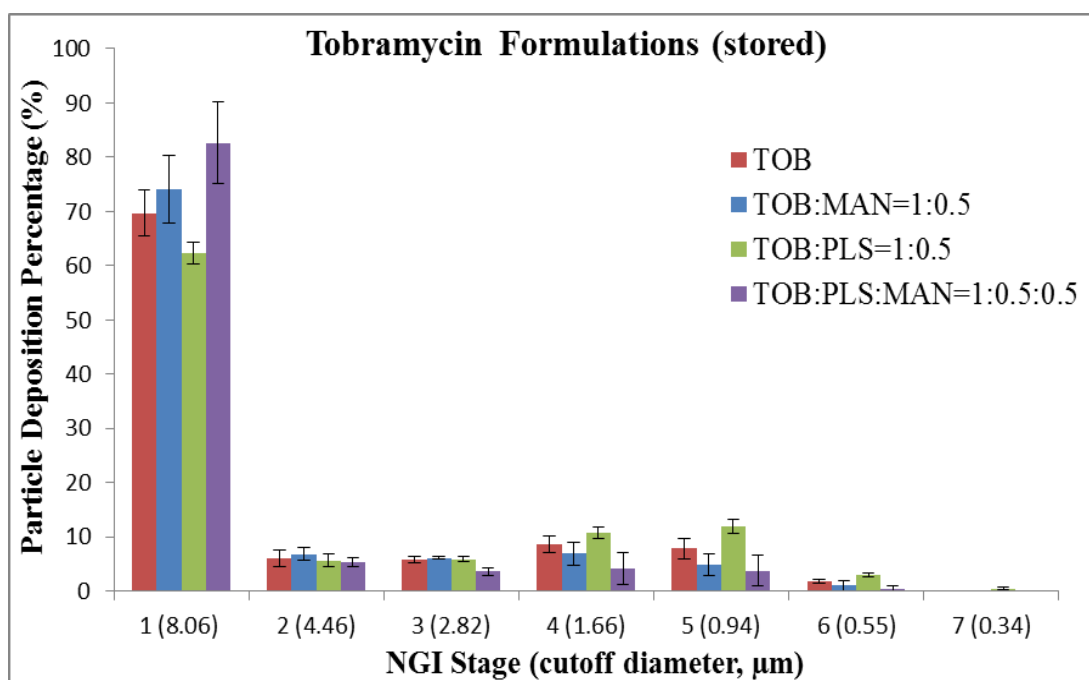
### 6.3.2 Aerosol Dispersion Performance

On this Section, the aerosol performances of stored formulations were examined. Aerosol dispersion performance parameters have been described in Section of 5.2.2.1 in Chapter 5. The SD tobramycin particles stored at 40% and 75% RH formed aggregates through particle crystallization with a color change precluding their use in aerosol pulmonary delivery. Therefore, only the particles stored at 11% RH and 40°C were used to conduct aerosol dispersion performance. Studies were carryout employing the next generation impactor (NGI) with the Handihaler<sup>®</sup> after 3 months of storage. The aerosol particle deposition of SD tobramycin particles on each stage in the NGI is depicted for both fresh formulations (Figure 6.11a) and stored formulations (Figure 6.11b). Fresh particles deposited less than stored particles on stage 1. In addition, it was observed that fine particle deposition mode was on stage 4 or 5 for fresh particles. However, the fine particle deposition mode was not evident for stored particles. The stored particles had a relatively even deposition on stages 2-7 with approximately less than 10% particle deposited on each stage.

The aerosol dispersion performance parameters of the tobramycin formulations are summarized in Table 6.1. The aerosol dispersion performance parameters (i.e. FPF and RF) of the stored SD tobramycin formulations were significantly lowered, resulting in higher values of MMAD ( $>5\mu\text{m}$ ) compared to their corresponding freshly-prepared powder. However, only stored TOB:PLS=1:0.5 and TOB:PLS:MAN=1:0.5:0.5 resulted in higher GSD values compared to the fresh powder. The GSD values were not significantly different for fresh and stored SD pure TOB and TOB:MAN=1:0.5. Overall, the fresh and stored SD tobramycin powders resulted in similar ED values.



(a)



(b)

**Figure 6.11.** Aerosol dispersion performance using the NGI under an airflow rate ( $Q$ ) of 60 L/min with the HandiHaler<sup>®</sup> DPI device for: (a) fresh SD tobramycin powders; and (b) stored SD tobramycin powders at 11% RH and 40°C (mean  $\pm$  SD,  $n=3$ ).

The NGI aerosol particle deposition results of SD pure AZI, AZI:MAN=1:0.5, AZI:PLS=1:0.5, and AZI:PLS:MAN=1:0.5:0.5 are shown in Figures 6.12, 6.13, 6.14, and 6.15, respectively. The fresh particles deposited less on stage 1 than stored particles except for the formulation of AZI:PLS:MAN=1:0.5:0.5. For AZI (Figure 6.12) and AZI:MAN=1:0.5 (Figure 6.13), the fine particle deposition was lowered after storage, especially on stage 4-7. On the other hand, for stored AZI:PLS=1:0.5 (Figure 6.14), the fine particle deposition mode shifted from stage 5 to stage 4 or 2, indicating a growth in particle size. However, AZI:PLS:MAN=1:0.5:0.5 particles from storage conditions of 11% and 40% RH exhibited a fine deposition mode on stage 4 (Figure 6.15). In contrast, AZI:PLS:MAN=1:0.5:0.5 particles from storage conditions of RH 75% shifted fine particle deposition mode from stage 4 to stage 3.

Listed in Table 6.2 are the aerosol performance parameters of the AZI formulations. SD pure AZI and AZI:MAN=1:0.5 aerosols exhibited a decrease in FPF and RF values with storage RH % increased. MMAD and GSD values increased as storage RH % increased. However, all MMAD values remained about  $\leq 5\mu\text{m}$  after storage. Overall, AZI:PLS=1:0.5 and AZI:PLS:MAN=1:0.5:0.5 exhibited a lowered aerosol dispersion performance with increased storage RH %. At RH of 11% and 40%, the MMAD values increased (but remained about  $\leq 5\mu\text{m}$ ) compared to the values from fresh samples. The MMAD values dramatically increased ( $>5\mu\text{m}$ ) when AZI:PLS=1:0.5 and AZI:PLS:MAN=1:0.5:0.5 were stored at 75% RH and 40°C. In general, there was no observed trend for FPF and RF values when comparing fresh and stored samples under the conditions of 11% and 40% RH.

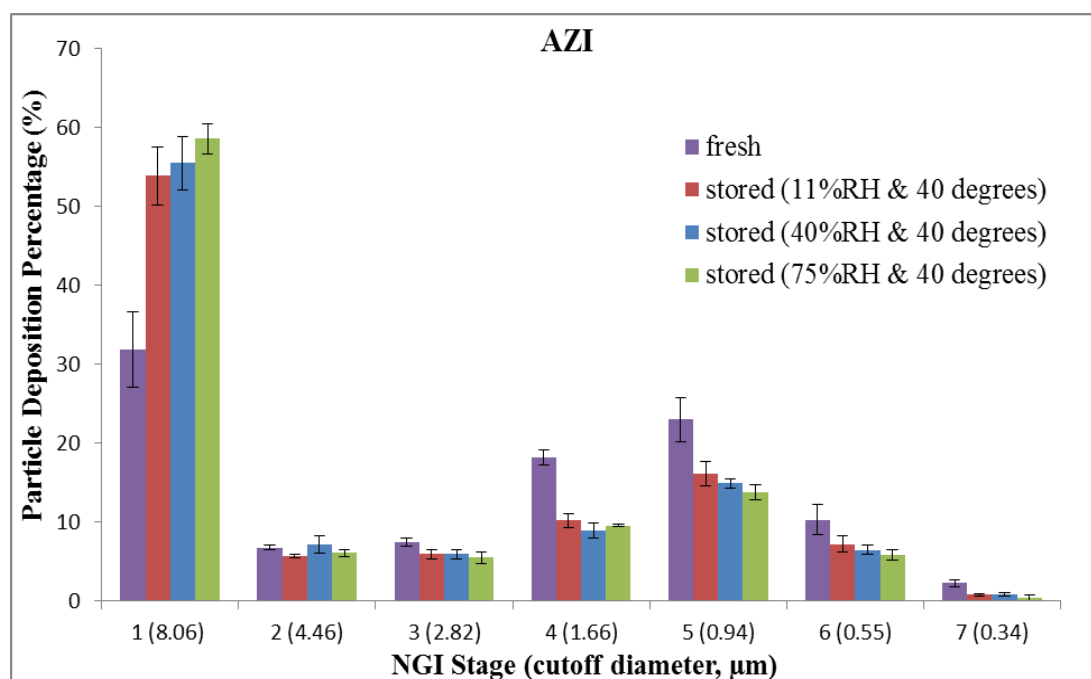


**Figure 6.12.** Aerosol dispersion performance using the NGI under an airflow rate (Q) of 60 L/min with the HandiHaler<sup>®</sup> DPI device for fresh and stored SD pure azithromycin at three different RH % and 40°C (mean  $\pm$  SD, n=3).

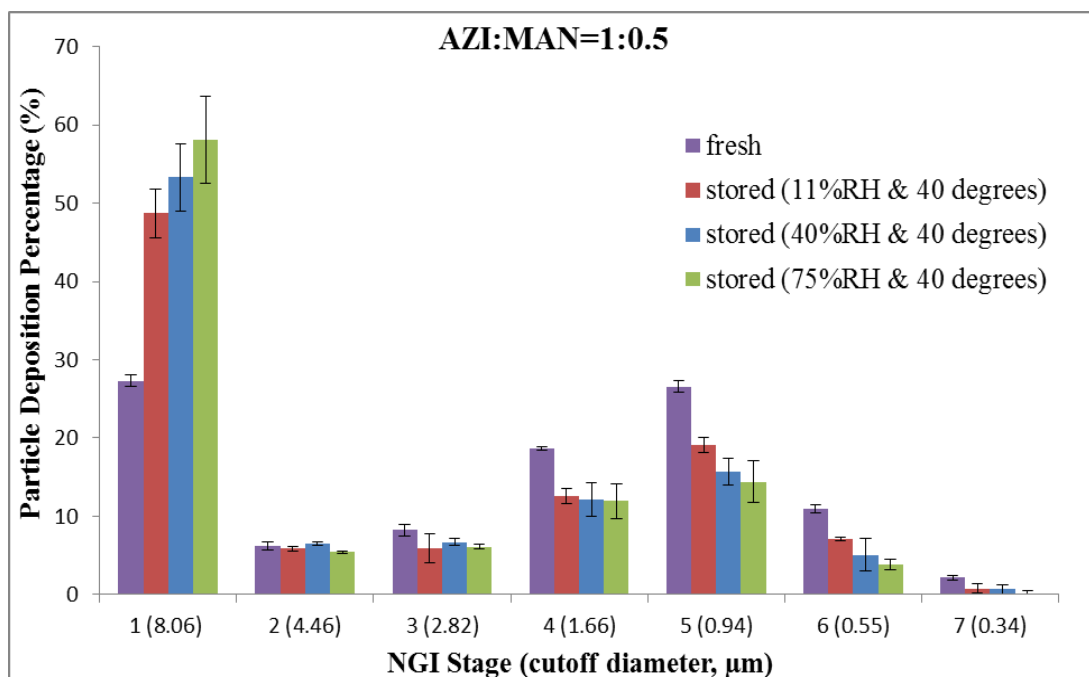


**Figure 6.13.** Aerosol dispersion performance using the NGI under an airflow rate (Q) of 60 L/min with the HandiHaler<sup>®</sup> DPI device for fresh and stored SD azithromycin:mannitol=1:0.5 at three different RH % and 40°C (mean  $\pm$  SD, n=3).

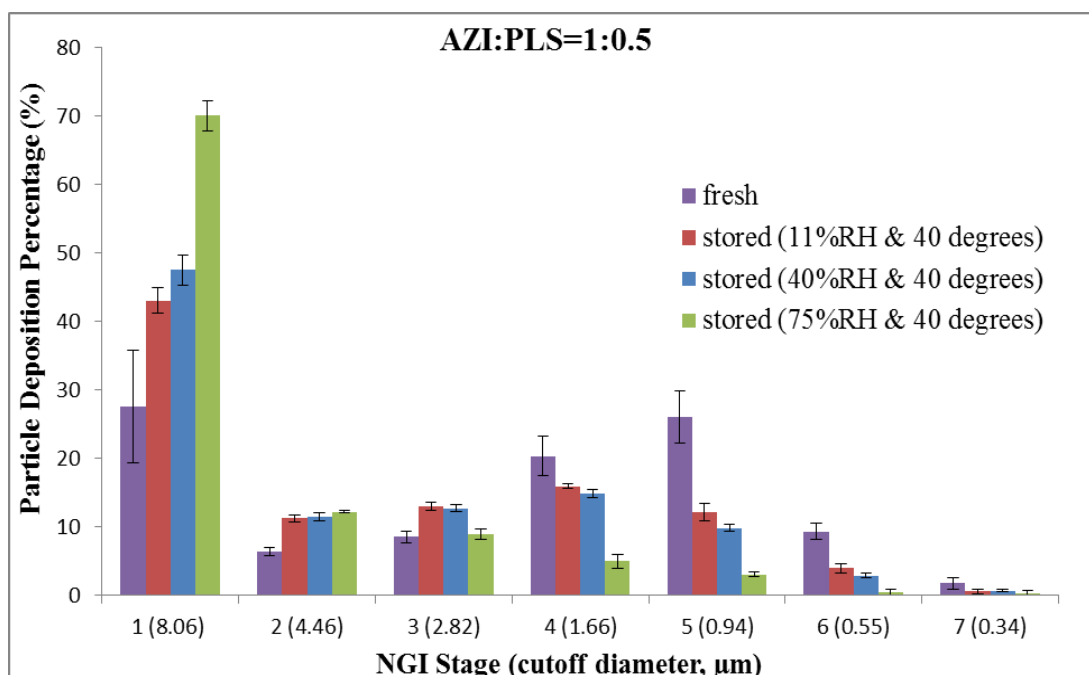


**Figure 6.14.** Aerosol dispersion performance using the NGI under an airflow rate (Q) of 60 L/min with the HandiHaler<sup>®</sup> DPI device for fresh and stored SD azithromycin:phospholipids=1:0.5 at three different RH % and 40°C (mean  $\pm$  SD, n=3).

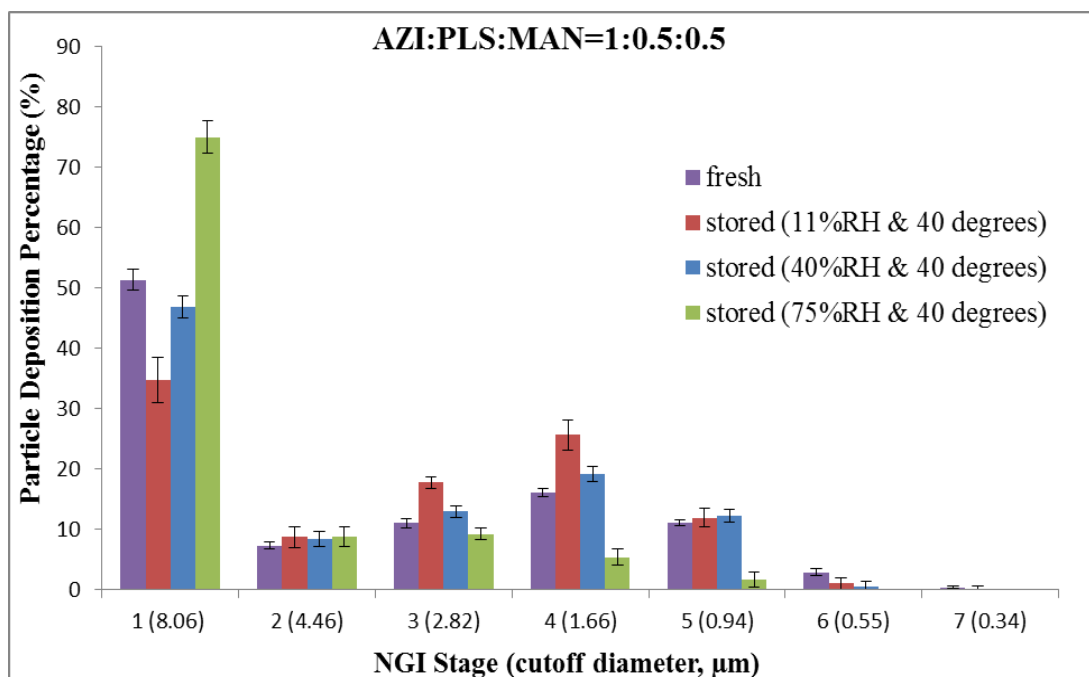


**Figure 6.15.** Aerosol dispersion performance using the NGI under an airflow rate (Q) of 60 L/min with the HandiHaler<sup>®</sup> DPI device for fresh and stored SD azithromycin:phospholipids:mannitol=1:0.5:0.5 at three different RH % and 40°C (mean  $\pm$  SD, n=3).



**Table 6.1.** Aerosol dispersion performance parameters of SD tobramycin powders (fresh vs stored at 11% RH and 40°C) (mean  $\pm$  SD, n=3). Definition: ED[%]=emitted dose fraction; FPF[%]=fine particle fraction; RF[%]=respirable fraction; MMAD[ $\mu$ m]=mass median aerodynamic diameter; GSD=geometric standard deviation.

System (Molar Ratio)	Treatment	Aerosol Dispersion Performance Parameters				
		ED[%]	FPF[%]	RF[%]	MMAD[ $\mu$ m]	GSD
Pure TOB	fresh	96.2 $\pm$ 0.5	28.5 $\pm$ 3.4	43.7 $\pm$ 4.2	5.0 $\pm$ 1.1	3.3 $\pm$ 0.5
	stored @11% RH	93.6 $\pm$ 2.1	20.3 $\pm$ 3.5	30.3 $\pm$ 4.3	10.6 $\pm$ 2.8	3.6 $\pm$ 0.4
TOB:MAN (1:0.5)	fresh	90.7 $\pm$ 6.7	25.0 $\pm$ 3.2	39.6 $\pm$ 6.5	6.1 $\pm$ 1.6	3.8 $\pm$ 0.2
	stored @11% RH	94.7 $\pm$ 3.1	17.7 $\pm$ 5.0	26.0 $\pm$ 6.2	14.9 $\pm$ 5.3	3.7 $\pm$ 0.0
TOB:PLS (1:0.5)	fresh	86.9 $\pm$ 1.0	47.4 $\pm$ 3.4	82.5 $\pm$ 6.5	1.7 $\pm$ 0.1	1.9 $\pm$ 0.1
	stored @11% RH	91.3 $\pm$ 1.9	28.0 $\pm$ 0.7	37.8 $\pm$ 2.0	6.6 $\pm$ 1.0	3.3 $\pm$ 0.3
TOB:PLS:MAN (1:0.5:0.5)	fresh	93.0 $\pm$ 0.9	42.7 $\pm$ 3.8	66.8 $\pm$ 6.4	2.6 $\pm$ 0.3	2.1 $\pm$ 0.2
	stored @11% RH	95.2 $\pm$ 2.9	11.5 $\pm$ 5.1	17.3 $\pm$ 7.5	28.4 $\pm$ 15.1	4.0 $\pm$ 0.2

**Table 6.2.** Aerosol dispersion performance parameters of SD azithromycin powders (fresh vs stored at three different RH % and 40°C) (mean  $\pm$  SD, n=3). Definition: ED[%]=emitted dose fraction; FPF[%]=fine particle fraction; RF[%]=respirable fraction; MMAD[ $\mu$ m]=mass median aerodynamic diameter; GSD=geometric standard deviation.

System (Molar Ratio)	Treatment	Aerosol Dispersion Performance Parameters				
		ED[%]	FPF[%]	RF[%]	MMAD[ $\mu$ m]	GSD
Pure AZI	fresh	90.3 $\pm$ 5.9	47.0 $\pm$ 3.3	68.1 $\pm$ 4.8	2.3 $\pm$ 0.3	2.3 $\pm$ 0.2
	stored @11% RH	93.7 $\pm$ 1.1	30.3 $\pm$ 1.6	46.1 $\pm$ 3.7	4.0 $\pm$ 0.7	3.0 $\pm$ 0.3
	stored @40% RH	95.1 $\pm$ 2.4	29.7 $\pm$ 2.6	44.5 $\pm$ 3.4	4.6 $\pm$ 0.5	3.2 $\pm$ 0.1
	stored @75% RH	94.9 $\pm$ 1.4	27.4 $\pm$ 1.2	41.4 $\pm$ 1.9	5.1 $\pm$ 0.5	3.2 $\pm$ 0.1
AZI:MAN (1:0.5)	fresh	88.1 $\pm$ 1.3	46.4 $\pm$ 1.0	72.7 $\pm$ 0.7	2.0 $\pm$ 0.1	2.1 $\pm$ 0.1
	stored @11% RH	92.2 $\pm$ 2.4	34.9 $\pm$ 4.3	51.3 $\pm$ 3.1	3.3 $\pm$ 0.2	2.6 $\pm$ 0.2
	stored @40% RH	87.9 $\pm$ 1.4	32.6 $\pm$ 4.0	46.7 $\pm$ 4.3	4.4 $\pm$ 0.8	2.9 $\pm$ 0.4
	stored @75% RH	92.5 $\pm$ 2.3	29.2 $\pm$ 2.2	41.9 $\pm$ 5.5	5.2 $\pm$ 1.5	2.9 $\pm$ 0.4
AZI:PLS (1:0.5)	fresh	95.1 $\pm$ 1.0	37.4 $\pm$ 3.5	72.4 $\pm$ 8.2	2.2 $\pm$ 0.3	2.1 $\pm$ 0.2
	stored @11% RH	89.7 $\pm$ 2.1	38.8 $\pm$ 1.6	57.0 $\pm$ 1.9	4.4 $\pm$ 0.3	2.6 $\pm$ 0.1
	stored @40% RH	89.2 $\pm$ 1.9	35.4 $\pm$ 1.8	52.5 $\pm$ 2.2	5.3 $\pm$ 0.3	2.8 $\pm$ 0.0
	stored @75% RH	95.3 $\pm$ 1.1	19.2 $\pm$ 2.4	29.9 $\pm$ 2.2	14.7 $\pm$ 2.2	3.5 $\pm$ 0.7
AZI:PLS:MAN (1:0.5:0.5)	fresh	96.7 $\pm$ 0.2	32.6 $\pm$ 0.6	48.6 $\pm$ 1.8	4.9 $\pm$ 0.3	2.7 $\pm$ 0.1
	stored @11% RH	95.0 $\pm$ 2.9	36.7 $\pm$ 4.3	65.3 $\pm$ 3.7	3.5 $\pm$ 0.3	2.0 $\pm$ 0.1
	stored @40% RH	94.5 $\pm$ 1.3	31.1 $\pm$ 3.6	53.2 $\pm$ 1.8	4.3 $\pm$ 0.1	2.2 $\pm$ 0.1
	stored @75% RH	100.1 $\pm$ 1.3	14.3 $\pm$ 1.4	25.0 $\pm$ 2.7	14.6 $\pm$ 2.3	3.0 $\pm$ 0.3

## 6.4 Discussion

Moisture may have a significant impact on the physical and chemical stability of aerosol particles, particular for small particles due to their high surface area to volume ratio and the presence of large interstitial space[41]. Moisture may cause irreversible particle agglomeration, leading to failure to generate aerosol particles in respirable size[45]. Individual particles may also undergo changes in crystallinity and polymorphism[41]. Chemical instability could be a potential issue when particle component is hygroscopic[155, 156].

Spray-dried sugar excipients (trehalose and raffinose)[211] and spray-dried sodium cromoglicate[212] aerosol particles have been studied for physical stability under various conditions. The particles were placed in open jars stored in glass chambers, maintained either at 60% RH at 25°C or contained silica gel at 25°C and 4°C. At different time intervals, samples were assessed by SEM, XRPD, DSC and aerosolization. The spray-dried particles, stored at silica gel/25°C or 4°C, exhibited no significant change in particle morphology, physical phase (amorphous), and aerosolization. However, stored at 60% RH/25°C, the spray-dried particles collapsed with a disappearance of porous particle structure, leading to a decrease in the aerosol performance. Singh et al.[213] studied room temperature (60% RH & 25°C for 12 months) and accelerated (75% RH & 40°C for 6 months) stability tests of terbutaline sulfate-loaded chitosan microspheres for pulmonary delivery. At specified time intervals, samples were evaluated for drug content, particle size, FPF. These stability tests were conducted with the powder directly exposed to studied RH %. It was found that the fine particle fraction was slightly decreased at both storage conditions, due to an increase in moisture content and a subsequent increase in particle size after storage. In addition, no significant change in drug content was observed in this study.

El-gendy et al.[214] reported on HPMC capsules preloaded with budesonide nano-cluster dry powder stored at conditions of shelf-life (60% RH & 25°C for 12months) and accelerated (75% RH & 40°C for 6month) stability conditions. The results suggested that the chemical and physical stability were unchanged during storage. The MMAD and GSD values appeared to be constant. FPF of particles at accelerated conditions exhibited no significant change compared to fresh powder. Only a slight decrease in FPF was observed for particles stored at shelf-life storage conditions. Pilcer et al.[215] hand-filled spray-dried tobramycin powder into capsules sealed in aluminum/aluminum blisters. Using moisture-protective packaging, this test method was close to the compliance from FDA guideline on stability test of dry powder for inhalation. The stability study was conducted at 75% RH/40°C, 65% RH/30°C, and 60% RH/25°C. The data revealed that the spray-dried powders remained unchanged in physical phase, drug content, particle size distribution, and FPF.

FDA recommends that stability tests should be performed on the drug product with the packaging configuration (i.e., primary, secondary or additional protective) intended for marketing under the appropriate test storage conditions[209]. As an alternative to packaging suitable for marketing, we employed aluminum foil as a moisture-protective wrapping. Three different RH % were chosen to represent low (11%), medium (40%), and high (75%) values to encompass a range of practical

storage conditions. In order to have at least one standard storage test conditions (75% RH & 40°C; accelerated storage conditions), the temperature of 40°C was chosen in this study. We used XRPD and the NGI to correlate the physical phase stability and aerosol dispersion performance of the particles during storage.

Under the storage stability test conditions of 40% and 75% RH at 40°C, the SD tobramycin formulations partially crystallized into agglomerates (Figure 6.1-6.4) and underwent a color change (on surface layer of agglomerates) as shown in Figure 6.5 at times as short as 2 weeks. The XRPD data (Figure 6.1 to 6.4) indicate that the crystallized component was probably from tobramycin. The hygroscopic nature of tobramycin along with a high tendency to crystallize was also shown in GVS data (Figure 4.13-4.16 in Chapter 4). The color change of the particles strongly indicated that tobramycin chemically degraded. The chemical degradation pathway of tobramycin has been reported[216]. However, another possibility for color change could arise from the presence of a different polymorph for TOB by phase transition (e.g. ROY[217] polymorphs with striking feature in color of red, orange, and yellow). Pilcer et al.[215] suggested no degradation of tobramycin was observed over 12 months by HPLC when the capsule-containing foil blisters were stored at 75% RH and 40°C. As expected, the results in Figure 6.5 clearly suggested that moisture could penetrate into the capsules hand-wrapped with aluminum foil. The storage stability data for SD pure mannitol (not shown) indicate that the hand-wrapped aluminum foil probably delayed rather than prevented moisture penetration into the capsule. As shown in Figure 6.2, the mannitol component possibly partially crystallized into beta polymorphic crystal form in TOB:MAN=1:0.5 at conditions of 40% and 75% RH. However, it was not observed for TOB:PLS:MAN=1:0.5:0.5. These results were possibly due to the mannitol component being enriched in TOB:MAN=1:0.5 compared to TOB:PLS:MAN=1:0.5:0.5. In addition, the possible interaction between phospholipids and mannitol in TOB:PLS:MAN=1:0.5:0.5 may impede mannitol crystallization. A similar mechanism of hydrogen-bonding interaction between trehalose and phospholipids has previously been cited in the literature[218].

Based on XRPD data (Figure 6.1 to 6.4), there was no evident crystal formation in SD tobramycin particles stored at 11% RH and 40°C. However, in comparison to freshly-prepared samples, the aerosol dispersion performance of stored samples significantly decreased. The MMAD values for stored particles were all above 5µm (Table 6.1). This indicated the stored tobramycin particles would not be able to reach deep lung regions at adult airflow rate using the Handihaler<sup>®</sup>. Given in the simplified Equation 6.1, the aerodynamic diameter of a particle is the product of particle diameter and square root of particle density.

$$d_{ae} = \sqrt{\rho_p} d \quad (\text{Equation 6.1})$$

Where  $d_{ae}$  is the aerodynamic diameter of a particle,  $d$  is the spherical particle diameter, and  $\rho_p$  is the particle density.

The increased geometric size ( $d$ ) and/or density ( $\rho_p$ ) of particles could potentially decrease the aerosol dispersion performance of dry powder formulations[41]. It was not likely the RH as low as 11% (comparable to the RH % maintained by desiccants in real DPI products) caused the decrease in aerosol dispersion performance of the

powders. Although the storage temperature 40°C was below the glass transition temperatures (~45 to 50°C) of SD tobramycin formulations, the drug could still be susceptible to crystallization. For instance, the DSC thermogram (Figure 6.6c) of stored SD pure tobramycin exhibited similar characteristics to that of the as received tobramycin rather than that of the SD pure tobramycin. As a classical drug model, amorphous indomethacin has clearly been shown to exhibit sufficient molecular mobility to trigger crystallization over a period of days at temperature 30°C below its  $T_g$ [219]. Therefore it is possible that stored SD pure tobramycin may partially crystallize through the storage period, however, at a level not detected by XRPD. It is also possible that the partially crystallized SD pure tobramycin particles may form particle aggregation through solid-solid bridging (between particles). It has been reported that storage of the excipient (mannitol) crystallization resulted in increased particle size (e.g., interparticle growth) and adverse effects on the aerosol dispersion performance of spray dried protein powders[192]. Moreover, the crystallized aggregates were expected to have a higher density than fresh particles due to the loss of free volume in particles after crystallization with more organized molecular packing. Similar to SD pure tobramycin particles, the possible partial crystallization process was also noticed in other tobramycin containing particles under storage at 11% RH and 40°C.

The XRPD data (Figure 6.7 to 6.8) shows that SD pure AZI and AZI: MAN=1:0.5 lacked long-range molecular order after storage at all conditions through three months. As seen from Table 6.2, the aerosol dispersion performance was lowered with increased RH % after three-month storage for the two formulations. It is well known that interparticulate forces that influence particle interactions during the dispersion of powder aerosols include van der Waals, electrostatic, capillary, and mechanical interlocking forces[41, 63, 64]. The capillary force arises from moisture condensation which form high tensile liquid bridge in the gap between two contiguous surfaces, and becomes dominant as the relative humidity increases[41, 64]. Therefore, capillary force is highly expected to play a key role in aerosolization efficiency for the two formulations exposed to various RH %. Moisture content of the formulations was not measured after storage.

As seen from Figure 6.9 to 6.10, the phospholipid bilayer structure was retained for AZI:PLS=1:0.5 and AZI:PLS:MAN=1:0.5:0.5 during storage. In addition, the mannitol component appeared to lack long-range of molecular order in AZI:PLS:MAN=1:0.5:0.5. After one month storage, the crystalline peaks of AZI dihydrate (identical to XRPD of as received AZI, but with a lower intensity) were observed for AZI:PLS=1:0.5 and AZI:PLS:MAN=1:0.5:0.5 only at conditions of 75% RH and 40°C. These results suggest that the phospholipid component decreased the physical phase stability of azithromycin component in AZI:PLS=1:0.5 and AZI:PLS:MAN=1:0.5:0.5 under these conditions possibly by the association of water molecules with hydrophilic head groups of phospholipids[167]. Presumably, the azithromycin could interact with absorbed water molecules to form azithromycin dihydrate. The hand-wrapped aluminum foil wrapping slowed the rate of physical phase inter-conversion, but did not ultimately stop the process (Figure 6.9 to 6.10). On the other hand, the GVS data (Figure 4.14-4.16 in Chapter 4) did not directly support this hypothesis, although the experimental temperature of DVS (25°C) and stability test (40°C) were different. Both water vapor sorption isotherms of

AZI:PLS=1:0.5 and AZI:PLS:MAN=1:0.5:0.5 were lower than SD AZI:MAN=1:0.5 (no azithromycin crystallization was observed).

With MMAD values of about  $\leq 5\mu\text{m}$ , the FPF value of AZI:PLS=1:0.5 and AZI:PLS:MAN=1:0.5:0.5 stored at 11% and 40% RH, respectively, was relatively comparable to the corresponding fresh samples. However, after the partial crystallization of azithromycin into dihydrate form in particles, the aerosol dispersion performance of stored AZI:PLS=1:0.5 and AZI:PLS:MAN=1:0.5:0.5 at 75% RH was poor as evident by MMAD values of  $\sim 15\mu\text{m}$ . Similar to the discussion in aerosol dispersion performance of SD tobramycin particles, the effect of irreversible crystallization of azithromycin on the particle dispersion may possibly be explained by the hypothesized mechanisms, such as particle aggregation and formation of densified particles.

## 6.5 Conclusions

An indicated, possible chemical degradation of tobramycin by a color change was observed in SD tobramycin particles stored at 40% and 75% RH (at 40°C). Compared to the corresponding freshly-prepared particles, tobramycin particles stored at 11% RH and 40°C exhibited decreased the aerosol dispersion performance. The decreased in aerosol dispersion performance was possibly caused by a low level of partial crystallization of tobramycin in formulations. Possibly due to enhanced capillary force, the aerosol dispersion performance was lowered with increasing RH % for the stored SD pure AZI and AZI: MAN=1:0.5. Stored AZI:PLS=1:0.5 and AZI:PLS:MAN=1:0.5:0.5 from conditions of 11% and 40% RH (at 40°C) showed relatively comparable aerosol dispersion performance to the corresponding fresh samples. The aerosol dispersion performance of phospholipids-containing azithromycin formulations stored at 75% RH (40°C) was highly impeded due to partial crystallization of azithromycin. In addition, the phospholipid bilayer structure was retained in all formulations. Mannitol component was lacking in long-range molecular order in all formulations except for TOB:MAN=1:0.5 stored at 40% and 75% RH (at 40°C).

## Chapter 7 *in vitro* Drug Release

### 7.1 Introduction

The proposed lung surfactant-mimic phospholipids (dipalmitoylphosphatidylcholine (DPPC):dipalmitoylphosphatidylglycerol sodium (DPPG) in 4:1 molar ratio; PLS) and mucolytic agent mannitol (MAN) were selectively incorporated into spray dried (SD) azithromycin (AZI) particles. Despite the advantages from a pharmacological perspective by incorporating PLS and MAN into SD AZI particles, the impact of incorporation of PLS or/and MAN on *in vitro* free drug release profiles of SD AZI particles needs to be assessed.

There are no specific pharmacopoeial methods used for testing *in vitro* drug release from inhaled powders delivered to the respiratory tract[220]. Several *in vitro* drug release methods were reported for pulmonary drug delivery formulations[221-231]. O'Hara et al.[224] reported the suspension of dispersed rifampicin loaded microspheres was centrifuged and an aliquot sample was taken from the supernatant. After the aliquots were removed, the entire supernatant was replenished in order to maintain sink condition. However, it was not clear if the centrifugal force was sufficient to sediment small particles, especially for nano-sized particles. Additionally, it was not experimentally demonstrated that sink condition was maintained by replenishing the supernatant at each time point. In another study, diffusion cell was employed to assess the release of terbutaline sulphate from microspheres into release medium[223]. A membrane (pore size of 0.45 $\mu$ m) was chosen to allow free diffusion of the drug into the receiver and prevent entry of microparticles. Nonetheless, it may have limited use for *in vitro* drug release of SD AZI particles. The SD particles (micro- and nano-sized) and thereafter the possible AZI-containing liposomes (formed from PLS released from SD AZI particles incorporated with PLS) may be sufficiently small to pass through the membrane during the experiment. Moreover, simulated interstitial lung fluid (SILF) and simulated surfactant lung fluid (SSLF) were used as alternative release medium[232-234] besides phosphate buffer, which may make complicate the *in vitro* drug release mechanism.

The *in vitro* drug release method used in this Chapter was relatively simple to carry out. It examined free AZI drug release from SD particles in PBS at pH of 7.4 and temperature of 37°C with initial drug loading below the apparent solubility of SD pure AZI particles. A sink condition[235], defined as the volume of medium at least three times greater than that required to form a saturated solution of a drug substance, was not used mainly due to the detection limit of AZI by high performance liquid chromatogram (HPLC) assay. In addition, without replacing refresh release medium during studies may potentially reduce experimental procedures and minimize experimental errors. Due to the small size and lacking in long-range molecular order of AZI component, it is expected that SD AZI particles may exhibit a relatively fast initial drug release with application of rotation force. The effect of phospholipid bilayer structure with low integrity on significantly lowering drug release rate would not be anticipated for SD AZI particles. Moreover, the drug release of SD AZI particles would possibly be enhanced with the potential presence of molecular

interaction between AZI and MAN components in the SD AZI particles.

## 7.2 Materials and Methods

### 7.2.1 Materials

The spray-dried (SD) formulations of pure azithromycin (AZI), azithromycin:mannitol (AZI:MAN)=1:0.5, azithromycin:phospholipids (AZI:PLS)=1:0.5, 1:1, and 1:2, azithromycin:phospholipids:mannitol (AZI:PLS:MAN)=1:0.5:0.5 and 1:2:2 (in molar ratio) were selected for *in vitro* drug release. The selected formulations were all generated from spray drying employing a 50% pump rate (15 ml/min). Phosphate buffered saline (PBS) tablets were purchased from Sigma (USA). The phosphate buffer with concentration of 0.01M was prepared by dissolving 1 tablet in 200ml of water. The organic solvents (methanol, chloroform, and acetonitrile) used were all HPLC grade. Methanol and chloroform were obtained from Fisher Scientific (USA). Acetonitrile was obtained from Acros (USA). Millipore deionized water was used in this study.

### 7.2.2 Methods

The *in vitro* drug release of selected formulations was conducted in polyethylene (PE) vials (anti-static, 20ml; PerkinElmer, USA). In order to achieve initial drug loading below the apparent solubility of SD pure AZI particles, certain amount of SD powder equal to ~8mg of pure AZI were suspended in 20ml preheated PBS (37°C) in PE vials. The suspensions were kept rotated by using Labquake tube shaker (Barnstead Thermolyne). The *in vitro* drug release was conducted at 37°C in a temperature well-controlled incubator (Precision, USA). At each planned time point, 0.5ml of drug release medium was taken from PE vials. Sufficient sample of free AZI was collected in filtrate after passing through a regenerated cellulose membrane of Amicon<sup>®</sup> Ultra (Millipore Corporation, USA) with 30K molecular weight cutoff (MWCO) by using Eppendorf centrifuge 5417R (USA) at 14,000g (based on the recommended method from the manufacturer of filters) for 1min. The concentration of free AZI was determined by using high performance liquid chromatogram (HPLC) with UV detector at 210nm of wavelength. The HPLC chromatograms were acquired by Shimadzu CLASS-VP V5.032. All formulations were done in triplicate.

## 7.3 Results

### 7.3.1 Validations

#### 7.3.1.1 Linearity of HPLC Assay for Azithromycin

The employed high performance liquid chromatogram (HPLC) system consisted of an LC compact system (Shimadzu, Japan), and equipped with an autosampler (SIL-10AD VP), a binary pump (LC-10AD VP), and a UV detector (SPD-10A VP). The HPLC analysis for AZI concentration determination was slightly modified from a previously published method[236]. The column was a Luna C18(2) (5μ, 100A,



250×4.60mm) (Phenomenex, USA) operated at 30°C. The analytical mobile phase, composed of potassium phosphate dibasic-acetonitrile (35/65%, v/v), was passed through the analytical column at a flow rate of 1.0 mL/min with the UV detector wavelength set at 210nm. The pH of potassium phosphate dibasic (0.05 mole/L) was adjusted to 8.2 with 20% phosphoric acid. 30µL sample was injected into HPLC.

To validate the HPLC assay, three independent groups of standard solutions were prepared with concentration of 1000, 400, and 100 µg/mL, respectively. A typical chromatogram of AZI parent compound is shown in Figure 7.1. The coefficients of variation (CV) for the peak height and peak area for the successive injections of a single standard were 3.1% and 3.1%, respectively. Peak carry-over was not observed. The mean and CV of mean response factors for the standard concentrations are shown in Table 7.1. The student t-tests for linearity were performed to compare the mean response factors of standard solutions with different concentrations. At degrees of freedom of 4, the t statistic values for 1000 vs 400 µg/mL, 1000 vs 100 µg/mL, and 400 vs 100 µg/mL were 0.783, 1.471, and 0.838, respectively. This suggests that there was no statistically significant difference between the two mean response factors at the p=0.025 significant level (degree of freedom: 4,  $t_{0.975}=2.776$ ).

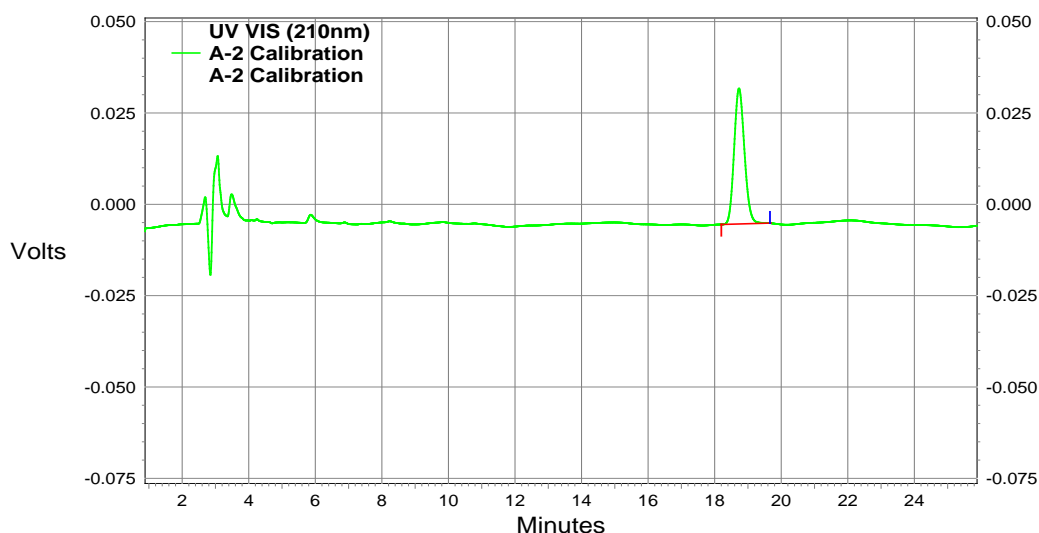


**Figure 7.1.** A representative HPLC chromatogram of a standard azithromycin solution.

**Table 7.1.** The mean response factor and coefficient of variance for each standard azithromycin solution.

Standard Concentration (µg/mL)	Mean Response Factor (mL/µg)	Coefficient of Variance (%)
100	1959	3.4
400	1919	2.6
1000	1884	3.1

### 7.3.1.2 Stability Indicating Capability of HPLC Assay for Azithromycin

The HPLC assay validated in Section 6.3.1.1 was tested for ability to resolve degradation products from the parent compound of AZI. A 1:5 dilution of stock solution (5 mg/mL in methanol) in (a) 0.1N HCl, (b) 0.1N NaOH, and (c) deionized H<sub>2</sub>O were prepared. The storage condition was 25°C for all solutions. Additionally, a H<sub>2</sub>O solution at 37°C was studied. All samples were light-protected during the study. There were 5 vials in each study condition. At planned time points, samples were withdraw and analyzed by the same HPLC assay.

The data indicated that the validated HPLC assay was able to differentiate the AZI parent molecule and its degradation products, which is similar to the report[236]. A typical chromatogram of AZI is shown in Figure 7.2. The retention time of azithromycin parent molecule peak was ~16min, while the retention times of azithromycin degradation products ranged from ~5 to 7min. The stability indicating assay suggests that ~21%, ~24%, ~8%, and ~3% of AZI degraded in HCl (25°C), NaOH (25°C), H<sub>2</sub>O (37°C), and H<sub>2</sub>O (25°C), respectively.

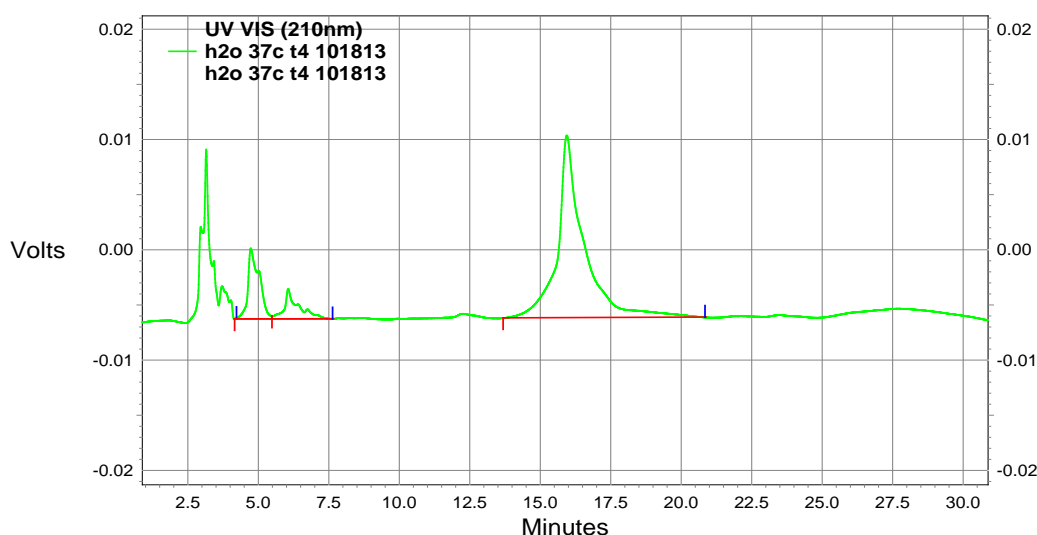


**Figure 7.2.** A representative HPLC chromatogram of an azithromycin solution in stability indicating assay.

### 7.3.1.3 Selection of Centrifugal Filter Unit

The centrifugal filter units with three different molecular weight cutoff (MWCO) sizes (3K, 10K, and 30K, respectively) were used to assess possible drug adsorbance on the filter membrane (regenerated cellulose). Three independent AZI standard solutions with concentration of ~300 µg/mL were used in this assay. Three centrifugal filter units of each MWCO size filled with each standard solution were immediately centrifuged. The filtrates were analyzed by HPLC assay. In addition, the standard solutions were directly analyzed by HPLC assay as a control group. The data are summarized in Table 7.2.

**Table 7.2.** The azithromycin adsorbance data for centrifugal filter units.

Standard No.	Solution	Control (µg/mL)	3K (µg/mL)	10K (µg/mL)	30K (µg/mL)
1		295	201	-	292
2		299	181	280	286
3		297	185	305	-
Mean		297	189	293	289
SD		1.9	10.6	17.7	4.5

The differences between the mean AZI drug concentration in solution filtered through from 10K and 30K (one value missing from each group) and control group were not statistically significant (t-test,  $\alpha=0.05$ ). The results of the 3K filter unit group suggests high drug adsorbance on regenerated cellulose since the mean concentration in the filtrate was significantly lower than the control. The high total membrane surface area of 3K, compared to 10K and 30K, may be responsible for the decreased concentration after filtration. The 30K filter unit was selected for the AZI *in vitro* drug release study due to its low adsorbance variability compared to 10K filter unit.

#### 7.3.1.4 Selection of Release Medium Container

In order to choose a suitable type of drug release medium container, the 20ml glass scintillation and polyethylene (PE) vials were compared for their potential drug adsorbance. Two vials of each type were filled with a standard AZI solution with concentration of  $\sim 507 \mu\text{g/mL}$  and rotated in Labquake tube shaker at  $37^\circ\text{C}$ . At time points of 3h and 24h, samples were withdrawn and analyzed by HPLC assay.

The data are shown in Table 7.3. Apparently PE vials adsorbed less of the drug ( $\sim 3$  to  $4\%$ ) at each time point compared to glass scintillation vials. Therefore, PE vials were chosen for AZI *in vitro* drug release studies. The reason why two type vials behaved differently was not explored.

**Table 7.3.** The azithromycin absorbance data for release vials.

Vial Type	Time Points	Concentration (µg/mL)	Percentage (%)
PE Vial	3h	487	96.0
	24h	492	97.0
Scintillation Vial	3h	353	69.7
	24h	256	50.4

#### 7.3.2 Release Data

Figure 7.3 shows the *in vitro* apparent release profile of SD pure AZI formulation. There was a fast burst observed with  $\sim 45\%$  of drug being release at 5min. The relatively high variation of drug release at first 40min was possibly due to poor

dispersion of SD pure AZI powder in the release medium and due to the sampling frequency. Thereafter particles continuously released the drug until 60min with ~92% released. The drug release profile appeared to approach a plateau after 1h.

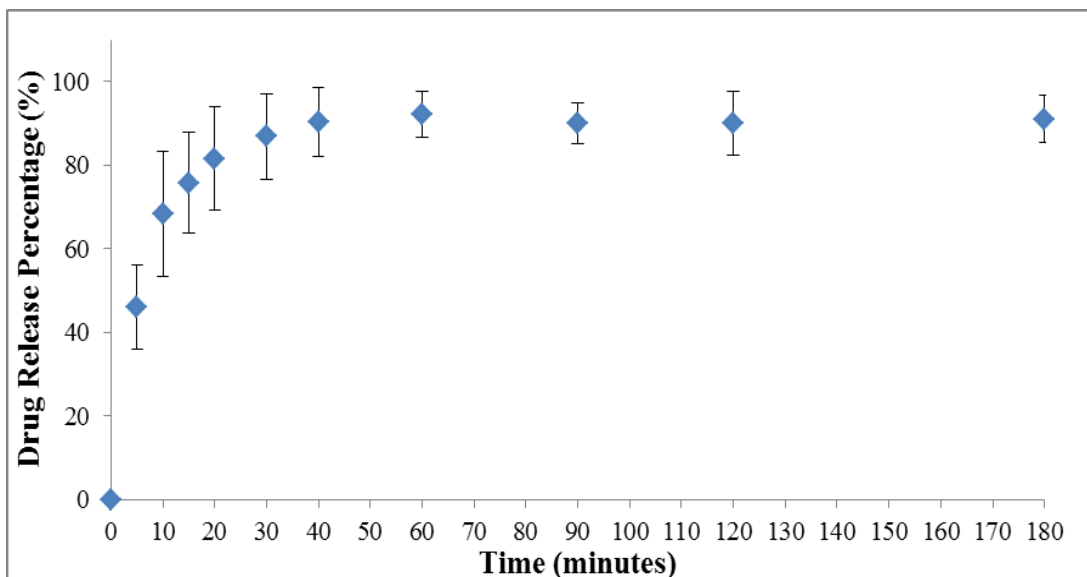
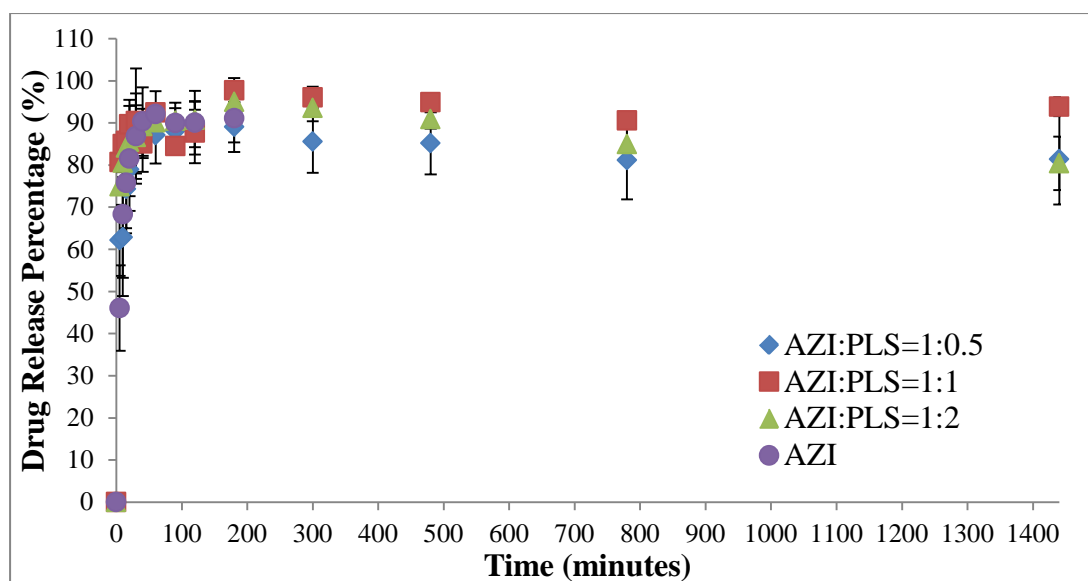


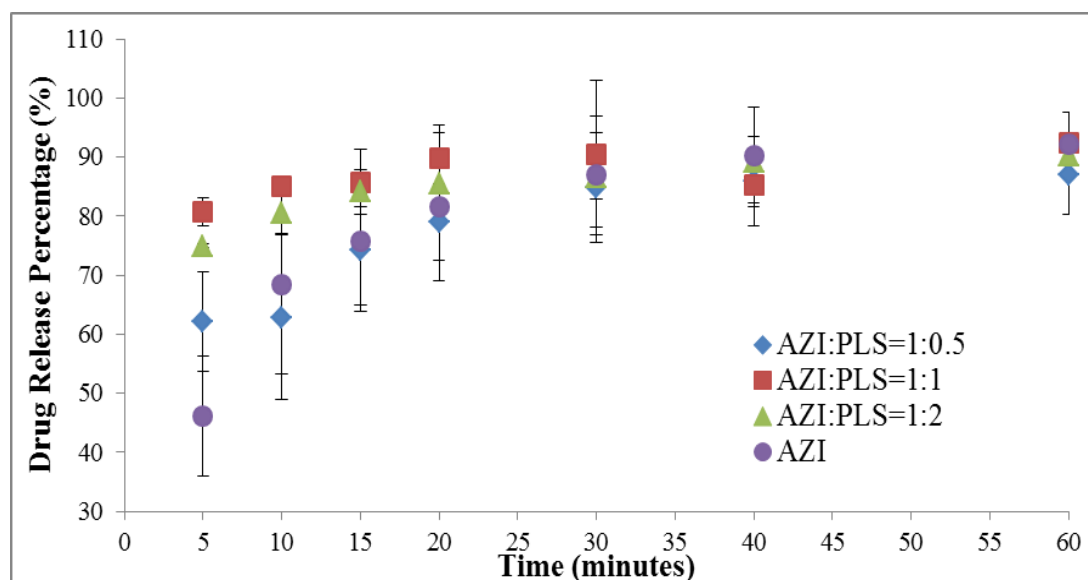
**Figure 7.3.** The apparent *in vitro* release profile of SD pure azithromycin formulation in PBS at 37°C.

### 7.3.2.1 Effect of Phospholipids on Apparent *in vitro* Release of Azithromycin

Compared to SD pure AZI, the effect of PLS on *in vitro* drug release was studied in the formulations of AZI:PLS=1:0.5, 1:1, and 1:2 for up to 24h. The AZI:PLS formulations released AZI in similar fashion with approximately ~85% release in the first 30min (Figure 7.4b). The formulations reached highest release percentage (average of ~94%) at 3h and, thereafter, followed by a slight loss of drug up to 13h (Figure 7.4a). Incorporation of PLS into SD particles significantly enhanced initial release in the first 5min (Figure 7.4b). Within AZI:PLS formulations, AZI:PLS=1:1 had statistically relatively higher release percentage in the first 10min, followed by AZI:PLS=1:2 and AZI:PLS=1:0.5, respectively (Figure 7.4b).



(a)



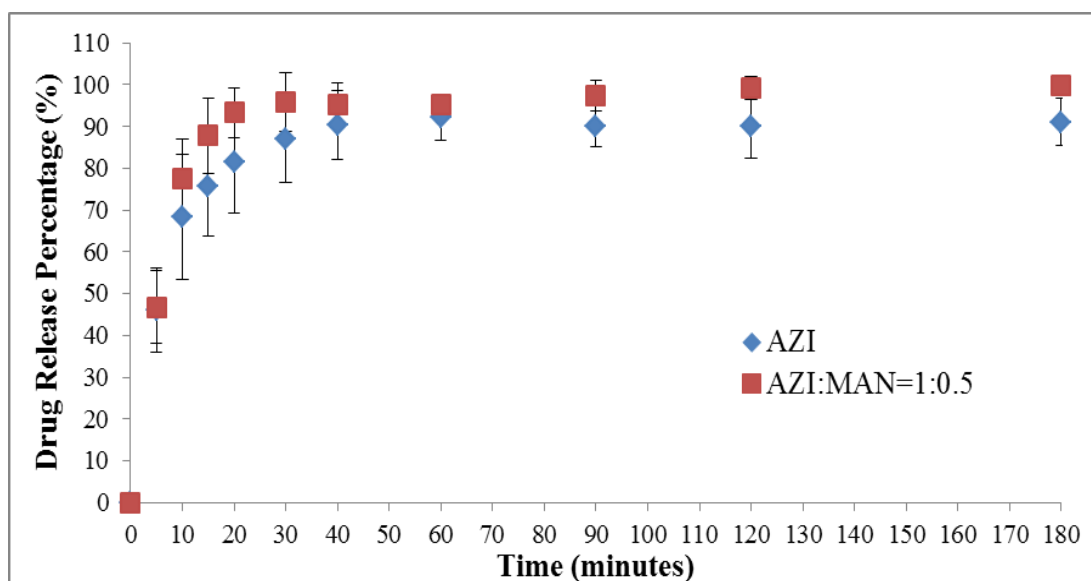
(b)

**Figure 7.4.** The apparent *in vitro* release (a) full profiles and (b) first 60min profiles of azithromycin:phospholipids vs azithromycin in PBS at 37°C.

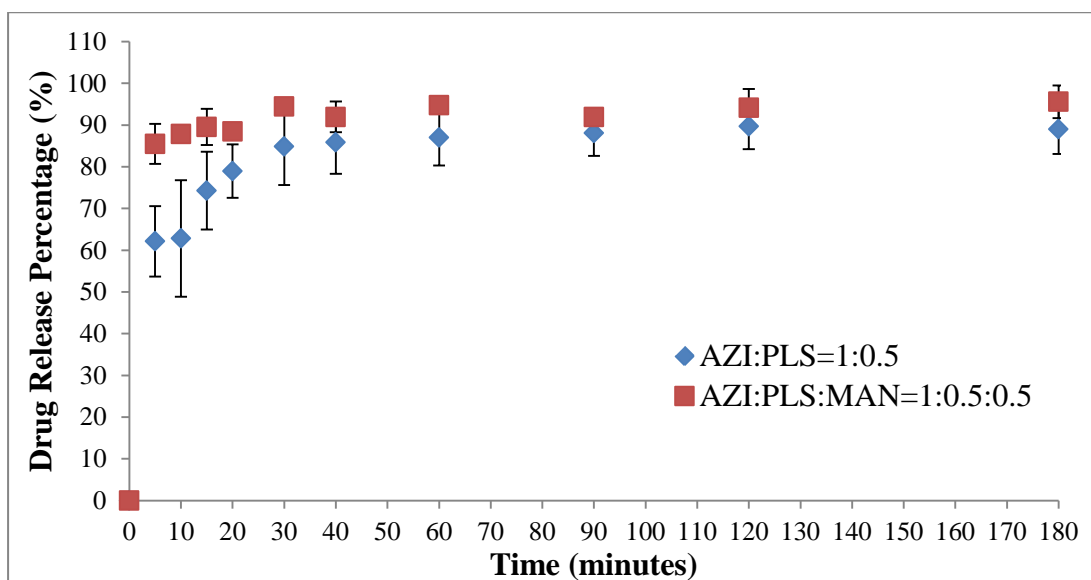
### 7.3.2.2 Effect of Mannitol on Apparent *in vitro* Release of Azithromycin

To examine the effect of MAN on *in vitro* AZI release, AZI vs AZI:MAN=1:0.5, AZI:PLS=1:0.5 vs AZI:PLS:MAN=1:0.5:0.5, and AZI:PLS=1:2 vs AZI:PLS:MAN=1:2:2 were paired, respectively. The MAN component appeared to have no significant effect on the both corresponding formulations of SD pure AZI (Figure 7.5a) and AZI:PLS=1:2 (Figure 7.5c). However, the comparison of AZI:PLS=1:0.5 vs AZI:PLS:MAN=1:0.5:0.5 (Figure 7.5b) revealed that the

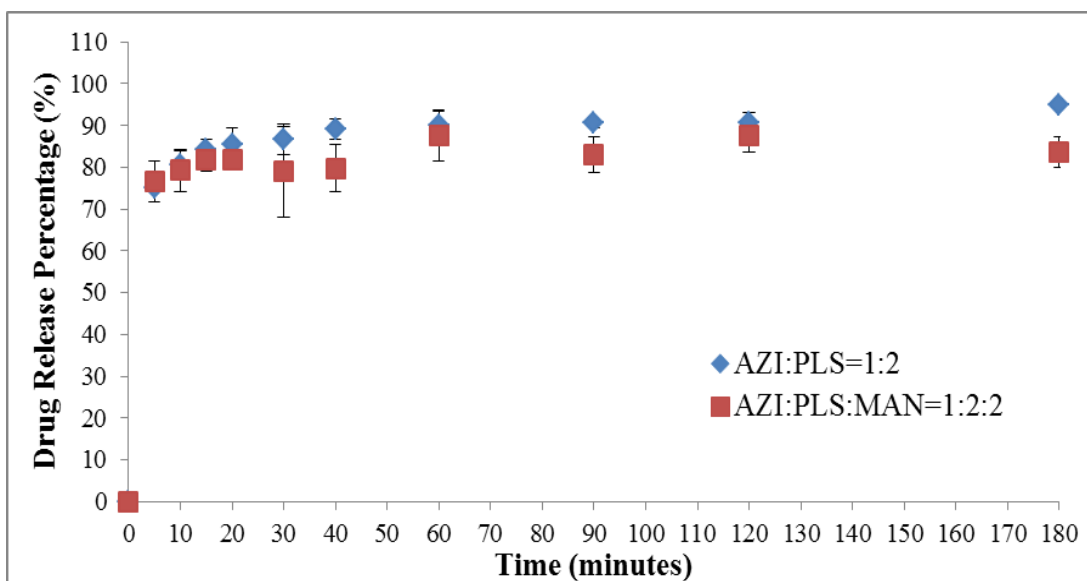
incorporation of MAN component statistically significantly enhance the AZI release for the up to 30min. After 30 minutes, there was no difference in the release profiles.



(a)



(b)



(c)

**Figure 7.5.** The apparent *in vitro* release profiles of (a) azithromycin vs azithromycin:mannitol=1:0.5, (b) azithromycin:phospholipids=1:0.5 vs azithromycin:phospholipids:mannitol=1:0.5:0.5, and (c) azithromycin:phospholipids=1:2 vs azithromycin:phospholipids:mannitol=1:2:2 in PBS at 37°C.

## 7.4 Discussion

### 7.4.1 Validation of Release Assumptions

Several assumptions are made in the *in vitro* drug release study: 1) degradation of AZI does not affect release profiles; 2) only free drug concentration of AZI is determined in release study; 3) three components are all in one particle. In order to validate the assumptions, several experiments or calculations were conducted to validate the results shown in Figure 7.3-7.5.

#### 7.4.1.1 Validation of Degradation of AZI Does Not Affect Release Profiles

As Section 6.3.1.2 suggested, AZI may degrade under conditions in *in vitro* drug release. In order to assess the degradation effect on drug release profiles, the degradation rate constant needs to be obtained. The degradation rate constants of AZI (at 25°C and 37°C) were estimated based on the findings in the report[236] and by using Arrhenius equation (Equation 7.1).

$$\ln k_{\text{obs}} = \ln A - \frac{E_a}{RT} \quad (\text{Equation 7.1})$$

Where A is the frequency factor,  $E_a$  is the energy of activation, R is the universal gas constant, and T is the absolute temperature. Assuming the degradation reaction mechanism (base catalysis with positive slope) is the same at pH value of 6.3 and 7.4 (Figure 3 in [236]) and given that the values of  $E_a$  (96.8 kJ/mol at pH value of 6.3) and

$k_{80}$  ( $9.37 \times 10^{-4} \text{ min}^{-1}$  at pH value of 7.4 and at  $80^\circ\text{C}$ ) (recalculated from the value from Figure 3 in [236]), the reaction rate constants of  $k_{25}$  (at  $25^\circ\text{C}$ ) and  $k_{37}$  (at  $37^\circ\text{C}$ ) were calculated to be  $\sim 2.13 \times 10^{-6} \text{ min}^{-1}$  and  $\sim 9.66 \times 10^{-6} \text{ min}^{-1}$ , respectively.

$$C = C_0 e^{-kt} \quad (\text{Equation 7.2})$$

The exponential decay equation for the integrated first-order rate law is shown in Equation 7.2. Where  $C$  and  $C_0$  are the concentrations of drug at time  $t$  and time 0 (initial time),  $e$  is exponential number,  $k$  is first-order reaction rate constant, and  $t$  is release time.

To determine if putative degradation had any effect on the release profiles, the values for AZI (Figure 7.3) were modified according to Equation 7.2. The two corrected profiles were named as “one-correction” profile and “two-correction” profile, respectively. The one-correction profile was carried out to correct for the possible degradation of AZI during *in vitro* drug release using  $k_{37}$  (at  $37^\circ\text{C}$ ) and collection time during the study. The two-correction method was used to correct for possible degradation of AZI both in the time of *in vitro* drug release by using  $k_{37}$  (at  $37^\circ\text{C}$ ) and the time between the samples were collected and analyzed by HPLC using  $k_{25}$  (at  $25^\circ\text{C}$ ). The data suggest that there were no significant differences between the apparent, “one-correction” and “two-correction” profiles. Similar results were validated for other AZI formulations with release up to 24h. These results suggest that no excessive degradation of AZI occurred during the time of release assay. Therefore, only the apparent *in vitro* drug release profiles of formulations were plotted in Results Section.

#### 7.4.1.2 Validation of Only Free Drug Concentration of AZI Is Determined in Release Study

It has been assumed that only free AZI was present in the filtrate. In order to determine if phospholipids-associated AZI was also present in the filtrate, the ability of the filter to prevent passage of phospholipids was studied. In order to detect the presence of the phosphatidylcholine (PC) headgroup irrespective of hydrophobic chain type for PLS content in filtrate, AZI:PLS=1:1 formulation was assessed by HPLC using an evaporative light scattering detector (ELSD) as previously reported by Modi et al.[237]. At 24h *in vitro* drug release, the release medium was collected and centrifuged at 5,000g for 5min through a 30K filter unit of 15ml to obtain 10mL filtrate. The filtrate was immediately dried by nitrogen gas and reconstituted in 1mL chloroform. The precipitated phosphate salt (from PBS release medium) was filtered through polytetrafluoroethylene (PTFE) syringe filter (organic solvent resistant, 0.22 $\mu\text{m}$  pore size; Tisch Scientific, USA) and a gas-tight glass syringe. The standard DPPC and DPPG solutions were prepared by dissolving known amounts of DPPC and DPPG in chloroform, based upon solubility limit and ELSD assay calibration range for distearoylphosphatidylcholine (DSPC)[237]. The final concentrations for DPPC and DPPG in each standard solution were prepared as 0.3 mg/mL and 0.05 mg/mL, respectively. The pure chloroform, chloroform through PTFE filter, and AZI solution in chloroform were also used as negative controls.



Shown in Figure 7.6, is the ELSD chromatograms (last two chromatograms at bottom) for the pure chloroform and chloroform through the PTFE syringe filter. No significant peaks were detected. AZI standard showed a peak with a retention time of approximately 1.75min. The DPPG standard showed no peak over 10min, suggesting that the concentration may be below the limit of detection. The DPPC standard exhibited a peak with a retention time at ~3min.

On the representative chromatogram of AZI:PLS=1:1 (named as A:L=1:1 in Figure 7.6) with high injection volume (50 $\mu$ L), the first peak (with retention time of ~1.9min) and the second peak (with retention time of ~2.5min) were possibly from the parent AZI and the degradation product(s) of the parent AZI. With low volume injection (et. ~2 $\mu$ L; data not shown), the possible degradation product(s) peak was not detected by this assay. These results demonstrate that the DPPC, the major phospholipid in the formulation, was not detected in the AZI:PLS=1:1. Therefore, there was no PLS penetrated into filtrate and the AZI concentration analyzed by the HPLC assay was only from free drug.

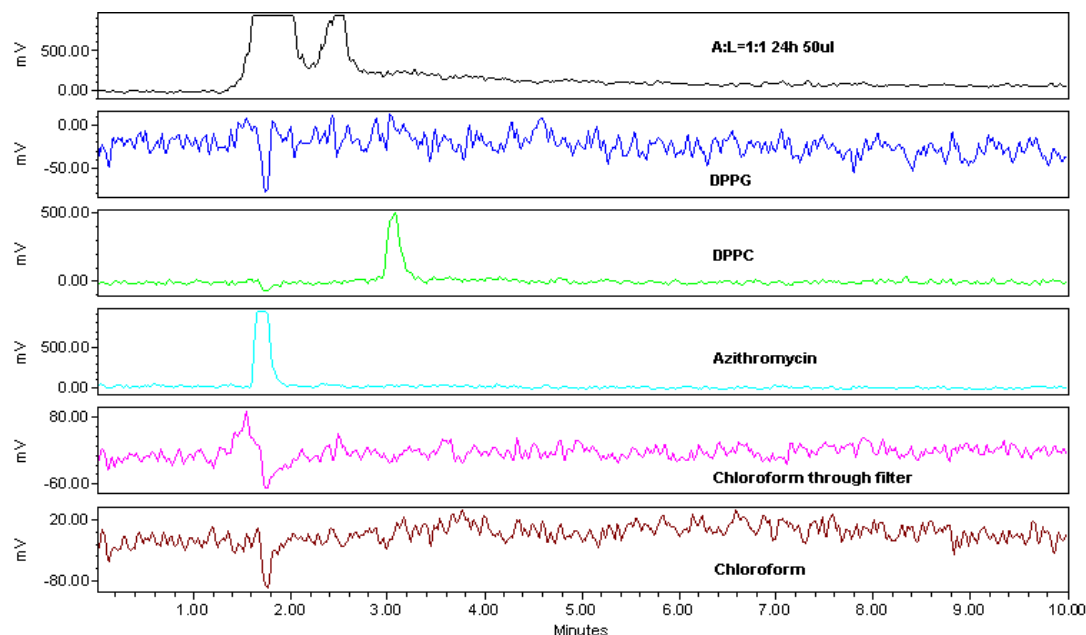


**Figure 7.6.** The representative HPLC chromatograms of the samples in phospholipids assay.

#### 7.4.1.3 Validation of Three Components Are All in One Particle

It is interesting to know that whether all three component (AZI, PLS, and MAN) are all in one particle. Due to limitation of particle size (approximately > 2 $\mu$ m), it is difficult to verify it with current available techniques. However, it is still reasonable to assume that all three components are present in one particle. The starting solution was prepared by dissolving all three components in methanol spray drying. Therefore it is expected that, in the process of atomization, each of the droplets generated should possess all three components since they were in uniform methanol dilute solution. Thus the solid-state particle was highly expected to possess the three components after the droplet was dried.

### 7.4.2 Drug Release

It was noticed that there was ~90 to 100% of drug release from formulations that was achieved in *in vitro* drug release in PBS at 37°C. The degradation and absorbance of the drug were not likely to be the reasons to explain why there was drug remaining during release study as we have discussed. AZI has limited intrinsic solubility with ~200 µg/mL at 25°C[238, 239]. A water solubility of 514 µg/mL of AZI was also predicted[240]. Our preliminary data of as-received AZI (in dihydrate rich) and SD pure AZI showed solubility of ~225 and ~490 µg/mL in water at 25°C, respectively. The preliminary data highly agreed with reported values. The SD pure AZI particles were amorphous rich and was expected to have extremely high surface area. Therefore, the apparent solubility of SD pure AZI was much higher than its intrinsic solubility of crystalline AZI. The AZI loading with 400 µg/mL was selected for SD AZI formulations in the study. Although the selected drug loading (400 µg/mL) was lower than the apparent solubility (~490 µg/mL), it was higher than the intrinsic solubility (~200 µg/mL). Moreover, the solubility of azithromycin at 37°C was reported to be slightly lower than the one at 25°C[239]. Therefore, the remaining percentage of AZI loading possible either was not dissolved or precipitated after being dissolved during release.

#### 7.4.2.1 Effect of Phospholipids on Apparent *in vitro* Drug Release of Azithromycin

In Section 6.4.1., compared to SD pure AZI, relatively statistically significant fast initial (at 5min) free drug burst was observed for the SD AZI particles containing PLS components. This result was somewhat surprising as it was expected that the presence of phospholipids might slow the release process. At present, it is only possible to speculate about the mechanism driving these results. Surfactants are well known to have wetting effect[241] on hydrophobic drug particles. It was observed that the PLS incorporated SD AZI particles were well suspended in release medium in comparison to the particle floating issue for SD pure SD AZI, especially at the initial time points. This possibly resulted in a fast burst release for SD AZI with PLC incorporated with ~72% at 5min. In addition, it could also be reasonably assumed that high fraction of AZI molecules located on the particle surface, although drug release is an indirect means of attempting to assess component location and direct methods would need to be used to assess surface components. To help understand the proposed effect of PLS on AZI release, Figure 7.7 illustrates three possible particle structures.

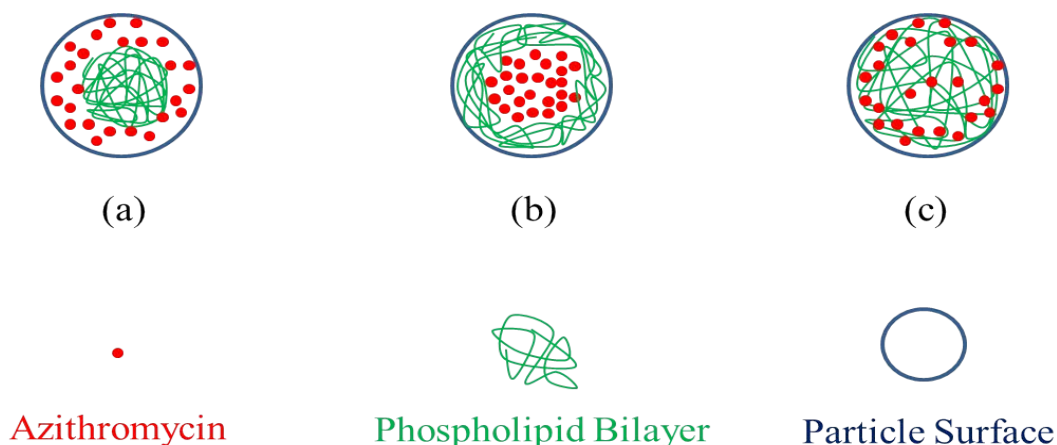


**Figure 7.7.** The proposed scenarios of location of azithromycin drug molecules and phospholipid bilayer in SD azithromycin:phospholipids particles.

Two extreme particle structures with phase separation are shown by structure (a) and (b) in Figure 7.7. The AZI phase either surrounds phospholipid bilayer structure (structure (a)) or is covered by phospholipid bilayer structure in particle (structure (b)). The possibility of phase separation particle structure was ruled out by DSC (Table 4.3 & 4.4 in Chapter 4) and XRPD (Figure 4.3 & 4.4 in Chapter 4) data. The data suggests that the integrity of phospholipid bilayer structure was diminished compared to intact one from pure SD PLS particles. In addition, no delay at early time points in drug release profiles further indicates the possible AZI:PLS phase separation in particle structure (Figure 7.7b) was not likely to be the case. As shown in Figure 7.7c, the *in vitro* drug release data of AZI:PLS might suggest the possibility that the phospholipid bilayer is uniformly distributed in the SD particle and AZI molecules are predominately located on or close to the particle surface. However, it is equally possible that AZI and PLS are both evenly distributed within the particle, possibly supported by the confocal Raman microscopy data (not shown).

Other factor might also influence the rate of AZI release. SEM micrograph of the SD AZI:PLS=1:2 particles (Figure 3.4d in Chapter 3), with aerodynamic diameter  $>5\mu\text{m}$  (Table 5.6 in Chapter 5), appeared to show fused aggregates. The formation of aggregates would dramatically decrease the area-to-volume ratio especially for particles under micron-sized. AZI:PLS=1:1 and 1:0.5 particles with better particle formation (Figure 3.4e & 3.4f in Chapter 3) released more AZI for the first 10min. Perhaps the relatively lower area-to-volume ratio of AZI:PLS=1:2 may offset the wetting effect from PLS. Thus the apparent drug release profile of AZI:PLS=1:2 appeared to be somewhere between AZI:PLS=1:0.5 and 1:1 rather than exhibiting fastest initial release (up to 10min). The slight loss of drug after 3h could be attributed to partition of released drug into the liposomes in PBS from the released PLS, or into the PLS matrix in dispersed particles. The similar slopes for drug loss were not well understood given the fact that SD particles had different PLS content. Apparently the slight loss of drug ended at 24h could possibly suggest the equilibrium among the release of free AZI from SD particles, the formation of liposomes, and the partition of free azithromycin molecules into liposomes or into PLS matrix in SD particles had been reached. This study may also indicate the release of AZI and the release of PLS from particles may follow different release modes with time.

#### 7.4.2.2 Effect of Mannitol on Apparent *in vitro* Drug Release of Azithromycin

The addition of MAN to AZI:PLS=1:0.5 significantly enhanced MAN release in timescale up to 30min. Similar primary particle size (AZI:PLS=1:0.5 *vs* AZI:PLS:MAN=1:0.5:0.5) (SEM: Figure 3.4f *vs* Figure 3.5h in Chapter 3; Size: Table 3.7 *vs* Table 3.8 in Chapter 3) suggests the enhanced dissolution of free AZI may result from another factor. One possibility is an increased amorphous fraction of AZI in the MAN-containing sample. MAN has been reported to exhibit intermolecular hydrogen bonding in solid dispersion[242, 243]. The possible increased amorphous fraction could arise from the hydrogen bonding interaction between AZI and MAN in the SD AZI:PLS:MAN=1:0.5:0.5 particles. Support for this hypothesis is the observation of an increase in glass transition temperature of AZI from ~76 to ~85°C was observed by adding MAN to AZI:PLS=1:0.5. This change in glass transition temperature could be possibly attributed by an increased amorphous phase of AZI in AZI:PLS:MAN=1:0.5:0.5 compared to AZI:PLS=1:0.5. The addition of MAN had no significant effect on the profiles of *in vitro* AZI release to SD pure AZI and AZI:PLS=1:2. In addition, AZI:PLS=1:2 and AZI:PLS:MAN=1:2:2 formulations were excipient abundant. Therefore, the addition of MAN to AZI:PLS=1:2 had no significant effect on the amorphous content of AZI component in particles. However, as discussed in Section 6.5.2.1, it could not be ignored that the effect of MAN on apparent *in vitro* drug release could essentially originate from how particle wettability is changed.

### 7.5 Conclusions

In general, the SD azithromycin formulations had a burst release (~50 to 80% at 5min) and approached a plateau (until ~30 to 60min) in PBS at 37°C *in vitro* drug release profiles. The AZI:PLS containing phospholipids exhibited a faster initial release (at 5min) in comparison to SD pure AZI particles. At the expense of increased particle size, the increased wetting effect from increased phospholipids in AZI:PLS could be minimized in the drug release profile. Data indirectly suggest that AZI may possibly predominantly locate on the surface of particle with a uniform distribution of phospholipid bilayer structure in particle. However, it is equally possible that AZI is uniformly distributed with PLS as confocal Raman microscopy data may indicate. As mannitol incorporated into particles, a relatively faster initial drug release could be achieved. This could possibly result from the increase fraction of azithromycin amorphous phase existing in particles with hydrogen bonding interaction between mannitol and azithromycin in solid dispersion. Overall the *in vitro* drug release of azithromycin was mainly dependent upon the particle composition and corresponding particle size.

## Chapter 8 Summary and Conclusions

### 8.1 General Conclusions

The work in this dissertation showed that multi-component dry powder aerosols of (non-destructive) mucolytic agent, antimicrobial drug, and lung surfactant mimic phospholipids have been successfully produced by spray drying from organic solution. In general, the microparticulate and nanoparticulate (typically 0.5 to 2  $\mu\text{m}$ ) multi-component respirable aerosol particles possessed essential particle properties suitable for deep lung penetration by sedimentation and diffusion, respectively. The essential particle properties (e.g., narrow size distribution (typically 0.5 to 2  $\mu\text{m}$ ), spherical particle and smooth surface morphologies, and low water content (or water vapor sorption)) are expected to minimize interparticulate forces such as van der Waals forces, electrostatic forces, mechanical interlocking, and capillary forces. As a result of these properties, the majority of spray-dried (SD) multi-component aerosols (including two-component and three-component systems) exhibited ability of deep lung penetration with values of mass median aerodynamic diameter (MMAD) and fine particle fraction (FPF) being approximately less than 5.0  $\mu\text{m}$  and above 30.0% up to 60.4%, respectively.

In the studied formulation compositions of multi-component particles with phospholipid incorporation, phospholipid bilayer structure was retained after spray drying. It was observed that the intensity of phospholipid bilayer structure was mainly dependent upon the biophysical properties of incorporated antimicrobial drug. A relatively lower intensity of phospholipid bilayer structure was observed for azithromycin formulations compared to tobramycin formulations. This may possibly explain the observed *in vitro* drug release profiles of phospholipid-containing azithromycin formulations with no characteristics of extended drug release under the conditions studied and using the particular *in vitro* release method described. In fact, phospholipid-containing azithromycin formulations exhibited an enhanced burst release likely due to the wetting effect from phospholipids in the particles.

The other components in SD multi-component particles are shown to lack long-range molecular order. Partial crystallization of azithromycin (starting after one-month storage at 40°C) in (phospholipid-containing) particles stored at 75% relative humidity (RH) strongly impeded aerosol dispersion performance of the SD powder. However, the SD azithromycin particles stored at conditions of 11% and 40% RH retained the ability of deep lung penetration. Tobramycin in SD multi-component particles were chemically unstable with an indication of color change at 40% and 75% RH. Although no evident phase transition was detected, SD tobramycin multi-component particles stored at 11% RH exhibited MMAD > 5  $\mu\text{m}$ . This may be caused by the well-known hygroscopic nature of tobramycin. Mannitol in SD multi-component formulations remained unchanged in physical phase after storage at all studied conditions.

## 8.2 Future Work

To further support the specific application of SD multi-component aerosol particles for chronic infection diseases in the deep lungs, some future studies might need to be carried out.

### 1) Expand the molar ratio for SD multi-component particles

In this dissertation, high (antimicrobial) drug loading formulation was focused on with the goal of achieving high local concentrations while reducing the aerosol treatment burden and the potential for causing bacterial resistance in the lungs. Patients with chronic infections in deep lungs may have various conditions during disease progress[244, 245]. Therefore, there are some demands on tailoring formulation compositions specifically treat individual patient with certain disease conditions in various stages. However, expansion of the formulation compositions may possibly have a significant change in physicochemical properties of the formulations, affecting aerosol dispersion performance, storage stability, and *in vitro* drug release profiles of the powders. Therefore, physicochemical evaluation and formulation performance for SD multi-component formulations with expansion in molar ratios are important to be studied.

### 2) Equilibrium spreading pressure of phospholipid-containing SD particles by using Langmuir surface biophysical analysis

Pulmonary surfactants can lower the surface tension of interfacial layer. Studies has been shown that pulmonary surfactants promote the displacement of particles from air to mucus or aqueous phase and that the extent of particle immersion depends on the surface tension of the surface active film[246-249]. The data showed that a greater immersion of the latex particles into the subphase of an alveolar lining layer could be achieved by lowering the surface tension of the layer. The enhancement in particle penetration into mucus would potentially help decrease bacteria (such as *Pseudomonas aeruginosa* colonized in mucus with formation of biofilm[250]) density in mucus as particles could release antimicrobial drug to the sites where bacteria reside. The enhancement of particle penetration into mucus may only benefit for the subsequent dosing in our study. The equilibrium spreading pressure[251-253] ( $\pi_e = \gamma_0 - \gamma_{eq}$ ;  $\gamma_0$  and  $\gamma_{eq}$  are the surface tension before and after adding formulation, respectively), a measure of surface tension change, will be examined with phospholipids-containing SD particles. The method has been established by our research group[251, 253] using Langmuir surface analysis. In addition, surface tension in deep lung region may play a critical role in respiratory control, regulation of pulmonary immunity, and etc.[9, 10]. Therefore, it will be also necessary to monitor the surface tension ( $\gamma_{eq}$ ) of air-liquid interface as SD multi-component particles release phospholipids. The studies will be conducted on the mucus from patients with chronic infections in deep lungs (or phosphate buffer saline (PBS) at PH 7.4, and *in vitro* model of lung fluid[233]) at 37°C.

### 3) *in vitro* release of mannitol and phospholipids from SD multi-component particles

Mannitol and phospholipids (dipalmitoylphosphatidylcholine (DPPC):dipalmitoylphosphatidylglycerol (DPPG)=4:1 (molar ratio)) are proposed to act as (non-destructive) mucolytic agent and lung surfactant mimic phospholipids for

the treatment of chronic deep lung infection diseases, respectively. Therefore, the release patterns of mannitol and phospholipids from SD multi-component particles needs to be studied. A dry powder for inhalation (DPI) formulation of mannitol as a marketed pharmaceutical product (Bronchitol<sup>TM</sup>) is approved in Europe and has been very recently approved for clinical trials in the US.[44] It is used as an osmotic agent, also known as non-destructive mucolytic agent, to dilute mucus density.[108] In addition, a similar release pattern of DPPC and DPPG from the particles would be beneficial to maintain a constant ratio of DPPC to DPPG. The release study can be conducted in PBS at PH 7.4 (or *in vitro* model of lung fluid[233], and mucus from patients with chronic infections in the deep lungs). The concentration of mannitol and phospholipids could be determined by high pressure liquid chromatography (HPLC) equipped with a refractive index detector[254] and a evaporative light scattering detector[255], respectively.

#### 4) *in vivo* animal study of SD multi-component particles

It is important to examine whether the respiratory functions of *in vivo* animal model with chronic infections in the deep lungs can be improved after administration of the multi-component powders. The diseases such as cystic fibrosis (CF) could be possibly studied. The mice, pigs or ferrets CF models[256] could be used for this study. The larger animal models (pigs and ferrets) have phenotypes that appear to closely resemble human CF disease seen in newborns. Formulation with different compositions could be tested. The initial dosing of aerosol particles to animals would be determined for eliciting bacterial killing on infected sputum from CF patients, quantifying the bacterial killing concentrations needed.

## **Appendices**

This section contains the following additional information:

Appendix A: Spray-Dried Mannitol Aerosols

Appendix B: Spray-Dried Trehalose Aerosols

Appendix C: Spray-Dried Itraconazole Aerosols



## Appendix A Spray-Dried Mannitol Aerosols

### Design, Characterization, and Aerosol Dispersion Performance Modeling of Advanced Spray-Dried Microparticulate/Nanoparticulate Mannitol Powders for Targeted Pulmonary Delivery as Dry Powder Inhalers

Xiaojian Li<sup>1</sup>, M.S., Frederick G. Vogt<sup>2</sup>, Ph.D., Don Hayes Jr.<sup>3,4</sup>, M.D., M.S., M.Ed., Heidi M. Mansour<sup>1,5\*</sup>, Ph.D., R.Ph.

<sup>1</sup>University of Kentucky College of Pharmacy, Department of Pharmaceutical Sciences-Drug Development Division, 789 S. Limestone St., Lexington, KY 40536-0596, USA

<sup>2</sup> GlaxoSmithKline, Analytical Sciences, Product Development, King of Prussia, PA, USA 19406

<sup>3</sup>The Ohio State University College of Medicine, Departments of Pediatrics and Internal Medicine, Lung and Heart-Lung Transplant Programs, Columbus, OH 43205, USA

<sup>4</sup>The Ohio State University College of Medicine, The Davis Heart and Lung Research Institute, Columbus, OH 43205, USA

<sup>5</sup> University of Arizona-Tucson, College of Pharmacy, Skaggs Pharmaceutical Sciences Center, 1703 E. Mabel St, Tucson, AZ. 85712-0207, USA.

**Journal of Aerosol Medicine & Pulmonary Drug Delivery**  
**Invited ISAM 2013 Congress Research Paper (Invited Workshop Speaker)**  
**(2014) 27 (2) Page:81-93**

\***Corresponding Author:** Heidi M. Mansour, Ph.D., R.Ph., University of Arizona-Tucson, College of Pharmacy, Skaggs Pharmaceutical Sciences Center, 1703 E. Mabel St, Tucson, AZ. 85712-0207. USA. Email: mansour@pharmacy.arizona.edu

## Abstract

**Background:** The purpose was to design and characterize inhalable microparticulate/nanoparticulate dry powders of mannitol with essential particle properties for targeted dry powder delivery for cystic fibrosis mucolytic treatment by dilute organic solution spray-drying, and, in addition, to tailor and correlate aerosol dispersion performance delivered as dry powder inhalers (DPIs) based on spray-drying conditions and solid-state physicochemical properties. **Methods:** Organic solution advanced spray drying from dilute solution followed by comprehensive solid-state physicochemical characterization and *in vitro* dry powder aerosolization was used. **Results:** The particle size distribution of the spray-dried (SD) powders was narrow, unimodal, and in the range of ~500 nm to 2.0  $\mu\text{m}$ . The particles possessed spherical particle morphology, relatively smooth surface morphology, low water content and vapor sorption (crystallization occurred at exposure above 65% relative humidity), and retention of crystallinity by polymorphic interconversion. The emitted dose, fine particle fraction (FPF) and respirable fraction (RF) were all relatively high. The mass median aerodynamic diameters were below 4  $\mu\text{m}$  for all SD mannitol aerosols. **Conclusion:** The *in vitro* aerosol deposition stage patterns could be tailored based on spray-drying pump rate. Positive linear correlation was observed between both FPF and RF values with spray-drying pump rates. The interplay between various spray-drying conditions, particle physicochemical properties, and aerosol dispersion performance was observed and examined, which enabled tailoring and modeling of high aerosol deposition patterns.

**Keywords:** cystic fibrosis, aerosol performance modeling; osmotic agent; respiratory; lung; confocal Raman chemical imaging; DPI; particle engineering design; solid-state

## Introduction

Cystic fibrosis (CF) is the most common life-shortening, chronic hereditary disease among the Caucasian population, affecting approximately 60,000 individual worldwide[116]. CF leads to accumulation of thick and sticky mucus that affects the lungs. This lung disease is characterized by a cycle of bacterial infection and lung damage, causing death in early ages for CF patients[257]. Pulmonary delivery of therapeutic dose to local lung has tremendous advantages over other administration routes[69]. Pulmonary drug delivery systems include nebulizers, pressurized metered-dose inhalers (pMDIs), soft-mist inhalers (SMIs), and dry powder inhalers (DPIs). Within each class further differentiation is based on metering, means of dispersion, or design. DPIs have unique advantages including high dose delivery, higher chemical stability relative to the liquid state, and the potential to tailor particle properties in the solid-state. The performance of DPI formulations is influenced by several particle properties including size, size distribution, morphology, and particle surface properties (i.e. surface morphology and interparticulate forces including van der Waals, mechanical interlocking, electrostatic, and capillary forces), as described in detail by the authors[68, 69, 184, 258-263].

There are several methods available to make respirable particles, including micronization, precipitation, freeze drying, and spray drying[68-70]. Spray drying is a high-throughput process with the ability to produce particles in a more controlled manner, such as directing particle size and size distribution, and particle morphology, which are important particle features for pulmonary dry powder drug delivery by inhalation. As the chronic lung infection of CF resides in lower respiratory tract and small peripheral airways[133] where disease progression starts[264, 265], the microparticulate and nanoparticulate aerosols ( $\sim 0.5\text{-}2\mu\text{m}$  in diameter)[134-136] have particle deposition by sedimentation and diffusion[266] mechanisms, respectively.

The advantages of particle engineering by spray drying for the design of DPI formulations are related to the optimization of important particle properties such as surface morphology, particle morphology, particle size, and size distribution by controlling and tailoring spray-drying parameters such as feeding solution conditions (i.e. solvent type, concentration, and feeding rate) and drying gas conditions (i.e. gas type, inlet and outlet temperatures, and flow rate)[68, 70]. Organic solution advanced spray drying in closed-mode for pulmonary applications as DPIs has been reported in our previous studies[161-164]. The essential particle properties for targeted delivery to smaller airways and deep lung region include microparticulate/nanoparticulate size range with relatively narrow unimodal sizing distribution (enhance dosing reproducibility), spherical particle morphology with relatively smooth surface morphology (reduce mechanical interlocking, van der Waal and electrostatic forces), and low water content (lower capillary condensation)[41, 63].

D-mannitol is a non-reducing sugar alcohol that is used as an osmotic agent[267]. D-mannitol has also been used as sugar carriers in carrier-based dry powder for inhalation[46]. Dry powder mannitol, when inhaled, creates an osmotic gradient that facilitates an efflux of water into the airway lumen by which it increases the water content in the airway surface liquid (ASL) and promotes the clearance of mucus by ciliary movement and cough action. The detailed mechanisms are described in

literature[108, 268-272]. A DPI formulation of mannitol as a marketed pharmaceutical product (Bronchitol<sup>TM</sup>) is approved in Europe and has been very recently approved in the United States. The polymorphic system of D-mannitol has been well documented[175, 273].

In this comprehensive and systematic study, the organic solution closed-mode advanced spray-drying technique was employed using organic solvent (i.e. an alcohol) to minimize the residual water content and reduce the primary particle size in the solid state. In addition, inhalable mannitol aerosol powders were designed and optimized to target the lung regions where excess viscous mucus is present in CF lungs. In this study, the interplay between spray-drying conditions, mannitol polymorphic interconversion behavior, physicochemical properties in the solid-state, and their influence on *in vitro* aerosol dispersion performance deposition patterns as high performing microparticulate/nanoparticulate DPIs are reported for the first time.

## **Materials and Methods**

### **Materials**

Raw D-mannitol (C<sub>6</sub>H<sub>14</sub>O<sub>6</sub>; M.W.: 182.17 g/mol) was from Sigma-Aldrich (St. Louis, Missouri). Methanol (HPLC grade, ACS-certified grade, purity 99.9%) and chloroform (HPLC grade, ACS-certified grade, purity 99.9%) were obtained from Fisher Scientific (Fair Lawn, New Jersey). HYDRANAL<sup>®</sup>-Coulomat AD was from Sigma-Aldrich (St. Louis, Missouri). AQUA STAR methanol was from EMD chemical Inc. (Gibbstown, New Jersey). Raw D-mannitol was used as received and stored under room conditions. Ultra-high purity (UHP) nitrogen gas (Scotts Gross, Lexington, KY) was used for all experiments.

### **Methods**

#### **Preparation of Spray Dried Particles by Organic Solution Advanced Spray-Drying (no water) in Closed-Mode**

Organic solution advanced spray-drying process in the absence of water using dilute drug solutions was performed in closed-mode using a Büchi B-290 Mini Spray Dryer with a high performance cyclone and UHP dry nitrogen gas as the atomizing drying gas, and connected to the B-295 Inert Loop (Büchi Labortechnik AG, Flawil, Switzerland). The feeding solution was prepared by dissolving mannitol in methanol to make a dilute drug solution with a concentration of 0.1% w/v. The following optimized conditions, as reported in our previous studies[161-164], were used during spray drying: atomization rate, 600 L/h; aspirate rate, 35 m<sup>3</sup>/h; pump rate (%): 3 ml/min (10%) (low pump rate), 15 ml/min (50%) (medium pump rate), and 30 ml/min (100%) (high pump rate). The inlet temperature was set at 150°C. The corresponding outlet temperatures for each spray-dried (SD) mannitol formulations were summarized in Table A.1. The stainless steel nozzle diameter was 0.7mm. SD mannitol particles were separated from the nitrogen drying air in the cyclone and

collected in a sample collection vial. All SD powders were carefully stored in sealed glass vials that were stored in sealed glass desiccators over indicating Drierite/Drierite<sup>TM</sup> desiccant at -20°C under ambient pressure.

**Table A.1.** Summary of organic solution advanced spray drying in closed-mode conditions.

Chemical agent	Pump Rate (%)	Inlet Temperature (°C)	Outlet Temperature (°C)
Mannitol	10	150	82
	50	150	58
	100	150	38

### Scanning Electron Microscopy (SEM)

Using conditions previously reported,[161-164] visual imaging and analysis of particle size, morphology, and surface morphology were achieved by SEM using a Hitachi S-800 microscope (Tokyo, Japan). Samples were placed on double-sided adhesive carbon tabs (TedPella, inc.) which were adhered to aluminum stubs (TedPella, inc.) and were coated with gold/palladium alloy thin film using a Hummer VI sputtering system from Technics. The coating process operated at 10mA in AC with 8kV of voltage for 3min. The electron beam with an accelerating voltage of 20kV was used at a working distance of 30mm. SEM images were captured by Evex NanoAnalysis. Several magnification levels were used.

### Laser Light Diffraction Particle Sizing and Size Distribution

Using conditions previously reported,[161-164] the mean size and size distribution of SD mannitol particles in chloroform suspension were determined by ultraviolet laser diffraction of nano particle size analyzer SALD-7101 (Shimadzu Scientific Instruments, Japan) as reported[161-164]. Samples were dispersed in chloroform and ultrasonicated for 10s in water bath ultrasonicator Branson 5210 (Danbury, Connecticut) before measuring particle size. Sample particle dispersion was immediately transferred to particle size measuring cell and kept stirring during measuring in nano particle size analyzer. The low refractive index 1.60-0.10 was used. A volume-based dimension of particle amount distribution was obtained for samples.  $D_{V10}$ ,  $D_{V50}$ , and  $D_{V90}$  were used as particle size characterization parameters. The span value was calculated using the equation defined as  $[(D_{V90}-D_{V10})/D_{V50}]$ . All experiments were done in triplicate (n=3).

### X-Ray Powder Diffraction (XRPD)

Using conditions previously reported,[161-164] XRPD patterns of mannitol samples were collected with a Rigaku X-ray diffractometer (Japan) with Cu  $K\alpha$  radiation (40kV, 44mA, and  $\lambda=1.5406\text{\AA}$ ) between 5.0 – 60.0° ( $2\theta$ ) with a scan rate of 2.00°/min at ambient temperature as reported[161-164]. The sample was placed on a quartz plate in an aluminum sample holder without further grinding.

### **Differential Scanning Calorimetry (DSC)**

Using conditions previously reported,[161-164] thermal properties of mannitol samples were measured using a TA Q200 DSC (TA Instruments, New Castle, DE, USA) equipped with T-Zero<sup>®</sup> technology and an automated computer-controlled RSC-90 cooling accessory as reported[161-164]. Approximate 2mg sample was packed into hermetic anodized aluminum T-Zero<sup>®</sup> DSC pan which was then hermetically sealed with the Tzero hermetic sealer (TA Instruments, New Castle, DE, USA). An empty hermetically sealed aluminum pan was used as the reference pan. UHP nitrogen was used as a purging gas at a rate of 50 ml/min. The sample was heated from 10-200°C at a scanning rate of 5.00°C/min. All experiments were done in triplicate (n=3).

### **Hot-Stage Microscopy (HSM) Under Cross-Polarizers**

Using conditions previously reported,[161-164] HSM studies were performed under OLYMPUS BX51 polarized microscope (Olympus, Japan) equipped with INSTEC STC200 heat unit and INSTEC HCS302 hot stage (Boulder, Colorado) as reported[161-164]. The polarized light was filtered by  $\gamma$  530nm U-TP530 (Olympus, Japan). Mannitol samples were mounted on cover glass and heated from 25°C (room temperature) to 200°C at a heating rate of 5.00°C/min. The heating program was controlled by WinTemp software. Pictures of the samples were captured by a SPOT insight digital camera (Diagnostic Instruments, Inc.).

### **Karl Fischer (KF) Coulometric Titration**

Using conditions previously reported,[161-164] the water content of mannitol powders was assessed by KF coulometric titration. The measurements were performed with a 737 KF Coulometer coupled with 703 Ti Stand (Metrohm Ltd., Antwerp, Belgium) as reported[161-164]. Around 6 to 7mg of sample was dissolved in AQUA STAR methanol with a 5mL volumetric. The sample solution was injected into reaction cell filled with HYDRANAL KF reagent. The water content of sample was obtained from simple calculation. The experiments were done in triplicate (n=3).

### **Gravimetric Vapor Sorption (GVS)**

Using conditions previously reported,[161, 162, 164, 165] water vapor sorption isotherms were measured gravimetrically using an automated microelectronic balance coupled to a computerized VTI SGA-CX symmetric vapor sorption analyzer (Hialeah, Florida). All measurements were taken at 25°C using a sample size of  $\sim$ 1.0 to 1.5mg. Samples were subjected to drying treatment at 25°C under 0% relative humidity (RH) (nitrogen gas purging) for up to a maximum of 7h with equilibrium criterion of weight change less than or equal to 0.0001% in 10min interval. At the end of the drying cycle, the samples were exposed to a sequence of increasing RH with increment of 5% RH on each step, which started at 5% RH until 95% RH. The criterion used to establish equilibrium during adsorption was a weight change of less than or equal to 0.03% in 10min interval for up to 3h. The data point was acquired at every 2min or 0.01% weight change. The standby temperature was set as 25°C.

## **Confocal Raman Microscopy (CRM) and Spectroscopy for Chemical Imaging and Mapping**

CRM has demonstrated utility in the non-invasive and non-destructive microspectroscopic analysis of DPI aerosol formulations as described in detail by the authors[274, 275]. Using conditions previously reported[163, 275], dispersive Raman spectra and mapping images of mannitol samples were obtained using an Aramis confocal Raman spectrometer and fluorescence microscope system (Horiba Jobin Yvon, Edison, NJ, USA). The system is equipped with an Olympus BX41 confocal optical microscope, an Olympus U-LH 100W Hg lamp, and U-RFL-T power source used for fluorescence excitation and brightfield illumination (Olympus America, Inc., Chester Valley, PA). Raman spectra were obtained using both a 785nm diode laser and a 633nm HeNe laser. Raman spectral maps were obtained using a  $\times 10$  objective with the stage moved in increments of 5 to 10 $\mu\text{m}$ . Each map point was acquired using 32 to 128 accumulations each with 2s of detector exposure time. A confocal hole of 500 $\mu\text{m}$ , a grating of 600-900 grooves/mm, and a slit width of 100 $\mu\text{m}$  were used. Spectra were subjected to baseline correction and smoothing prior to further analysis.

Fourier-transform Raman (FT-Raman) experiments were performed using a Nicolet FT-Raman 960 spectrometer equipped with InGaAs and Ge detectors (ThermoFisher Scientific, Madison, WI). Samples were analyzed using a 180° collector or a horizontal video-controlled stage with a 50 $\mu\text{m}$  spot size, and 32 to 1024 co-added scans were collected at 4 $\text{cm}^{-1}$  resolution. A 1.064 $\mu\text{m}$  laser was used with a power setting of 0.6W.

## **Attenuated Total Reflectance-Fourier Transform Infrared Spectroscopy (ATR-FTIR)**

A Varian FTS-7000e FTIR spectrometer (Varian Inc., CA) equipped with a DTGS detector and a PIKE MIRacle ATR ZnSe accessory was used for all experiments. Each spectrum was collected for 32 scans at a spectral resolution of 8 $\text{cm}^{-1}$  over the wavelength number range of 4,000-700 $\text{cm}^{-1}$ . A background spectrum was done under the same experimental conditions and was subtracted from each sample spectrum. Spectral data were acquired with Varian Resolutions Pro software.

## ***In Vitro* Aerosol Dispersion Performance by the Next Generation Impactor (NGI)**

In accordance with United States Pharmacopeia (USP) Chapter <601> specifications on aerosols[178] and using conditions previously reported[161, 163], the aerosol dispersion performance of SD mannitol was conducted using the next generation impactor (NGI; Corporation, Shoreview, MN) with a stainless steel induction port (i.e. USP throat) attachment (NGI Model 170, MSP Corporation), equipped with specialized stainless steel NGI gravimetric insert cups (MSP Corporation) and the HandiHaler® (a high shear stress DPI device, Boehringer-Ingelheim Inc., Germany). The airflow rate (Q) of 60 L/min (adult airflow rate) was adjusted and measured before each experiment by a Copley DFM 2000 flow meter (Copley Scientific, United Kingdom). The NGI was coupled with a Copley HCP5 vacuum pump (Copley

Scientific) and a Copley TPK 2000 critical flow controller (Copley Scientific). The aerosolization was experimentally designed by Design Expert 8.0.7.1 software (Stat-Ease Corp., MN). The mass of powder deposited on each stage was quantified by gravimetric method using type A/E glass fiber filters with diameter 55mm (PALL Corporation, NY). Each HP-clear size 3 capsule (Quali-V®) (QUALICAPS, Spain) contained about 10 mg of powder. Three capsules were used in each experiment. *In vitro* aerosolization experiments were conducted in triplicate under ambient conditions.

For the NGIQ=60 L/min, the effective cutoff diameter ( $D_{a50}$ ) for each NGI stage was calibrated by the manufacturer and stated as: stage 1 (8.06 $\mu$ m); stage 2 (4.46 $\mu$ m); stage 3 (2.82 $\mu$ m); stage 4 (1.66 $\mu$ m); stage 5 (0.94 $\mu$ m); stage 6 (0.55 $\mu$ m); and stage 7 (0.34 $\mu$ m). The emitted dose (ED) was determined as the difference between the initial mass of powder loaded in the capsules and the remaining mass of powder in the capsules following aerosolization. The emitted dose fraction (ED[%]; Equation A.1) was used to express the percentage of ED based on the total dose (TD) used. The fine particle dose (FPD) was defined as the dose deposited on stage 2 through 7. The fine particle fraction (FPF[%]; Equation A.2) was expressed as the percentage of FPD to ED. The respirable fraction (RF[%]; Equation A.3) was used as the percentage of FPD to total deposited dose (DD) on all impactor stages.

$$\text{Emitted dose fraction (ED[\%])} = \frac{\text{ED}}{\text{TD}} \times 100\% \quad (\text{Equation A.1})$$

$$\text{Fine particle fraction (FPF[\%])} = \frac{\text{FPD}}{\text{ED}} \times 100\% \quad (\text{Equation A.2})$$

$$\text{Respirable fraction (RF[\%])} = \frac{\text{FPD}}{\text{DD}} \times 100\% \quad (\text{Equation A.3})$$

In addition, the mass median aerodynamic diameter (MMAD) of aerosol particles and geometric standard deviation (GSD) calculated by using a mathematic program written by Dr. Warren Finlay[183]. All experiments were done in triplicate (n=3).

## Data and Statistical Analysis

All experiments were performed in at least triplicate. The results were analyzed statistically using Microsoft Office Excel 2007 (Microsoft Corp., WA, USA). The results are expressed as mean  $\pm$  standard deviation. The aerosolization studies were experimentally designed using design of experiments by Design Expert™ 8.0.7.1 software (Stat-Ease Corp., MN). The level of statistical significance was performed at 0.05.

## Results

### Scanning Electron Microscopy (SEM)

Three different batches of SD mannitol particles were successfully produced by using low (10%), medium (50%), and high (100%) pump rates from dilute organic solution advanced spray drying. The detailed spray-drying conditions were introduced in Methods sections and Table A.1. The particle morphology and surface structure of the mannitol samples were visualized via SEM in Figure A.1. The particle shape of raw



D-mannitol (Figure A.1a) was irregular. The particle size of raw D-mannitol was far beyond the respiratory size for dry powder inhalation (DPI) which is less than 10 $\mu$ m. Generally, the smooth and spherical mannitol particles (Figure A.1b-d) were produced at each spray-drying condition. However, as the pump rate increased from 10% (low) to 100% (high), the surface of SD mannitol particles became slightly rougher. In addition both nanoparticles and microparticles of SD mannitol (linear geometry) were produced by spray drying under optimized conditions.

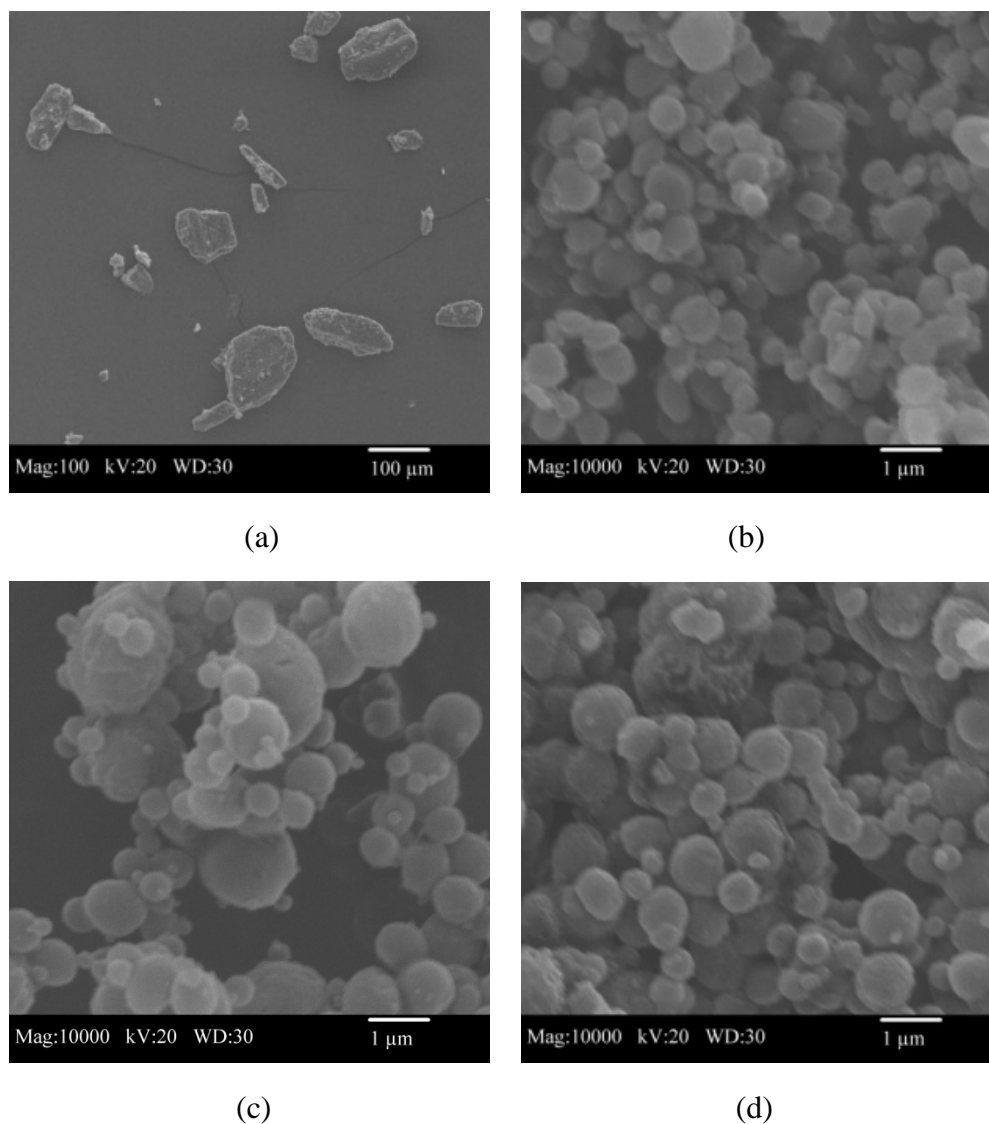


**Figure A.1.** SEM micrographs of raw (magnification 100X) and SD mannitol particles (magnification 10,000X) for: (a) Raw D-mannitol; (b) SD mannitol (10%P); (c) SD mannitol (50%P); (d) SD mannitol (100%P).

## Laser Light Diffraction Particle Sizing and Size Distribution

The laser sizing data of SD mannitol particles are summarized in Table A.2. The particle size distributions of SD mannitol were all in unimodal distribution by laser light diffraction. The median diameter ( $D_{V50}$ ) increased from  $0.486\mu\text{m}$  to  $0.702\mu\text{m}$  for SD mannitol as spray-drying pump rate increased from 10% (low) to 100% (high). The  $D_{90}$  was slightly above micro-size with  $1.147\sim 1.302\mu\text{m}$  for SD mannitol particles. Therefore, the majority of SD mannitol particles were under micro-size range. The span value for SD mannitol was between 1 and 2.

**Table A.2.** Laser sizing of SD mannitol particles (mean  $\pm$  SD, n=3).

Particles	Pump Rate (%)	$D_{V10}$ ( $\mu\text{m}$ )	$D_{V50}$ ( $\mu\text{m}$ )	$D_{V90}$ ( $\mu\text{m}$ )	Span Value
Mannitol	10	$0.346\pm 0.002$	$0.486\pm 0.006$	$1.147\pm 0.205$	$1.646\pm 0.398$
	50	$0.354\pm 0.003$	$0.521\pm 0.016$	$1.302\pm 0.101$	$1.819\pm 0.145$
	100	$0.482\pm 0.132$	$0.702\pm 0.141$	$1.247\pm 0.016$	$1.156\pm 0.498$

## X-Ray Powder Diffraction (XRPD)

X-ray powder diffraction patterns (Figure A.2) of raw D-mannitol showed sharp and intensive peaks indicating the existence of long-range molecular order. SD mannitol samples remained peaks after spray-drying process. The XRPD data reflected that raw D-mannitol and SD mannitol samples were in crystalline phase. However the peaks positions and intensity varied with samples.

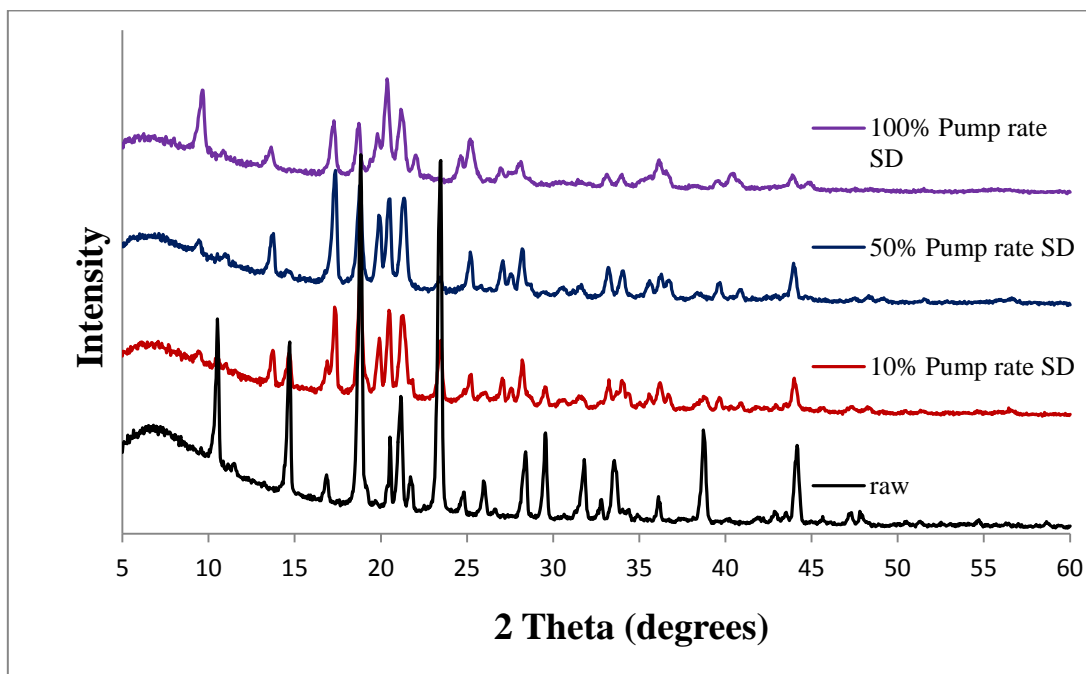


**Figure A.2.** X-ray powder diffraction patterns for raw and SD mannitol particles.

## Differential Scanning Calorimetry (DSC)

The thermograms obtained from mannitol samples are shown in Figure A.3 and the detailed values of melting peak enthalpy and temperature are tabulated in Table A.3. It was seen that raw D-mannitol had one sharp endotherm with peak temperature at  $\sim 166.4^{\circ}\text{C}$  and enthalpy of  $303.4\text{J/g}$  in Figure A.3a. Interestingly, the endothermic temperature and enthalpy of SD mannitol samples decreased from  $\sim 165.3^{\circ}\text{C}$ ,  $164.7^{\circ}\text{C}$ , and  $164.3^{\circ}\text{C}$  and  $\sim 304.2\text{J/g}$ ,  $288.7\text{J/g}$ , and  $282.4\text{J/g}$  as the spray drying pump rates increased from 10% (low) to 100% (high), respectively.

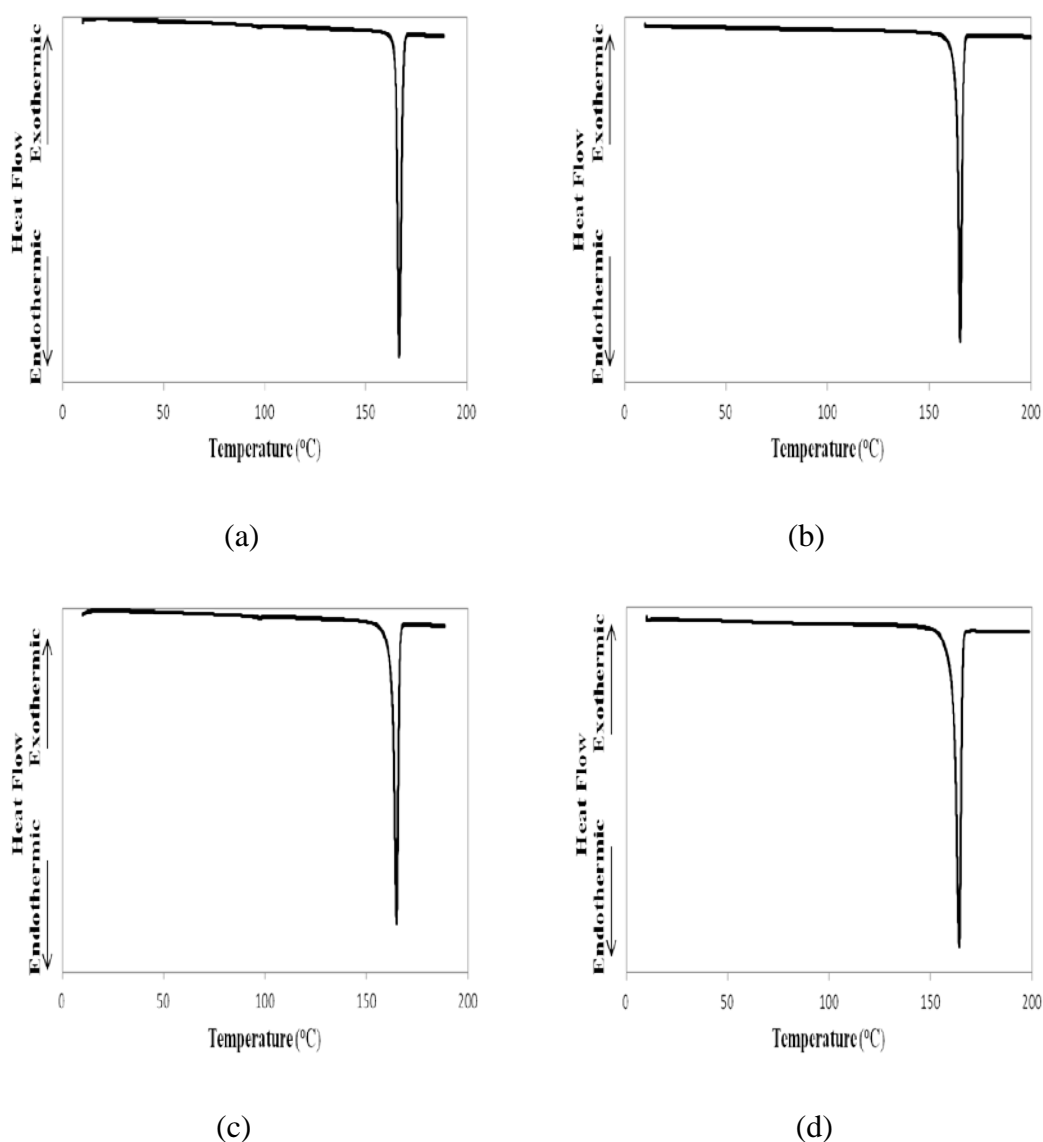


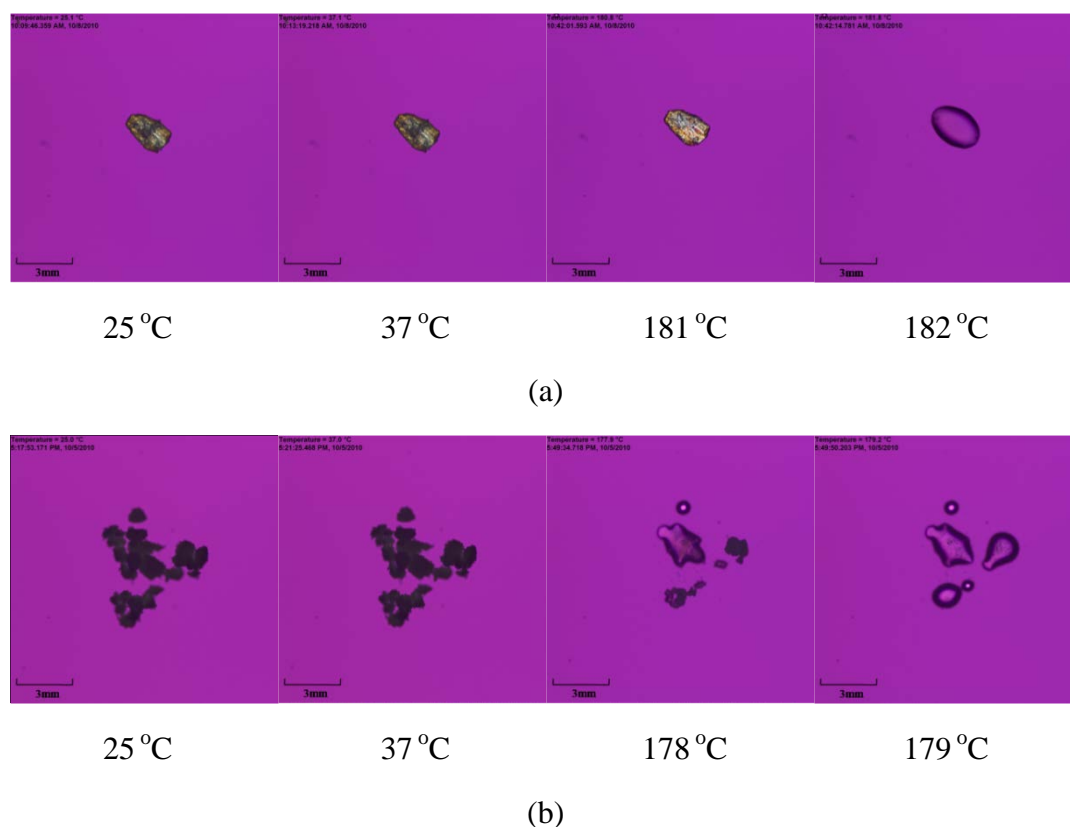
**Figure A.3.** DSC thermograms of raw and SD mannitol particles for: (a) Raw D-mannitol; (b) SD mannitol (10%P); (c) SD mannitol (50%P); (d) SD mannitol (100%P).

**Table A.3.** DSC thermal analysis of raw and SD mannitol particles (mean  $\pm$  SD, n=3).

Samples	Enthalpy (J/g)	Melting Point ( $^{\circ}$ C)	
		Onset	Peak
Raw	303.40 $\pm$ 2.21	165.04 $\pm$ 0.03	166.41 $\pm$ 0.19
SD 10%P	304.23 $\pm$ 9.06	163.69 $\pm$ 0.03	165.34 $\pm$ 0.04
SD 50%P	288.67 $\pm$ 10.47	162.66 $\pm$ 0.04	164.68 $\pm$ 0.06
SD 100%P	282.43 $\pm$ 4.45	161.40 $\pm$ 0.45	164.29 $\pm$ 0.14

### Hot-Stage Microscopy (HSM) Under Cross-Polarizers

Raw and SD mannitol (from 50% (medium) pump rate as a representative sample) powders were visualized under cross-polarized light microscopy as a function of increasing temperature for the presence/absence of birefringency. There were no obvious differences at room temperature (25 $^{\circ}$ C) and physiologic temperature (37 $^{\circ}$ C) in terms of morphology or shape for both samples in Figure A.4. The raw D-mannitol crystal was highly crystalline as seen from HSM pictures in Figure A.4a. The evident phase transition (thermodynamic melting phase transition) of D-mannitol initialized from 181 $^{\circ}$ C with subtle change in birefringency and finished at 182 $^{\circ}$ C, which was in a relatively narrow temperature range. The SD mannitol had phase transition of melting at a slightly lower temperature (178 $^{\circ}$ C) than the raw D-mannitol. As raw D-mannitol, the melting temperature range for SD mannitol was narrow as well.

**Figure A.4.** HSM micrographs of raw and SD mannitol (50%P) particles for: (a) raw D-mannitol; (b) SD mannitol (50%P).

### Karl Fischer (KF) Coulometric Titration

The residual water content in the powders is summarized in Table A.4. It was noted that the water content of raw D-mannitol had a lower value (~0.53% (w/w)) than its SD counterparts. The water content for SD mannitol increased with spray-drying pump rates from low to high and was higher than raw D-mannitol. However, the water content values were all below 2% (i.e. very low) which is significantly important for chemical and formulation stability. The low water content value ruled out the possibility of hemihydrates of mannitol[276].

**Table A.4.** Water content of raw and SD mannitol particles (mean  $\pm$  SD, n=3).

Samples	Water Content (% (w/w))
Raw	0.53 $\pm$ 0.26
SD (10% pump rate)	1.16 $\pm$ 0.04
SD (50% pump rate)	1.69 $\pm$ 0.08
SD (100% pump rate)	1.96 $\pm$ 0.32

### Gravimetric Vapor Sorption (GVS)

The dynamic water vapor sorption profiles are plotted in Figure A.5 for raw and SD mannitol (from 50% (medium) pump rate as a representative sample). Overall the mass of raw mannitol almost did not change across the whole RH range from 0% to 95% RH. The SD mannitol followed the same behavior upon RH increments except the small increase at 95% RH. This was in agreement with the fact that mannitol is the least hygroscopic of polyols and does not start to sorb moisture until the RH is over 90%[277]. However, there was a small weight loss observed from the RH range of 65% to 90%.

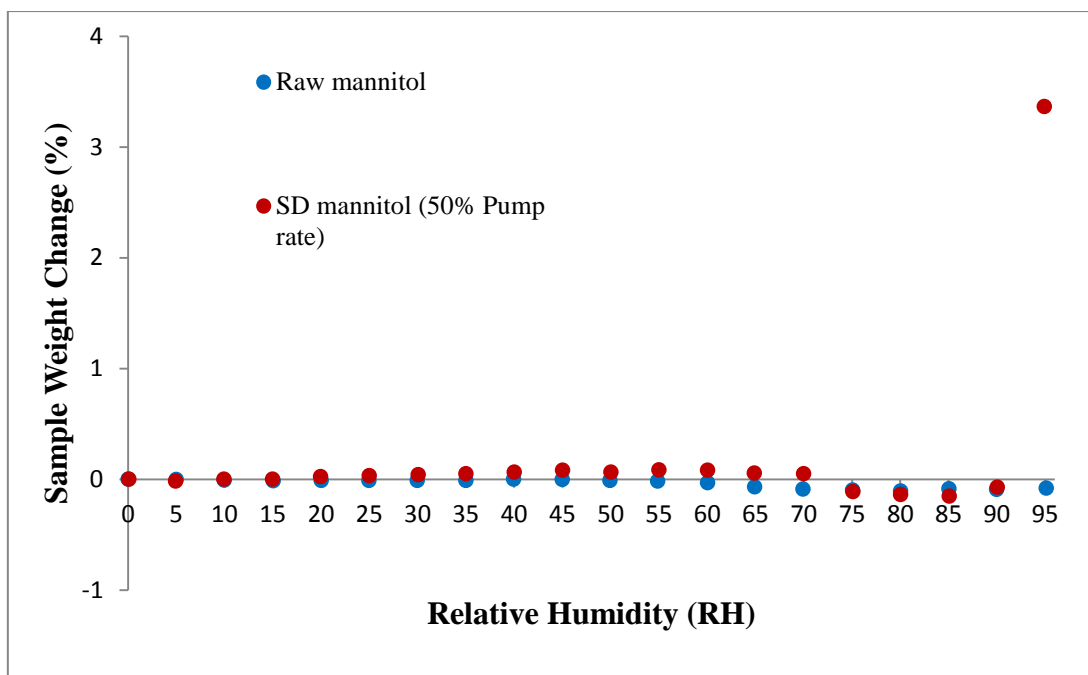


**Figure A.5.** Water vapor sorption isotherms at 25°C for raw and SD mannitol (50%P) particles (Weight Change % vs RH).

### Confocal Raman Microscopy (CRM) and Spectroscopy for Chemical Imaging and Mapping

Raman spectroscopy is highly sensitive to the polymorphic form of mannitol, as shown by the FT-Raman spectra of bulk samples of each phase in Figure A.6a obtained using a 1.064μm laser. The bulk samples of alpha, beta, and delta mannitol were prepared by rapid evaporation from water, slow evaporation from water, and lyophilization, respectively, and were checked by XRPD. As shown in Figure A.6a, the Raman spectral region between 2850 and 3000cm<sup>-1</sup> was particularly specific for each polymorphic form. These results can be compared to the spectra obtained by CRM of a mapped region (2910 to 2940cm<sup>-1</sup>) of SD mannitol from a 50% (medium) pump rate experiment, as shown in Figures A.6b and A.6c. The CRM spectra were obtained using a 633nm laser as mannitol shows minimal fluorescence. From examination of the map and spectra in Figures A.6b and A.6c, the material was seen to be primarily the alpha polymorph of mannitol. No indication of heterogeneity was observed in the map in Figure A.6b for bands in the 2910 to 2940cm<sup>-1</sup> region associated with alpha mannitol, with the only trend observed being the result of sample topology differences. Spectra taken from three individual points in this map were compared in Figure A.6c, highlighting the lack of significant differences observed and the close similarity with the reference spectrum of the alpha phase shown in Figure A.6a. A similar analysis of Raman bands in the region of 860 to 900cm<sup>-1</sup> (not shown), which are also selective for D-mannitol polymorphic form, yielded the same result.

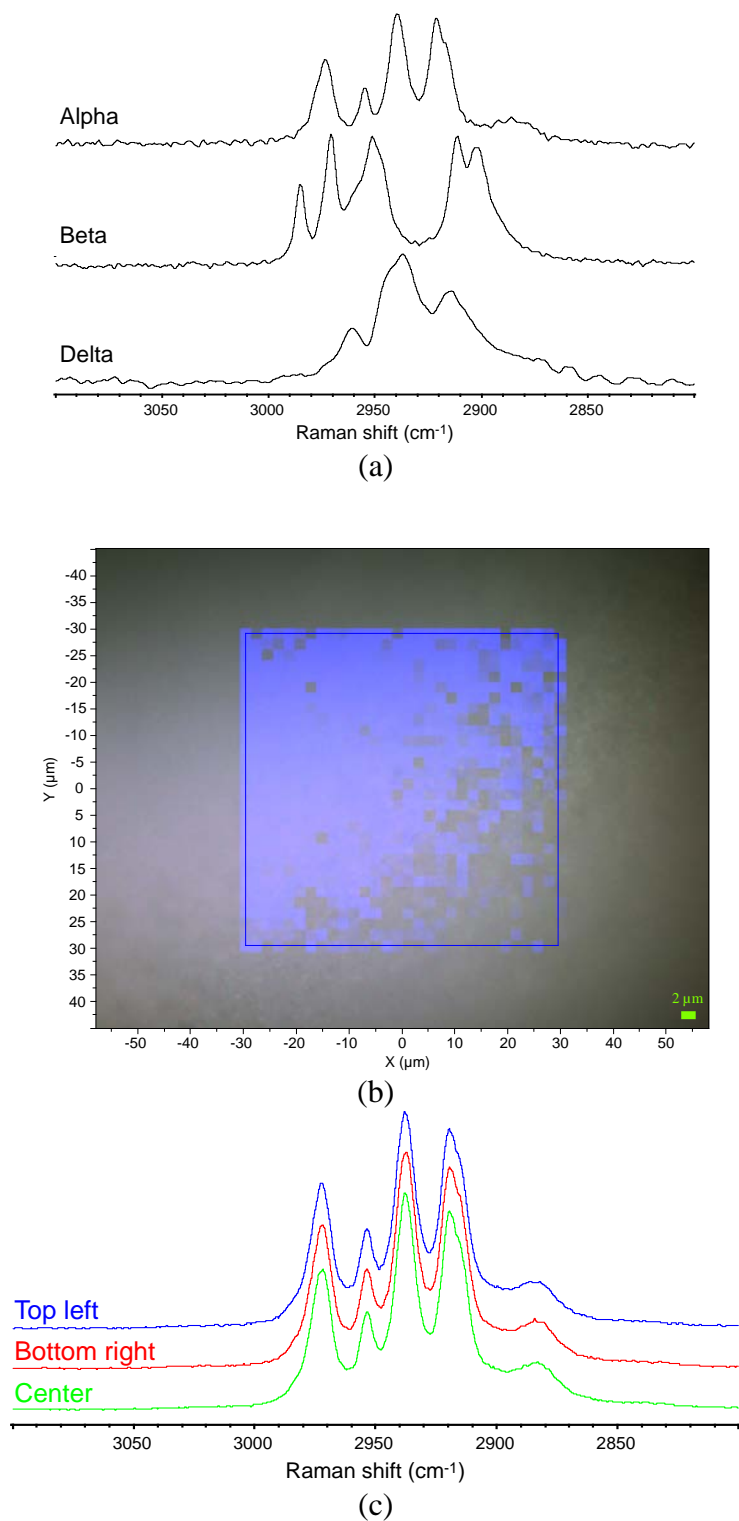


**Figure A.6.** (a) FT-Raman spectrum of bulk phases of mannitol; (b) CRM map of a region of flattened SD mannitol (50%P) particles obtained using a  $\times 50$  objective, showing Raman band intensity between 2910 and 2940  $\text{cm}^{-1}$  as blue intensity; (c) Expanded CRM spectra of three points on the map in (b).

## Attenuated Total Reflectance-Fourier Transform Infrared Spectroscopy (ATR-FTIR)

Figure A.7 shows the FT-IR spectra of mannitol particles. Differences were mainly detected in the band range of  $1500\text{--}1200\text{cm}^{-1}$ , indicating the differences of C-H deformation vibration. These were attributed to different mannitol polymorphs[278].

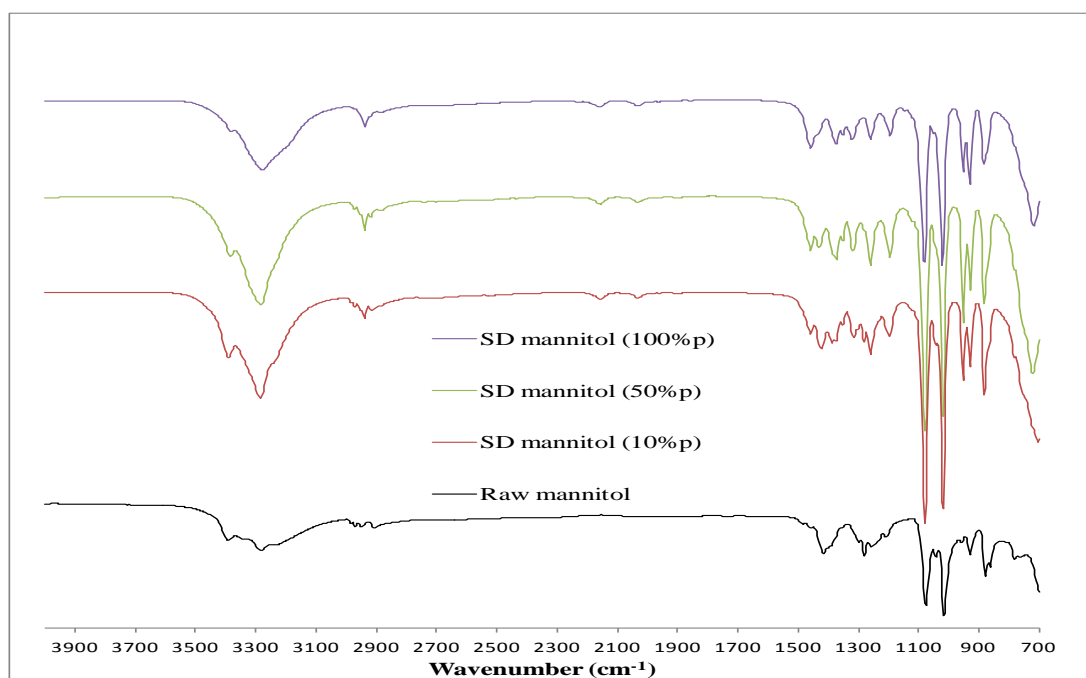


**Figure A.7.** ATR-FTIR spectra for raw and SD mannitol particles.

## *In Vitro* Aerosol Dispersion Performance by the Next Generation Impactor (NGI)

Figure A.8 shows SD particle deposition profiles on each of the NGI stage at airflow rate ( $Q$ ) of 60 L/min. As indicated in the profile, the SD mannitol powder produced from high spray-drying pump rate exhibited low particle deposition on stage 1 (effective cutoff diameter of  $8.06\mu\text{m}$ ) and high particle deposition on stages 2-4. However, compared to the other two formulations, particle deposition fraction was reduced for particles generated from high pump rate on stages 5-7 that was in the aerodynamic nanometer size range. The aerosol dispersion performance parameter values are listed in Table A.5. The FPF and RF of SD mannitol particles exhibited high, while having similar ED, as pump rates increased for spray drying. All SD mannitol powder had MMAD  $<4\mu\text{m}$  from the HandiHaler<sup>®</sup> under  $Q$  of 60 L/min. However, the GSD decreased, indicating aerodynamic size distribution being narrower, as the pump rates increased from 10% to 100%.



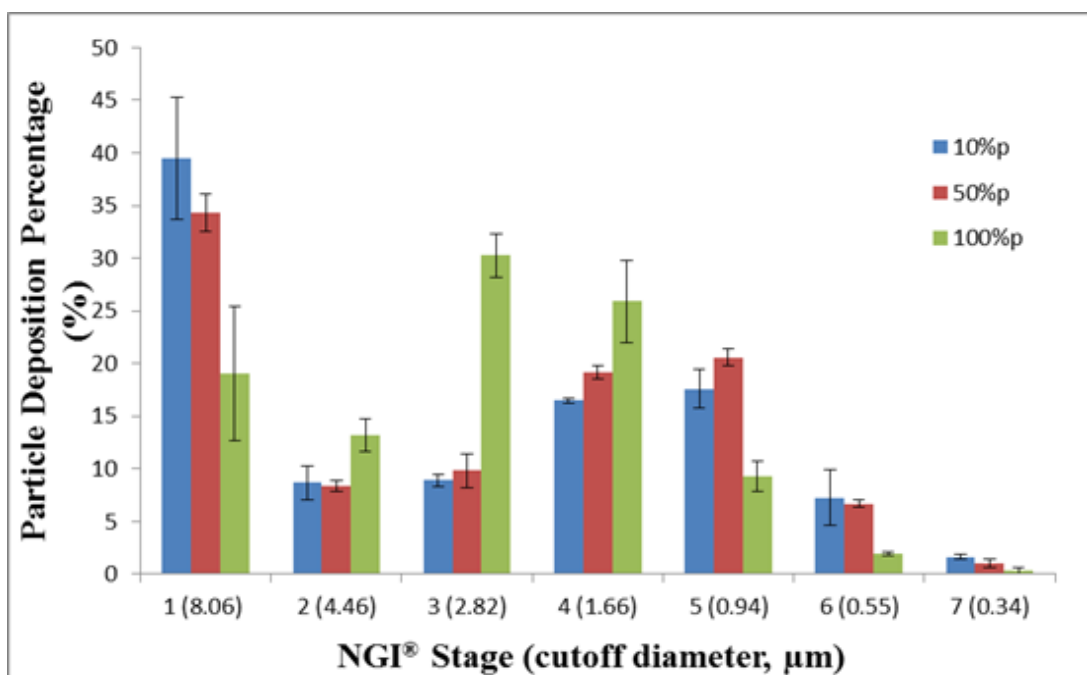


**Figure A.8.** *In vitro* aerosol dispersion performance using the NGI under an airflow rate (Q) of 60 L/min with the HandiHaler® DPI device for SD mannitol (n=3).

**Table A.5.** Aerosol dispersion performance parameters of SD mannitol particles (mean ± SD, n=3).

SD Mannitol Aerosol Dispersion Performance Parameters					
Pump Rate (%)	ED (%)	FPF (%)	RF (%)	MMAD (μm)	GSD
10	85.07±2.13	36.02±3.70	60.54±5.77	3.16±0.47	2.57±0.18
50	83.72±2.58	44.18±2.77	65.67±1.74	2.76±0.09	2.32±0.12
100	82.33±10.61	54.84±4.84	80.95±6.36	3.49±0.36	1.85±0.08

## Discussion

The present work clearly demonstrated that mannitol micro/nanoparticulate aerosols can be successfully produced by advanced spray drying dilute organic solutions. By using advanced spray-drying technique with low concentration of organic solvent solution, the microparticulate/nanoparticulate aerosols were successfully produced with narrow particle size distribution, low water content, suitable particle shape and morphology. The narrow particle size distribution is essentially critical for pulmonary dry powder inhalation, as it enables the aerosols to target a specific lung region without spreading the dose in the whole lungs. Targeted aerosols lower the therapeutic dose and toxic effects. Therefore they enhance the therapeutic outcome.

More importantly microparticulate/nanoparticulate aerosols ensure particle penetration to middle and deep lung regions of CF patients where excessive mucus locates. In addition, particle engineering process of spray drying can optimize particle size, shape, as well as morphology, which will result in better aerosol dispersion performance given as dry powder formulations. Low water content (< 6% w/w) of particles slows down chemical degradation process via hydrolysis and, in addition, decreases capillary forces between particles.

In general the majority of SD mannitol particle was in nanoparticulate primary size range of  $\sim 0.5\text{-}1\mu\text{m}$  (Table A.2), which is beneficial for deep lung penetration by diffusion of particle deposition mechanism, while the particles with size range of  $\sim 1\text{-}2\mu\text{m}$  would have particle deposition by sedimentation. On the other side, the narrow particle size distribution with span value of 1-2 (Table A.2) theoretically indicates reproducible aerosol particle aerodynamic performance, which is clinically important for therapeutic reproducibility.

As pump rates in spray-drying process increased from 10% (low) to 100% (high), the  $D_{V50}$  increased from  $\sim 0.486\mu\text{m}$  to  $\sim 0.702\mu\text{m}$  for SD mannitol. The increased particle size ( $D_{V50}$  in Table A.2), particle surface roughness (Figure A.1b-d), and water content (Table A.4) of SD mannitol were attributed to the formation of larger droplet size of solution as pump rates increased during atomization given at same primary drying temperature and period in spray drying.

From the XRPD patterns (Figure A.2), it can be seen that SD mannitol particles presented many intensive peaks in their patterns, indicating SD particles retained long-range molecular order/crystalline phase. Mannitol polymorphic behavior has been previously reported[175, 273]. The simulated X-ray diffractograms of alpha, beta, and delta forms (thermodynamic stability order:  $\text{beta} > \text{alpha} > \text{delta}$ ) of anhydrous mannitol are shown in Figure A.9. Interestingly, the beta form has highest melting point and lowest enthalpy value, while delta form has lowest melting point and highest enthalpy value. The characteristic peaks of each polymorph in diffractograms were symbolized for identification purpose. The alpha form was identified using the peaks at  $13.6^\circ$  and  $17.2^\circ$   $2\theta$ . The peaks at  $14.6^\circ$  and  $23.4^\circ$   $2\theta$  were used to label the beta form. The delta form was validated using a peak at  $9.7^\circ$   $2\theta$ . Based upon the XRPD patterns in Figure A.2, it indicated that the raw D-mannitol was in the beta polymorphic form that was the most thermodynamic stable form verified by DSC data (Figure A.3a and Table A.3) and in agreement with the literature[279]. The SD mannitol powders were a mixture of different polymorphs. As the pump rate increased, the alpha and beta polymorphic content decreased along with increasing polymorphic delta form content based on intensity of characteristic peaks of each polymorph. According to the XRPD data (Figure A.2), SD mannitol from low to high pump rates consisted of beta and alpha polymorphic forms (10% pump rate), a majority of alpha polymorph (50% pump rate), and alpha and delta (100% pump rate) polymorphs, respectively. This observed trend of polymorphic composition was also supported by melting temperature data in Table A.3 since their melting peak temperatures descended as more metastable mannitol crystalline forms were present. On the other hand, the enthalpy data in Table A.3 also suggested that a small amount amorphous phase may remain in SD mannitol and the content of amorphous phase may increase with pump rate. Contrastingly, Michiko Kumon[280] et al. reported that

SD mannitol was in the beta polymorph form under their spray-drying condition which is different from the spray-drying conditions reported here. The CRM results in Figure A.6 for the 50% (medium) pump rate sample indicated the presence of homogeneous alpha mannitol, supported by XRPD results showing dominant alpha form in Figure A.2. In addition, the comparison the FT-IR spectrum of SD mannitol from 50% (medium) pump rate (as shown in Figure A.7) with the literature data[278] suggested the existence of mainly the alpha form of mannitol.

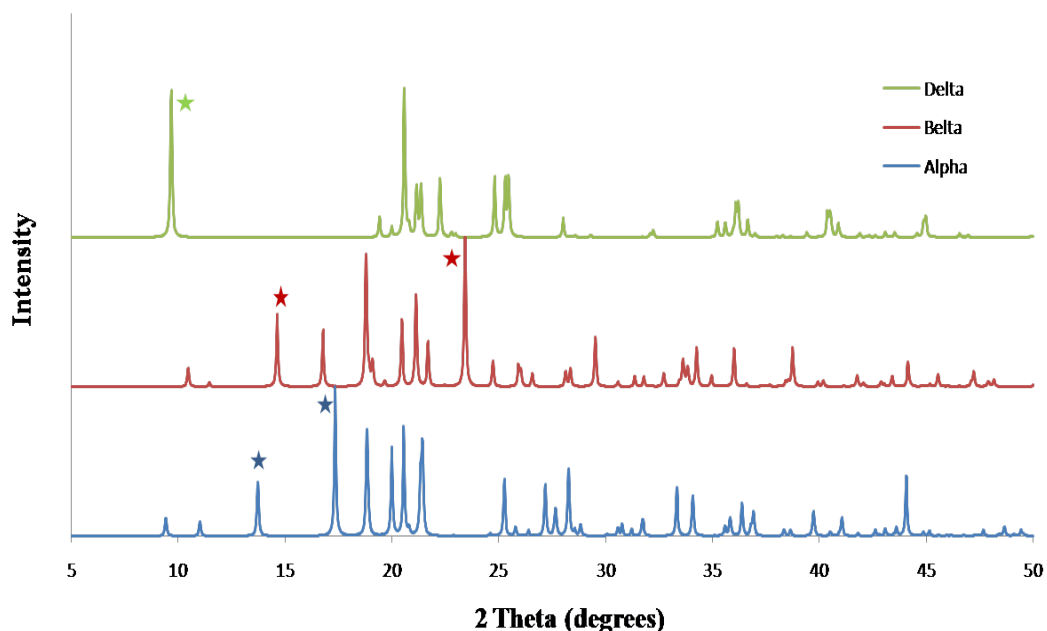


**Figure A.9.** Reference X-ray patterns of different polymorphs of mannitol obtained from Cambridge structure database program of ConQuest 1.10 (The Cambridge Crystallographic Data Center, UK). The symbol,★, indicates characteristic peaks of alpha, beta, and delta mannitol, respectively, which were used for identification in this study.

The small weight loss of raw and SD mannitol from 65% to 90% RH may suggest crystallization of mannitol. It is reported that SD composited formulation of salmon calcitonin and mannitol had a weight loss at 60% RH due to the crystallization of mannitol in GVS at 25°C[158]. Upon storage, amorphous mannitol transformed to the delta polymorphic form during RH exposure at 51%, which crystallized further into alpha polymorphic form at 69% RH[158]. A solution-mediated transformation was suggested based on their findings. The deliquescence point of the delta polymorphic form is approximately 85% RH, above which beta polymorph may form. The stoichiometric plot of water vapor sorbed/dry compound vs relative humidity (RH) (Figure A.10), translated from the gravimetric water vapor sorption equilibrium data (Figure A.5), provides insightful molecular information. The SD mannitol reached ~0.5 mole/mole ratio at equilibrium of 95% RH. It suggested that SD thermodynamic metastable microparticulate/nanoparticulate mannitol particles [50% (medium) pump rate] with more surface area and higher surface energy took up a high percentage of moisture at 95% RH level, or this may simply indicate the formation of mannitol hemihydrate[276]. Due to the increased surface area/energy[145] the SD mannitol had

slightly higher water content than raw D-mannitol (Table A.4), but they were all under 2% (i.e. very low). The low water vapor sorption (Figure A.5) and water content (Table A.4) of SD mannitol is critical for formulation stability issues such as chemical stability[281], polymorphic interconversion[282] and interparticulate capillary forces[41, 63].

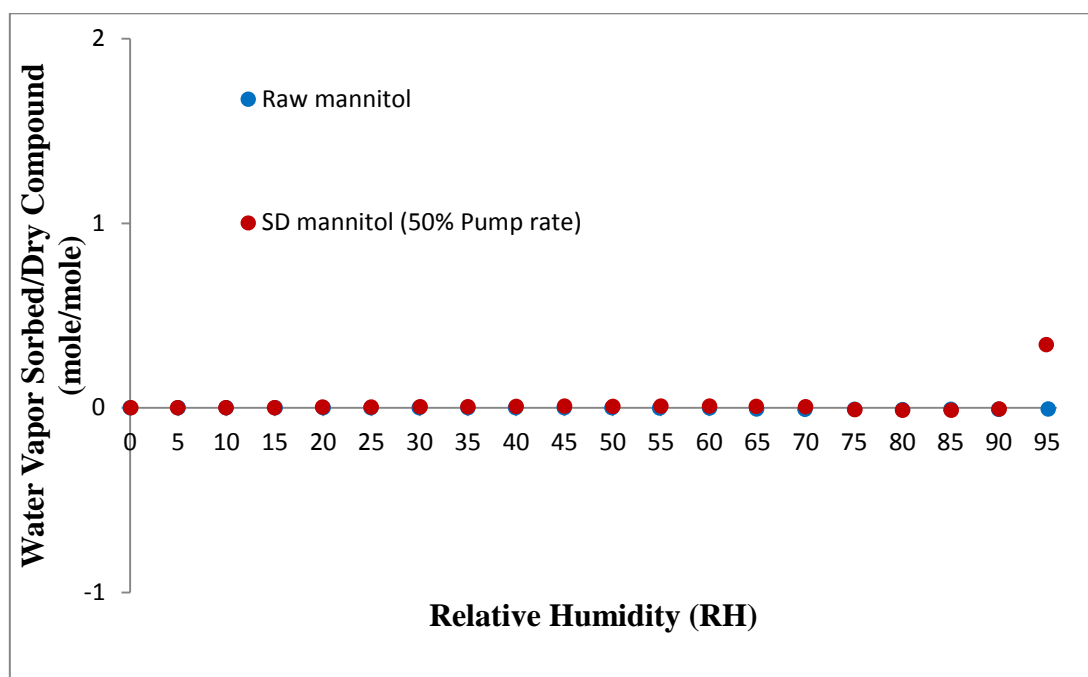
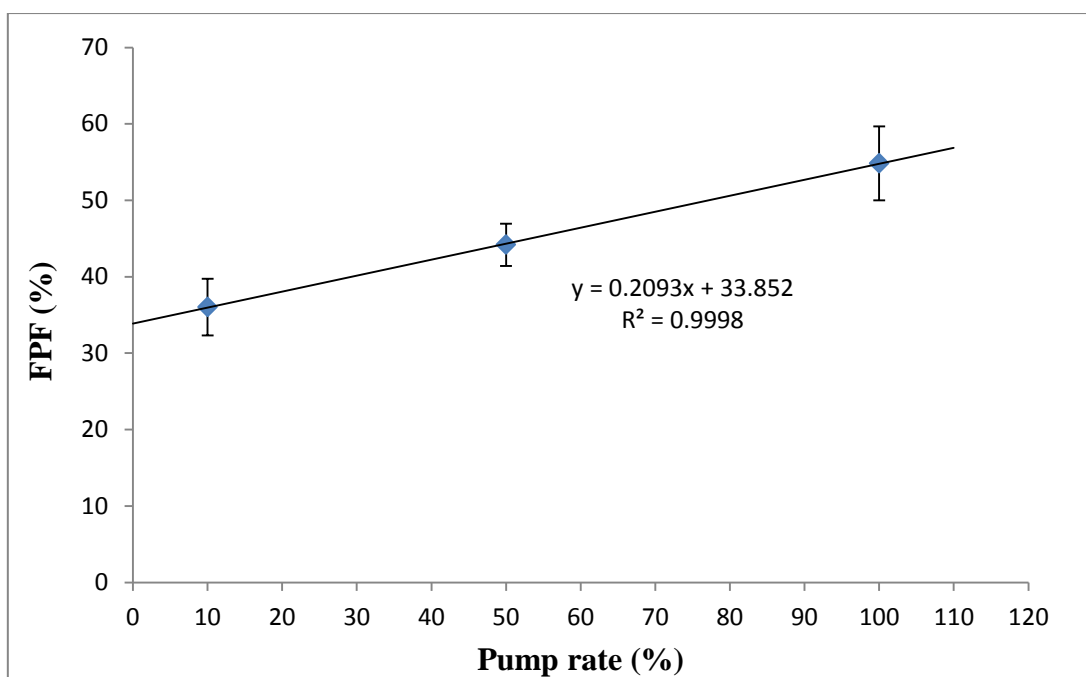
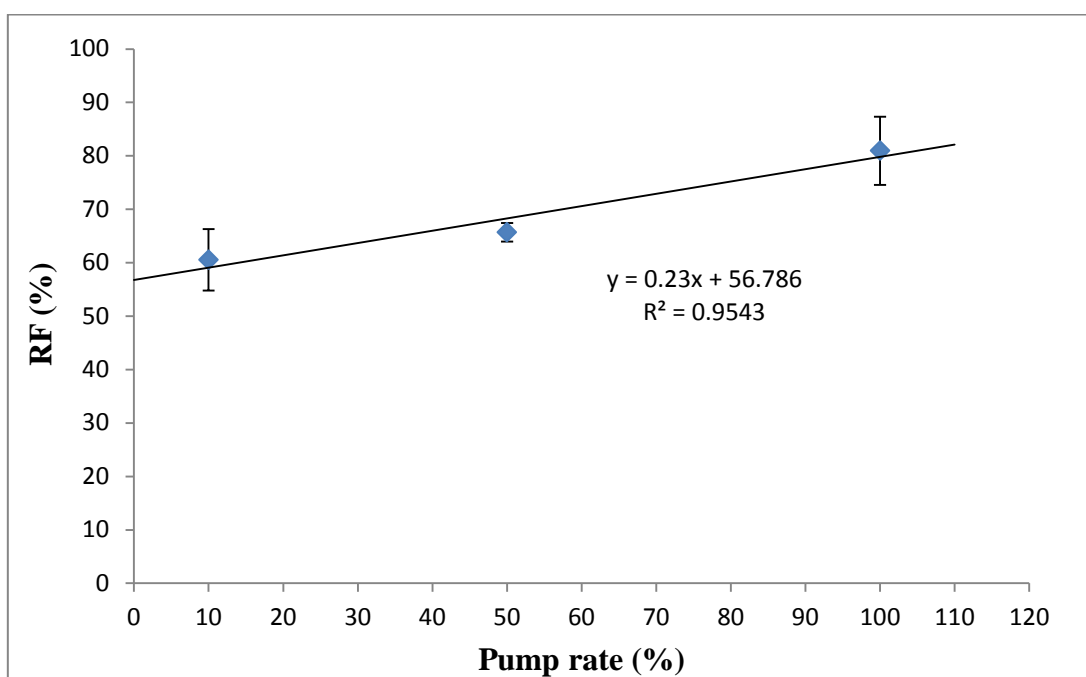


**Figure A.10.** Water vapor sorption isotherms at 25°C for raw and SD mannitol (50%P) particles (Water Vapor Sorbed/Dry Compound mole/mole vs RH).

Excellent aerosol dispersion performance of SD mannitol particles was achieved at Q of 60 L/min (adult airflow rate) with the HandiHaler<sup>®</sup> which gave low particle deposition on stage 1 (below 40% deposition) as in Figure A.8. The HandiHaler<sup>®</sup> is a high shear stress DPI device[283]. The particles on stage 1 would be predicted to deposit in larger airways (i.e. bronchi) *in vivo*[64]. The respiratory aerosol formulation with ability to effectively reach the smaller airways (i.e. bronchioles) or even the bronchioalveolar regions penetration is crucial for enhanced effective treatment of CF[134-136]. As demonstrated here for the first time, the SD mannitol particles from different pump rates and organic solution (closed-mode) had a significant effect on their aerosol dispersion performance. High pump rate (100%) particles exhibited FPF ~55% and RF ~81%. The MMAD values for all aerosols were suitable for efficiently targeting the smaller airways as inhaled dry powder aerosols. Interestingly, positive linear correlation of FPF and RF with spray drying pump rates (Figure A.11a and A.11b) exhibited excellent linear regression correlation values of  $r^2$  of 0.9998 and 0.9543, respectively.



(a)



(b)

**Figure A.11.** Linear correlation plots of (a) FPF and (b) RF vs spray drying pump rates for SD mannitol.

The difference in aerosol dispersion performance among SD mannitol particles may arise from the presence of different polymorphic composition after organic solution advanced spray drying in closed-mode from dilute mannitol solution in methanol

resulting in distinctive physicochemical properties (thermal properties, XRPD, water vapor sorption, etc.) of aerosols and particle properties (water content, sizing, etc.). SD mannitol particles from medium and particularly from low pump rate exhibited higher particle deposition on stage 1. Those deposited particles on stage 1 represented the aerosolized agglomerates (not primary particles)[284]. However, for all aerosols, the primary particles or reduced aggregates were entrained and deposited on stages 5-7 which have lower  $D_{a50}$  cutoffs into the nanometer aerodynamic size. It is known that the interparticulate forces (i.e. interfacial forces) increase as particle size decreases because the surface area per volume increases[64], the SD microparticulate/nanoparticulate particles do aerosolize, as shown from deposition profiles on stages 5-7 in Figure A.8. The excellent aerosol dispersion properties of such particles can be advantageous in the treatment of CF and other pulmonary diseases by DPIs.

## **Conclusions**

This study has demonstrated for the first time that the SD microparticulate/nanoparticulate DPI aerosols of mannitol were successfully produced at three pump rates (high, medium, and low) from dilute mannitol solution (methanol) using organic solution advanced spray drying in closed-mode. The primary SD mannitol particles possessed necessary particle and surface properties that minimize the interparticulate interactions and provide excellent aerosol performance as DPIs. Comprehensive physicochemical characterization of SD mannitol particles indicated that crystallinity was retained following organic solution advanced spray drying due to polymorphic interconversion. The type of crystalline polymorphs present was correlated with spray drying pump rate. As high-performing DPIs, aerosol deposition patterns for all three pump rates were distinct. Positive linear correlation between aerosol dispersion parameters (FPF and RF) and spray drying pump rate revealed this interplay.

## **Acknowledgements**

The authors gratefully acknowledge fellowship support from the UK Center of Membrane Sciences, the Graduate School Academic Year Fellowship and the Daniel R. Reedy Quality Achievement Fellowship awarded to Xiaojian Li. The authors thank Dr. Dicky Sick Ki Yu for SEM access, Dr. Tonglei Li for XRPD and HSM access, and Dr. Hilt for ATR-FTIR access at University of Kentucky.

## **Author Disclosure Statement**

The authors declare that there are no conflicts of interest.

Appendix A was reproduced with kind permission from: Li, X, Vogt, F.G., Hayes, D. Jr., and Mansour, H.M. Design, Characterization, and Aerosol Dispersion Performance Modeling of Advanced Spray-Dried Microparticulate/Nanoparticulate Mannitol Powders for Targeted Pulmonary Delivery as Dry Powder Inhalers. *Journal of Aerosol Medicine & Pulmonary Drug Delivery*, 2014, 27(2):81-93. Copyright © 2014 Mary Ann Liebert.

Copyright © Xiaojian Li 2014

## Appendix B Spray-Dried Trehalose Aerosols

### **Physicochemical Characterization and Water Vapor Sorption of Organic Solution Advanced Spray-Dried Inhalable Trehalose Microparticles and Nanoparticles for Targeted Dry Powder Pulmonary Inhalation Delivery**

Xiaojian Li and Heidi M. Mansour<sup>\*</sup>

University of Kentucky College of Pharmacy, Department of Pharmaceutical Sciences-Drug Development Division, Lexington, KY, USA 40536-0596

**Invited Paper to AAPS PharmSciTech**  
**Special Issue- Advances in Pharmaceutical Excipients Research and Use: Novel Materials, Functionalities and Testing**  
Vol. 12, No. 4, December 2011, page:1420-1430

***\*Corresponding Author:*** Heidi M. Mansour, Ph.D., R.Ph., Assistant Professor of Pharmaceutics & Pharmaceutical Technology, Faculty Associate-UK Center of Membrane Sciences, University of Kentucky, College of Pharmacy, Department of Pharmaceutical Sciences-Drug Development Division, 789 S. Limestone Street, Lexington, KY 40536-0596, USA. Telephone: (859) 257-1571. Email: heidi.mansour@uky.edu



## Abstract

Novel advanced spray dried inhalable trehalose microparticulate/nanoparticulate powders with low water content were successfully produced by organic solution advanced spray-drying from dilute solution under various spray-drying conditions. Laser diffraction was used to determine the volumetric particle size and size distribution. Particle morphology and surface morphology was imaged and examined by scanning electron microscopy (SEM). Hot-stage microscopy (HSM) was used to visualize the presence/absence of birefringency before and following particle engineering design pharmaceutical processing, as well as phase transition behavior upon heating. Water content in the solid-state was quantified by Karl Fisher (KF) coulometric titration. Solid-state phase transitions and degree of molecular order were examined by differential scanning calorimetry (DSC) and X-ray powder diffraction (XRPD), respectively. Scanning electron microscopy showed a correlation between particle morphology, surface morphology, and spray drying pump rate. All advanced spray-dried (SD) microparticulate/nanoparticulate trehalose powders were in the respirable size range and exhibited a unimodal distribution. All spray-dried powders had very low water content, as quantified by KF. The absence of crystallinity in spray-dried particles was reflected in the X-ray powder diffractograms and confirmed by thermal analysis. DSC thermal analysis indicated that the novel advanced spray dried inhalable trehalose microparticles and nanoparticles exhibited a clear glass transition ( $T_g$ ). This is consistent with the formation of the amorphous glassy state. Spray-dried amorphous glassy trehalose inhalable microparticles and nanoparticles exhibited vapor-induced (lyotropic) phase transitions with varying levels of relative humidity as measured by gravimetric vapor sorption (GVS) at 25°C and 37°C.

**Keywords:** microparticulate/nanoparticulate inhalable powders; non-reducing sugar excipient; organic solution advanced spray drying; Respiratory delivery; trehalose

## Introduction

Pulmonary inhalation drug delivery offers attractive advantages in delivering high concentrations of drug directly to the disease site in lungs while minimizing systemic bioavailability[69]. Many mortal lung infectious diseases such as cystic fibrosis reside at both mid and low airway regions[91, 285-287]. Therefore, local drug delivery for treatment can be enhanced through the use of microparticles and nanoparticles[288, 289] in pulmonary delivery[70]. These particles can efficiently deposit in the lungs by physical sedimentation and diffusion of particle deposition mechanism, respectively[290]. Three main delivery systems have been utilized for the inhalation of aerosolized drugs, namely, nebulizers, pressurized metered-dose inhalers (MDIs) and dry powder inhalers (DPIs)[68, 69]. Various interparticulate interactions[291] influence DPI dispersion performance and include intermolecular van der Waals force, capillary force, and electrostatic force[64, 261, 262].

Freeze drying and spray drying are two most common processes which allow the conversion of the formulation from liquid state to solid state particularly for dry powder inhalation formulation design and development[68]. Nevertheless, freezing and thermal stresses associated with both processes are often observed. Therefore, cryoprotectants[292] and thermoprotectants[73] are frequently incorporated in the formulation for the purpose of protection of drug stability. Carbohydrates[293, 294] are commonly used as cryoprotectants and thermoprotectants. Trehalose can be successfully included in inhalation formulations that contain biotherapeutic drugs (biologics)[295], including aqueous solution spray-freeze dried formulations to produce large trehalose particles for nasal vaccination delivery[296]. It has many advantages over other sugars, such as less hygroscopicity, an absence of internal hydrogen bonds that allows more flexible formation of hydrogen bonds with drugs, low chemical reactivity and high glass transition temperature[297]. Moreover, trehalose dihydrate has notable similarities to the pulmonary sugar carrier, lactose monohydrate, as both are crystalline disaccharides and both are hydrates. Notable differences with lactose monohydrate are that trehalose dihydrate is a non-reducing sugar, and hence, it is not susceptible to the solid-state chemical degradation Mallaird reaction. Additionally, it is not metabolized by bacteria due to its non-reducing property. Freeze-dried trehalose[298-300] and aqueous solution spray-dried trehalose[300-302] have been reported for non-inhalation dry powder dosage forms.

Exploring alternative sugar carriers for pulmonary inhalation formulation is of considerable interest[303]. It has been demonstrated that trehalose can effectively improve dry powder aerosolization by increasing the fine particle fraction (FPF)[304]. Recently, trehalose dihydrate as an aerosol drug carrier for dry powder inhalation delivery has been systematically studied and was found to be an effective alternative to lactose monohydrate carrier[46]. Additionally, trehalose has been used as a lyoprotectant stabilizing excipient in dry powder inhalation aerosol formulations[274].

The unique features of spray drying involve the ability of particle design, formation and drying in a continuous single-step that starts with a liquid and ends with the powder formulation. It provides the theoretical framework for a rational design of

structured aerosol particles[68, 70, 305]. Typically, the spray drying process consists of atomization of feed into a spray, spray-air contact, solvent evaporation of the spray, and separation of the dried particles from the drying air[306]. However, particle engineering requires a deeper understanding of particle formation processes since many process and formulation variables need to be tuned correctly to achieve the desired structured particles for inhalation.

By using organic solvent in feedstock with no water present, much lower moisture content and significantly smaller particle size can be achieved down to ~400 nm. The non-aqueous nature and inherently lower surface tension of an organic solvent combined with a low (dilute) solute concentration enables particle production in the solid-state down to the inhalable nanometer size range while maintaining a unimodal and narrow particle size distribution in the solid-state. To the authors' knowledge, this study is the first to use and report this novel approach to rationally design and produce inhalable dry powder microparticles/nanoparticles for pulmonary delivery. These novel particles are produced by organic solution advanced spray drying from dilute solution under rationally chosen spray drying conditions. The goal of this study was to produce and optimize low water content trehalose microparticles and nanoparticles to be suitable for pulmonary delivery as dry powder inhalers (DPIs) and to comprehensively and systematically investigate the physicochemical and particle properties of spray-dried and raw trehalose particles.

## Materials and Methods

### Materials

The chemical structure of D-(+)-trehalose dihydrate ( $C_{12}H_{26}O_{13}$ ; Molecular Weight: 378.33 g/mol;  $\geq 98.5\%$  purity, Sigma-Aldrich Inc., St. Louis, MO) is shown in Figure B.1 (ChemDraw Ultra 10.0, ChemOffice, Cambridge, MA) and its molecular model has been previously reported by Mansour and Hickey[274]. Methanol (HPLC grade) and chloroform were obtained from Fisher Scientific (Fair Lawn, New Jersey). HYDRANAL<sup>®</sup>-Coulomat AD was from Sigma-Aldrich (St. Louis, Missouri). AQUA STAR methanol was from EMD chemical Inc. (Gibbstown, New Jersey).

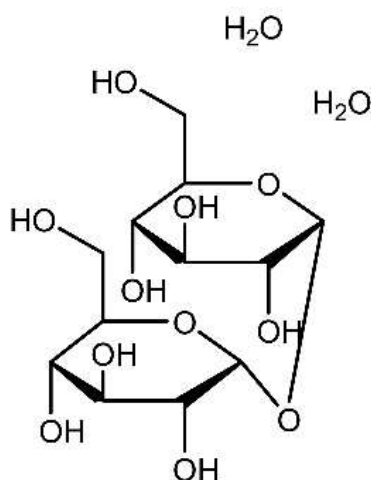


**Figure B.1.** The chemical structure of D-(+)-trehalose dihydrate

## Methods

### Organic Solution Advanced Spray-Drying from Dilute Solution

The advanced spray-drying process was performed using the Büchi Mini Spray Dryer B-290 (Büchi, Switzerland) coupled with the Inert Loop B-295 (Büchi, Switzerland) and the high performance (HP) cyclone (Büchi, Switzerland). The spray drying process was in closed mode. The feeding solution was prepared by dissolving D-(+)-trehalose dihydrate in methanol to form a dilute solution with a concentration of 0.3% w/v. The following spray-drying conditions were rationally chosen and used: atomization gas flow rate was 600 L/h; aspiration rate was 35 m<sup>3</sup>/h; three different pump rates were rationally chosen to represent the “high”, “medium” and “low” pump rates which were 100% (30 mL/min), 50% (15 mL/min), and 10% (3 mL/min), respectively. The inlet temperature was set at 150°C and this represents the temperature maintained the first drying process. The corresponding outlet temperature for the secondary drying process at the three different pump rates were 39°C (high pump rate), 45°C (medium pump rate), and 53°C (low pump rate). The nozzle diameter of the stainless steel nozzle was 0.7mm. The spray-dried (SD) particles were separated from the hot nitrogen drying gas in a cyclone and collected in a sample collector. Ultra-high purity grade compressed nitrogen gas from Scott-Gross (Lexington, Kentucky) was used as the spray-drying gas during closed mode spray-drying.

All spray-dried powders were carefully stored in sealed glass vials that were stored in sealed glass desiccators over Indicating Drierite/Drierite<sup>TM</sup> desiccant at 25°C under ambient pressure.

### Laser Light Diffraction Particle Sizing and Size Distribution

The mean size and size distribution of the particles in chloroform suspension were determined by ultraviolet laser diffraction of nano particle size analyzer SALD-7101 (Shimadzu, Japan). Using the method previously reported by Mansour et al[46], powders were dispersed in chloroform and ultrasonicated for 10 s (Branson 5210 Ultrasonicator Bath, Danbury, Connecticut) to break up the agglomerates without reducing the primary particle size before particle size measurements were carried out. Sample particle dispersion was immediately transferred to the particle size measuring quartz glass cell under stirred conditions. The low refractive index 1.60-0.10 was used. Number-based dimension of particle amount distribution was obtained for samples. In addition to acquiring the particle size distributions, the  $D_{v10}$ ,  $D_{v50}$ , and  $D_{90}$  parameters were measured. The Span value was calculated using the equation defined as  $[(D_{v90}-D_{v10})/D_{v50}]$ .

### Scanning Electron Microscopy (SEM)

The shape and surface morphology of particles was evaluated by SEM, using a Hitachi S-800 microscope (Tokyo, Japan). Samples were placed on double-sided adhesive carbon tabs (TedPella, Inc.) which were adhered to aluminum stubs

(TedPella, inc.) and were coated with gold/palladium alloy thin film using a Hummer VI sputtering system from Technics. The coating process was operated at 10 AC mA for 3 min. The electron beam with an accelerating voltage of 20 kV was used at a working distance of 30mm. SEM images were captured using Evex NanoAnalysis software. Several magnification levels were used.

### **X-ray Powder Diffraction (XRPD)**

XRPD patterns of powder samples were measured by a Rigaku Multiflex X-ray diffractometer (Japan) with a slit-detector Cu K $\alpha$  radiation (40 kV, 44 mA, and  $\lambda=1.5406$  Å) source. Scan range was 5.0 – 50.0 ( $2\theta$ ) ° with a scan rate of 2.00°/min at ambient temperature. The sample was placed on a horizontal quartz glass sample holder plate.

### **Differential Scanning Calorimetry (DSC)**

Thermal analysis and phase transition measurements were carried out using a TA Q200 DSC system (TA Instruments, New Castle, Delaware) equipped with T-Zero<sup>®</sup> technology and an automated computer-controlled RSC-90 cooling accessory (TA Instruments, New Castle, Delaware). Approximately 3 mg of powder was carefully weighed into hermetic anodized aluminum T-Zero<sup>®</sup> DSC pans (TA Instruments T-Zero<sup>®</sup>, New Castle, Delaware) and were sealed with the T-Zero<sup>®</sup> hermetic sealer (TA Instruments New Castle, Delaware). Ultra-high purity (UHP) nitrogen gas (Scotts Gross, Lexington, KY) was used as the purging gas at a purge rate of 50 mL/min. The heating range was 10-250°C at a heating scan rate of 5.00°C/min.

### **Karl Fisher (KF) Coulometric Titration**

The water content of all powders was chemically quantified by Karl Fisher (KF) coulometric titration. The measurements were performed with a 737 KF Coulometer coupled with 703 Ti Stand (Metrohm Ltd., Antwerp, Belgium). Approximately 10 mg of powder was dissolved in AQUASTAR<sup>®</sup> anhydrous methanol in a 5-mL volumetric flask. The sample solution was injected into the reaction cell that contained HYDRANAL<sup>®</sup> KF reagent. The water content was then calculated.

### **Gravimetric Vapor Sorption (GVS)**

Water vapor absorption isotherms were measured gravimetrically using an automated ultra-high sensitivity Cahn microelectronic balance (Thermoscientific Instruments) coupled to a computerized VTI SGA-CX symmetric vapor sorption analyzer (VTI Corporation, Hialeah, Florida). All measurements were taken at 25°C and 37°C (ie. biological temperature) at using a sample size of 1.0-1.5 mg. Samples were subjected to drying treatment at 25°C (for absorption at 25°C) and at 37°C (for absorption at 37°C) under ultra-high purity (UHP) nitrogen gas (Scotts Gross, Lexington, KY) for 7 h. At the end of the drying cycle, the samples were exposed to an automated computerized sequence of increasing relative humidity (RH) in steps of 5% RH. The

RH range was from 0% RH to 95% RH. Sample data acquisition was collected in 2-minute intervals. The equilibrium criterion was a weight change of  $\leq 0.03\%$  (w/w) in a 10-minute interval, per manufacturer recommendations and as reported previously by Mansour and Zografi[167].

### Hot-stage Microscopy (HSM) under Cross-Polarizers

HSM studies were performed under OLYMPUS BX51 polarized microscope (Olympus, Japan) equipped with an INSTEC STC200 heating unit and an INSTEC HCS302 hot stage (Boulder, Colorado). The polarized light was filtered by a  $\gamma$  530nm U-TP530 (Olympus, Japan) filter lens. Powder samples were mounted on a cover glass and heated from 25°C to 250°C at a heating rate of 5°C/min. The heating program was controlled by WinTemp software. Images were digitally captured by a SPOT Insight digital camera (Diagnostic Instruments, Inc.).

## Results

### Laser Light Diffraction Particle Sizing and Size Distribution

The particle sizing data and calculated span values are tabulated in Table B.1. The particle size distributions for all spray-dried powders were unimodal with narrow particle distribution, as reflected in the span values. The raw trehalose dihydrate had a large volume-median particle size of  $\sim 60\mu\text{m}$  as tabulated in Table B.1. Great reduction of particle size was achieved by organic solution advanced spray drying from dilute solution to create microparticulate/nanoparticulate powders that are in the respirable size range.

**Table B.1.** Particle size parameters of spray-dried (SD) trehalose and raw trehalose dihydrate particles (mean  $\pm$  SD, n=3)

Pump rate	D <sub>10</sub> ( $\mu\text{m}$ )	D <sub>50</sub> ( $\mu\text{m}$ )	D <sub>90</sub> ( $\mu\text{m}$ )	Span Value
10%	0.549 $\pm$ 0.003	0.752 $\pm$ 0.008	1.177 $\pm$ 0.012	0.836 $\pm$ 0.010
SD 50%	0.710 $\pm$ 0.006	0.993 $\pm$ 0.013	1.544 $\pm$ 0.019	0.840 $\pm$ 0.030
100%	0.646 $\pm$ 0.109	0.947 $\pm$ 0.071	1.648 $\pm$ 0.228	1.080 $\pm$ 0.455
Raw	35.139 $\pm$ 2.602	59.854 $\pm$ 3.296	110.460 $\pm$ 1.568	1.263 $\pm$ 0.122

### Scanning Electron Microscopy (SEM)

The particle morphology and surface morphology (ie. surface roughness) of the samples were visualized and analyzed using SEM. As shown in Figure B.2, smooth and spherical particles were produced by 10% SD pump feeding rate. However, as the pump % feeding rate approached 100% (high), the surface roughness increased and the proportion of irregular particles also increased. Interestingly, raisin-like dimpled particles were produced at the high pump % feeding rate of 100%. SEM analysis of

the particle size agreed with the laser sizing data in that all spray-dried powders were in the suitable size range for inhalation delivery, in addition to having suitable particle morphology. Contrastingly, the raw trehalose dihydrate particles were much larger (too large for pulmonary inhalation delivery) and non-spherical with a smooth but rectangular shape which are not suitable for inhalation delivery.

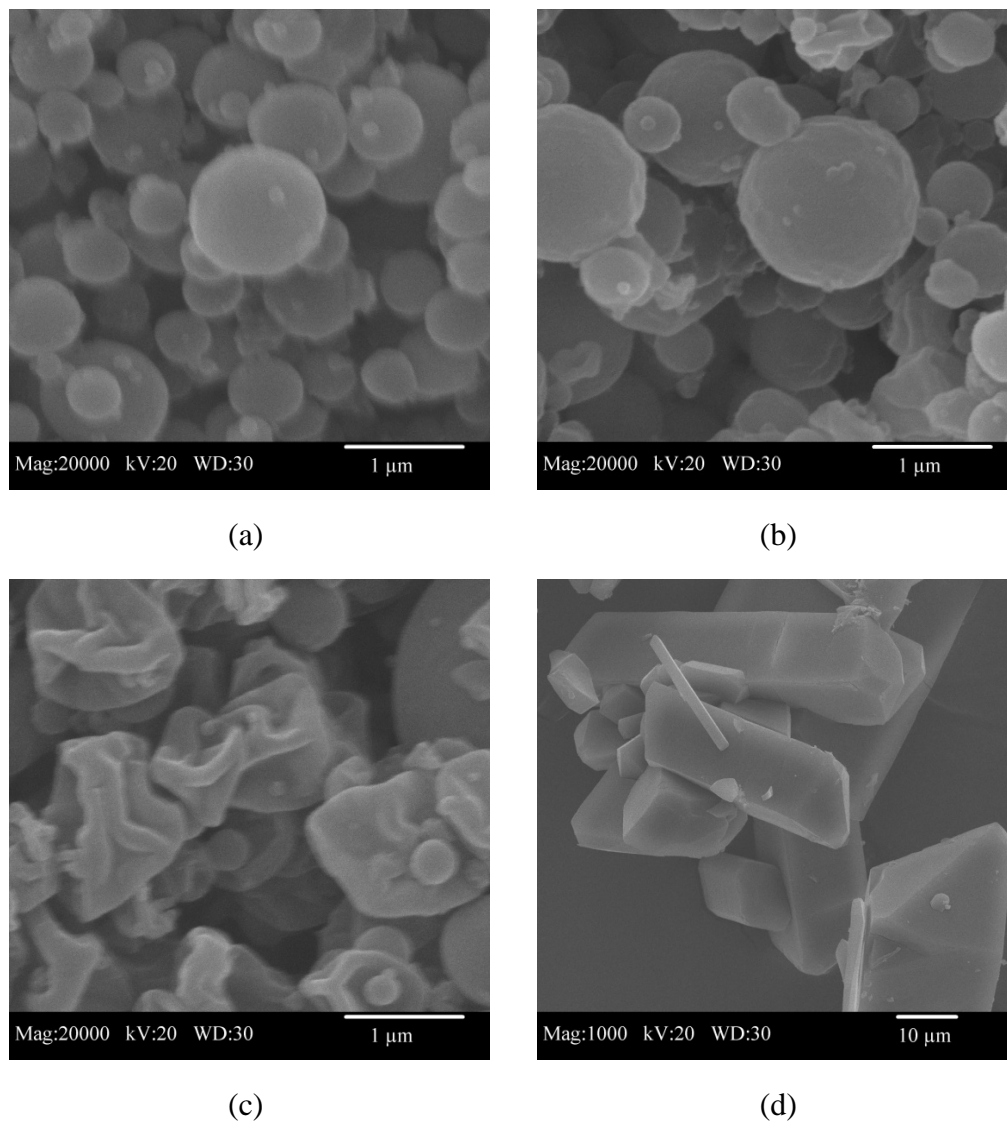


**Figure B.2.** SEM photographs of spray-dried (SD) trehalose and raw trehalose dihydrate particles. (A) SD trehalose from 10% pump feeding rate, magnification 20,000X; (B) SD trehalose from 50% pump feeding rate, magnification 20,000X; (C) SD trehalose from 100% pump feeding rate, magnification 20,000X; (D) raw D-(+)-trehalose dihydrate, magnification 1,000X.

### X-ray Powder Diffraction (XRPD)

X-ray powder diffraction patterns (Figure B.3) indicated that the organic solution spray drying process produced amorphous phase trehalose particles, as exemplified by the absence of sharp peaks and the presence of the characteristic non-crystalline “halo” which can be attributed to the loss of crystal character following the loss of the two

bound water molecules (ie. tightly bound to the crystal lattice by thermodynamically favorable H-bonding) during the organic solution advanced spray drying process from dilute solution. In contrast, the raw trehalose dihydrate had many intense peaks indicative of the presence of long-range molecular order due to crystallinity. The peaks represented that the raw trehalose dihydrate was highly crystalline which is in a good agreement with the University of Cambridge database and by results reported by Mansour et al[46]. The loss of characteristic crystalline peaks (“halo”) is in good agreement with previous reports on aqueous solution spray-dried trehalose under different conditions[307].

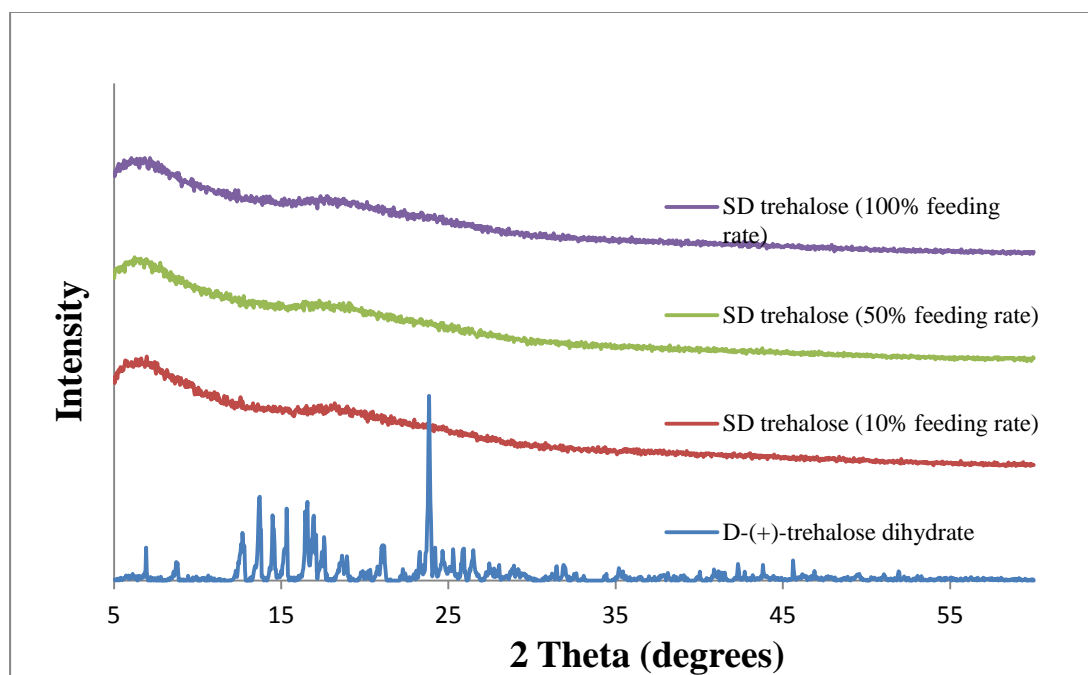


**Figure B.3.** X-ray powder diffractograms of SD trehalose and raw trehalose dihydrate powders.

### Differential Scanning Calorimetry (DSC)

The thermograms obtained from raw trehalose dihydrate and SD trehalose are shown in Figure B.4. There were three endothermic peaks observed for raw trehalose dihydrate which are characteristic for order-to-disorder thermotropic phase transitions. Similar DSC thermograms were obtained for single crystals of trehalose dihydrate[308] and for raw trehalose dihydrate powder[296]. The two endothermic order-to-disorder peaks at  $\sim 100^{\circ}\text{C}$  and  $140^{\circ}\text{C}$  correspond to two dehydration processes due to the loss of unbound water at  $\sim 100^{\circ}\text{C}$  (ie. vaporization of unbound water) and vaporization of the bound water molecules at  $140^{\circ}\text{C}$  which vaporize at a temperature significantly greater than  $100^{\circ}\text{C}$  due to thermodynamically favorable H-bonding of the water molecules within the trehalose dihydrate crystal lattice. The third endothermic order-to-disorder peak at  $210^{\circ}\text{C}$  represented the fusion of anhydrous  $\beta$  form of trehalose[309]. All SD trehalose samples showed an amorphous glassy-to-rubbery phase transition,  $T_g$ , (ie. characteristic baseline shift) at  $\sim 50^{\circ}\text{C}$ ,



followed by an exothermic disorder-to-order phase transition near 95°C which suggests crystallization at  $T_c$  from the amorphous rubbery state. A small endothermic order-to-disorder peak was observed in the temperature range of 140-150°C for the SD trehalose samples. To the authors' knowledge, this peak has not been reported previously in the literature. The fusion of the  $\beta$  form of trehalose was observed in this same temperature range as the raw trehalose dihydrate.

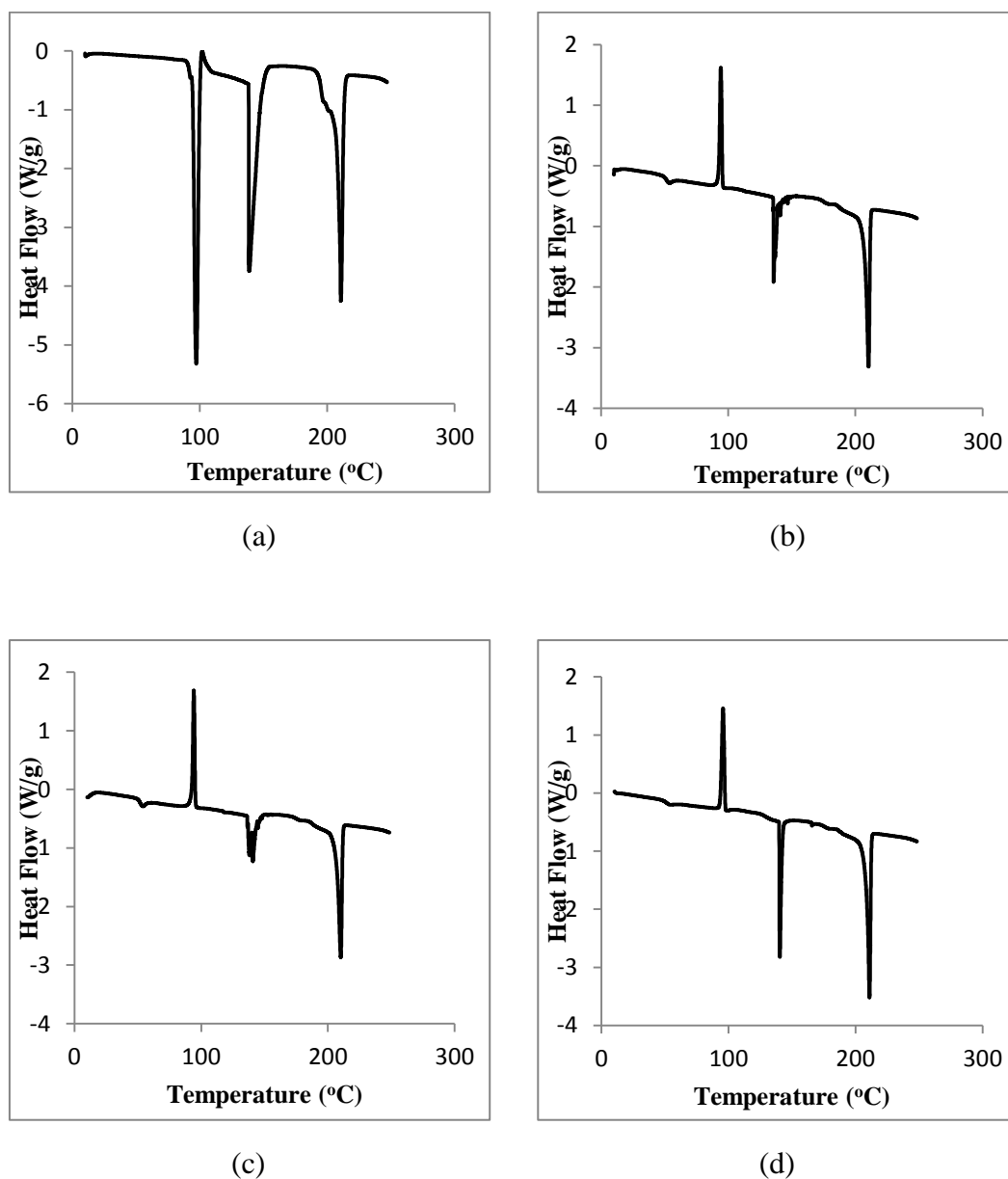


**Figure B.4.** DSC thermograms of SD trehalose and raw trehalose dihydrate particles at a heating scan rate of 5.00°C/minute. (A) raw D-(+)-trehalose dihydrate; (B) SD trehalose (10% pump feeding rate); (C) SD trehalose (50% pump feeding rate); (D) SD trehalose (100% pump feeding rate).

## Karl Fisher (KF) Coulometric Titration

The water content data are plotted in Figure B.5. The mean total water content of raw trehalose dihydrate was 9.62% (w/w) with a standard deviation (std. dev.) value of  $\pm 0.08\%$  (w/w). This data is in excellent agreement with the literature[308]. By comparing the theoretical minimum water content of raw trehalose dihydrate (9.52% (w/w)), it suggested that there was a trace amount of water (0.1% (w/w)) adsorbed to its surface, as the sample was stored under ambient conditions (approximately 55% RH and 25°C). As stated in the Experimental section, all spray-dried trehalose powders were stored in a sealed glass desiccator containing Drierite<sup>®</sup>/Indicating Drierite<sup>®</sup> desiccant under room temperature of 25°C. The water content values were 0.73% (w/w) (std. dev. =  $\pm 0.25\%$  (w/w)), 0.86% (w/w) (std. dev. =  $\pm 0.09\%$  (w/w)), and 1.51% (w/w) (std. dev. =  $\pm 0.01\%$  (w/w)) for samples produced by 10% (low), 50% (medium), and 100% (high) pump feeding rates, respectively.

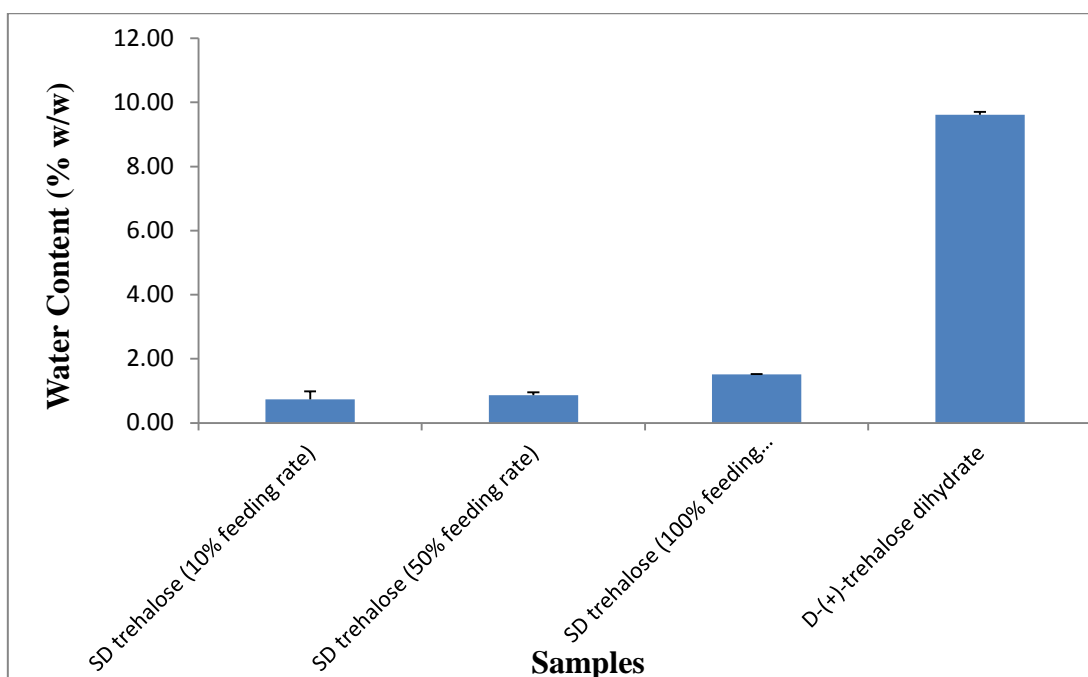


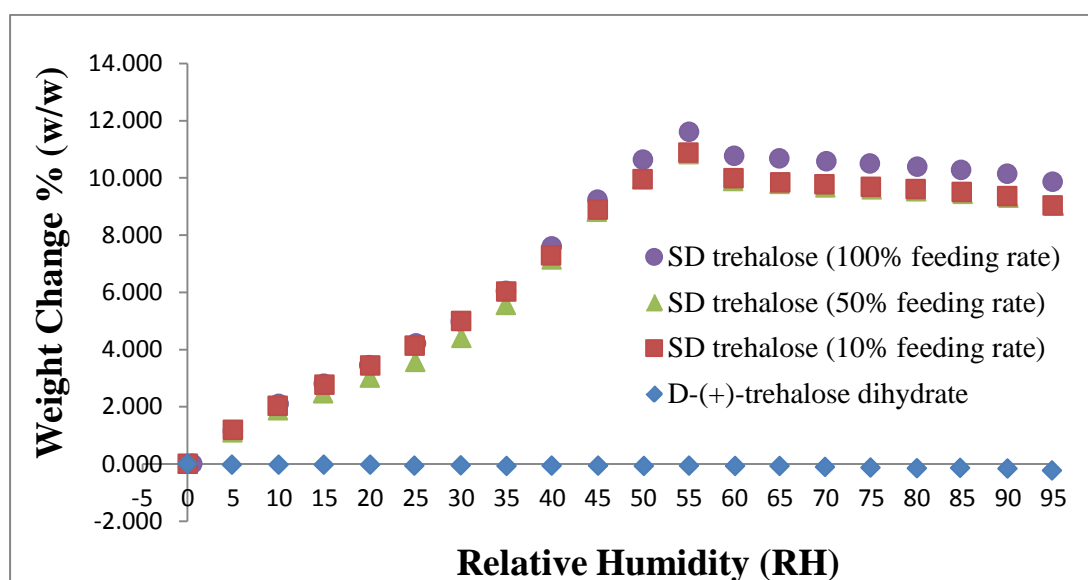
**Figure B.5.** Water content quantification (% w/w) of SD trehalose and raw trehalose dihydrate powders by Karl Fisher coulometric titration.

## Gravimetric Vapor Sorption (GVS)

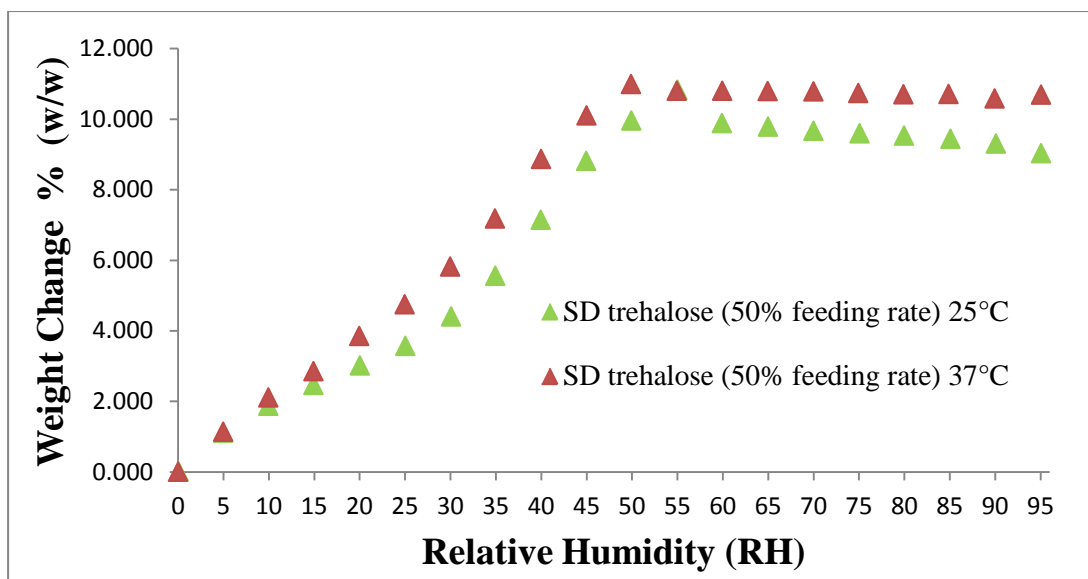
The gravimetric vapor sorption isotherms of the three spray-dried trehalose and raw trehalose dihydrate samples are plotted in Figure B.6a. From 0% to 55% of RH, all three SD samples underwent a rising curve with respect to their mass changes, reflecting an increasing capability of water vapor uptake. Interestingly, a transition point of water vapor sorption took place at 30% RH. This may be due to the SD trehalose samples passing through the lyotropic vapor-induced glass transition, from lower molecular mobility of glassy state to higher molecular mobility of the rubbery state. The uptake of water vapor of the sample continued to increase after the lyotropic vapor-induced glass transition. The amorphous trehalose relaxed to its more

stable crystalline state through crystallization at 55%-60% RH and the water vapor sorption capacity decreased sharply over a very narrow RH range followed by a plateau in vapor absorption. A slight desorption of water was observed for SD trehalose samples after 60% RH followed by the plateau region suggestive of the recrystallization process from the amorphous state to the crystalline state. It also suggests the transition from unbound water to bound water, as occurs during the process of crystallization.

The water vapor sorption isotherms of SD trehalose particles (50% pump feeding rate) at 25°C and 37°C were measured as shown in Figure B.6b. The water vapor absorption isotherm at 37°C appeared to reach the equilibrium faster than at 25°C in terms of RH %. For example, the SD amorphous trehalose reached its highest weight change percentage at 50% RH at 37°C vs 55% RH at 25°C. In addition, the SD amorphous trehalose exhibited more water vapor uptake at 37°C than at 25°C across the whole RH % range studied while retaining the similar isothermal profile trend.



(a)



(b)

**Figure B.6.** Water vapor sorption isotherms of SD trehalose and raw trehalose dihydrate particles (weight change (%) vs relative humidity (RH)): (A) Comparison of water vapor absorption between SD trehalose and raw trehalose dihydrate particles at 25°C; (B) Comparison of water vapor absorption of SD trehalose particles (50% feeding rate) at 25°C and 37°C.

### Hot-Stage Microscopy (HSM) under Cross-Polarizers

The HSM pictures of raw trehalose dihydrate and SD trehalose (50% feeding rate) upon heating are shown in Figure B.7. Under cross-polarized light, the birefringency of raw trehalose dihydrate were observed at 25°C and 37°C. The birefringency of raw trehalose dihydrate started to diminish at 108°C and disappeared finished at 116 °C. This phase transition may correspond to its first endothermic order-to-disorder phase transition, as seen in Figure B.4 for raw trehalose dihydrate. This may be due to the first dehydration process ie. loss of unbound water. As seen in Figure B.7, the crystal shape was retained during this transition. However, during the second endothermic order-to-disorder phase transition, the crystal shape disappeared in the temperature range 146-160°C. Subtle birefringency reemerged in the temperature range of 200-227°C which may suggest a subtle recrystallization event which was not observed in the DSC thermogram. Melting was visualized in the temperature range of 231-234°C as evident by liquid droplet formation.

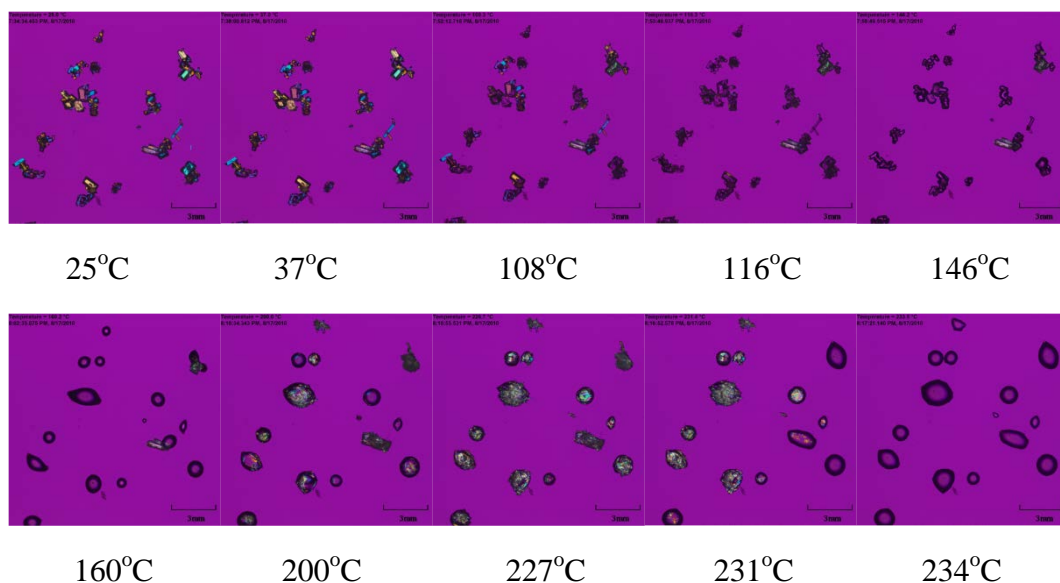


**Figure B.7.** HSM of raw trehalose dihydrate particles

SD trehalose from 50% feeding rate (Figure B.8) showed dark agglomerates lacking birefringency at 25°C and 37°C, as would be expected for non-crystalline amorphous materials. The recrystallization of SD trehalose with increasing temperature was not visually evident due to the small particle size of SD trehalose (Table B.1). The first phase transition visualized by HSM appears to correlate with the small order-to-disorder endotherm (perhaps due to a metastable phase transition or a pretransition), as observed in the DSC thermogram at 140-150°C in Figure B.4c. The melting process occurred at higher temperatures as evident by liquid droplet formation seen in the micrographs.

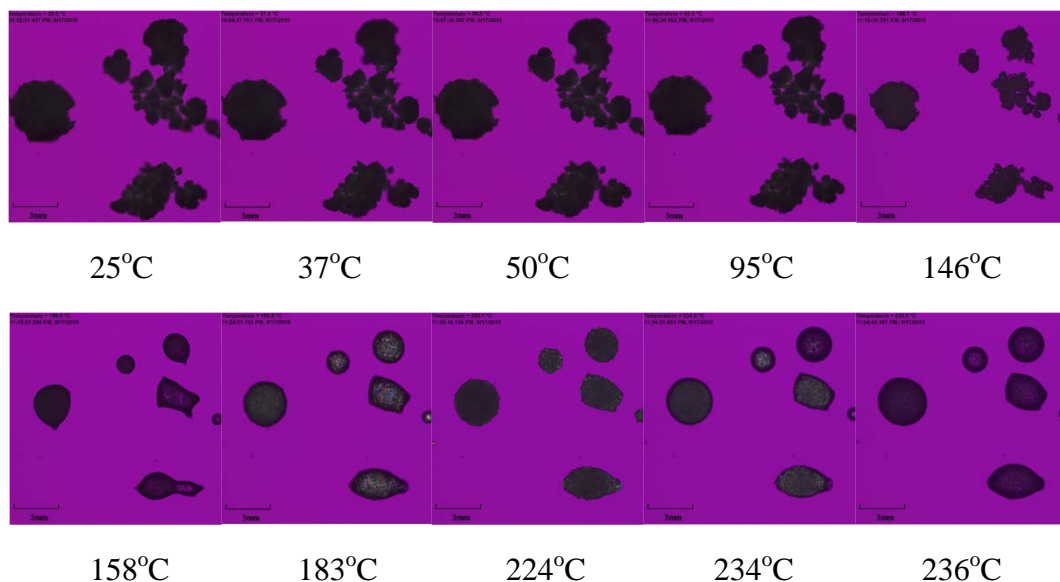


**Figure B.8.** HSM of SD trehalose particles (50% pump feeding rate)

## Discussion

The present work demonstrates that low water content trehalose microparticles and nanoparticles with particle properties necessary for inhalation dry powder delivery can be successfully produced by organic solution advanced spray drying from dilute solution using rationally selected spray drying conditions. By using low concentration of organic solvent solution, the unimodal narrow particle size distribution of SD trehalose microparticulate/nanoparticulate powders was achieved. The unimodal narrow particle size distribution is critical for pulmonary dry powder inhalation, as it enables the particles to target a specific lung region which consequently can lower the therapeutic dose. In addition, the water content of final product can be reduced via spray drying the organic solution of trehalose instead of water solution. Since the size of inhalable particles is small, residual water can have a significant influence on the dispersion of dry powder during aerosolization through capillary force[64]. However, the water content of SD trehalose increased a bit as the pump rate increased but was still at the level that is considered to be low.

The surface morphology, as visualized by SEM, changed with increasing pump feeding rates. Specifically, smooth particles and corrugated particles were produced by low feeding rate and high feeding rate, respectively. Research studies[141, 263] have demonstrated that the particle morphology of dry powder can impact the aerosol performance.

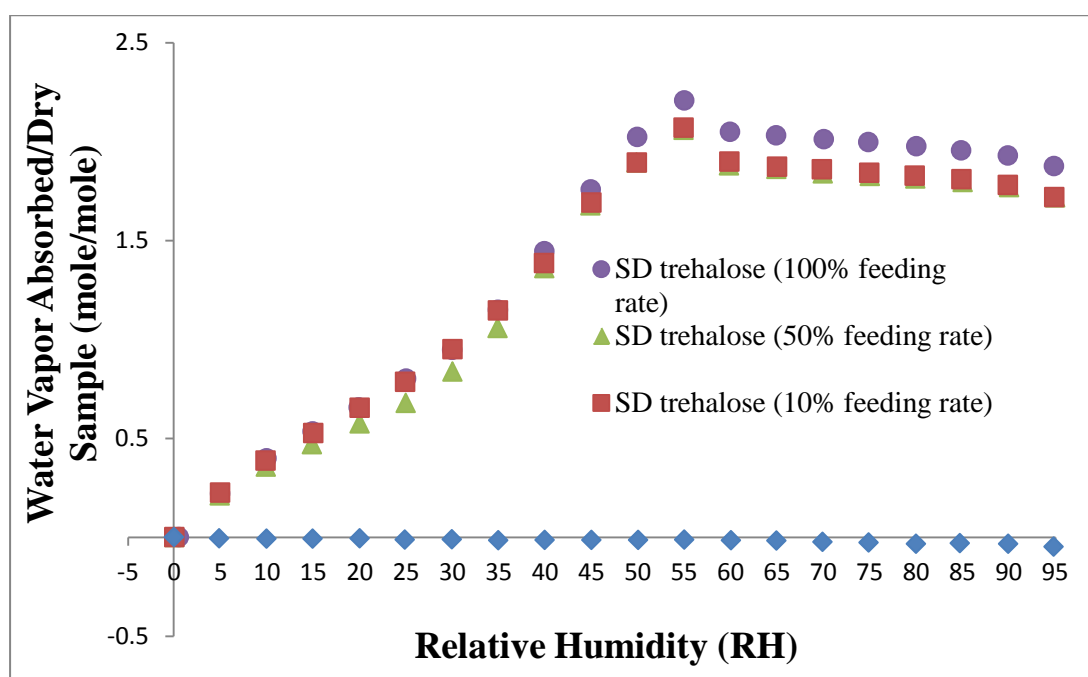
From the XRPD and DSC data, they showed that the organic solution advanced spray drying process from dilute changed raw crystalline trehalose dihydrate into SD amorphous glassy trehalose. The change of pump rate did not significantly affect the XRPD and DSC data for SD trehalose particles. However, DSC thermal analysis for SD trehalose appears to suggest that amorphous rubbery trehalose crystallizes to a relatively more ordered phase at a  $T_c \sim 95^\circ\text{C}$ , as seen by the distinct disorder-to-order exothermic phase transition present in the thermograms.

Gravimetric vapor sorption study illustrated water vapor lyotropic effect on SD trehalose particles microparticulate/nanoparticulate powders. A vapor-induced phase transition suggestive of a glass transition occurred at 30% RH, after which point water vapor uptake continued to increase up to  $\sim 55\%$  RH. The crystallization process appeared to occur during vapor absorption in the RH range of 55-60% RH, as evident by the sharp decrease in water vapor uptake over a narrow RH range followed by the plateau in vapor uptake. It is generally recognized that temperature and RH are two important factors on the phase transition behavior and stability on amorphous phases[310, 311]. As expected for crystalline hydrate powders, raw trehalose dihydrate did not absorb any significant amounts of water vapor over the entire range of RH, as it is in its thermodynamically stable state.

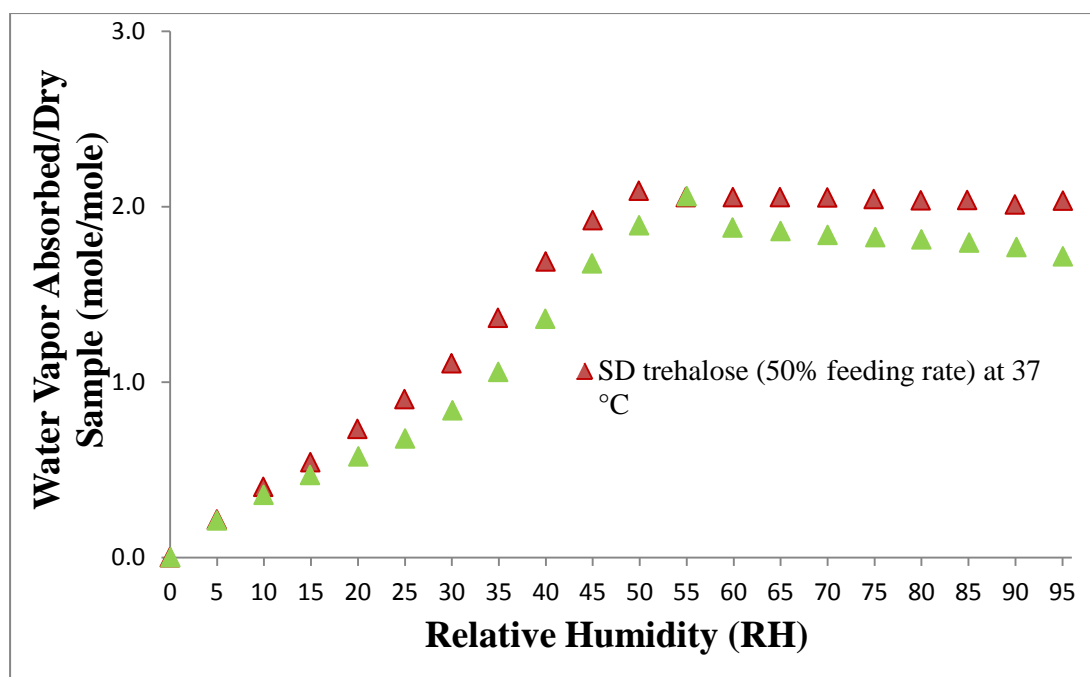
Figure B.9 shows water vapor uptake lyotropic phase behavior at  $25^\circ\text{C}$  (ambient temperature) and  $37^\circ\text{C}$  (biological temperature) on a molar basis for stoichiometric water content analysis and insight. Figure B.9a shows that the raw trehalose dihydrate does not exhibit any significant water vapor uptake on a molar basis. This is expected for crystalline materials especially for crystalline hydrate powders, as crystalline

materials are in a relatively lower thermodynamic energy state.

All spray-dried trehalose amorphous glassy particles, produced using three different pump feeding rates, had similar water vapor sorption profiles but were significantly greater than raw crystalline trehalose dihydrate, as shown in Figure B.9a. The stoichiometric molar ratio reached to 2.1 (i.e. dihydrate) at 55% RH and remained at this level in the plateau region which suggests a lyotropic phase transition from the amorphous rubbery state (i.e. higher energy state) to the thermodynamically stable dihydrate crystal (lower energy state). It decreased slightly followed by a plateau region. There appears to be a slight ratio decrease for SD trehalose at 25°C starting from the crystallization point, reaching to 1.8 moles (i.e. dihydrate) in the plateau region. Figure B.9b shows that the SD trehalose particles had a lesser decrease in the stoichiometric molar ratio at 37°C (biological temperature) at the recrystallization point and was essentially constant at 2 moles (i.e. dihydrate) at higher RH % levels.



(a)



(b)

**Figure B.9.** Water vapor sorption of SD trehalose and raw trehalose dihydrate particles (water vapor absorbed/dry sample (mole/mole) vs relative humidity (RH)): (A) Comparison of water vapor absorption between SD trehalose and raw trehalose dihydrate particles at 25°C; (B) Comparison of water vapor absorption of SD trehalose particles (50% feeding rate) at 25°C and 37°C.

## Conclusions

This study has demonstrated for the first time that the inhalable trehalose microparticles and nanoparticles with different particle morphology were rationally designed and successfully produced via organic solution advanced spray drying from dilute solution. The use of organic solvent has several important advantages to produce unimodal microparticulate/nanoparticulate inhalable powders with greatly reduced residual water content which can improve product stability and performance. The SD trehalose particles from various feeding rates possessed similar amorphous phase and capacity of water vapor sorption. Pharmaceutical processing conditions correlated in a meaningful manner with changes in important physicochemical and particle properties essential for targeted pulmonary delivery as DPIs. The thermotropic and lyotropic phase transition at 25°C and 37°C (biological temperature) were correlated with the amorphous glass vs rubbery state and solid-state phase transitions.

## Acknowledgements

The authors gratefully acknowledge financial support from the UK Daniel P. Reedy Fellowship and Fellowship support from the UK Center of Membrane Sciences



awarded to Xiaojian Li. The authors thank Dr. Dicky Sick Ki Yu for SEM access and Dr. Tonglei Li for XRPD and HSM access.

Appendix B was reproduced with kind permission from: Li, X and Mansour, H.M. Physicochemical Characterization and Water Vapor Absorption of Organic Solution Advanced Spray Dried Trehalose Microparticles and Nanoparticles for Targeted Dry Powder Pulmonary Inhalation Delivery. AAPS PharmSciTech, 2011, 12(4):1420-1430. Copyright © 2011 Springer Science + Business Media.

Copyright © Xiaojian Li 2014

## Appendix C Spray-Dried Itraconazole Aerosols

### C.1 Materials

Two itraconazole formulation systems were produced at the same spray-drying conditions (50% pump rate) as shown in Section 3.2.2.1 in Chapter 3. The itraconazole two-component systems are itraconazole:mannitol and itraconazole:trehalose. The itraconazole three-component systems are itraconazole:phospholipids:mannitol and itraconazole:phospholipids:trehalose.

### C.2 Results

#### C.2.1 Spray-dried Itraconazole Two-component Systems

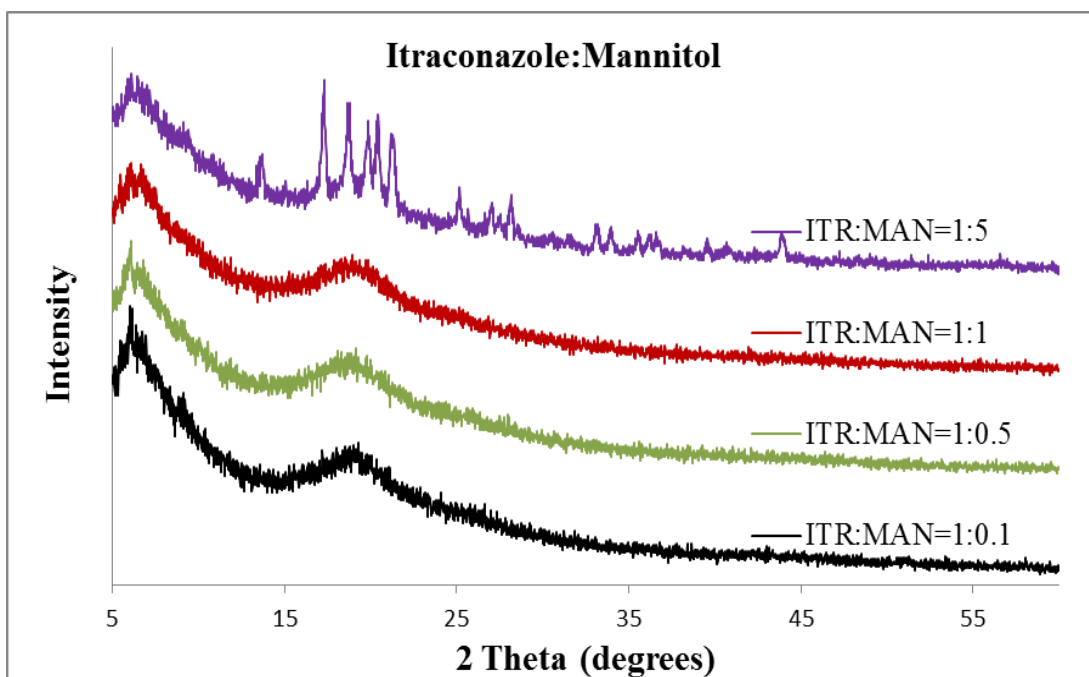
##### C.2.1.1 X-ray Powder Diffraction

The XRPD patterns suggest that SD itraconazole:mannitol (ITR:MAN) (Figure C.1a) and SD itraconazole:trehalose (ITR:TRE) (Figure C.1b) were lacking in long-range molecular order except for ITR:MAN=1:5. By comparing to the XRPD of mannitol (in Appendix A), it suggests that the characteristic peaks correspond to alpha form of MAN.

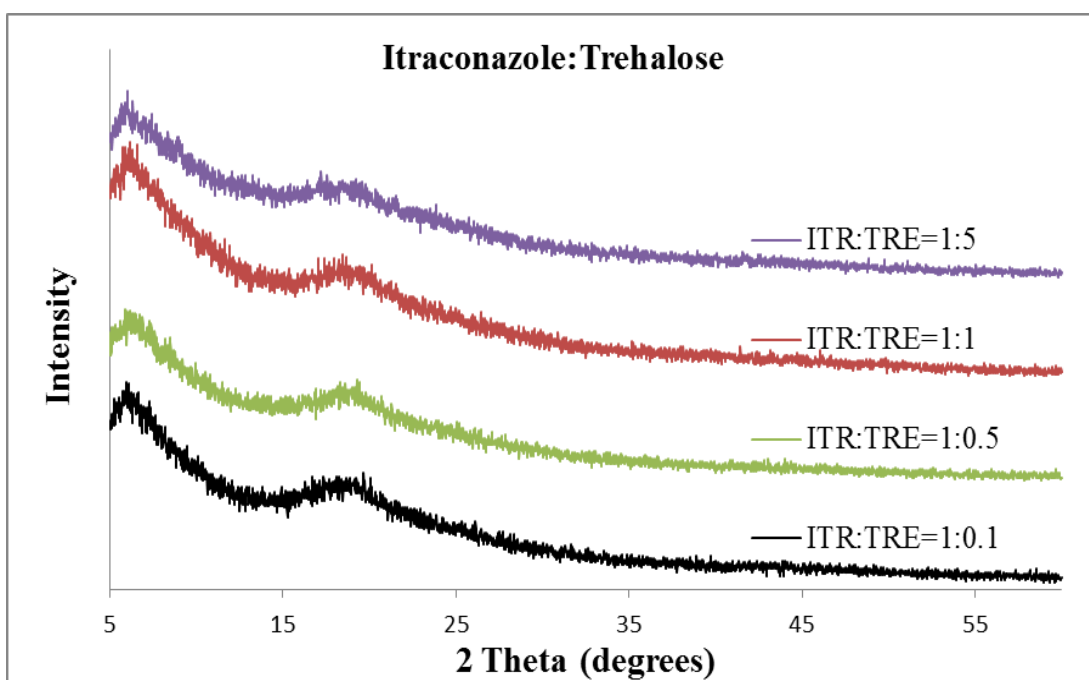
##### C.2.1.2 *In Vitro* Aerosol Dispersion Performance

As shown in Figure C.2a, SD ITR:MAN=1:5 aerosol powder exhibited a relatively higher particle deposition on stage 1 compared to the formulations with other ratios. The deposition mode of fine particles was on stage 4 and stage 2 for the powders of ITR:MAN=1:0.1, 1:0.5, and 1:1, and ITR:MAN=1:5, respectively. Compared to other formulations, ITR:MAN=1:5 aerosol particles exhibited an lower value in FPF and RF, and an higher value in MMAD of 14.3 $\mu$ m. The data indicate that ITR:MAN=1:0.1, 1:0.5, and 1:1, with a MMAD value being approximately  $\leq 5\mu$ m, could be able to penetrate into deep lung regions. However, ITR:MAN=1:5, after partial crystallization, showed a MMAD value far beyond respirable size of 10 $\mu$ m. The detailed values are listed in Table C.1.

SD ITR:TRE aerosol powders (Figure C.2b) shifted fine particle deposition mode from stage 4 to stage 5 with increasing amount of TRE. The FPF, RF, and MMAD of ITR:TRE aerosol particles ranged from 27.9% to 45.9%, 41.7% to 74.7%, and 2.0 $\mu$ m to 4.6 $\mu$ m, respectively. These data suggest that ITR:TRE powders were suitable for deep lung penetration. The detailed values are listed in Table C.2.

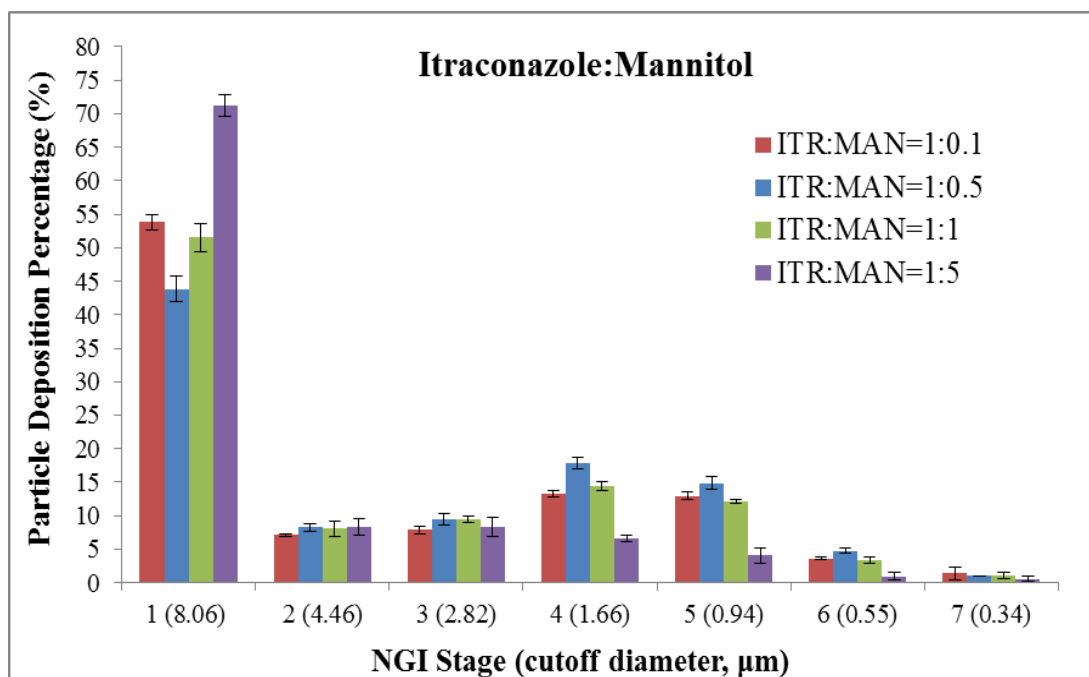


(a)

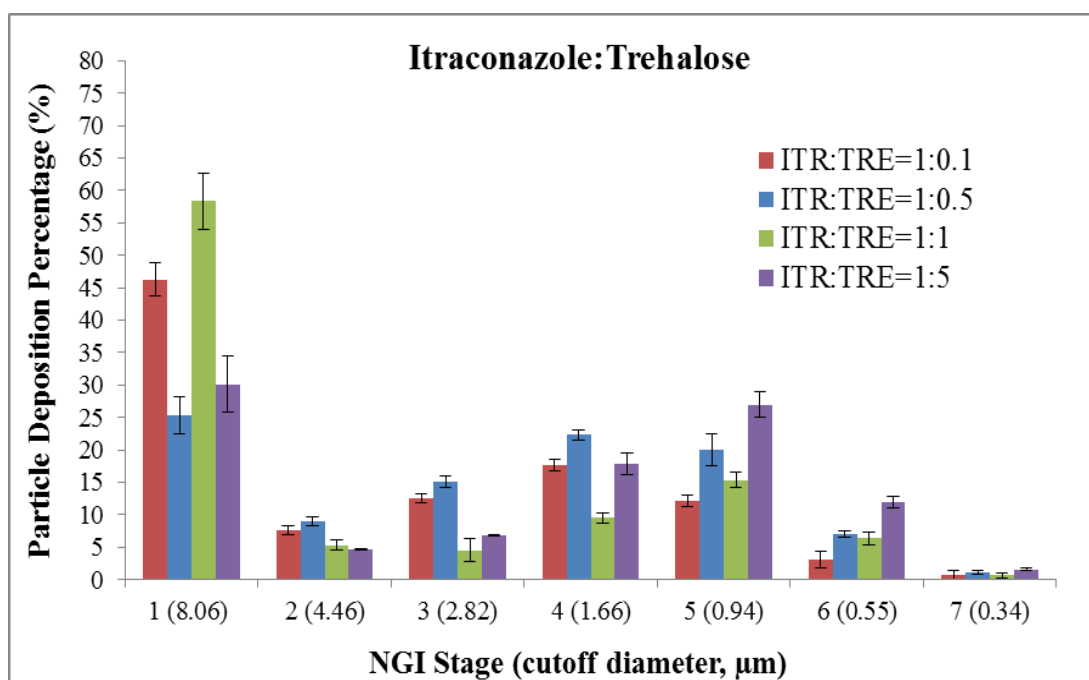


(b)

**Figure C.1.** X-ray powder diffraction patterns for: (a) SD itraconazole:mannitol formulations; and (b) SD itraconazole:trehalose formulations.



(a)



(b)

**Figure C.2.** Aerosol dispersion performance using the NGI under an airflow rate ( $Q$ ) of 60 L/min with the HandiHaler<sup>®</sup> DPI device for: (a) itraconazole:mannitol powders; and (b) itraconazole:trehalose powders (mean  $\pm$  SD,  $n=3$ ).

**Table C.1.** Aerosol dispersion performance parameters of SD itraconazole:mannitol particles (mean  $\pm$  margin of error for 95% confidence, n=3).

ITR:MAN		Aerosol Dispersion Performance Parameters			
Molar Ratio	ED[%]	FPF[%]	RF[%]	MMAD[ $\mu$ m]	GSD
1:0.1	98.1 $\pm$ 1.4	28.2 $\pm$ 1.0	46.2 $\pm$ 1.3	5.2 $\pm$ 0.3	3.2 $\pm$ 0.4
1:0.5	97.0 $\pm$ 0.4	35.9 $\pm$ 1.3	56.1 $\pm$ 2.1	3.8 $\pm$ 0.3	2.6 $\pm$ 0.1
1:1	97.0 $\pm$ 1.4	29.7 $\pm$ 2.8	48.5 $\pm$ 2.3	5.1 $\pm$ 0.4	3.0 $\pm$ 0.2
1:5	98.9 $\pm$ 0.4	16.9 $\pm$ 1.3	28.8 $\pm$ 1.9	14.3 $\pm$ 0.3	3.9 $\pm$ 0.7

**Table C.2.** Aerosol dispersion performance parameters of SD itraconazole:trehalose particles (mean  $\pm$  margin of error for 95% confidence, n=3).

ITR:TRE		Aerosol Dispersion Performance Parameters			
Molar Ratio	ED[%]	FPF[%]	RF[%]	MMAD[ $\mu$ m]	GSD
1:0.1	97.7 $\pm$ 1.0	31.5 $\pm$ 2.6	53.7 $\pm$ 2.9	4.4 $\pm$ 0.4	2.6 $\pm$ 0.1
1:0.5	96.3 $\pm$ 0.7	45.9 $\pm$ 3.5	74.7 $\pm$ 3.1	2.7 $\pm$ 0.3	2.2 $\pm$ 0.1
1:1	97.0 $\pm$ 0.7	27.9 $\pm$ 3.6	41.7 $\pm$ 5.0	4.6 $\pm$ 0.7	3.1 $\pm$ 0.2
1:5	97.7 $\pm$ 1.1	39.4 $\pm$ 2.1	69.9 $\pm$ 5.0	2.0 $\pm$ 0.2	2.0 $\pm$ 0.1

## C.2.2 Spray-dried Itraconazole Three-component Systems

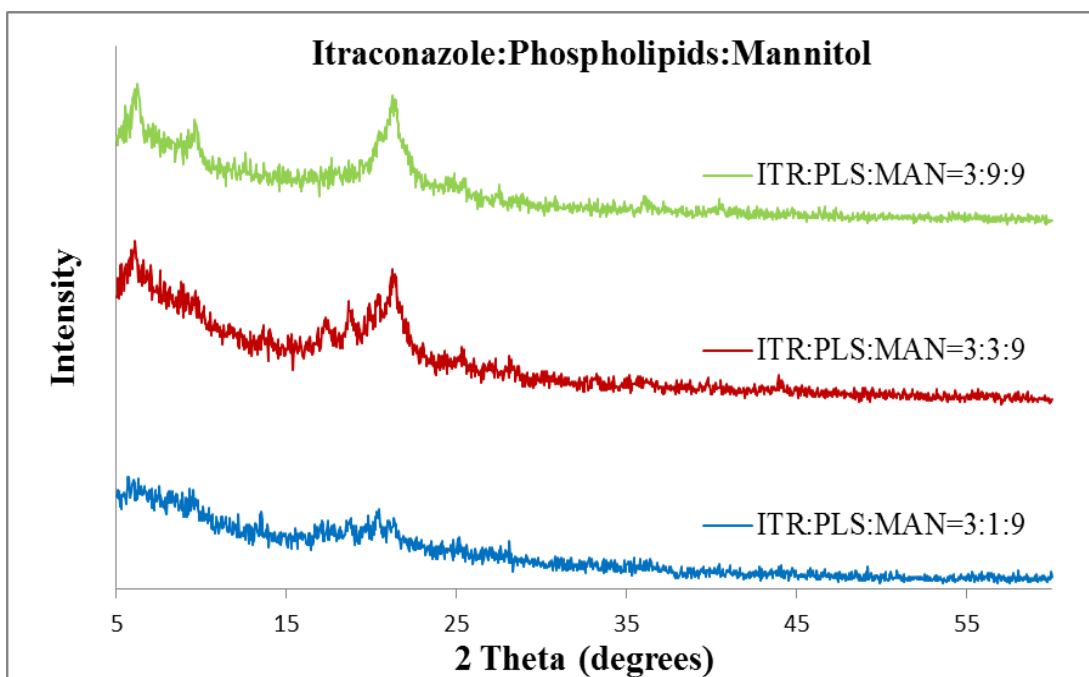
### C.2.2.1 X-ray Powder Diffraction

The XRPD patterns suggest (Figure C.3a) that SD itraconazole:phospholipids:mannitol (ITR:PLS:MAN) formulations lacked long-range molecular order at molar ratio of 3:1:9. Some characteristic crystalline peaks were observed in both ITR:PLS:MAN=3:3:9 and 3:9:9 powders. SD itraconazole:phospholipids:trehalose (ITR:PLS:TRE) particles (Figure C.3b) were lacking in long-range molecular order. The phospholipid bilayer structure was retained after spray drying for both formulation systems.

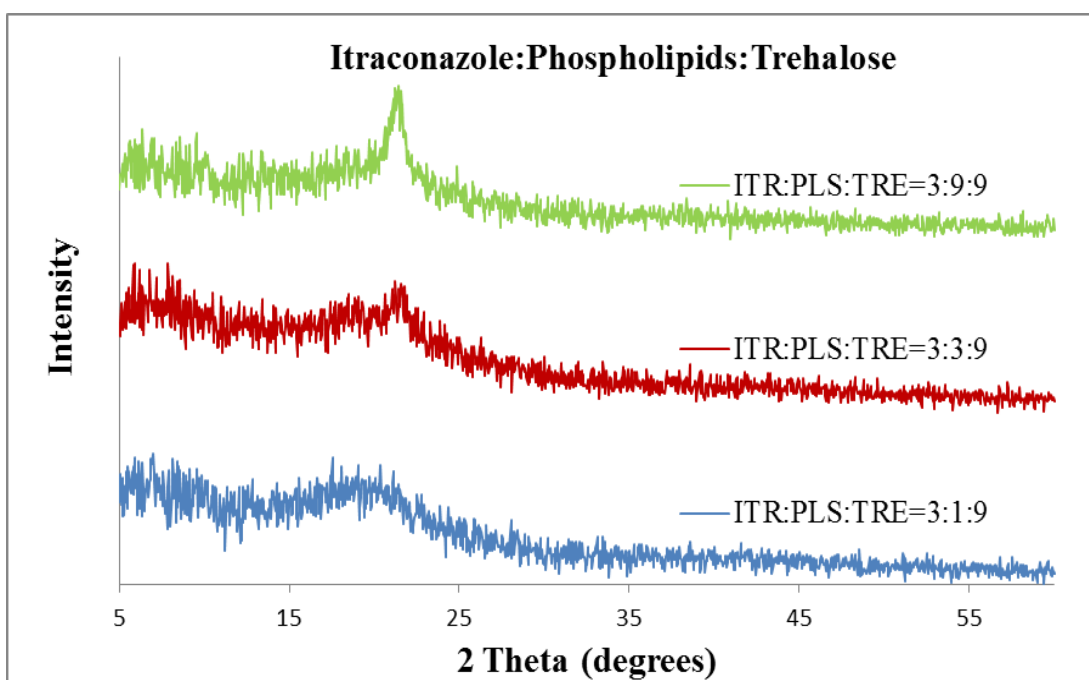
### C.2.2.2 *In Vitro* Aerosol Dispersion Performance

As shown in Figure C.4a, SD ITR:PLS:MAN=3:1:9 aerosols exhibited an extremely low particle deposition of 2.4% on stage 1 compared to other two partially crystalline formulations. The deposition mode of fine particles was on stage 4 and stage 2 for aerosol powders of ITR:PLS:MAN=3:1:9, and ITR:PLS:MAN=3:3:9 and 3:9:9, respectively. ITR:PLS:MAN=3:1:9 aerosols exhibited FPF, RF, and MMAD as 66.3%, 97.6%, and 2.8 $\mu$ m, respectively. As shown for MMAD of being from 28.3 $\mu$ m to 34.3 $\mu$ m, ITR:PLS:MAN=3:3:9 and 3:9:9 aerosol were not suitable for dry powder for inhalation. Therefore, only ITR:PLS:MAN=3:1:9 aerosol powder was suitable to be delivered to deep lung regions. The detailed values are listed in Table C.3.

SD ITR:PLS:TRE (Figure C.4b) aerosol particles exhibited deposition mode of fine particles on stage 4 or stage 5. With FPF, RF, and MMAD being of 36.5%, 70.4%, and 1.9 $\mu$ m, ITR:PLS:MAN=3:3:9 aerosols appeared to have a superior aerosol dispersion performance to the others. ITR:PLS:MAN=3:1:9 and 3:3:9 aerosol particles, exhibiting MMAD values  $\leq$  5 $\mu$ m, were suitable for deep lung delivery. The detailed values are listed in Table C.4.

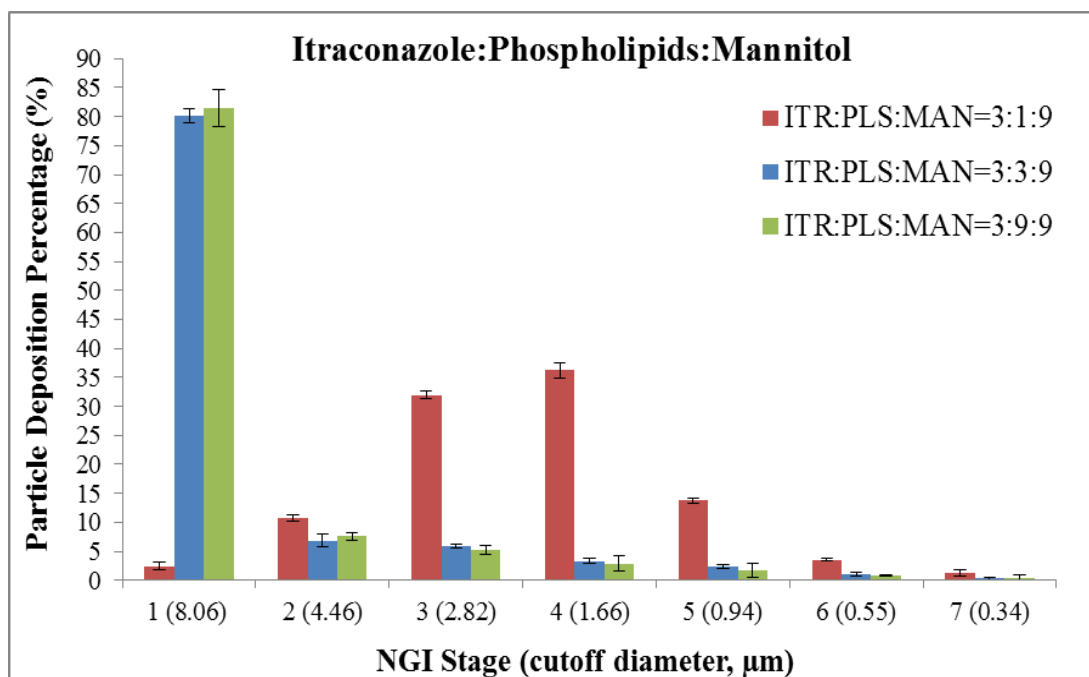


(a)

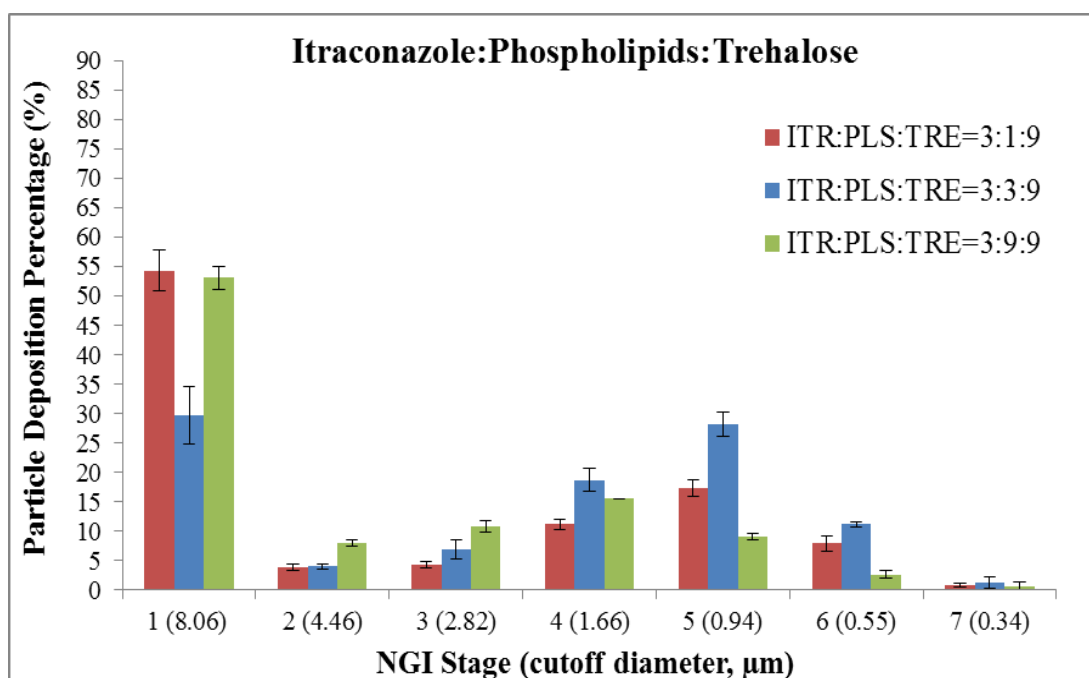


(b)

**Figure C.3.** X-ray powder diffraction patterns for: (a) SD itraconazole:phospholipids:mannitol formulations; and (b) SD itraconazole:phospholipids:trehalose formulations.



(a)



(b)

**Figure C.4.** Aerosol dispersion performance using the NGI under an airflow rate (Q) of 60 L/min with the HandiHaler<sup>®</sup> DPI device for: (a) itraconazole:phospholipids:mannitol powders; and (b) itraconazole:phospholipids:trehalose powders (mean  $\pm$  SD, n=3).



**Table C.3.** Aerosol dispersion performance parameters of SD itraconazole:phospholipids:mannitol particles (mean  $\pm$  margin of error for 95% confidence, n=3).

ITR:PLS:MAN		Aerosol Dispersion Performance Parameters			
Molar Ratio	ED[%]	FPF[%]	RF[%]	MMAD[ $\mu$ m]	GSD
3:1:9	95.4 $\pm$ 0.9	66.3 $\pm$ 0.6	97.6 $\pm$ 0.8	2.8 $\pm$ 0.1	1.8 $\pm$ 0.0
3:3:9	99.4 $\pm$ 0.2	12.3 $\pm$ 0.9	19.8 $\pm$ 1.3	28.3 $\pm$ 2.0	4.9 $\pm$ 0.2
3:9:9	99.2 $\pm$ 0.4	10.1 $\pm$ 2.4	18.5 $\pm$ 3.6	34.3 $\pm$ 7.8	5.5 $\pm$ 2.7

**Table C.4.** Aerosol dispersion performance parameters of SD itraconazole:phospholipids:trehalose particles (mean  $\pm$  margin of error for 95% confidence, n=3).

ITR:PLS:TRE		Aerosol Dispersion Performance Parameters			
Molar Ratio	ED[%]	FPF[%]	RF[%]	MMAD[ $\mu$ m]	GSD
3:1:9	96.7 $\pm$ 0.5	23.9 $\pm$ 2.3	45.7 $\pm$ 4.0	3.6 $\pm$ 0.6	2.8 $\pm$ 0.2
3:3:9	93.2 $\pm$ 0.9	36.5 $\pm$ 3.1	70.4 $\pm$ 5.6	1.9 $\pm$ 0.1	2.0 $\pm$ 0.1
3:9:9	98.0 $\pm$ 0.2	29.6 $\pm$ 1.9	46.9 $\pm$ 2.2	5.6 $\pm$ 0.3	2.9 $\pm$ 0.3

## References

1. *Pulmonary/respiratory system*. 2000. Accessed 2014. Available from: <http://webschoolsolutions.com/patts/systems/lungs.htm>.
2. Patton, J.S. and P.R. Byron, *Inhaling medicines: delivering drugs to the body through the lungs*. Nat Rev Drug Discov, 2007. **6**(1): p. 67-74.
3. Weibel, E.R., *Morphometry of the human lung*. 1963. Berlin: Springer.
4. Horsfield, K., G. Dart, D.E. Olson, G.F. Filley, and G. Cumming, *Models of the human bronchial tree*. J Appl Physiol, 1971. **31**(2): p. 207-17.
5. Hickey, A.J., *Pharmaceutical inhalation aerosol technology*. 2nd ed. Drugs and the pharmaceutical sciences. 2004. New York: M. Dekker.
6. *Exam 3 review: chapter 22: alveoli*. Accessed 2014. Available from: <http://apbrwww5.apsu.edu/thompsonj/Anatomy%20&%20Physiology/2020/2020%20Exam%20Reviews/Exam%203/CH22%20Alveoli.htm>.
7. Parra, S.C., R. Burnette, H.P. Price, and T. Takaro, *Zonal distribution of alveolar macrophages, type II pneumonocytes, and alveolar septal connective tissue gaps in adult human lungs*. Am Rev Respir Dis, 1986. **133**(5): p. 908-12.
8. *Ozone & our lungs*. 2010. Accessed 2014. Available from: [http://www.bio.davidson.edu/people/kabern/berndcv/lab/online\\_website2/ethanol.html](http://www.bio.davidson.edu/people/kabern/berndcv/lab/online_website2/ethanol.html).
9. Fehrenbach, H., *Alveolar epithelial type II cell: defender of the alveolus revisited*. Respir Res, 2001. **2**(1): p. 33-46.
10. Pilcer, G., *New highly effective dry powder tobramycin formulations for inhalation in the treatment of cystic fibrosis*. 2008, University of Brussels.
11. Wright, J.R., *Immunomodulatory functions of surfactant*. Physiol Rev, 1997. **77**(4): p. 931-62.
12. Morgenroth, K. and J. Bolz, *Morphological features of the interaction between mucus and surfactant on the bronchial mucosa*. Respiration, 1985. **47**(3): p. 225-31.
13. Matalon, S., B.A. Holm, R.R. Baker, M.K. Whitfield, and B.A. Freeman, *Characterization of antioxidant activities of pulmonary surfactant mixtures*. Biochim Biophys Acta, 1990. **1035**(2): p. 121-7.
14. Suarez, S. and A.J. Hickey, *Drug properties affecting aerosol behavior*. Respir Care, 2000. **45**(6): p. 652-66.
15. *Snow, rain, and the Stokes number*. Accessed 2014. Available from: <http://s3.danielcromer.com/resources/SnowRainStokesNo.pdf>.
16. Xu, Z., *Heterogeneous particle deaggregation and its implication for therapeutic aerosol performance*. 2010, University of North Carolina at Chapel Hill.
17. Chan, H.K. and I. Gonda, *Respirable form of crystals of cromoglycic acid*. J Pharm Sci, 1989. **78**(2): p. 176-80.
18. Ikegami, K., Y. Kawashima, H. Takeuchi, H. Yamamoto, N. Isshiki, D. Momose, and K. Ouchi, *Improved inhalation behavior of steroid KSR-592 in vitro with Jethaler by polymorphic transformation to needle-like crystals (beta-form)*. Pharm Res, 2002. **19**(10): p. 1439-45.

19. Ikegami, K., Y. Kawashima, H. Takeuchi, H. Yamamoto, K. Mimura, D. Momose, and K. Ouchi, *A new agglomerated KSR-592 beta-form crystal system for dry powder inhalation formulation to improve inhalation performance in vitro and in vivo*. J Control Release, 2003. **88**(1): p. 23-33.
20. Hinds, W.C., *Aerosol technology : properties, behavior, and measurement of airborne particles*. 2nd ed. 1999. New York: Wiley.
21. Crowder, T.M., J.A. Rosati, J.D. Schroeter, A.J. Hickey, and T.B. Martonen, *Fundamental effects of particle morphology on lung delivery: predictions of Stokes' law and the particular relevance to dry powder inhaler formulation and development*. Pharm Res, 2002. **19**(3): p. 239-45.
22. Lippmann, M. and R.B. Schlesinger, *Interspecies comparisons of particle deposition and mucociliary clearance in tracheobronchial airways*. J Toxicol Environ Health, 1984. **13**(2-3): p. 441-69.
23. Wang, C.-s., *Inhaled particles*. 1st ed. Interface science and technology. 2005. Amsterdam ; Boston: Elsevier Academic Press.
24. Finlay, W.H., *The mechanics of inhaled pharmaceutical aerosols : an introduction*. 2001. San Diego: Academic Press.
25. Muchao, F.P. and L.V. Filho, *Advances in inhalation therapy in pediatrics*. J Pediatr (Rio J), 2010. **86**(5): p. 367-76.
26. Sebt, T. and K. Amighi, *Preparation and in vitro evaluation of lipidic carriers and fillers for inhalation*. Eur J Pharm Biopharm, 2006. **63**(1): p. 51-8.
27. Cipolla, D., I. Gonda, and S.J. Shire, *Characterization of aerosols of human recombinant deoxyribonuclease I (rhDNase) generated by jet nebulizers*. Pharm Res, 1994. **11**(4): p. 491-8.
28. Reyckler, G., C. Dupont, J.C. Dubus, G.A.T. pour le, and G. le, *Disinfection of devices for nebulization: stakes, difficulties, and improvement proposals*. Rev Mal Respir, 2007. **24**(10): p. 1351-61.
29. Newman, S.P., G.R. Pitcairn, P.H. Hirst, and L. Rankin, *Radionuclide imaging technologies and their use in evaluating asthma drug deposition in the lungs*. Advanced Drug Delivery Reviews, 2003. **55**(7): p. 851-867.
30. Hickey, A.J., *Inhalation aerosols : physical and biological basis for therapy*. Lung biology in health and disease. 1996. New York: M. Dekker.
31. Swarbrick, J., *Encyclopedia of pharmaceutical technology*. 3rd ed. 2007. New York: Informa Healthcare.
32. Pritchard, J. *The future of metered-dose inhalers*. 2005. Accessed 2014. Available from: <http://www.pharmtech.com/pharmtech/Analytical/The-Future-of-Metered-Dose-Inhalers/ArticleStandard/Article/detail/176027>.
33. Polli, G.P., W.M. Grim, F.A. Bacher, and M.H. Yunker, *Influence of formulation on aerosol particle size*. Journal of Pharmaceutical Sciences, 1969. **58**(4): p. 484-486.
34. Newman, S.P., *Principles of metered-dose inhaler design*. Respir Care, 2005. **50**(9): p. 1177-90.
35. Molina, M.J. and F.S. Rowland, *Stratospheric sink for chlorofluoromethanes - chlorine atom catalyzed destruction of ozone*. Bulletin of the American Meteorological Society, 1974. **55**(5): p. 491-491.

36. Crompton, G.K., *Problems patients have using pressurized aerosol inhalers*. European Journal of Respiratory Diseases, 1982. **63**: p. 101-104.
37. Liu, D., *Aerosol delivery of recombinant antigen 85B in microparticle vaccine systems for protection against tuberculosis*. 2007, University of North Carolina at Chapel Hill.
38. *Use of ozone-depleting substances; removal of essential-use designation*. 2005, U.S. Food and Drug Administration.
39. *Montreal protocol on substances that deplete the ozone layers*. 1987, Montreal Protocol.
40. *SPIRIVA-tiotropium bromide monohydrate capsule*. 2009. Accessed 2014. Available from: <http://dailymed.nlm.nih.gov/dailymed/archives/fdaDrugInfo.cfm?archiveid=10358>.
41. Dunbar, C.A., A.J. Hickey, and P. Holzner, *Dispersion and characterization of pharmaceutical dry powder aerosols*. KONA, 1998. **16**: p. 7-45.
42. Daniher, D.I. and J. Zhu, *Dry powder platform for pulmonary drug delivery*. Particuology, 2008. **6**(4): p. 225-238.
43. Li, X., F.G. Vogt, D. Hayes, Jr., and H.M. Mansour, *Physicochemical characterization and aerosol dispersion performance of organic solution advanced spray-dried microparticulate/nanoparticulate antibiotic dry powders of tobramycin and azithromycin for pulmonary inhalation aerosol delivery*. Eur J Pharm Sci, 2014. **15**: p. 191-205.
44. Li, X., F.G. Vogt, D. Hayes, Jr., and H.M. Mansour, *Design, characterization, and aerosol dispersion performance modeling of advanced spray-dried microparticulate/nanoparticulate mannitol powders for targeted pulmonary delivery as dry powder inhalers*. J Aerosol Med Pulm Drug Deliv, 2014. **27**(2): p. 81-93.
45. Telko, M.J. and A.J. Hickey, *Dry powder inhaler formulation*. Respir Care, 2005. **50**(9): p. 1209-27.
46. Mansour, H.M., Z. Xu, and A.J. Hickey, *Dry powder aerosols generated by standardized entrainment tubes from alternative sugar blends: 3. Trehalose dihydrate and D-mannitol carriers*. J Pharm Sci, 2010. **99**(8): p. 3430-41.
47. Xu, Z., H.M. Mansour, T. Mulder, R. McLean, J. Langridge, and A.J. Hickey, *Dry powder aerosols generated by standardized entrainment tubes from drug blends with lactose monohydrate: 2. Ipratropium bromide monohydrate and fluticasone propionate*. J Pharm Sci, 2010. **99**(8): p. 3415-29.
48. Xu, Z., H.M. Mansour, T. Mulder, R. McLean, J. Langridge, and A.J. Hickey, *Dry powder aerosols generated by standardized entrainment tubes from drug blends with lactose monohydrate: 1. Albuterol sulfate and disodium cromoglycate*. J Pharm Sci, 2010. **99**(8): p. 3398-414.
49. Dalby, R., M. Spallek, and T. Voshaar, *A review of the development of Respimat Soft Mist Inhaler*. Int J Pharm, 2004. **283**(1-2): p. 1-9.
50. Podczec, F., *Particle-particle adhesion in pharmaceutical powder handling*. 1998. London, UK: Imperial College Press.
51. de Boer, A.H., P. Hagedoorn, D. Gjaltema, J. Goede, and H.W. Frijlink, *Air classifier technology (ACT) in dry powder inhalation. Part 1. Introduction of a novel force distribution concept (FDC) explaining the performance of a basic air classifier on adhesive mixtures*. Int J Pharm, 2003. **260**(2): p. 187-200.

52. Weiler, C., M. Egen, M. Trunk, and P. Langguth, *Force control and powder dispersibility of spray dried particles for inhalation*. Journal of Pharmaceutical Sciences, 2010. **99**(1): p. 303-316.
53. Concessio, N.M. and A.J. Hickey, *Descriptors of irregular particle morphology and powder properties*. Adv Drug Deliv Rev, 1997. **26**(1): p. 29-40.
54. Young, P.M., A. Sung, D. Traini, P. Kwok, H. Chiou, and H.K. Chan, *Influence of humidity on the electrostatic charge and aerosol performance of dry powder inhaler carrier based systems*. Pharm Res, 2007. **24**(5): p. 963-70.
55. Larhrib, H., G.P. Martin, C. Marriott, and D. Prime, *The influence of carrier and drug morphology on drug delivery from dry powder formulations*. Int J Pharm, 2003. **257**(1-2): p. 283-96.
56. Young, P.M., D. Cocconi, P. Colombo, R. Bettini, R. Price, D.F. Steele, and M.J. Tobyn, *Characterization of a surface modified dry powder inhalation carrier prepared by "particle smoothing"*. J Pharm Pharmacol, 2002. **54**(10): p. 1339-44.
57. Zeng, X.M., G.P. Martin, C. Marriott, and J. Pritchard, *The influence of carrier morphology on drug delivery by dry powder inhalers*. Int J Pharm, 2000. **200**(1): p. 93-106.
58. Buckton, G., *Characterisation of small changes in the physical properties of powders of significance for dry powder inhaler formulations*. Advanced Drug Delivery Reviews, 1997. **26**(1): p. 17-27.
59. Dickhoff, B.H.J., A.H. de Boer, D. Lambregts, and H.W. Frijlink, *The effect of carrier surface and bulk properties on drug particle detachment from crystalline lactose carrier particles during inhalation, as function of carrier payload and mixing time*. European Journal of Pharmaceutics and Biopharmaceutics, 2003. **56**(2): p. 291-302.
60. Le, V.N.P., H. Bierend, E. Robins, H. Steckel, and M.P. Flament, *Influence of the lactose grade within dry powder formulations of fluticasone propionate and terbutaline sulphate*. International Journal of Pharmaceutics, 2012. **422**(1-2): p. 75-82.
61. Traini, D., P.M. Young, F. Thielmann, and M. Acharya, *The influence of lactose pseudopolymorphic form on salbutamol sulfate-lactose interactions in DPI formulations*. Drug Development and Industrial Pharmacy, 2008. **34**(9): p. 992-1001.
62. Wagner, K.G., U. Dowe, and J. Zadnik, *Highly loaded interactive mixtures for dry powder inhalers: Prediction of the adhesion capacity using surface energy and solubility parameters*. Pharmazie, 2005. **60**(5): p. 339-344.
63. Wu, X., X. Li, and H.M. Mansour, *Surface analytical techniques in solid-state particle characterization for predicting performance in dry powder inhalers*. Kona Powder and Particle Journal, 2010(28): p. 3-19.
64. Hickey, A.J., H.M. Mansour, M.J. Telko, Z. Xu, H.D. Smyth, T. Mulder, R. McLean, J. Langridge, and D. Papadopoulos, *Physical characterization of component particles included in dry powder inhalers. I. Strategy review and static characteristics*. J Pharm Sci, 2007. **96**(5): p. 1282-301.
65. Salama, R., S. Hoe, H.K. Chan, D. Traini, and P.M. Young, *Preparation and characterisation of controlled release co-spray dried drug-polymer microparticles for inhalation 1: Influence of polymer concentration on*

- physical and in vitro characteristics*. European Journal of Pharmaceutics and Biopharmaceutics, 2008. **69**(2): p. 486-495.
66. Begat, P., D.A. Morton, J.N. Staniforth, and R. Price, *The cohesive-adhesive balances in dry powder inhaler formulations II: influence on fine particle delivery characteristics*. Pharm Res, 2004. **21**(10): p. 1826-33.
  67. Hooton, J.C., M.D. Jones, and R. Price, *Predicting the behavior of novel sugar carriers for dry powder inhaler formulations via the use of a cohesive-adhesive force balance approach*. J Pharm Sci, 2006. **95**(6): p. 1288-97.
  68. Hickey, A.J. and H.M. Mansour, *Formulation challenges of powders for the delivery of small molecular weight molecules as aerosols*, in *Modified-release drug delivery technology*, e.a. M.J. Rathbone, Editor. 2008, Informa Healthcare: New York. p. 573-602.
  69. Hickey, A.J. and H.M. Mansour, *Delivery of drugs by the pulmonary route*, in *Modern Pharmaceutics*, A.T. Florence and J. Siepmann, Editors. 2009, Taylor & Francis: New York. p. 191-219.
  70. Mansour, H.M., Y.S. Rhee, and X. Wu, *Nanomedicine in pulmonary delivery*. Int J Nanomedicine, 2009. **4**: p. 299-319.
  71. Franks, F., *Freeze-drying of bioproducts: putting principles into practice*. European Journal of Pharmaceutics and Biopharmaceutics, 1998. **45**(3): p. 221-229.
  72. *Laboratory scale spray drying of lactose: a review*. 2010. Accessed 2014. Available from: <http://www.guispyer.com/views/38715-b-290-bb-57-laboratory-scale-spray-drying-of-lactose-a-review-en-01/>.
  73. Bosquillon, C., P.G. Rouxhet, F. Ahimou, D. Simon, C. Culot, V. Preat, and R. Vanbever, *Aerosolization properties, surface composition and physical state of spray-dried protein powders*. J Control Release, 2004. **99**(3): p. 357-67.
  74. Rabbani, N.R. and P.C. Seville, *The influence of formulation components on the aerosolisation properties of spray-dried powders*. Journal of Controlled Release, 2005. **110**(1): p. 130-140.
  75. Seville, P.C., H.Y. Li, and T.P. Learoyd, *Spray-dried powders for pulmonary drug delivery*. Crit Rev Ther Drug Carrier Syst, 2007. **24**(4): p. 307-60.
  76. Masters, K., *Spray drying handbook*. 5th ed. 1991. New York: Longman Scientific & Technical.
  77. Pennington, J., *Respiratory infections : diagnosis and management*. 2nd ed. 1989. New York: Raven Press.
  78. Mueller, R.E., D.L. Keble, J. Plummer, and S.H. Walker, *The prevalence of chronic bronchitis, chronic airway obstruction, and respiratory symptoms in a Colorado city*. Am Rev Respir Dis, 1971. **103**(2): p. 209-28.
  79. Ballal, S.G., *Respiratory symptoms and occupational bronchitis in chromite ore miners, Sudan*. J Trop Med Hyg, 1986. **89**(5): p. 223-8.
  80. Cullen, K.J., J. Elder, A.R. Adams, and N.S. Stenhouse, *Additional factors in chronic bronchitis*. Br Med J, 1970. **1**(5693): p. 394-5.
  81. Enterline, P.E., *The effects of occupation on chronic respiratory disease*. Arch Environ Health, 1967. **14**(1): p. 189-200.
  82. Fauci, A.S., *Harrison's principles of internal medicine / editors, Anthony S. Fauci ... [et al.]*. 17th ed. 2008. New York: McGraw-Hill Medical.

83. Lamy, M.E., F. Pouthier-Simon, and E. Debacker-Willame, *Respiratory viral infections in hospital patients with chronic bronchitis. Observations during periods of exacerbation and quiescence*. Chest, 1973. **63**(3): p. 336-41.
84. Ruuskanen, O., E. Lahti, L.C. Jennings, and D.R. Murdoch, *Viral pneumonia*. Lancet, 2011. **377**(9773): p. 1264-75.
85. Boucher, R.C., *Human airway ion transport. Part two*. Am J Respir Crit Care Med, 1994. **150**(2): p. 581-93.
86. Davis, P.B., M. Drumm, and M.W. Konstan, *Cystic fibrosis*. Am J Respir Crit Care Med, 1996. **154**(5): p. 1229-56.
87. Rowe, S.M., S. Miller, and E.J. Sorscher, *Mechanisms of disease: Cystic fibrosis*. New England Journal of Medicine, 2005. **352**(19): p. 1992-2001.
88. Kerem, E., S. Conway, S. Elborn, H. Heijerman, and C. Consensus, *Standards of care for patients with cystic fibrosis: a European consensus*. J Cyst Fibros, 2005. **4**(1): p. 7-26.
89. Ramsey, B.W., M.S. Pepe, J.M. Quan, K.L. Otto, A.B. Montgomery, J. Williams-Warren, K.M. Vasiljev, D. Borowitz, C.M. Bowman, B.C. Marshall, S. Marshall, and A.L. Smith, *Intermittent administration of inhaled tobramycin in patients with cystic fibrosis. Cystic Fibrosis Inhaled Tobramycin Study Group*. N Engl J Med, 1999. **340**(1): p. 23-30.
90. Gilligan, P.H., *Microbiology of airway disease in patients with cystic fibrosis*. Clin Microbiol Rev, 1991. **4**(1): p. 35-51.
91. Sexauer, W.P. and S.B. Fiel, *Aerosolized antibiotics in cystic fibrosis*. Semin Respir Crit Care Med, 2003. **24**(6): p. 717-26.
92. Sermet-Gaudelus, I., A. Lesne-Hulin, G. Lenoir, E. Singlas, P. Berche, and C. Hennequin, *Sputum itraconazole concentrations in cystic fibrosis patients*. Antimicrob Agents Chemother, 2001. **45**(6): p. 1937-8.
93. Cimon, B., J. Carrere, J.P. Chazalotte, J.L. Ginies, P. Six, J.F. Vinatier, D. Chabasse, and J.P. Bouchara, *Fungal colonization and immune response to fungi in cystic fibrosis*. Journal De Mycologie Medicale, 1995. **5**(4): p. 211-216.
94. Mroueh, S. and A. Spock, *Allergic bronchopulmonary aspergillosis in patients with cystic fibrosis*. Chest, 1994. **105**(1): p. 32-6.
95. Simmonds, E.J., J.M. Littlewood, and E.G. Evans, *Cystic fibrosis and allergic bronchopulmonary aspergillosis*. Arch Dis Child, 1990. **65**(5): p. 507-11.
96. Laufer, P., J.N. Fink, W.T. Bruns, G.F. Unger, J.H. Kalbfleisch, P.A. Greenberger, and R. Patterson, *Allergic bronchopulmonary aspergillosis in cystic fibrosis*. J Allergy Clin Immunol, 1984. **73**(1 Pt 1): p. 44-8.
97. Hennequin, C., N. Benailly, C. Silly, M. Sorin, P. Scheinmann, G. Lenoir, J.L. Gaillard, and P. Berche, *In vitro susceptibilities to amphotericin B, itraconazole, and miconazole of filamentous fungi isolated from patients with cystic fibrosis*. Antimicrob Agents Chemother, 1997. **41**(9): p. 2064-6.
98. Griesse, M., P. Birrer, and A. Demirsoy, *Pulmonary surfactant in cystic fibrosis*. European Respiratory Journal, 1997. **10**(9): p. 1983-8.
99. Griesse, M., A. Duroux, A. Schams, A.G. Lenz, and N. Kleinsasser, *Tracheobronchial surface active material in cystic fibrosis*. Eur J Med Res, 1997. **2**(3): p. 114-20.

100. Berka, R.M., G.L. Gray, and M.L. Vasil, *Studies of phospholipase C (heat-labile hemolysin) in Pseudomonas aeruginosa*. Infect Immun, 1981. **34**(3): p. 1071-4.
101. Berka, R.M. and M.L. Vasil, *Phospholipase C (heat-labile hemolysin) of Pseudomonas aeruginosa: purification and preliminary characterization*. J Bacteriol, 1982. **152**(1): p. 239-45.
102. Liu, P.V., *Extracellular toxins of Pseudomonas aeruginosa*. J Infect Dis, 1974. **130 Suppl**(0): p. S94-9.
103. Lucchesi, G.I. and C.E. Domenech, *A simple and reliable method for the purification of Pseudomonas aeruginosa phospholipase C produced in a high phosphate medium containing choline*. Int J Biochem, 1994. **26**(2): p. 155-62.
104. Stinson, M.W. and C. Hayden, *Secretion of phospholipase C by Pseudomonas aeruginosa*. Infect Immun, 1979. **25**(2): p. 558-64.
105. Cystic fibrosis foundation. 2011. Accessed 2014. Available from: <http://www.cff.org/>.
106. Elkins, M.R., M. Robinson, B.R. Rose, C. Harbour, C.P. Moriarty, G.B. Marks, E.G. Belousova, W. Xuan, P.T. Bye, and G. National Hypertonic Saline in Cystic Fibrosis Study, *A controlled trial of long-term inhaled hypertonic saline in patients with cystic fibrosis*. N Engl J Med, 2006. **354**(3): p. 229-40.
107. Ratjen, F., *Restoring airway surface liquid in cystic fibrosis*. N Engl J Med, 2006. **354**(3): p. 291-3.
108. King, M. and B.K. Rubin, *Pharmacological approaches to discovery and development of new mucolytic agents*. Adv Drug Deliv Rev, 2002. **54**(11): p. 1475-90.
109. Smyth, A.R., A. Barbato, N. Beydon, H. Bisgaard, K. de Boeck, P. Brand, A. Bush, B. Fauroux, J. de Jongste, M. Korppi, C. O'Callaghan, M. Pijnenburg, F. Ratjen, K. Southern, D. Spencer, A. Thomson, H. Vyas, A. Warris, and P.J. Merkus, *Respiratory medicines for children: current evidence, unlicensed use and research priorities*. Eur Respir J, 2010. **35**(2): p. 247-65.
110. Bell, S.L., I.A. Khatri, G.Q. Xu, and J.F. Forstner, *Evidence that a peptide corresponding to the rat Muc2 C-terminus undergoes disulphide-mediated dimerization*. European Journal of Biochemistry, 1998. **253**(1): p. 123-131.
111. Perez-Vilar, J. and R.L. Hill, *The structure and assembly of secreted mucins*. J Biol Chem, 1999. **274**(45): p. 31751-4.
112. Baum, G.L., *Cilia, mucus, and mucociliary interactions*. 1998. New York: Marcel Dekker.
113. Pedersen, S.S., T. Jensen, N. Hoiby, C. Koch, and E.W. Flensburg, *Management of Pseudomonas aeruginosa lung infection in Danish cystic fibrosis patients*. Acta Paediatr Scand, 1987. **76**(6): p. 955-61.
114. Smith, A.L., G. Redding, C. Doershuk, D. Goldmann, E. Gore, B. Hilman, M. Marks, R. Moss, B. Ramsey, T. Rubio, and et al., *Sputum changes associated with therapy for endobronchial exacerbation in cystic fibrosis*. J Pediatr, 1988. **112**(4): p. 547-54.
115. Feng, C.H., S.J. Lin, H.L. Wu, and S.H. Chen, *Trace analysis of tobramycin in human plasma by derivatization and high-performance liquid chromatography with ultraviolet detection*. J Chromatogr B Analyt Technol Biomed Life Sci, 2002. **780**(2): p. 349-54.



116. Gibson, R.L., J.L. Burns, and B.W. Ramsey, *Pathophysiology and management of pulmonary infections in cystic fibrosis*. Am J Respir Crit Care Med, 2003. **168**(8): p. 918-51.
117. Yankaskas, J.R., B.C. Marshall, B. Sufian, R.H. Simon, and D. Rodman, *Cystic fibrosis adult care: consensus conference report*. Chest, 2004. **125**(1 Suppl): p. 1S-39S.
118. Sermet-Gaudelus, I., Y. Le Cocguic, A. Ferroni, M. Clairicia, J. Barthe, J.P. Delaunay, V. Brousse, and G. Lenoir, *Nebulized antibiotics in cystic fibrosis*. Paediatr Drugs, 2002. **4**(7): p. 455-67.
119. Yankaskas, J.R. and M.R. Knowles, *Cystic fibrosis in adults*. 1999. Philadelphia: Lippincott-Raven.
120. Mannes, G.P., S. van der Heide, W.M. van Aalderen, and J. Gerritsen, *Itraconazole and allergic bronchopulmonary aspergillosis in twin brothers with cystic fibrosis*. Lancet, 1993. **341**(8843): p. 492.
121. Dennis, C., N. Caine, L. Sharples, R. Smyth, T. Higenbottam, S. Stewart, T. Wreghitt, S. Large, F.C. Wells, and J. Wallwork, *Heart-lung transplantation for end-stage respiratory disease in patients with cystic fibrosis at Papworth Hospital*. J Heart Lung Transplant, 1993. **12**(6 Pt 1): p. 893-902.
122. Gross, C.R., K. Savik, R.M. Bolman, 3rd, and M.I. Hertz, *Long-term health status and quality of life outcomes of lung transplant recipients*. Chest, 1995. **108**(6): p. 1587-93.
123. Yankaskas, J.R. and G.B. Mallory, Jr., *Lung transplantation in cystic fibrosis: consensus conference statement*. Chest, 1998. **113**(1): p. 217-26.
124. Cooper, J.D., M.S. Pohl, and G.A. Patterson, *An update on the current status of lung transplantation: report of the St. Louis International Lung Transplant Registry*. Clin Transpl, 1993: p. 95-100.
125. Senn, J. *Cystic fibrosis and gene therapy*. 1998. Accessed 2014. Available from: <http://www.ndsu.edu/pubweb/~mcclean/plsc431/students98/senn.htm>.
126. Griesenbach, U., D.M. Geddes, and E.W. Alton, *Gene therapy progress and prospects: cystic fibrosis*. Gene Ther, 2006. **13**(14): p. 1061-7.
127. Mueller, C. and T.R. Flotte, *Gene therapy for cystic fibrosis*. Clin Rev Allergy Immunol, 2008. **35**(3): p. 164-78.
128. Ramsey, B.W., *Management of pulmonary disease in patients with cystic fibrosis*. N Engl J Med, 1996. **335**(3): p. 179-88.
129. Knowles, M.R., N.L. Church, W.E. Waltner, J.R. Yankaskas, P. Gilligan, M. King, L.J. Edwards, R.W. Helms, and R.C. Boucher, *A pilot study of aerosolized amiloride for the treatment of lung disease in cystic fibrosis*. N Engl J Med, 1990. **322**(17): p. 1189-94.
130. Tomkiewicz, R.P., E.M. App, J.G. Zayas, O. Ramirez, N. Church, R.C. Boucher, M.R. Knowles, and M. King, *Amiloride inhalation therapy in cystic fibrosis. Influence on ion content, hydration, and rheology of sputum*. Am Rev Respir Dis, 1993. **148**(4 Pt 1): p. 1002-7.
131. Bennett, W.D., K.N. Olivier, K.L. Zeman, K.W. Hohneker, R.C. Boucher, and M.R. Knowles, *Effect of uridine 5'-triphosphate plus amiloride on mucociliary clearance in adult cystic fibrosis*. Am J Respir Crit Care Med, 1996. **153**(6 Pt 1): p. 1796-801.
132. Olivier, K.N., W.D. Bennett, K.W. Hohneker, K.L. Zeman, L.J. Edwards, R.C. Boucher, and M.R. Knowles, *Acute safety and effects on mucociliary*

- clearance of aerosolized uridine 5'-triphosphate +/- amiloride in normal human adults*. Am J Respir Crit Care Med, 1996. **154**(1): p. 217-23.
133. Taylor, R.F., D.W. Morgan, P.S. Nicholson, I.S. Mackay, M.E. Hodson, and T.L. Pitt, *Extrapulmonary sites of Pseudomonas aeruginosa in adults with cystic fibrosis*. Thorax, 1992. **47**(6): p. 426-8.
  134. Usmani, O.S., M.F. Biddiscombe, and P.J. Barnes, *Regional lung deposition and bronchodilator response as a function of beta2-agonist particle size*. Am J Respir Crit Care Med, 2005. **172**(12): p. 1497-504.
  135. Stahlhofen, W., J. Gebhart, and J. Heyder, *Experimental determination of the regional deposition of aerosol particles in the human respiratory tract*. Am Ind Hyg Assoc J, 1980. **41**(6): p. 385-98a.
  136. Murray, J.F. and J.A. Nadel, *Textbook of respiratory medicine*. 1988. Philadelphia: Saunders.
  137. Westmeier, R. and H. Steckel, *Combination particles containing salmeterol xinafoate and fluticasone propionate: Formulation and aerodynamic assessment*. J Pharm Sci, 2008. **97**(6): p. 2299-310.
  138. Corrigan, D.O., O.I. Corrigan, and A.M. Healy, *Physicochemical and in vitro deposition properties of salbutamol sulphate/ipratropium bromide and salbutamol sulphate/excipient spray dried mixtures for use in dry powder inhalers*. Int J Pharm, 2006. **322**(1-2): p. 22-30.
  139. Learoyd, T.P., J.L. Burrows, E. French, and P.C. Seville, *Sustained delivery by leucine-modified chitosan spray-dried respirable powders*. Int J Pharm, 2009. **372**(1-2): p. 97-104.
  140. Adi, H., P.M. Young, H.K. Chan, P. Stewart, H. Agus, and D. Traini, *Cospray dried antibiotics for dry powder lung delivery*. J Pharm Sci, 2008. **97**(8): p. 3356-66.
  141. Adi, S., H. Adi, P. Tang, D. Traini, H.K. Chan, and P.M. Young, *Micro-particle corrugation, adhesion and inhalation aerosol efficiency*. Eur J Pharm Sci, 2008. **35**(1-2): p. 12-8.
  142. Chantrapromma, S., T. Suwunwong, N. Boonnak, and H.K. Fun, *A second ortho-rhom-bic polymorph of (Z)-3-(9-anthr-yl)-1-(2-thien-yl)prop-2-en-1-one*. Acta Crystallogr Sect E Struct Rep Online. **66**(Pt 2): p. o312-3.
  143. Li, X., F.G. Vogt, D. Hayes, Jr., and H.M. Mansour, *Design, characterization, and aerosol dispersion performance modeling of advanced co-spray dried antibiotics with mannitol as respirable microparticles/nanoparticles for targeted pulmonary delivery as dry powder inhalers*. J Pharm Sci, 2014. In Press.
  144. Tong, H.H.Y. and A.H.L. Chow, *Control of physical forms of drug particles for pulmonary delivery by spray drying and supercritical fluid processing*. Kona Powder and Particle Journal, 2006(24): p. 27-40.
  145. Li, X. and H.M. Mansour, *Physicochemical characterization and water vapor sorption of organic solution advanced spray-dried inhalable trehalose microparticles and nanoparticles for targeted dry powder pulmonary inhalation delivery*. AAPS PharmSciTech, 2011. **12**(4): p. 1420-1430.
  146. Alexander, K. and C.J. King, *Factors governing surface-morphology of spray-dried amorphous substances*. Drying Technology, 1985. **3**(3): p. 321-348.

147. Chew, N.Y.K., P. Tang, H.K. Chan, and J.A. Raper, *How much particle surface corrugation is sufficient to improve aerosol performance of powders?* Pharmaceutical Research, 2005. **22**(1): p. 148-152.
148. Liao, Y.H., M.B. Brown, A. Quader, and G.P. Martin, *Investigation of the physical properties of spray-dried stabilised lysozyme particles.* J Pharm Pharmacol, 2003. **55**(9): p. 1213-21.
149. Rodriguez-Spong, B., C.P. Price, A. Jayasankar, A.J. Matzger, and N. Rodriguez-Hornedo, *General principles of pharmaceutical solid polymorphism: a supramolecular perspective.* Adv Drug Deliv Rev, 2004. **56**(3): p. 241-74.
150. Singhal, D. and W. Curatolo, *Drug polymorphism and dosage form design: a practical perspective.* Adv Drug Deliv Rev, 2004. **56**(3): p. 335-47.
151. Giron, D., C. Goldbronn, M. Mutz, S. Pfeffer, P. Piechon, and P. Schwab, *Solid state characterizations of pharmaceutical hydrates.* Journal of Thermal Analysis and Calorimetry, 2002. **68**(2): p. 453-465.
152. Carstensen, J.T., *Pharmaceutics of solids and solid dosage forms.* 1977. New York: Wiley.
153. Carpenter, J.F., M.J. Pikal, B.S. Chang, and T.W. Randolph, *Rational design of stable lyophilized protein formulations: some practical advice.* Pharm Res, 1997. **14**(8): p. 969-75.
154. Meyer, A.S. and C.M. Boyd, *Determination of water by titration with coulometrically generated Karl Fischer reagent.* Analytical Chemistry, 1959. **31**(2): p. 215-219.
155. Maggi, L., R. Bruni, and U. Conte, *Influence of the moisture on the performance of a new dry powder inhaler.* International Journal of Pharmaceutics, 1999. **177**(1): p. 83-91.
156. Hickey, A.J., I. Gonda, W.J. Irwin, and F.J. Fildes, *Effect of hydrophobic coating on the behavior of a hygroscopic aerosol powder in an environment of controlled temperature and relative humidity.* J Pharm Sci, 1990. **79**(11): p. 1009-14.
157. Braun, M.A., R. Oschmann, and P.C. Schmidt, *Influence of excipients and storage humidity on the deposition of disodium cromoglycate (DSCG) in the Twin Impinger.* International Journal of Pharmaceutics, 1996. **135**(1-2): p. 53-62.
158. Chan, H.K., A.R. Clark, J.C. Feeley, M.C. Kuo, S.R. Lehrman, K. Pikal-Cleland, D.P. Miller, R. Vehring, and D. Lechuga-Ballesteros, *Physical stability of salmon calcitonin spray-dried powders for inhalation.* J Pharm Sci, 2004. **93**(3): p. 792-804.
159. Mansour, H.M. and A.J. Hickey, *Raman characterization and chemical imaging of biocolloidal self-assemblies, drug delivery systems, and pulmonary inhalation aerosols: a review.* AAPS PharmSciTech, 2007. **8**(4): p. E99.
160. Park, C.W., Y.S. Rhee, F.G. Vogt, D. Hayes, Jr., J.B. Zwischenberger, P.P. DeLuca, and H.M. Mansour, *Advances in microscopy and complementary imaging techniques to assess the fate of drugs ex vivo in respiratory drug delivery: an invited paper.* Adv Drug Deliv Rev, 2012. **64**(4): p. 344-56.
161. Janaswamy, S. and R. Chandrasekaran, *Heterogeneity in iota-carrageenan molecular structure: insights for polymorph II-->III transition in the presence of calcium ions.* Carbohydr Res, 2008. **343**(2): p. 364-73.

162. Lee, Y.H., J.K. Clegg, L.F. Lindoy, G.Q. Lu, Y.C. Park, and Y. Kim, *A second polymorph with composition Co(3)(PO(4))(2).H(2)O*. Acta Crystallogr Sect E Struct Rep Online, 2008. **64**(Pt 10): p. i69-i70.
163. Romanowski, G., M. Wera, and A. Sikorski, *A monoclinic polymorph of di-mu-oxido-bis-({2-[2-(methyl-amino)ethyl-imino-methyl]phenolato-kappaN, N',O}oxi dovanadium(V))*. Acta Crystallogr Sect E Struct Rep Online, 2008. **64**(Pt 12): p. m1548-9.
164. Basu Baul, T.S., S. Kundu, H.D. Arman, and E.R. Tiekink, *An ortho-rhom-bic polymorph of 5-[(4-methyl-phen-yl)diazen-yl]salicylaldehyde*. Acta Crystallogr Sect E Struct Rep Online, 2009. **65**(Pt 12): p. o3061.
165. Kia, R., H.K. Fun, and H. Kargar, *A second monoclinic polymorph of 4,4'-[butane-1,4-diylbis(nitrilo-methyl-idyne)]dibenzonitrile*. Acta Crystallogr Sect E Struct Rep Online, 2008. **64**(Pt 12): p. o2388.
166. Meenach, S.A., F.G. Vogt, K.W. Anderson, J.Z. Hilt, R.C. McGarry, and H.M. Mansour, *Design, physicochemical characterization, and optimization of organic solution advanced spray-dried inhalable dipalmitoylphosphatidylcholine (DPPC) and dipalmitoylphosphatidylethanolamine poly(ethylene glycol) (DPPE-PEG) microparticles and nanoparticles for targeted respiratory nanomedicine delivery as dry powder inhalation aerosols*. Int J Nanomedicine, 2013. **8**: p. 275-93.
167. Mansour, H.M. and G. Zografi, *The relationship between water vapor absorption and desorption by phospholipids and bilayer phase transitions*. J Pharm Sci, 2007. **96**(2): p. 377-96.
168. Dash, A.K. and R. Suryanayanan, *Solid-state properties of tobramycin*. Pharm Res, 1991. **8**(9): p. 1159-65.
169. Gandhi, R., O. Pillai, R. Thilagavathi, B. Gopalakrishnan, C.L. Kaul, and R. Panchagnula, *Characterization of azithromycin hydrates*. Eur J Pharm Sci, 2002. **16**(3): p. 175-84.
170. Jivraj, I.I., L.G. Martini, and C.M. Thomson, *An overview of the different excipients useful for the direct compression of tablets*. Pharm Sci Technolo Today, 2000. **3**(2): p. 58-63.
171. Burnett, D.J., F. Thielmann, and J. Booth, *Determining the critical relative humidity for moisture-induced phase transitions*. Int J Pharm, 2004. **287**(1-2): p. 123-33.
172. Hulse, W.L., R.T. Forbes, M.C. Bonner, and M. Getrost, *Influence of protein on mannitol polymorphic form produced during co-spray drying*. Int J Pharm, 2009. **382**(1-2): p. 67-72.
173. Yu, L., N. Milton, E.G. Groleau, D.S. Mishra, and R.E. Vansickle, *Existence of a mannitol hydrate during freeze-drying and practical implications*. J Pharm Sci, 1999. **88**(2): p. 196-8.
174. Berquand, A., N. Fa, Y.F. Dufrene, and M.P. Mingeot-Leclercq, *Interaction of the macrolide antibiotic azithromycin with lipid bilayers: effect on membrane organization, fluidity, and permeability*. Pharm Res, 2005. **22**(3): p. 465-75.
175. Burger, A., J.O. Henck, S. Hetz, J.M. Rollinger, A.A. Weissnicht, and H. Stottner, *Energy/temperature diagram and compression behavior of the polymorphs of D-mannitol*. J Pharm Sci, 2000. **89**(4): p. 457-68.

176. Lightbown, J.W. and H. Dixon, *The first International Reference Preparation of Tobramycin*. J Biol Stand, 1982. **10**(2): p. 157-68.
177. Yuan, X.D., B.P. Carter, and S.J. Schmidt, *Determining the Critical Relative Humidity at which the Glassy to Rubbery Transition Occurs in Polydextrose Using an Automatic Water Vapor Sorption Instrument*. Journal of Food Science, 2011. **76**(1): p. E78-E89.
178. <601> Aerosols, Nasal Sprays, Metered-Dose Inhalers, and Dry Powder Inhalers Monograph, in *USP 29-NF 24 The United States Pharmacopoeia and The National Formulary: The Official Compendia of Standards*. 2006, The United States Pharmacopeial Convention, Inc.: Rockville, MD. p. 2617-2636.
179. Odziomek, M., T.R. Sosnowski, and L. Gradon, *Conception, preparation and properties of functional carrier particles for pulmonary drug delivery*. Int J Pharm, 2012. **433**(1-2): p. 51-9.
180. Taki, M., S. Ahmed, C. Marriott, X.M. Zeng, and G.P. Martin, *The 'stage-by-stage' deposition of drugs from commercial single-active and combination dry powder inhaler formulations*. Eur J Pharm Sci, 2011. **43**(4): p. 225-35.
181. Kumar, A., *Nanomedicine in drug delivery*. 2013. Boca Raton: CRC Press/Taylor & Francis Group.
182. Lyapustina, S.A., *Good cascade impactor practices, AIM and EDA for orally inhaled products*. 2013. New York: Springer.
183. Finlay, W.H. *The ARLA respiratory deposition calculator*. 2008. Accessed 2012. Available from: [http://www.mece.ualberta.ca/arla/impactor\\_mmاد\\_calculator.html](http://www.mece.ualberta.ca/arla/impactor_mmاد_calculator.html).
184. Josef, K., M. Heidi, P. Robert, K. Pavel, and T. Marek, *Expression of CD66 in non-Hodgkin lymphomas and multiple myeloma*. Eur J Haematol, 2010. **85**(6): p. 496-501.
185. Baskin, M.I., A.G. Abd, and J.S. Ilowite, *Regional deposition of aerosolized pentamidine. Effects of body position and breathing pattern*. Ann Intern Med, 1990. **113**(9): p. 677-83.
186. Baltimore, R.S., C.D. Christie, and G.J. Smith, *Immunohistopathologic localization of Pseudomonas aeruginosa in lungs from patients with cystic fibrosis. Implications for the pathogenesis of progressive lung deterioration*. Am Rev Respir Dis, 1989. **140**(6): p. 1650-61.
187. Potts, S.B., V.L. Roggli, and A. Spock, *Immunohistologic quantification of Pseudomonas aeruginosa in the tracheobronchial tree from patients with cystic fibrosis*. Pediatr Pathol Lab Med, 1995. **15**(5): p. 707-21.
188. Adler, M., M. Unger, and G. Lee, *Surface composition of spray-dried particles of bovine serum albumin/trehalose/surfactant*. Pharm Res, 2000. **17**(7): p. 863-70.
189. Elversson, J., K. Andersson, and A. Millqvist-Fureby, *An atomic force microscopy approach for assessment of particle density applied to single spray-dried carbohydrate particles*. J Pharm Sci, 2007. **96**(4): p. 905-12.
190. Elversson, J. and A. Millqvist-Fureby, *Particle size and density in spray drying-effects of carbohydrate properties*. J Pharm Sci, 2005. **94**(9): p. 2049-60.

191. Elversson, J., A. Millqvist-Fureby, G. Alderborn, and U. Elofsson, *Droplet and particle size relationship and shell thickness of inhalable lactose particles during spray drying*. J Pharm Sci, 2003. **92**(4): p. 900-10.
192. Costantino, H.R., J.D. Andya, P.A. Nguyen, N. Dasovich, T.D. Sweeney, S.J. Shire, C.C. Hsu, and Y.F. Maa, *Effect of mannitol crystallization on the stability and aerosol performance of a spray-dried pharmaceutical protein, recombinant humanized anti-IgE monoclonal antibody*. J Pharm Sci, 1998. **87**(11): p. 1406-11.
193. Yoshinari, T., R.T. Forbes, P. York, and Y. Kawashima, *Crystallisation of amorphous mannitol is retarded using boric acid*. International Journal of Pharmaceutics, 2003. **258**(1-2): p. 109-120.
194. Bechinger, B., *Detergent-like properties of magainin antibiotic peptides: a 31P solid-state NMR spectroscopy study*. Biochim Biophys Acta, 2005. **1712**(1): p. 101-8.
195. Krishnaswamy, R., V. Rathee, and A.K. Sood, *Aggregation of a peptide antibiotic alamethicin at the air-water interface and its influence on the viscoelasticity of phospholipid monolayers*. Langmuir, 2008. **24**(20): p. 11770-7.
196. Maget-Dana, R., *The monolayer technique: a potent tool for studying the interfacial properties of antimicrobial and membrane-lytic peptides and their interactions with lipid membranes*. Biochim Biophys Acta, 1999. **1462**(1-2): p. 109-40.
197. Olak, C., A. Muentner, J. Andra, and G. Brezesinski, *Interfacial properties and structural analysis of the antimicrobial peptide NK-2*. J Pept Sci, 2008. **14**(4): p. 510-7.
198. Unlu, N., S. Calis, M. Sumnu, and A.A. Hincal, *Evaluation of the interfacial properties of a new potent antimicrobial surfactant C31G*. Boll Chim Farm, 1991. **130**(6): p. 234-8.
199. Weiner, N.D., H.C. Parreira, and G. Zografi, *Interfacial properties of antimicrobial long-chain quaternary ammonium salts. II. Soluble films at the oil-water interface*. J Pharm Sci, 1966. **55**(2): p. 187-91.
200. Weiner, N.D. and G. Zografi, *Interfacial Properties of Antimicrobial Long-Chain Quaternary Ammonium Salts. I. Soluble Films at the Air-Water Interface*. J Pharm Sci, 1965. **54**: p. 436-42.
201. Padhi, B.K., M.B. Chougule, and A. Misra, *Aerosol performance of large respirable particles of amikacin sulfate produced by spray and freeze drying techniques*. Curr Drug Deliv, 2009. **6**(1): p. 8-16.
202. Saleem, I., H. Smyth, and M. Telko, *Prediction of dry powder inhaler formulation performance from surface energetics and blending dynamics*. Drug Dev Ind Pharm, 2008. **34**(9): p. 1002-10.
203. Chew, N.Y.K. and H.K. Chan, *The role of particle properties in pharmaceutical powder inhalation formulations*. Journal of Aerosol Medicine-Deposition Clearance and Effects in the Lung, 2002. **15**(3): p. 325-330.
204. Islam, N., P. Stewart, I. Larson, and P. Hartley, *Effect of carrier size on the dispersion of salmeterol xinafoate from interactive mixtures*. Journal of Pharmaceutical Sciences, 2004. **93**(4): p. 1030-1038.

205. Podczeczek, F., *The relationship between physical properties of lactose monohydrate and the aerodynamic behaviour of adhered drug particles*. International Journal of Pharmaceutics, 1998. **160**(1): p. 119-130.
206. Begat, P., D.A.V. Morton, J.N. Staniforth, and R. Price, *The cohesive-adhesive balances in dry powder inhaler formulations II: Influence on fine particle delivery characteristics*. Pharmaceutical Research, 2004. **21**(10): p. 1826-1833.
207. Young, P.M., D. Cocconi, P. Colombo, R. Bettini, R. Price, D.F. Steele, and M.J. Tobyn, *Characterization of a surface modified dry powder inhalation carrier prepared by "particle smoothing"*. Journal of Pharmacy and Pharmacology, 2002. **54**(10): p. 1339-1344.
208. Zeng, X.M., G.P. Martin, C. Marriott, and J. Pritchard, *Lactose as a carrier in dry powder formulations: The influence of surface characteristics on drug delivery*. Journal of Pharmaceutical Sciences, 2001. **90**(9): p. 1424-1434.
209. *Metered dose inhaler (MDI) and dry powder inhaler (DPI) drug products*, M. Chemistry, and Controls, Editor. 1998, Food and Drug Administration.
210. Rockland, L.B., *Saturated salt solutions for static control of relative humidity between 5-degrees-c and 40-degrees-c*. Analytical Chemistry, 1960. **32**(10): p. 1375-1376.
211. Ogain, O.N., J.H. Li, L. Tajber, O.I. Corrigan, and A.M. Healy, *Particle engineering of materials for oral inhalation by dry powder inhalers. I-Particles of sugar excipients (trehalose and raffinose) for protein delivery*. International Journal of Pharmaceutics, 2011. **405**(1-2): p. 23-35.
212. Nolan, L.M., J.H. Li, L. Tajber, O.I. Corrigan, and A.M. Healy, *Particle engineering of materials for oral inhalation by dry powder inhalers. II-Sodium cromoglicate*. International Journal of Pharmaceutics, 2011. **405**(1-2): p. 36-46.
213. Singh, D.J., J.J. Parmar, D.D. Hegde, A.A. Lohade, P. Soni, A. Samad, and M.D. Menon, *Development and evaluation of dry powder inhalation system of terbutaline sulphate for better management of asthma*. International Journal of Advances in Pharmaceutical Sciences, 2010. **2**: p. 133-141.
214. El-Gendy, N., S. Huang, P. Selvam, P. Soni, and C. Berkland, *Development of budesonide nanocluster dry powder aerosols: formulation and stability*. J Pharm Sci, 2012. **101**(9): p. 3445-55.
215. Pilcer, G., F. Vanderbist, and K. Amighi, *Spray-dried carrier-free dry powder tobramycin formulations with improved dispersion properties*. J Pharm Sci, 2009. **98**(4): p. 1463-75.
216. Hanko, V.P., J.S. Rohrer, H.H. Liu, C. Zheng, S. Zhang, X. Liu, and X. Tang, *Identification of tobramycin impurities for quality control process monitoring using high-performance anion-exchange chromatography with integrated pulsed amperometric detection*. J Pharm Biomed Anal, 2008. **47**(4-5): p. 828-33.
217. Yu, L., *Polymorphism in molecular solids: an extraordinary system of red, orange, and yellow crystals*. Acc Chem Res, 2010. **43**(9): p. 1257-66.
218. Pereira, C.S., R.D. Lins, I. Chandrasekhar, L.C. Freitas, and P.H. Hunenberger, *Interaction of the disaccharide trehalose with a phospholipid bilayer: a molecular dynamics study*. Biophys J, 2004. **86**(4): p. 2273-85.

219. Yoshioka, M., B.C. Hancock, and G. Zografi, *Crystallization of indomethacin from the amorphous state below and above its glass transition temperature*. J Pharm Sci, 1994. **83**(12): p. 1700-5.
220. McConville, J.T., N. Patel, N. Ditchburn, M.J. Tobyn, J.N. Staniforth, and P. Woodcock, *Use of a novel modified TSI for the evaluation of controlled-release aerosol formulations. I. Drug Development and Industrial Pharmacy*, 2000. **26**(11): p. 1191-1198.
221. Park, C.W., X. Li, F.G. Vogt, D. Hayes, J.B. Zwischenberger, E.S. Park, and H.M. Mansour, *Advanced spray-dried design, physicochemical characterization, and aerosol dispersion performance of vancomycin and clarithromycin multifunctional controlled release particles for targeted respiratory delivery as dry powder inhalation aerosols*. International Journal of Pharmaceutics, 2013. **455**(1-2): p. 374-392.
222. Son, Y.J. and J.T. McConville, *Development of a standardized dissolution test method for inhaled pharmaceutical formulations*. International Journal of Pharmaceutics, 2009. **382**(1-2): p. 15-22.
223. Cook, R.O., R.K. Pannu, and I.W. Kellaway, *Novel sustained release microspheres for pulmonary drug delivery*. Journal of Controlled Release, 2005. **104**(1): p. 79-90.
224. O'Hara, P. and A.J. Hickey, *Respirable PLGA microspheres containing rifampicin for the treatment of tuberculosis: Manufacture and characterization*. Pharmaceutical Research, 2000. **17**(8): p. 955-961.
225. Son, Y.J. and J.T. McConville, *Preparation of sustained release rifampicin microparticles for inhalation*. J Pharm Pharmacol, 2012. **64**(9): p. 1291-302.
226. Salama, R.O., D. Traini, H.K. Chan, and P.M. Young, *Preparation and characterisation of controlled release co-spray dried drug-polymer microparticles for inhalation 2: evaluation of in vitro release profiling methodologies for controlled release respiratory aerosols*. Eur J Pharm Biopharm, 2008. **70**(1): p. 145-52.
227. Sung, J.C., D.J. Padilla, L. Garcia-Contreras, J.L. Verberkmoes, D. Durbin, C.A. Peloquin, K.J. Elbert, A.J. Hickey, and D.A. Edwards, *Formulation and pharmacokinetics of self-assembled rifampicin nanoparticle systems for pulmonary delivery*. Pharm Res, 2009. **26**(8): p. 1847-55.
228. El-Sherbiny, I.M., S. McGill, and H.D.C. Smyth, *Swellable Microparticles as Carriers for Sustained Pulmonary Drug Delivery*. Journal of Pharmaceutical Sciences, 2010. **99**(5): p. 2343-2356.
229. El-Sherbiny, I.M. and H.D. Smyth, *Biodegradable nano-micro carrier systems for sustained pulmonary drug delivery: (I) self-assembled nanoparticles encapsulated in respirable/swellable semi-IPN microspheres*. Int J Pharm, 2010. **395**(1-2): p. 132-41.
230. Guzman-Villanueva, D., I.M. El-Sherbiny, D. Herrera-Ruiz, and H.D. Smyth, *Design and in vitro evaluation of a new nano-microparticulate system for enhanced aqueous-phase solubility of curcumin*. Biomed Res Int, 2013. **2013**: p. 724763.
231. El-Sherbiny, I.M. and H.D. Smyth, *Controlled release pulmonary administration of curcumin using swellable biocompatible microparticles*. Mol Pharm, 2012. **9**(2): p. 269-80.



232. Moss, O.R., *Simulants of lung interstitial fluid*. Health Phys, 1979. **36**(3): p. 447-8.
233. Davies, N.M. and M.R. Feddah, *A novel method for assessing dissolution of aerosol inhaler products*. Int J Pharm, 2003. **255**(1-2): p. 175-87.
234. Dennis, N.A., H.M. Blauer, and J.E. Kent, *Dissolution fractions and half-times of single source yellowcake in simulated lung fluids*. Health Phys, 1982. **42**(4): p. 469-77.
235. Ahuja, S. and S. Scypinski, *Handbook of modern pharmaceutical analysis*. Separation science and technology. 2001. San Diego, CA: Academic Press.
236. Zhang, Y., X.L. Liu, Y. Cui, H.F. Huang, N. Chi, and X. Tang, *Aspects of degradation kinetics of azithromycin in aqueous solution*. Chromatographia, 2009. **70**(1-2): p. 67-73.
237. Modi, S., T.X. Xiang, and B.D. Anderson, *Enhanced active liposomal loading of a poorly soluble ionizable drug using supersaturated drug solutions*. J Control Release, 2012. **162**(2): p. 330-9.
238. Wallace, S.J., R.L. Nation, J. Li, and B.J. Boyd, *Physicochemical aspects of the coformulation of colistin and azithromycin using liposomes for combination antibiotic therapies*. J Pharm Sci, 2013. **102**(5): p. 1578-87.
239. Hou, C.D., J.X. Wang, Y. Le, H.K. Zou, and H. Zhao, *Preparation of azithromycin nanosuspensions by reactive precipitation method*. Drug Dev Ind Pharm, 2012. **38**(7): p. 848-54.
240. DrugBank. November 28, 2013; Available from: <http://www.drugbank.ca/drugs/DB00207>.
241. Bakatselou, V., R.C. Oppenheim, and J.B. Dressman, *Solubilization and Wetting Effects of Bile-Salts on the Dissolution of Steroids*. Pharmaceutical Research, 1991. **8**(12): p. 1461-1469.
242. Izutsu, K., C. Yomota, and N. Aoyagi, *Inhibition of mannitol crystallization in frozen solutions by sodium phosphates and citrates*. Chem Pharm Bull (Tokyo), 2007. **55**(4): p. 565-70.
243. Samy, A.M., M.A. Marzouk, A.A. Ammar, and M.K. Ahmed, *Enhancement of the dissolution profile of allopurinol by a solid dispersion technique*. Drug Discov Ther, 2010. **4**(2): p. 77-84.
244. Geller, D.E., W.H. Pitlick, P.A. Nardella, W.G. Tracewell, and B.W. Ramsey, *Pharmacokinetics and bioavailability of aerosolized tobramycin in cystic fibrosis*. Chest, 2002. **122**(1): p. 219-26.
245. Koch, C. and N. Hoiby, *Pathogenesis of cystic fibrosis*. Lancet, 1993. **341**(8852): p. 1065-9.
246. Gehr, P., S. Schurch, M. Geiser, and V.I. Hof, *Retention and Clearance Mechanisms of Inhaled Particles*. Journal of Aerosol Science, 1990. **21**: p. S491-S496.
247. Schurch, S., P. Gehr, V.I. Hof, M. Geiser, and F. Green, *Surfactant Displaces Particles toward the Epithelium in Airways and Alveoli*. Respiration Physiology, 1990. **80**(1): p. 17-32.
248. Gehr, P., M. Geiser, V. Im Hof, S. Schurch, U. Waber, and M. Baumann, *Surfactant and inhaled particles in the conducting airways: structural, stereological, and biophysical aspects*. Microsc Res Tech, 1993. **26**(5): p. 423-36.

249. Geiser, M., S. Schurch, and P. Gehr, *Influence of surface chemistry and topography of particles on their immersion into the lung's surface-lining layer*. Journal of Applied Physiology, 2003. **94**(5): p. 1793-1801.
250. Meers, P., M. Neville, V. Malinin, A.W. Scotto, G. Sardaryan, R. Kurumunda, C. Mackinson, G. James, S. Fisher, and W.R. Perkins, *Biofilm penetration, triggered release and in vivo activity of inhaled liposomal amikacin in chronic Pseudomonas aeruginosa lung infections*. Journal of Antimicrobial Chemotherapy, 2008. **61**(4): p. 859-868.
251. Mansour, H.M., S. Damodaran, and G. Zografi, *Characterization of the in situ structural and interfacial properties of the cationic hydrophobic heteropolypeptide, KL4, in lung surfactant bilayer and monolayer models at the air-water interface: Implications for pulmonary surfactant delivery*. Molecular Pharmaceutics, 2008. **5**(5): p. 681-695.
252. Mansour, H.M., D.S. Wang, C.S. Chen, and G. Zografi, *Comparison of bilayer and monolayer properties of phospholipid systems containing dipalmitoylphosphatidylglycerol and dipalmitoylphosphatidylinositol*. Langmuir, 2001. **17**(21): p. 6622-6632.
253. Mansour, H.M. and G. Zografi, *Relationships between equilibrium spreading pressure and phase equilibria of phospholipid bilayers and monolayers at the air-water interface*. Langmuir, 2007. **23**(7): p. 3809-3819.
254. Miki, K., R. Butler, D. Moore, and G. Davidson, *Rapid and simultaneous quantification of rhamnose, mannitol, and lactulose in urine by HPLC for estimating intestinal permeability in pediatric practice*. Clin Chem, 1996. **42**(1): p. 71-5.
255. Letter, W.S., *A rapid method for phospholipid class separation by HPLC using an evaporative light-scattering detector*. Journal of Liquid Chromatography, 1992. **15**(2): p. 253-266.
256. Fisher, J.T., Y. Zhang, and J.F. Engelhardt, *Comparative biology of cystic fibrosis animal models*. Methods Mol Biol, 2011. **742**: p. 311-34.
257. Elphick, H. and K. Southern, *Antifungal therapies for allergic bronchopulmonary aspergillosis in people with cystic fibrosis*. Cochrane Database Syst Rev, 2000(4): p. CD002204.
258. Karamertzanis, P.G., P. Raiteri, M. Parrinello, M. Leslie, and S.L. Price, *The thermal stability of lattice-energy minima of 5-fluorouracil: metadynamics as an aid to polymorph prediction*. J Phys Chem B, 2008. **112**(14): p. 4298-308.
259. Horchani-Naifer, K., A. Jouini, and M. Ferid, *A monoclinic polymorph of KY(PO<sub>3</sub>)(4)*. Acta Crystallogr Sect E Struct Rep Online, 2008. **64**(Pt 6): p. i34.
260. Wu, X., X. Li, and H.M. Mansour, *Surface Analytical Techniques in Solid-State Particle Characterization: Implications for Predicting Performance in Dry Powder Inhalers*. KONA Powder & Particle Journal, 2010(28): p. 3-19.
261. Erdemir, D., A.Y. Lee, and A.S. Myerson, *Polymorph selection: the role of nucleation, crystal growth and molecular modeling*. Curr Opin Drug Discov Devel, 2007. **10**(6): p. 746-55.
262. Xu, Z., H.M. Mansour, T. Mulder, R. McLean, J. Langridge, and A.J. Hickey, *Heterogeneous particle deaggregation and its implication for therapeutic aerosol performance*. J Pharm Sci, 2010. **99**(8): p. 3442-61.

263. Adi, H., D. Traini, H.K. Chan, and P.M. Young, *The influence of drug morphology on aerosolisation efficiency of dry powder inhaler formulations*. J Pharm Sci, 2008. **97**(7): p. 2780-8.
264. Tiddens, H.A., *Detecting early structural lung damage in cystic fibrosis*. Pediatr Pulmonol, 2002. **34**(3): p. 228-31.
265. Worlitzsch, D., R. Tarran, M. Ulrich, U. Schwab, A. Cekici, K.C. Meyer, P. Birrer, G. Bellon, J. Berger, T. Weiss, K. Botzenhart, J.R. Yankaskas, S. Randell, R.C. Boucher, and G. Doring, *Effects of reduced mucus oxygen concentration in airway Pseudomonas infections of cystic fibrosis patients*. J Clin Invest, 2002. **109**(3): p. 317-25.
266. Raabe, O.G., *Comparison of the criteria for sampling 'inhalable' and 'respirable' aerosols*. Ann Occup Hyg, 1982. **26**(1-4): p. 33-45.
267. Teper, A., A. Jaques, and B. Charlton, *Inhaled mannitol in patients with cystic fibrosis: A randomised open-label dose response trial*. Journal of Cystic Fibrosis, 2011. **10**(1): p. 1-8.
268. Daviskas, E., S.D. Anderson, S. Eberl, H.K. Chan, and I.H. Young, *The 24-h effect of mannitol on the clearance of mucus in patients with bronchiectasis*. Chest, 2001. **119**(2): p. 414-21.
269. Wills, P.J. and P.J. Cole, *Mucolytic and mucokinetic therapy*. Pulm Pharmacol, 1996. **9**(4): p. 197-204.
270. Brannan, J.D., M. Gulliksson, S.D. Anderson, N. Chew, and M. Kumlin, *Evidence of mast cell activation and leukotriene release after mannitol inhalation*. European Respiratory Journal, 2003. **22**(3): p. 491-6.
271. Daviskas, E. and S.D. Anderson, *Hyperosmolar agents and clearance of mucus in the diseased airway*. Journal of Aerosol Medicine-Deposition Clearance and Effects in the Lung, 2006. **19**(1): p. 100-9.
272. Jaques, A., E. Daviskas, J.A. Turton, K. McKay, P. Cooper, R.G. Stirling, C.F. Robertson, P.T. Bye, P.N. Lesouef, B. Shadbolt, S.D. Anderson, and B. Charlton, *Inhaled mannitol improves lung function in cystic fibrosis*. Chest, 2008. **133**(6): p. 1388-96.
273. Takada, A., S.L. Nail, and M. Yonese, *Influence of ethanol on physical state of freeze-dried mannitol*. Pharm Res, 2009. **26**(5): p. 1112-20.
274. Quan, L., H. Yin, and D. Wang, *A monoclinic polymorph of (nitrate-kappaO)tetra-phenyl-anti-mony(V)*. Acta Crystallogr Sect E Struct Rep Online, 2008. **65**(Pt 1): p. m23.
275. Frey, W., S. Schetter, F. Rominger, and A.S. Hashmi, *A new polymorph of N-(prop-2-yn-yl)tricyclo-[3.3.1.1]decane-1-carbox-amide*. Acta Crystallogr Sect E Struct Rep Online, 2008. **64**(Pt 8): p. o1495.
276. Nunes, C., R. Suryanarayanan, C.E. Botez, and P.W. Stephens, *Characterization and crystal structure of D-mannitol hemihydrate*. J Pharm Sci, 2004. **93**(11): p. 2800-9.
277. Mitchell, H., *Sweeteners and sugar alternatives in food technology*. 2006. Oxford ; Ames, Iowa: Blackwell Pub.
278. Ye, P. and T. Byron, *Characterization of D-Mannitol by Thermal Analysis, FTIR, and Raman Spectroscopy*. American Laboratory, 2008. **40**(14): p. 24-27.
279. Tang, P., H.K. Chan, H. Chiou, K. Ogawa, M.D. Jones, H. Adi, G. Buckton, R.K. Prud'homme, and J.A. Raper, *Characterisation and aerosolisation of*

- mannitol particles produced via confined liquid impinging jets*. Int J Pharm, 2009. **367**(1-2): p. 51-7.
280. Kumon, M., P.C. Kwok, H. Adi, D. Heng, and H.K. Chan, *Can low-dose combination products for inhalation be formulated in single crystalline particles?* Eur J Pharm Sci, 2010. **40**(1): p. 16-24.
  281. Tong, P. and G. Zografi, *Effects of water vapor absorption on the physical and chemical stability of amorphous sodium indomethacin*. AAPS PharmSciTech, 2004. **5**(2): p. e26.
  282. Yoshinari, T., R.T. Forbes, P. York, and Y. Kawashima, *Moisture induced polymorphic transition of mannitol and its morphological transformation*. Int J Pharm, 2002. **247**(1-2): p. 69-77.
  283. Donovan, M.J., S.H. Kim, V. Raman, and H.D. Smyth, *Dry powder inhaler device influence on carrier particle performance*. J Pharm Sci, 2011. **101**(3): p. 1097-107.
  284. Hickey, A.J., *Inhalation aerosols : physical and biological basis for therapy*. 2nd ed. Lung biology in health and disease. 2007. New York: Informa Healthcare.
  285. Katzenstein, A.L. and J.L. Myers, *Idiopathic pulmonary fibrosis: clinical relevance of pathologic classification*. Am J Respir Crit Care Med, 1998. **157**(4 Pt 1): p. 1301-15.
  286. Sethi, S., R. Sethi, K. Eschberger, P. Lobbins, X. Cai, B.J. Grant, and T.F. Murphy, *Airway bacterial concentrations and exacerbations of chronic obstructive pulmonary disease*. Am J Respir Crit Care Med, 2007. **176**(4): p. 356-61.
  287. Park, C.W., D.J. Hayes, and H.M. Mansour, *Pulmonary Inhalation Aerosols for Targeted Antibiotics Drug Delivery. Invited Paper*. European Pharmaceutical Review., 2011. **16**(1): p. 32-36.
  288. Rhee, Y.S. and H.M. Mansour, *Nanopharmaceuticals I: Nanocarrier Systems in Drug Delivery. Invited Paper*. International Journal of Nanotechnology: Special Issue-Nanopharmaceuticals., 2011. **8**((1/2)): p. 84-114.
  289. Wu, X. and H.M. Mansour, *Nanopharmaceuticals II: Application of Nanoparticles and Nanocarrier Systems in Pharmaceutics and Nanomedicine. Invited Paper*. International Journal of Nanotechnology: Special Issue-Nanopharmaceuticals., 2011. **8**((1/2)): p. 115-145.
  290. Patton, J.S. and P.R. Byron, *Inhaling medicines:delivering drugs to the body through the lungs*. Nature Reviews Drug Discovery, 2007. **6**(1): p. 67-74.
  291. Zeng, X.M., G.P. Martin, and C. Marriott, *Particulate Interactions in Dry Powder Formulations for Inhalation*. 2001. New York, NY: Taylor & Francis.
  292. Chacon, M., J. Molpeceres, L. Berges, M. Guzman, and M.R. Aberturas, *Stability and freeze-drying of cyclosporine loaded poly(D,L lactide-glycolide) carriers*. Eur J Pharm Sci, 1999. **8**(2): p. 99-107.
  293. Abdelwahed, W., G. Degobert, S. Stainmesse, and H. Fessi, *Freeze-drying of nanoparticles: formulation, process and storage considerations*. Adv Drug Deliv Rev, 2006. **58**(15): p. 1688-713.
  294. Lo, Y.L., J.C. Tsai, and J.H. Kuo, *Liposomes and disaccharides as carriers in spray-dried powder formulations of superoxide dismutase*. J Control Release, 2004. **94**(2-3): p. 259-72.

295. Andya, J.D., Y.F. Maa, H.R. Costantino, P.A. Nguyen, N. Dasovich, T.D. Sweeney, C.C. Hsu, and S.J. Shire, *The effect of formulation excipients on protein stability and aerosol performance of spray-dried powders of a recombinant humanized anti-IgE monoclonal antibody*. Pharm Res, 1999. **16**(3): p. 350-8.
296. Garmise, R.J., H.F. Staats, and A.J. Hickey, *Novel dry powder preparations of whole inactivated influenza virus for nasal vaccination*. AAPS PharmSciTech, 2007. **8**(4): p. article E81.
297. Crowe, L.M., D.S. Reid, and J.H. Crowe, *Is trehalose special for preserving dry biomaterials?* Biophys J, 1996. **71**(4): p. 2087-93.
298. Surana, R., A. Pyne, and R. Suryanarayanan, *Effect of aging on the physical properties of amorphous trehalose*. Pharm Research, 2004. **21** (5): p. 867-874.
299. Fakes, M.G., M.V. Dali, T.A. Haby, K.R. Morris, S.A. Varia, and A.T. Serajuddin, *Moisture sorption behavior of selected bulking agents used in lyophilized products*. PDA J Pharm Sci Technol, 2000. **54**(2): p. 144-149.
300. Surana, R., A. Pyne, and R. Suryanarayanan, *Effect of preparation method on physical properties of amorphous trehalose*. Pharmaceutical Research, 2004. **21**: p. 1167-1176.
301. Moran, A. and G. Buckton, *Studies of the Crystallization of Amorphous Trehalose Using Simultaneous Gravimetric Vapor Sorption/Near IR (GVS/NIR) and "Modulated" GVS/NIR*. AAPS PharmSciTech, 2009. **10**(1): p. 297-302.
302. Moran, A. and G. Buckton, *Adjusting and understanding the properties and crystallisation behaviour of amorphous trehalose as a function of spray drying feed concentration*. International Journal of Pharmaceutics, 2007. **343**(1-2): p. 12-17.
303. Steckel, H. and N. Bolzen, *Alternative Sugars As Potential Carriers For Dry Powder Inhalations*. International Journal of Pharmaceutics 2004. **270**(1-2): p. 297-306.
304. Bosquillon, C., C. Lombry, V. Preat, and R. Vanbever, *Influence of formulation excipients and physical characteristics of inhalation dry powders on their aerosolization performance*. J Control Release, 2001. **70**(3): p. 329-39.
305. Vehring, R., *Pharmaceutical particle engineering via spray drying*. Pharm Res, 2008. **25**(5): p. 999-1022.
306. Masters, K., *Spray drying handbook*. 5th ed. 1991. Burnt Mill, Harlow, Essex, England, New York: Longman Scientific & Technical, Wiley.
307. Horvat, M., E. Mestrovic, A. Danilovski, and D.Q. Craig, *An investigation into the thermal behaviour of a model drug mixture with amorphous trehalose*. Int J Pharm, 2005. **294**(1-2): p. 1-10.
308. Jones, M.D., J.C. Hooton, M.L. Dawson, A.R. Ferrie, and R. Price, *Dehydration of trehalose dihydrate at low relative humidity and ambient temperature*. Int J Pharm, 2006. **313**(1-2): p. 87-98.
309. Taylor, L.S. and P. York, *Characterization of the phase transitions of trehalose dihydrate on heating and subsequent dehydration*. J Pharm Sci, 1998. **87**(3): p. 347-55.
310. Marsac, P.J., A.C. Rumondor, D.E. Nivens, U.S. Kestur, L. Stanciu, and L.S. Taylor, *Effect of temperature and moisture on the miscibility of amorphous*

- dispersions of felodipine and poly(vinyl pyrrolidone)*. J Pharm Sci. **99**(1): p. 169-85.
311. Takeuchi, H., T. Yasuji, H. Yamamoto, and Y. Kawashima, *Temperature- and moisture-induced crystallization of amorphous lactose in composite particles with sodium alginate prepared by spray-drying*. Pharm Dev Technol, 2000. **5**(3): p. 355-63.

## **Vita**

### **Xiaojian Li**

Place of Birth: Wenzhou, China

#### **EDUCATION**

2008-present	Ph.D. Candidate in Pharmaceutical Sciences, University of Kentucky, Lexington, KY, USA
2006-2008	M.S. in Pharmaceutical Sciences, University of Toledo, Toledo, Ohio, USA
2001-2005	B.S. in Pharmaceutical Sciences, Zhejiang University, Hangzhou, Zhejiang, China

#### **PROFESSIONAL EXPERIENCES**

2008-2014	Teaching/Research Assistant, College of Pharmacy, University of Kentucky
2013 (June-August)	Summer Intern, Pharmaceutical Development, Boehringer Ingelheim Pharmaceuticals, Ridgefield, CT, USA
2006-2008	Teaching Assistant, College of Pharmacy, University of Toledo

#### **HONORS/AWARDS**

1. S. Elizabeth Helton Memorial Scholarship Fund Spring Graduate Student Travel Award, 2012
2. UK Center of Membrane Sciences (CMS) Graduate Student Mentoring Fellowship (sponsored by UK CMS Endowment Award), 2010-2011
3. Graduate School Academic Year Fellowship, 2009-2010
4. Daniel R. Reedy Quality Achievement Fellowship Awards, 2008-2011
5. The Third Prize of Excellent Undergraduate Scholarship, 2001 – 2002

## PUBLICATIONS

### a) Full-Papers

1. **Li, X.**, Vogt, F.G., Hayes, D.Jr. and Mansour, H.M. *Design, Characterization, and Aerosol Dispersion Performance Modeling of Advanced Co-Spray Dried Antibiotics with Mannitol as Respirable Microparticles/Nanoparticles for Targeted Pulmonary Delivery from Dry Powder Inhalers.* (2014) Journal of Pharmaceutical Sciences: George Zografi Dedicated Issue (In press).
2. **Li, X.**, Vogt, F.G., Hayes, D.Jr. and Mansour, H.M. *Design, Characterization, and Aerosol Dispersion Performance Modeling of Organic Solution Advanced Spray Dried Microparticulate/Nanoparticulate Mannitol Powders for Targeted Pulmonary Delivery as Dry Powder Inhalation Aerosol.* Journal of Aerosol Medicine and Pulmonary Drug Delivery: 2013 ISAM World Congress Special Issue (2014) 27 (2): 81-93.
3. **Li, X.**, Vogt, F.G., Hayes, D.Jr. and Mansour, H.M. *Physicochemical Characterization and Aerosol Dispersion Performance of Organic Solution Advanced Spray Dried Microparticulate/Nanoparticulate Antibiotic Dry Powders of Tobramycin and Azithromycin for Pulmonary Inhalation Aerosol Delivery.* European Journal of Pharmaceutical Sciences (2014) 52: 191-205.
4. Zheng, Z., Zhang, W., Sun, W., **Li, X.**, Duan, J., Cui, J., Feng, Z., and Mansour, H.M. *Influence of the Carboxymethyl Chitosan Anti-Adhesion Solution on the TGF- $\beta$ 1 in a Postoperative Peritoneal Adhesion Rat.* Journal of Materials Sciences: Materials in Medicine (2013) 24 (11): 2549-2559.
5. Duan, J., Vogt, G.F., **Li, X.**, Hayes, D.Jr., and Mansour, H.M. *Design, Characterization and Aerosolization of Organic Solution Advanced Spray-Dried Moxifloxacin and Ofloxacin Dipalmitoylphosphatidylcholine (DPPC) Microparticulate/Nanoparticulate Powders for Pulmonary Inhalation Aerosol Delivery.* International Journal of Nanomedicine (2013) 8: 3489-3505.
6. Park, C.W., **Li, X.**, Vogt, G.F., Hayes, D.Jr., Zwischenberger, J.B., Park, E.S. and Mansour, H.M. *Advanced Spray-Dried Design, Physicochemical Characterization, and Aerosol Dispersion Performance of Vancomycin and Clarithromycin Multifunctional Controlled Release Particles for Targeted Respiratory Delivery as Dry Powder Inhalation Aerosols.* International Journal of Pharmaceutics (2013) 455 (1-2): 374-392.
7. **Li, X.** and Mansour, H.M. *Physicochemical Characterization and Water Vapor Sorption of Advanced Spray Dried Trehalose Microparticles and Nanoparticles in the Solid-state for Targeted Pulmonary Delivery as Dry Powders.* *An Invited Paper.* AAPS PharmSciTech: Special Issue-Advances in Pharmaceutical Excipients Research and Use: Novel Materials, Functionalities and Testing (2011) 12 (4): 1420-1430.
8. Wu, X., **Li, X.** and Mansour, H.M. *Surface Analytical Techniques in Solid-State Particle Characterization: Implications for Predicting Performance in Dry Powder Inhalers.* *An Invited Paper.* KONA Powder and Particle Journal (2010) 28: 1-19.



9. **Li, X.** and Alexander, K.S. *The Proteins Used As Sweeteners: A Review.* International Journal of Pharmaceutical Compounding (2007) 11 (6): 477-481.
- b) **Abstracts**
10. **Li, X.,** Hayes, D.Jr., and Mansour, H.M. *Targeted Lung Delivery by Inhalable Multifunctional Microparticulate/Nanoparticulate Aerosols for Cystic Fibrosis Combination Drug/Mucolytic Treatment.* Pediatric Pulmonology Journal (2011) 34: 346.
11. **Li, X.,** Vogt, G.F., Hayes, D.Jr, and Mansour, H.M. *Design and Aerosol Dispersion Performance of Organic Solution Advanced Spray-Dried Microparticulate/Nanoparticulate Mucolytic Powders for Targeted Pulmonary Delivery as Dry Powder Inhalers in Cystic Fibrosis.* Pediatric Pulmonology Journal (2012) 47: 360-361.

## PRESENTATIONS/MEETINGS

1. **Li, X.,** Vogt, F.G., Hayes, D.Jr. and Mansour, H.M. *Physicochemical Characterization and Aerosol Dispersion Performance of Organic Solution Advanced Co-Spray Dried Multifunctional Microparticulate/Nanoparticulate Antimicrobial Aerosol Formulations for Targeted Pulmonary Delivery as Dry Powder Inhalers for the Treatment of Cystic Fibrosis.* American Association of Pharmaceutical Scientists (AAPS) Annual Meeting & Exposition (Poster), San Antonio, TX. November 2013
2. **Li, X.,** Vogt, F.G., Hayes, D.Jr. and Mansour, H.M. *Design and Aerosol Dispersion Performance of Organic Solution Advanced Spray Dried Microparticulate/Nanoparticulate Mucolytic Powders for Targeted Pulmonary Delivery as Dry Powder Inhalers.* American Association of Pharmaceutical Scientists (AAPS) Annual Meeting & Exposition (Poster), Chicago, IL. October 2012
3. **Li, X.,** Vogt, F.G., Hayes, D.Jr. and Mansour, H.M. *Design and Aerosol Dispersion Performance of Organic Solution Advanced Co-Spray Dried Multifunctional Microparticulate/Nanoparticulate Aerosol Formulations for Targeted Pulmonary Delivery as Dry Powder Inhalers.* American Association of Pharmaceutical Scientists (AAPS) Annual Meeting & Exposition (Poster), Chicago, IL. October 2012
4. **Li, X.,** Vogt, F.G., Hayes, D.Jr. and Mansour, H.M. *Design and Aerosol Dispersion Performance of Multifunctional Microparticulate/Nanoparticulate Aerosol Formulations for Targeted Pulmonary Delivery as Dry Powder Inhalers for Cystic Fibrosis Treatment.* North American Cystic Fibrosis Conference (NACFC) Annual Meeting & Exhibition (Poster), Orlando, FL. October 2012
5. **Li, X.,** Hayes, D.Jr. and Mansour, H.M. *Advanced Spray-Dried Microparticles/Nanoparticles of Antibiotics and a Mucolytic in the Solid-State for Cystic Fibrosis Treatment by Targeted Pulmonary Delivery.* UK COP

- Symposium on Drug Discovery and Development (Poster), Lexington KY, September 2012
6. **Li, X.**, Hayes, D.Jr. and Mansour, H.M. *Targeted Lung Delivery by Inhalable Multifunctional Microparticulate/Nanoparticulate Aerosols for Cystic Fibrosis Combination Drug/Mucolytic Treatment*. North American Cystic Fibrosis Conference (NACFC) Annual Meeting & Exhibition (Poster), Anaheim, CA. November 2011
  7. **Li, X.**, Hayes, D.Jr. and Mansour, H.M. *Advanced Spray-Dried Microparticulate/Nanoparticulate Powders for Cystic Fibrosis Treatment by Targeted Pulmonary Delivery*. American Association of Pharmaceutical Scientists (AAPS) Annual Meeting & Exposition (Poster), Washington, DC. October 2011
  8. **Li, X.**, Hayes, D.Jr. and Mansour, H.M. *Advanced Spray-Dried Microparticles/Nanoparticles of Antibiotics and a Mucolytic in the Solid-State for Cystic Fibrosis Treatment by Targeted Pulmonary Delivery*. Controlled Release Society (CRS) Annual Meeting & Exposition (Poster), National Harbor, MD. July-August 2011
  9. **Li, X.** and Mansour, H.M. *Quality-By-Design for Excipient Functionality: Advanced Spray-Dried Trehalose Microparticles and Nanoparticles for Targeted Pulmonary Inhalation Delivery*. International Pharmaceutical Excipient Council (IPEC) Excipient Fest (Poster), Baltimore, MD. May 2011
  10. **Li, X.**, Hayes, D.Jr. and Mansour, H.M. *Targeted Pulmonary Delivery by Multifunctional Microparticulate/Nanoparticulate Pharmaceutical Inhalation Aerosols for Cystic Fibrosis Combination Drug/Mucolytic Treatment*. European Cystic Fibrosis Society (ECFS) Basic Science Conference (Poster), Tirrenia-Pisa, Italy. March-April 2011
  11. **Li, X.**, Hayes, D.Jr. and Mansour, H.M. *Comparison of Advanced Spray Dried Micro/Nanoparticulate Aerosols of Antibiotics, Tobramycin and Azithromycin, in the Solid-state for Cystic Fibrosis Treatment: I. Manufacture and Characterization of Pure Components*. UK COP Symposium on Drug Discovery and Development (Poster), Lexington KY, October 2010
  12. **Li, X.** and Mansour, H.M. *Physicochemical Characterization of Advanced Spray Dried Trehalose Microparticles and Nanoparticles in the Solid-state for Pulmonary Delivery*. UK COP Symposium on Drug Discovery and Development (Poster), Lexington KY, October 2010
  13. **Li, X.** and Mansour, H.M. *Physicochemical Characterization of Advanced Spray Dried Trehalose Microparticles and Nanoparticles in the Solid-state for Pulmonary Delivery*. Pharmaceutics Graduate Students Research Meeting (Poster), Columbus OH, June 2010
  14. **Li, X.** and Mansour, H.M. *Overview of Pulmonary Drug Delivery* (May 2009); *Advanced Multifunctional Inhalation Aerosol for Cystic Fibrosis* (March 2010); *Multifunctional Dry Powder Aerosols for the Treatment of Cystic Fibrosis* (March 2011); *Multifunctional Dry Powder Aerosols for the Treatment of Cystic Fibrosis (Fungal Infection)* (December 2011). UK College of Pharmacy Department Seminar, Lexington KY
  15. Pharmaceutics Graduate Students Research Meeting, West Lafayette IN, June

2009

16. **Li, X.**, Alexander, K.S. and Riga, A.T. *Polymorphism and Isothermal Crystallization Study of Sulfapyridine*. Pharmaceutics Graduate Students Research Meeting (Poster), Ann Arbor MI, June 2008
17. **Li, X.**, Alexander, K.S. and Riga, A.T. *Study on the Crystalline and Amorphous Thermal Kinetics of Lidocaine Hydrochloride, Prozac and Sulfapyridine*. North American Thermal Analysis Society annual conference (Presentation), East Lansing MI, August 2007
18. **Li, X.**, Alexander, K.S. and Riga, A.T. *Crystallization Behaviour of Sulfapyridine, Fluoxetine Hydrochloride and Lidocaine Hydrochloride*. Annual Great Lake Symposium (Poster), Pittsburgh PA, July 2007
19. NETZSCH Technical Seminar, Detroit MI, October 2007

Xiaojian Li  
\_\_\_\_\_  
Student's Signature

04/11/2014  
\_\_\_\_\_  
Date